ELECTRON-OPTICAL PROPERTIES

OF SINGLE-POLE MAGNETIC ELECTRON LENSES

A Thesis submitted for the Degree

of

DOCTOR OF PHILOSOPHY

in

The University of Aston in Birmingham

by

FATHI ZAKARIA ALI MARAI, B.Sc., M.Sc.

May, 1977

Department of Physics

SUMMARY

Electron optical properties of single-pole magnetic electron lenses.

Fathi Zakaria Ali Marai, Ph.D., 1977.

The thesis is concerned with the study of single-polepiece lens characteristics. These show, among other things, that the correction of spiral distortion in the electron microscope is feasible with a projector system using single-polepiece lenses for the intermediate and final projector lenses. It is shown that the optimum design for such a system is two single-pole lenses facing each other, in which the intermediate lens, with large bore, works as a correcting lens. Such an arrangement has the advantage of increasing the field of view and considerably reducing the length of the viewing chamber compared with that of current electron microscopes, especially high voltage electron microscopes. A critical appraisal of Scherzer's equation for the spiral distortion coefficient shows why it is difficult to design a correcting system for spiral distortion consisting entirely of conventional electron lenses.

Calculations for iron-free coils, which are relevant to superconducting windings have also been made. These show that there is a real optimum shape for such a lens, when used as an objective, in order to have minimum spherical aberration. However no such optimum could be found for coil lenses when used as projectors.

It is shown that the focal properties and aberration of practical single-polepiece lenses, can be deduced from the focal properties of the little known mathematical model of the exponential field distribution of Glaser. Finally some experimental results are described showing the feasibility of an improved high voltage projector lens and the possibility of correcting spiral distortion in magnetic projector lenses.

Key Words:

electron-optics, electron-microscopy, magnetic lens, aberration correction, lens computation.

LIST OF FIGURES

List of Symbols

$A(z)$	distance function ($A(z) = B(z)/NI$) used in the electron optical properties computations.
a	half of the half width of Glaser's "bell-shaped" field.
B	flux density.
C_c	chromatic aberration coefficient.
C_d	radial distortion coefficient.
C_s	spherical aberration coefficient.
C_{sp}	spiral distortion coefficient.
D	diameter.
D_{rad}	radial distortion coefficient ($D_{rad} = C_d/R^2$), ($D_{rad} = \frac{F}{G}$)
D_{sp}	spiral distortion coefficient ($D_{sp} = C_{sp}/R^2$), ($D_{sp} = \frac{F}{G}$)
$\bar{D}_{sp}$	the contribution to the spiral distortion coefficient from an intermediate individual element of the field distribution.
d	half width of the exponential field distribution.
e	electron charge.
F	general expression for the radial distortion coefficient from combined electrostatic and magnetic fields, given by Scherzer.
F'	general expression for spiral distortion coefficient from combined electrostatic and magnetic fields given by Scherzer.
f	focal length
G	magnification as used by Scherzer.
I	current.
K	excitation parameter ($K^2 = eB^2/8mV$)
k	excitation parameter ($k^2 = a^2eb^2/8mV$)
L	projection distance
ℓ	separation distance between two field distributions in a correcting system for spiral distortion.
M	magnification parameter $\left(M = \frac{fp_o}{f_p}\right)$

m	mass of electron.
N	number of turns.
n	integer number.
Pl	principal plane.
Q_{rad}	radial distortion parameter of magnetic electron lens ($Q_{rad} = \sqrt{D_{rad}}\ f_p$)
Q_{sp}	spiral distortion parameter of magnetic electron lens ($Q_{sp} = D_{sp}^{\frac{1}{2}}\ f_p$)
R	radius.
r	height of the beam from the axis.
S	gap width of the lens or width of the field distribution or coil winding.
U	distance of the source from the lens.
V	accelerating voltage.
V_r	relativistically corrected accelerating voltage.
v	distance of the image of the source from the lens.
X	ray solution to the paraxial ray equation with the condition $Xo_{z = -\infty} = Z - Z_o$ and $Xo'_{z = -\infty} = 1$
Y	ray solution to the paraxial ray equation with the condition $Y_o = 1$ and $Y'_o = o$
Z	distance along the axis of the lens
Z_f	focal point
Z_i	position of image plane
Z_o	position of object.
Z_p	the intersect point with the axis of the asypotatic to the ray at the end of the field.
Z_{pl}	position of principal plane.

θ angle of rotation of the image caused by the magnetic field of the lens.

ζ paraxial ray parameter for the exponential field distribution $\left(\zeta = \frac{k}{\ln^2} e^{-\ln 2 \frac{z}{d}}\right)$

ω paraxial ray parameter for the "bell-shaped" field $(\omega^2 = 1 + k^2)$

χ ray solution to the paraxial ray equation with the condition at the object plane $\chi_o = 0$ and $\chi_o' = 1$

ACKNOWLEDGMENTS

The author wishes to express his thanks to Professor T. Mulvey for his kind supervision and for his many helpful discussions throughout the course of the present investigation.

Thanks are due to the authorities of Assiut University in Egypt for granting study leave and to the Egyptian Government for financial support.

The author also wishes to thank Mr. E. Lambrakis for his assistance with some of the experiments carried out on the Intercol Electron-optical bench, and Mr. R. Keen for his general assistance in the experimental testing of the high voltage electron lens and the system for correcting spiral distortion. Thanks are also due to Mr. A. Al-Shwaikh for proof reading the thesis.

The author is grateful to the Rutherford Laboratory for computing the flux density distribution in the high voltage lens by means of their specialized computer program.

CONTENTS

1. INTRODUCTION

1.1 Progress in electron microscopy

1.1.1 The Transmission Electron Microscope (TEM)

In 1933, the first transmission electron microscope surpassing the optical microscope in resolution was built by Ruska. Since that time many attempts have been made to improve the quality of the electron microscope image so as to increase its usefulness in many fields of practical application. The improvements were concerned essentially, with the vacuum system, the electron gun and the electro-static and magnetic electron lenses. These improvements lead to high magnification and high resolution. In this respect, the search for a perfect lens, having minimum electron-optical defects, was necessary. Many theoreticians, such as Walter Glaser and Otto Scherzer to name only two, worked out the fundamentals of electron optics. In parallel with this, the work of developing the electron microscope itself, was carried out by Ruska, Brüche, Mahl, Marton and many others. In spite of these efforts, the distortions in the final image produced in the electron microscopes are still one of the most important problems in electron optics and electron microscopy, especially the anisotropic spiral distortion. To reduce this distortion, it was necessary, in conventional electron microscopes, to increase the length of the final projector stage, the so-called "projection distance" between lens and viewing screen, in order to restrict the image to rays passing close as possible to the electron-optical axis. This reduces the field of view as well as increasing the size and therefore the cost of the instrument. In this thesis, we shall discuss the properties of a new kind of lens, the "single-pole lens" and the advantages of using it in the projector system of an electron microscope.

1.1.2 Scanning electron microscope (SEM)

The study of solid specimens and surfaces requires a different instrument from the transmission electron microscope. This is the scanning electron microscope (SEM) employing scanning coils that scan an electron probe across the specimen under investigation. This kind of electron microscope uses demagnifying lenses to form the electron probe, and an image is produced using secondary electrons from the specimen. Generally speaking, the resolution in scanning electron microscopes is poorer than that of transmission electron microscopes, but this is accepted as the price for its advantage in using thick specimens. Crewe and his collaborators achieved better resolution in a scanning microscope, by forming the image sequentially, point-by-point, in a thin transmission specimen, which scanned by a small electron probe of atomic dimension. This instrument is known as the scanning transmission electron microscope (STEM). Such an instrument can also benefit from the new types of lenses investigated here.

1.1.3 High voltage electron microscope (HVEM)

The main defect that together with the electron wavelength limits the resolution in electron microscopes is the spherical aberration of the objective lens. The resolving power of an electron microscope can in principle be improved by employing high accelerating voltages. Increasing the accelerating voltage from 100 KV to 1000 KV should improve the resolving power by a factor of two. This is the starting point in building a high resolution electron microscope. The first very high voltage electron microscope (1.5 MV) was built in France by Gaston Dupouy; the first micrographs were obtained in 1960. Because of technological difficulties this instrument did not in fact surpass the 100 KV TEM in resolving power. The interest in building and improving high voltage electron microscopes has since been continued in many places. In the Cavendish Laboratory, Cosslett and Smith produced a 750 KV instrument which formed the prototype for the AEI EM7 million volt microscope. In Japan a whole range of commercial high voltage electron microscopes has been produced. In 1970 an experimental 3 MV electron microscope was produced by Dupouy in the Toulouse Laboratory. These instruments were very successful but were largely scaled-up versions of 100 KV electron microscopes. Further electron-optical investigations which are the subject of the present thesis suggests that considerable improvements in such instruments should be possible.

1.2 Magnetic electron lenses

1.2.1 Iron-free coils

An iron-free solenoid is the simplest form of a magnetic lens. It can consist of a wire or tape winding on non-magnetic core. Such lenses have recently become of renewed interest for superconducting lenses. The axial flux density produced by the coil can be calculated easily by Biot-Savart law. A detailed investigation of the properties and aberrations of this kind of lens is given in Chapter 4. It is shown that optimum designs for such a lens do in fact exist.

1.2.2 Double-polepiece lenses

The most commonly used magnetic electron lenses are the double polepiece lenses as introduced by Ruska in 1933. They consist essentially of a wire winding on a core of ferromagnetic material of high magnetic permeability. The iron core of the lens is bored to a diameter D along the axis of the coil to allow the electron beam to pass through a gap of width S is formed in the iron circuit between the two iron polepieces. The uniform magnetic field in the gap S is disturbed near the axis of the lens where the axial hole is located, and this causes the refractive action of the lens. The properties of this kind of lens can be expressed in terms of the ratio S/D of gap width to inner diameter. In Chapter 4, a recalculation of the distortion coefficients of such lenses has been made with improved data. These calculations have also been extended to the calculation of the distortion coefficients of lens geometries not previously studied in order to complete the picture of conventional double-polepiece lenses. In Chapter 2, the properties of two field models, the bell-shaped and square-top field distributions, that could be useful for double-polepiece lenses, are given in detail.

1.2.3 Single-polepiece lenses

If a double polepiece lens is cut in half and one of the halves is removed, one will be left with a "single-polepiece" lens. The shape of the axial magnetic field distribution in this case differs radically even from that of an asymmetrical double-polepiece lens. In particular, the field distribution falls outside the lens structure and the peak position of the field is located outside the lens a few millimeters from the poleface (snout). The focal properties of this kind of field distribution cannot be predicted from the published data for conventional lenses, and hence, it was necessary to search for a mathematical field model that was at least a first approximation to that of single-polepiece lenses. It was eventually found that the little-known exponential field distribution first discussed by Glaser (1952) could be useful. In Chapter 2, the properties of the exponential field model are discussed and evaluated in detail. The most important characteristic of the exponential field distribution, and in fact of all asymmetric field distributions, is that the lens aberrations are sensitive to the direction in which the electron enters the field distribution. This can be turned to advantage in the electron microscope. In Chapter 5, the properties of two practical designs of single-polepiece lenses, for the 100 KV and high voltage electron microscope, are discussed in detail.

1.2.4 Superconducting lenses

Some alloys such as niobium - tin, have the property of losing all electrical resistance at liquid helium temperatures. In the presence of a magnetic field above a critical value, the superconductivity is destroyed, even if the material is maintained below the critical temperature.

In the high voltage electron microscope, where one needs a high lens excitation NI in order to achieve high peak value of the magnetic field distribution without dissipating energy in the windings, superconducting lenses can be usefully employed. Superconducting screens can also be used in order to prevent the field distribution from spreading along the axis, since magnetic flux cannot penetrate into a superconductor. The maximum current density that can be achieved in superconducting windings depends on manufacturing methods but can be of the order of 20,000 A/cm^2 or more compared with perhaps 200 A/cm^2 in conventional windings. Superconducting windings are therefore much more compact than conventional ones.

1.2.5 Miniature lenses

Miniature lenses, using direct water cooling of the type developed in this University by Mulvey and his collaborators, have successfully proved themselves as having as good if not better electron-optical properties than those of conventional lenses. The reduction in lens size comes about since the current density of 20,000 A/cm^2 is comparable with that of superconducting lenses. This is achieved by using a flow of cold water for cooling the lens winding (cf. Juma 1975). Miniature single-pole lenses have proved themselves particularly as projectors in the high voltage electron microscope, (Chapter 5). Moreover they seem especially suitable for the correction of spiral distortion in the electron microscope. In Chapter 6 an experiment is described for correcting the spiral distortion by means of two single-pole lenses.

1.3 Rotation-free projector system

The image rotation caused by changing the excitation of the intermediate and projector lenses makes it inconvenient to interpret selected area diffraction micrographs in which the diffraction pattern of a crystalline structure and the corresponding image of the crystal is superimposed with different orientations. A rotation-free projector system in the electron microscope can eliminate this trouble. Today the use of miniature lenses, especially single-polepiece lenses, makes it possible, and Juma and Mulvey (1975) have produced the first rotation-free micrograph, taken by the EM6 electron microscope, in which the intermediate and projector lenses were replaced by a rotation-free system using simple polepiece lenses in which the diffraction pattern and the image of the crystal have the same orientation at any value of magnification. In this thesis a detailed study has been made of the electron-optical properties of projector systems for both conventional and single-polepiece lenses.

2. MATHEMATICAL MODELS FOR THE AXIAL FIELD DISTRIBUTION

2.1 Magnetic field models. All the focal properties of magnetic electron lenses may be calculated once the axial magnetic field distribution B(Z) of such a lens is known. The ideal method for determining the axial field distribution is to measure it accurately. However, this is not easy and an analytical expression that can adequately represent the actual field distribution is very useful in interpreting the electron-optical properties of a lens. It also gives a basis for the design of magnetic electron lenses. These analytical expressions are known as magnetic field models.

2.2 Magnetic field models for double-pole lenses. There are two magnetic field models which are useful in the study of double-polepiece magnetic lenses, Glaser's 'bell-shaped' model and the 'square-top' field model.

2.2.1 The bell-shaped field model. Glaser's bell-shaped field (Glaser 1941 b) takes the form

$$B(Z) = \frac{B_{max}}{1 + Z^2/a^2} \qquad 2.1$$

where B_{max} is the maximum magnetic field at the centre of the lens at Z = 0 and a is half of the 'half-width' of the field as shown in figure 2.1.

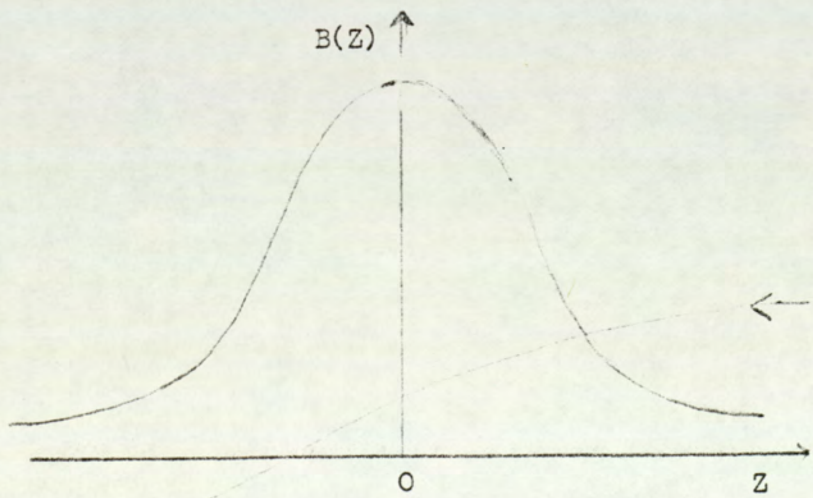

Figure (2.1). Glaser's bell-shaped field.

Putting $X = \frac{Z}{a}$ and $Y = \frac{r}{a}$, the paraxial ray equation becomes

$$\frac{d^2Y}{dX^2} + \frac{e \quad a^2}{8 \; m \; V_r} \; \frac{B_o^2}{(1 + X^2)^2} = 0 \qquad 2.2$$

This is of the form $\frac{d^2U}{d\phi^2} + \omega^2 \; U = 0$ $\qquad$ 2.3

where $\omega^2 = 1 + K^2 = 1 + \frac{e \quad a^2 \quad B_o^2}{8 \; m \; V_r}$ and V_r is the relativistically corrected accelerating voltage.

Now $\quad U(\phi) = Y(\phi) \sin \phi$

where $\frac{Z}{a} = X = \cot \phi \qquad (\pi > \phi > 0)$

with ϕ defined geometrically as in figure 2.2.

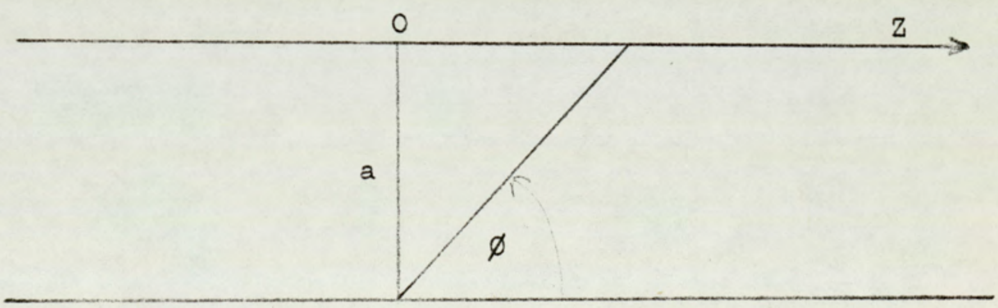

Figure 2.2. Geometrical illustration of the substitution $X = \cot \phi$

2.2.1 a <u>The asymptotic focal properties of the bell-shaped field</u>

If we start with a ray of height $Y = 1$ and slope $Y' = 0$ at $\phi = 0$ or $z = \infty$, the solution of equation 2.3 will be of the form

$$Y = \frac{\sin \omega \phi}{\omega \sin \phi} \qquad 2.4$$

and $Y' = \frac{1}{\omega}$ (sin $\omega\phi$. cos $\phi - \omega \sin\phi$. cos $\omega\phi$) 2.5

which gives $Y_i' = - \frac{\sin \omega\pi}{\omega}$ 2.6

at $\phi = \pi$ or $X = - \infty$ (the slope at the asymptotic image plane).

The projector focal length is given by

$$\frac{f_p}{a} = \frac{1}{Y_i'} = - \omega \operatorname{cosec} \omega\phi \qquad 2.7$$

Figure 2.3 shows the projector focal length f_p/a against the excitation parameter $NI/V_r^{\frac{1}{2}}$ calculated directly from equation 2.7 by the computer using the program described in 3.2.2. The figure shows good agreement between the curves calculated analytically and those calculated numerically. The values of $NI/V_r^{\frac{1}{2}}$ corresponding to different values of K were calculated as follows:

Since $\int_{-\infty}^{\infty} B(Z)\, dZ = \mu_o NI$

Since $X = \frac{Z}{a}$, $a \int_{-\infty}^{\infty} B(X)\, dX = \mu_o NI$

Hence $2aB_o \frac{dx}{1 + X^2} = \left[2aB_o \tan^{-1} X\right]_o^{\infty} = \mu_o NI$

Thus $a B_o = \frac{\mu o}{\pi} NI = 4 \times 10^{-7} NI$ 2.8

$$K = \left(\frac{e}{8m}\right)^{\frac{1}{2}} \cdot \frac{a B_o}{Vr^{\frac{1}{2}}} = \sqrt{\frac{e}{8m}} \frac{\mu o}{\pi} \cdot \frac{NI}{V_r^{\frac{1}{2}}}$$

$$= 4 \times 10^{-7} \sqrt{\frac{e}{8m}} \cdot \frac{NI}{V_r^{\frac{1}{2}}} = 5.93 \times 10^{-2} \cdot \frac{NI}{V_r^{\frac{1}{2}}} \qquad 2.9$$

Equation 2.9 enables us to use the excitation parameter $NI/V_r^{\frac{1}{2}}$ directly; equations 2.9 and 2.8 were used in the numerical calculation of the focal properties and aberration coefficients of the bell-shaped field model, carried out by the computer.

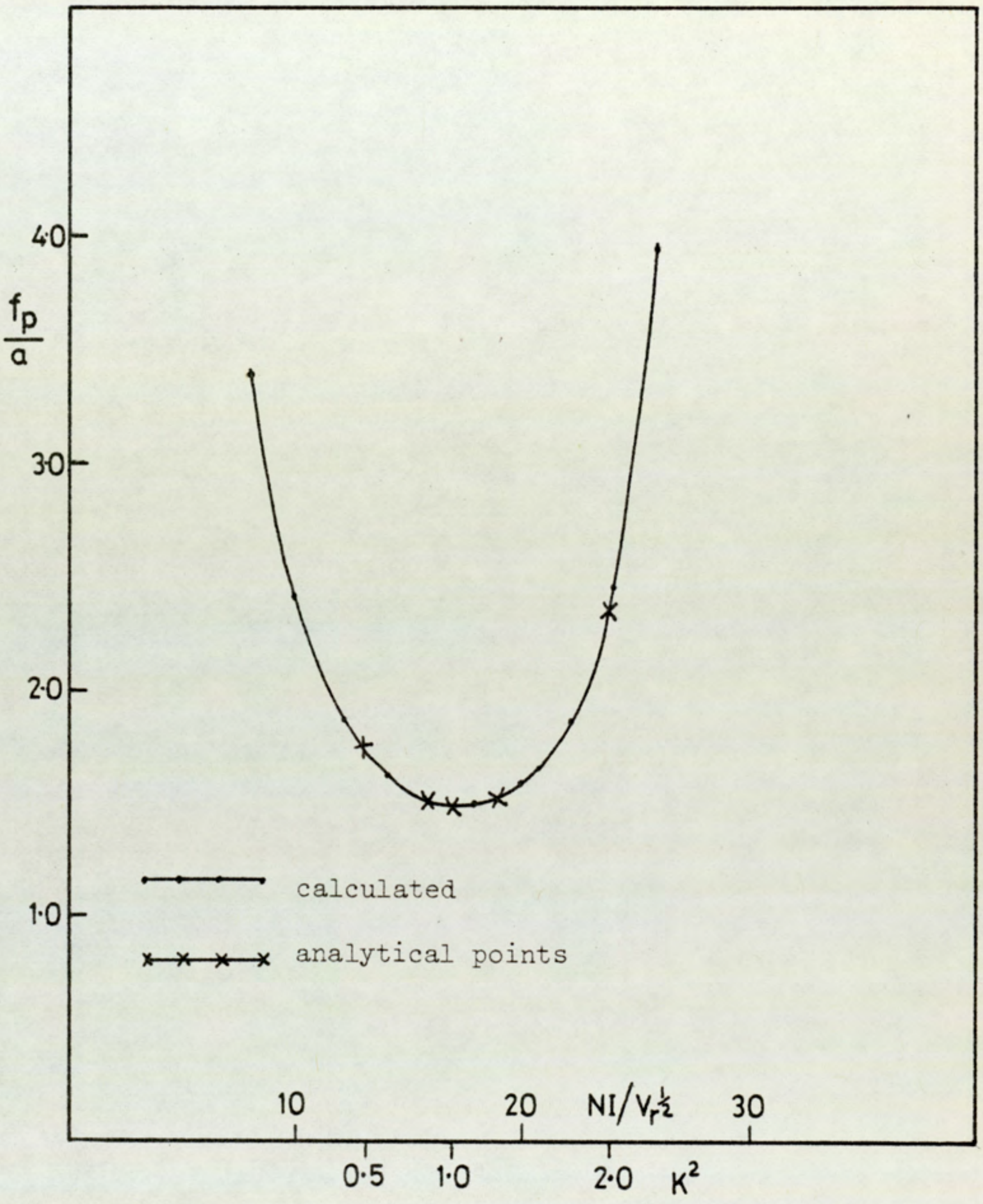

Figure 2.3 Projector focal length of 'bell-shaped' field as a function of excitation parameter $NI/V_r^{\frac{1}{2}}$

Figure 2.3 shows that the minimum projector focal length f_{min} in the first zone of operation equals 1.465a and occurs at an excitation parameter $NI/V_r^{\frac{1}{2}} = 17.28$ corresponding to a K^2 value = 1.05 (K = 1.025).

2.2.1 b <u>The aberrations of Glaser's bell-shaped field.</u> Glaser's bell-shaped field is one for which the aberration coefficients can be calculated analytically (Hawkes, 1972). The analytical expressions for the spherical aberration coefficient C_s, the chromatic aberration coefficient C_c and the radial distortion coefficient D as defined in Hawkes, (1972) at high magnification are given below in terms of a, where 2a is the half-width distribution of the field.

$$\frac{C_s}{a} = \left[\frac{k^2}{4\,\omega^3} - \frac{1}{8}\,\frac{4K^2 - 3}{4K^2 + 3}\,\sin\left(\frac{2\pi}{\omega}\right)\right]\mathrm{cosec}^4\,\frac{\pi}{\omega} \qquad 2.10\text{ a}$$

$$\frac{C_c}{a} = -\,\frac{\pi K^2}{2\,\omega^3}\,\mathrm{cosec}^2\,\frac{\pi}{\omega} \qquad 2.10\text{ b}$$

$$a^2 D = \frac{3}{2}\,\frac{\sin^2\,\omega\pi}{(4K^2 + 3)} + \frac{\pi K^2}{4}\,\frac{\cot\,\omega\pi}{\omega} - \frac{2K^2 + 3}{4\,\omega^2(4K^2 + 3)} \qquad 2.11$$

The first two coefficients have been studied extensively by previous authors. We have concentrated on working out the variation of the radial distortion coefficient D of equation 2.11 as a function of the excitation parameter $NI/V_r^{\frac{1}{2}}$. Figure 2.4 shows the variation of the radial distortion coefficient as a function of excitation parameter $NI/V_r^{\frac{1}{2}}$ calculated analytically using equation 2.11. For small values of $NI/V_r^{\frac{1}{2}}$, $a^2D = 0.25$; it then increases steadily until it reaches a maximum value 0.36 at an $/NI/V_r^{\frac{1}{2}}$ value equal to 10.7. It then falls rapidly to zero at $NI/V_r^{\frac{1}{2}} = 19.8$, before changing sign (indicating the presence of barrel distortion). The radial distortion coefficient is zero when $NI/NI_o = 1.146$.

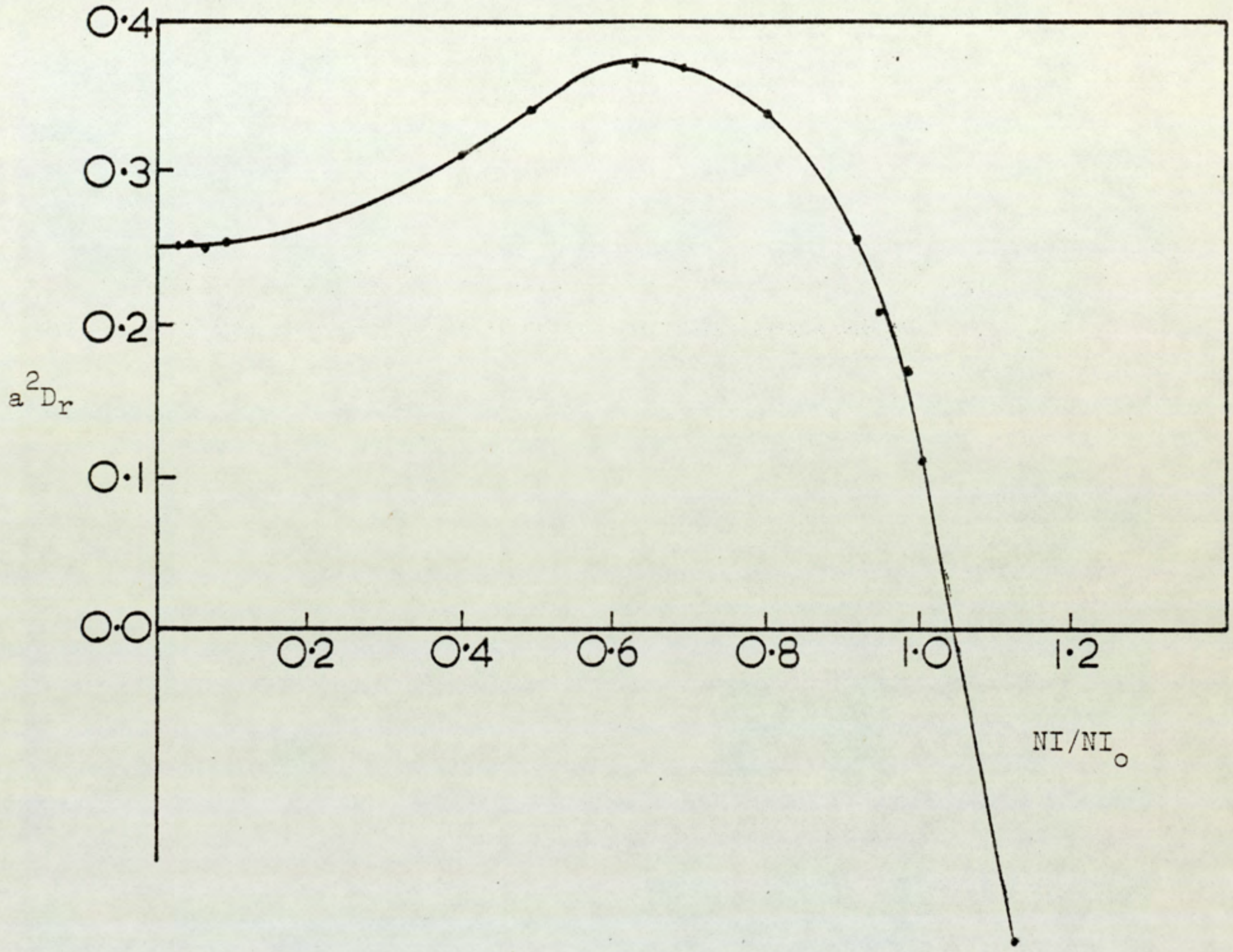

Fig. 2.4 Radial distortion of Glaser's 'bell-shaped' field (analytical solution)

As a check we calculated the radial and spiral distortion coefficients of Glaser's bell-shaped field numerically using Scherzer's general expressions (Scherzer 1937), (Grivet 1972), for combined electric and magnetic fields, namely,

$$F = \frac{G}{16\,\phi^{\frac{1}{2}}} \int_{z_o}^{z_i} Y^3 X \phi^{\frac{1}{2}} \left[f + g\left(3\,\frac{Y'}{Y} + \frac{X'}{X}\right) + h\left(\left(\frac{Y'}{Y}\right)^2 + \frac{Y'X'}{YX}\right)\right] dZ$$

$$+ \frac{G}{4} \left[Y^2 \left(\frac{\phi''}{8\phi} + \frac{5}{32}\left(\frac{\phi'}{\phi}\right)^2 + \frac{\phi'}{2\phi}\,\frac{Y'}{Y} + \frac{3}{2}\left(\frac{Y'}{Y}\right)^2 + \frac{e}{8m}\,\frac{B^2}{\phi} \right)\right]_{z_o}^{z_i} \qquad \ldots\ldots \quad 2.12\text{ a}$$

and

$$F' = \frac{G}{16}\sqrt{\frac{2e}{m}} \int_{z_o}^{z_i} \frac{BY^2}{\phi^2}\,\sqrt{\phi} \left[k - \frac{\phi'}{2}\,\frac{Y'}{Y} + \phi\left(\frac{Y'}{Y}\right)^2 \right] dZ$$

$$+ \frac{G}{32}\sqrt{\frac{2e}{m}} \left[\frac{BY^2}{\sqrt{\phi}} \left(\frac{3}{2}\,\frac{\phi'}{\phi} + \frac{2Y'}{Y} - \frac{B'}{B} \right)\right]_{z_o}^{z_i} \qquad \ldots\ldots \quad 2.12\text{ b}$$

where

$$f = \frac{5}{4}\left(\frac{\phi''}{\phi}\right)^2 + \frac{5}{24}\left(\frac{\phi'}{\phi}\right)^4 + \frac{e}{m}\,\frac{B'^2}{\phi} + \frac{3}{8}\left(\frac{e}{m}\right)^2 \frac{B^4}{\phi^2} + \frac{35}{10}\,\frac{e}{m}\left(\frac{\phi'}{\phi}\right)^2 \frac{B^2}{\phi} - \frac{3e}{m}\,\frac{\phi'}{\phi}\,\frac{BB'}{\phi},$$

$$g = \frac{7}{6}\left(\frac{\phi'}{\phi}\right)^2 - \frac{e}{2m}\,\frac{\phi'}{\phi}\,\frac{B^2}{\phi}, \qquad h = -\frac{3}{4}\left(\frac{\phi'}{\phi}\right)^2 - \frac{e}{2m}\,\frac{B^2}{\phi},$$

$$k = \frac{3}{8}\,\frac{e}{m}\,B^2 + \frac{9}{8}\,\frac{\phi'^2}{\phi} - \frac{\phi' B'}{B}$$

The integration is carried out from the object plane (z_o) to the image plane (z_i). In expressions 2.12 a and 2.12 b, G is the magnification, ϕ is the electrostatic potential and Y and X are two solutions for the paraxial ray equation. F and F' are the radial and spiral distortion coefficients as defined by Scherzer (1937), in the most general case. The deviation $\Delta\rho$ of the Gaussian image at the image plane is given by

$$(\Delta\rho)_{rad} = F\, r_o^3 \quad \text{and} \quad (\Delta\rho)_{sp} = F' \cdot r_o^3 \qquad \text{..... 2.13}$$

where r_o is the initial height of an electron beam entering the field of the lens. The Gaussian image radius ρ is given by

$$\rho = G\, r_o \qquad \text{..... 2.14}$$

Hence, the distortion in the image at the image plane $\frac{\Delta\rho}{\rho}$ is given by:

$$\left(\frac{\Delta\rho}{\rho}\right)_{rad} = \frac{F\, r_o^3}{G\, r_o} = D_{rad}\, r_o^2 \qquad \text{..... 2.15 a}$$

and

$$\left(\frac{\Delta\rho}{\rho}\right)_{sp} = \frac{F'\, r_o^3}{G\, r_o} = D_{sp}\, r_o^2 \qquad \text{..... 2.15 b}$$

$D_{rad} = \frac{F}{G}$ and $D_{sp} = \frac{F'}{G}$ are standard notation today for the radial and spiral distortion coefficients (Hawkes, 1972). For purely magnetic field and an object and image plane at infinity they are given by

$$D_{rad} = \frac{3}{8f_p^2} + \frac{e}{16\, mV_r} \int_{-\infty}^{\infty} \left[B'(Z)^2 + \frac{3}{8}\frac{e}{mV_r}\, B^4(Z) - B^2(Z)\left(\frac{Y'}{Y}\right)^2 \right] Y^3 X\, dZ \qquad \text{..... 2.16}$$

and

$$D_{sp} = \frac{1}{16V_r}\left(\frac{2\ e}{m\ V_r}\right)^{\frac{1}{2}} \int_{-\infty}^{\infty} B(Z)\left[\ \frac{3}{8}\,\frac{e}{m}\,B^2(Z) + V_r\left(\frac{Y}{Y}\right)^2\right] Y^2\, dZ \qquad \text{..... 2.17}$$

where Y and X are the two solutions of the paraxial ray equation with the following boundary conditions.

$$\text{Lim}\ Y_{(Z\ =\ -\infty)} = 1,\quad Y_{(Z\ =\ -\infty)} = 0 \qquad \text{..... 2.18 a}$$

and

$$\text{Lim}\ X_{(Z\ =\ -\infty)} = Z - Z_o,\quad X'_{(Z\ =\ -\infty)} = 1 \qquad \text{..... 2.18 b}$$

Equations 2.16 and 2.17 apply to any ray Y, satisfying the condition $Y_o = 1$ at the object plane, starting from the same point in the object plane and ending at the same point on the image plane. The total distortion that any of these rays suffered during its path through the field, at the image plane will be the same, since all come to the same point on the image plane (figure 2.5a). In practice we choose a ray with initial slope 0 for convenience.

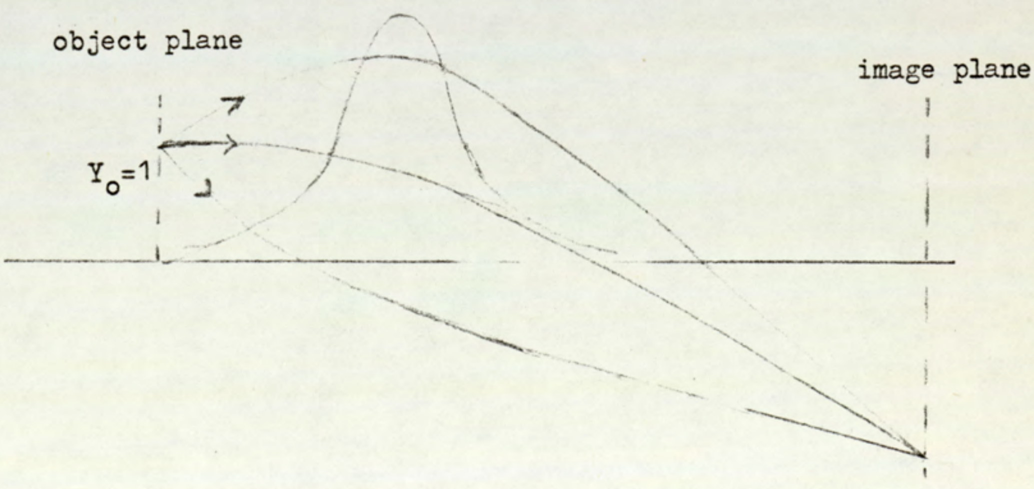

Figure (2.5a). Illustration of the ray Y.

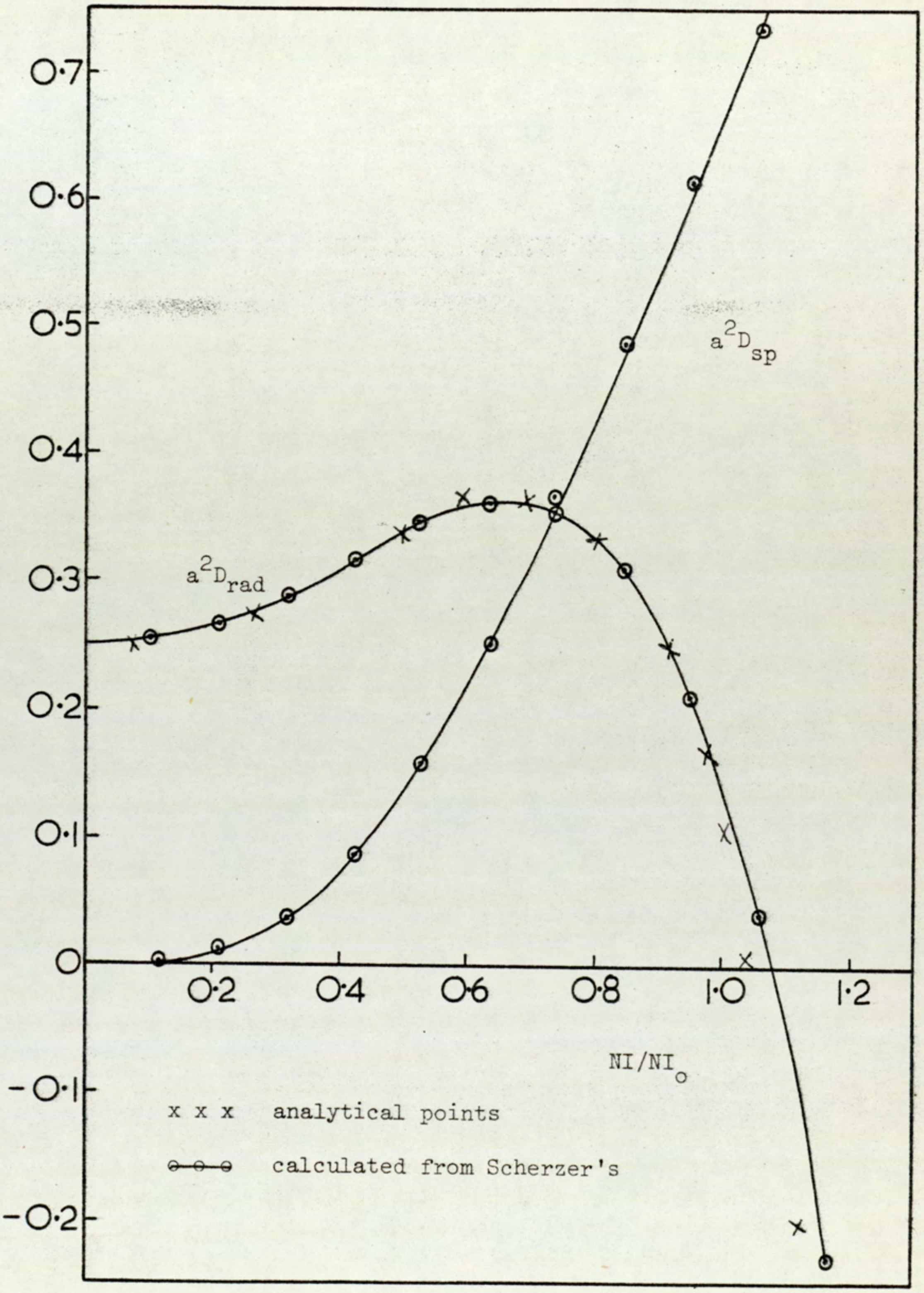

Fig. 2.5b a^2D_{rad} and a^2D_{sp} calculated for the bell-shaped field distribution

f_p and V_r are the projector focal length and the relativistic accelerating voltage along the z-axis of the lens.

In calculating the radial and spiral distortion coefficients for Glaser's bell-shaped field above, we used the substitution

$$B(Z) = \frac{B(Z)}{B_o} \cdot B_o = B\,R(Z) \cdot B_o$$

where $BR(Z) = \dfrac{1}{1 + \left(\frac{z}{a}\right)^2}$, noting that from equation 2.8 we obtain

$$a\,B(Z) = 4 \times 10^{-7}\,NI.\,B\,R(Z) \qquad \text{..... 2.19}$$

The computed results for a^2D_{rad} and a^2D_{sp} for the bell-shaped field are represented by the solid lines of figure 2.5 b. The crosses show the analytical points of the radial distortion coefficient a^2D. The figure shows excellent agreement between the calculated results and those obtained analytically. This indicates high accuracy in the program used for the calculation.

Another check on the values of a^2D_{rad} is given by using the approximation that when the lens is very weak the radial distortion coefficient is approximately equal to $\frac{C_s}{f^3}$. From equations 2.7 and 2.10 we get

$$\lim_{(K = 0)} a^2 \frac{C_s}{f^3} = 0.25 \qquad \text{..... 2.20}$$

which is the same as obtained from both analytical and calculated values of a^2D.

2.2.2 Square-top field model

Because of the simplicity of the paraxial ray equation for a ray passing through a constant magnetic field, the square-top field model is most convenient for evaluating the paraxial properties of magnetic electron lenses. No real lens has exactly the square-top field distribution, but to a first approximation we can divide any axial field distribution into successive intervals each of constant field strength and thus treat each region as a separate square top field.

2.2.2 a <u>Electron optical properties of the square-top field</u>

The paraxial ray equation

$$\frac{d^2r}{dZ^2} + \frac{e}{8m}\frac{B^2(Z)}{V_r}\, r = 0 \qquad \text{..... 2.21}$$

is easily solved for a paraxial ray passing through a square-top field with a constant axial field B (Z). For an incident ray of initial slope r_o' and distance r_o from the axis (Figure 2.6), the trajectory is given by

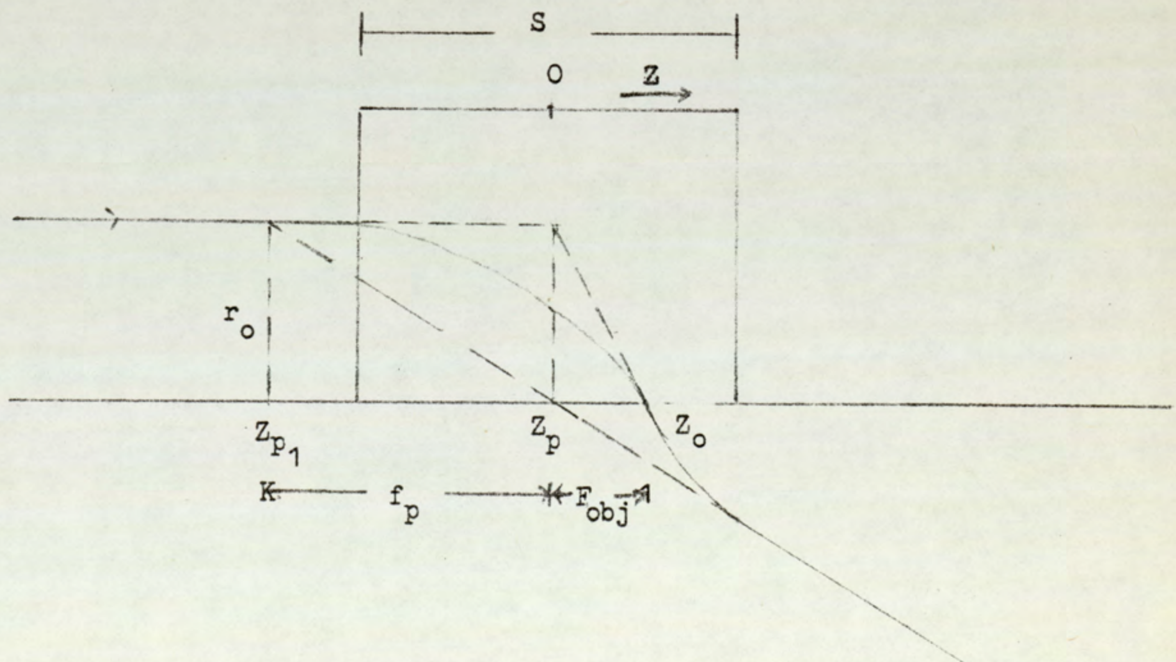

Figure (2.6). The square-top field.

$$r = r_o \cos\left[K\left(\frac{S}{2} + Z\right)\right] + \frac{r_o'}{K}\sin\left[K\left(\frac{S}{2} + Z\right)\right] \qquad \text{..... 2.22 a}$$

and the slope r' of the ray

$$r' = r_o' \cos\left[K\left(\frac{S}{2} + Z\right)\right] - K r_o \sin\left[K\left(\frac{S}{2} + Z\right)\right] \qquad \text{..... 2.22 b}$$

where Z is the axial distance from the centre of the lens (figure 2.6). $K^2 = \frac{e}{8m} \frac{B^2(Z)}{V_r}$ where S is the width of the field.

If the initial slope r_o' of the ray equals zero, equations 2.18 reduce to $r = r_o \cos\left[K\left(\frac{S}{2} + Z\right)\right]$ ..... 2.23 a

and

$$r' = - K r_o \sin\left[K\left(\frac{S}{2} + Z\right)\right] \qquad \text{..... 2.23 b}$$

The slope r' of the ray at $r = 0$ is equal to $r' = \frac{r_o}{f_{obj}}$

From equation 2.23b r' is given by:

$$r' = - K r_o \sin\left[K\left(\frac{S}{2} + Z_o\right)\right] \qquad \text{..... 2.24}$$

where Z_o is the objective "focal distance", i.e. for which $r = 0$

Hence

$$Z_o = \left[\frac{\pi}{2K} - \frac{S}{2}\right] \qquad \text{..... 2.25}$$

and $f_{obj} = \dfrac{1}{K \sin\left[K\left(Z_o + \frac{S}{2}\right)\right]} = \dfrac{1}{K \sin\left[K\left(\frac{\pi}{2K} - \frac{S}{2} + \frac{S}{2}\right)\right]}$

i.e. $f_{obj} = \frac{1}{KS}$ 2.26

Equation 2.26 applies only when Z_o is inside the lens. For a weak lens, i.e. up to an excitation $KS = \frac{\pi}{2}$, the projector and objective focal lengths are the same and are given by

$$f_p = \frac{r_o}{r'_{(Z = \frac{S}{2})}} = \frac{r_o}{-K\, r_o \sin (KS)}$$

i.e. $$\frac{f_p}{S} = \frac{1}{KS \sin (KS)} \qquad \text{..... 2.27}$$

The point at which the asymptote to the ray at $Z = \frac{S}{2}$ intersects the axis is at a distance Z_p from the origin given by

$$Z_p = \left[\frac{S}{2} + \frac{1}{K} \cot (KS) \right] \qquad \text{..... 2.28}$$

and hence, the principal plane of the lens p_1 is at a distance Z_{p1} from the origin, where

$$Z_{p1} = \left(Z_p - \frac{\operatorname{cosec} KS}{K} \right) = \left(\frac{S}{2} + \frac{\cot (KS)}{K} - \frac{\operatorname{cosec} (KS)}{K} \right) \qquad \text{..... 2.29}$$

Figure 2.7 illustrates the variation of $\frac{Z_o}{S}$, $\frac{Z_p}{S}$ and $\frac{Z_{pl}}{S}$ with KS.

2.2.2 b <u>An analytical expression for the spiral distortion coefficient of the square-top field</u>

In general, the square-top field does not lend itself mathematically for the calculation of aberrations. This is because most of the coefficients depend on the derivatives $\frac{dB}{dZ}$, $\frac{d^2B}{dZ^2}$ etc. of the axial field distribution. For the square-top field, the infinite slope at the boundaries of the field distribution causes a mathematical difficulty in calculating the derivatives and hence makes the calculation of the coefficients virtually impossible. However, for some coefficients, such as the spiral distortion coefficient (Equation 2.17), when the integration process takes place between $Z = -\infty$ and $Z = +\infty$, we can avoid this difficulty, as will be shown later. It seemed worth investigating, therefore, the possibility of deriving an analytical expression for the spiral distortion coefficient for the square-top field model, a topic which

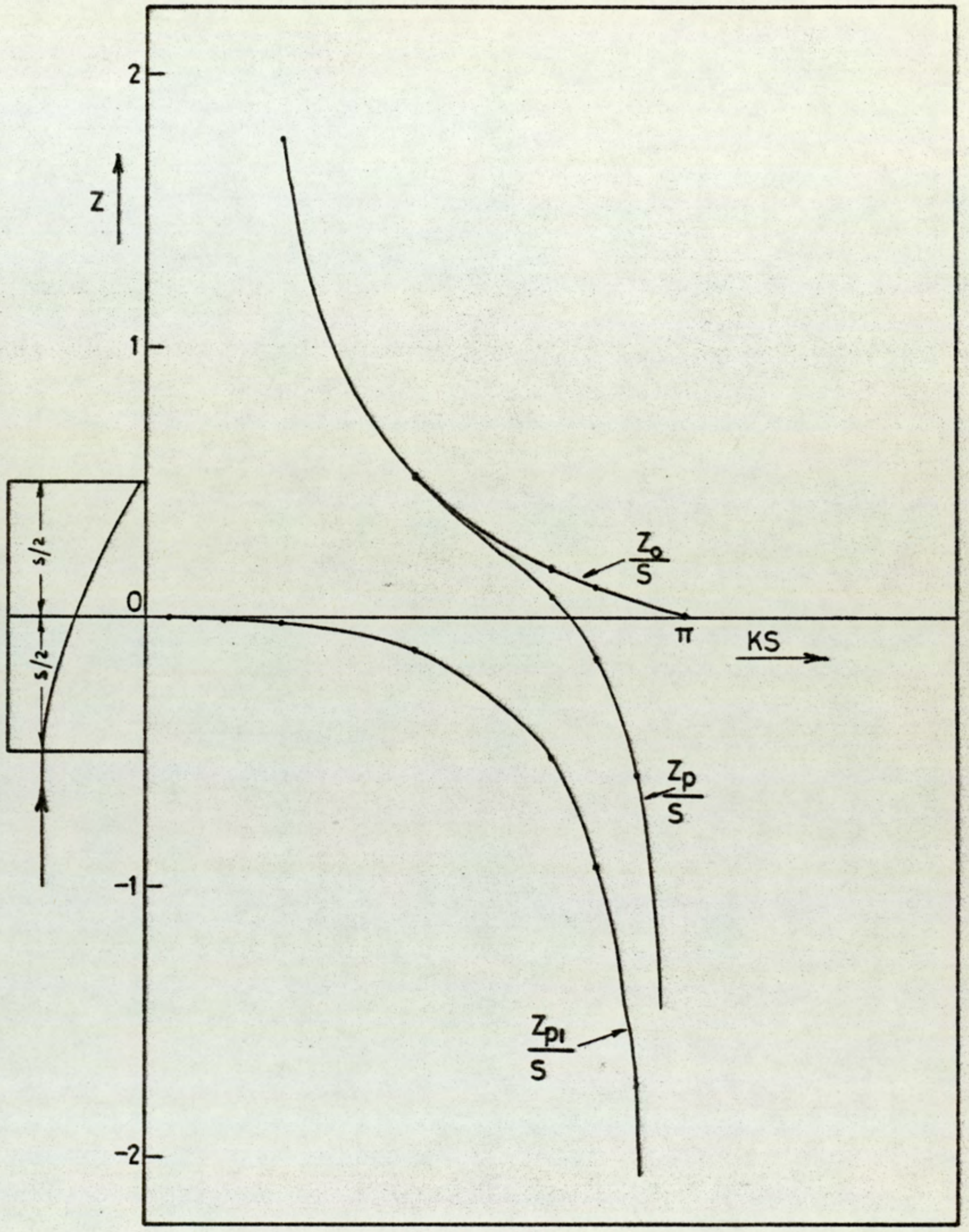

Figure 2.7 Variation of $\frac{Z_o}{S}$, $\frac{Z_p}{S}$ and $\frac{Z_{p1}}{S}$ with excitation parameter KS for the square-top field

to the best of our knowledge has not previously been discussed in the literature.

Equation 2.17, when applied to a single square-top field, will take the form

$$D_{sp} = \frac{1}{16}\left(\frac{2e}{mV_r}\right)^{\frac{1}{2}} \cdot \frac{3}{8}\,\frac{e}{m}\,\frac{B^3(Z)}{V_r}\int_{-\infty}^{\infty} Y^2 dZ + \frac{1}{16}\left(\frac{2e}{mV_r}\right)^{\frac{1}{2}} B(Z)\int_{-\infty}^{\infty} Y'^2\, dZ$$

which reduces to

$$D_{sp} = \frac{3}{4}\left(\frac{e}{8m}\right)^{3/2} \cdot \frac{B^2(Z)}{V_r}^{3/2}\int_{-\infty}^{\infty} Y^2 dZ + \frac{1}{4}\left(\frac{e}{8m}\right)^{\frac{1}{2}} \cdot \frac{B(Z)}{V_r^{\frac{1}{2}}}\int_{-\infty}^{\infty} Y'^2 dZ$$

$$= \frac{3}{4} K^3 \int_{-\infty}^{\infty} Y^2\, dZ + \frac{1}{4} K \int_{-\infty}^{\infty} Y'^2\, dZ \qquad \ldots\ldots\ 2.30$$

where $K^2 = \frac{e}{8m}\,\frac{B^2(Z)}{V_r}$

Substituting from equations 2.23 into 2.30 and putting $Z = \frac{S}{2}$, $Y_o = 1$ and $Y_o' = 0$, we get for a parallel beam of electrons entering the lens

$$D_{sp} = \frac{3}{4} K^3 \int_0^S \cos^2(KS)\, dZ + \frac{1}{4} K^3 \int_0^S \sin^2(KS)\, dZ$$

$$= \frac{K^3}{4}\left[\frac{3}{2}\int_0^S (1 + \cos(2KS))\, dZ + \frac{1}{2}\int_0^S (1 - \cos(2KS)) dZ\right.$$

$$= \frac{K^3}{8}\left[3Z + \frac{3}{2K}\sin(2KS) + Z - \frac{1}{2K}\sin(2KS)\right]_0^S$$

Thus $$D_{sp} = \frac{K^3}{8}\left[4S + \frac{\sin(2KS)}{K}\right] \qquad \ldots\ldots\ 2.31$$

$$= \frac{K^3 S}{2} - \frac{K^2}{8}\sin(2KS) \qquad \ldots\ldots\ 2.31\ a$$

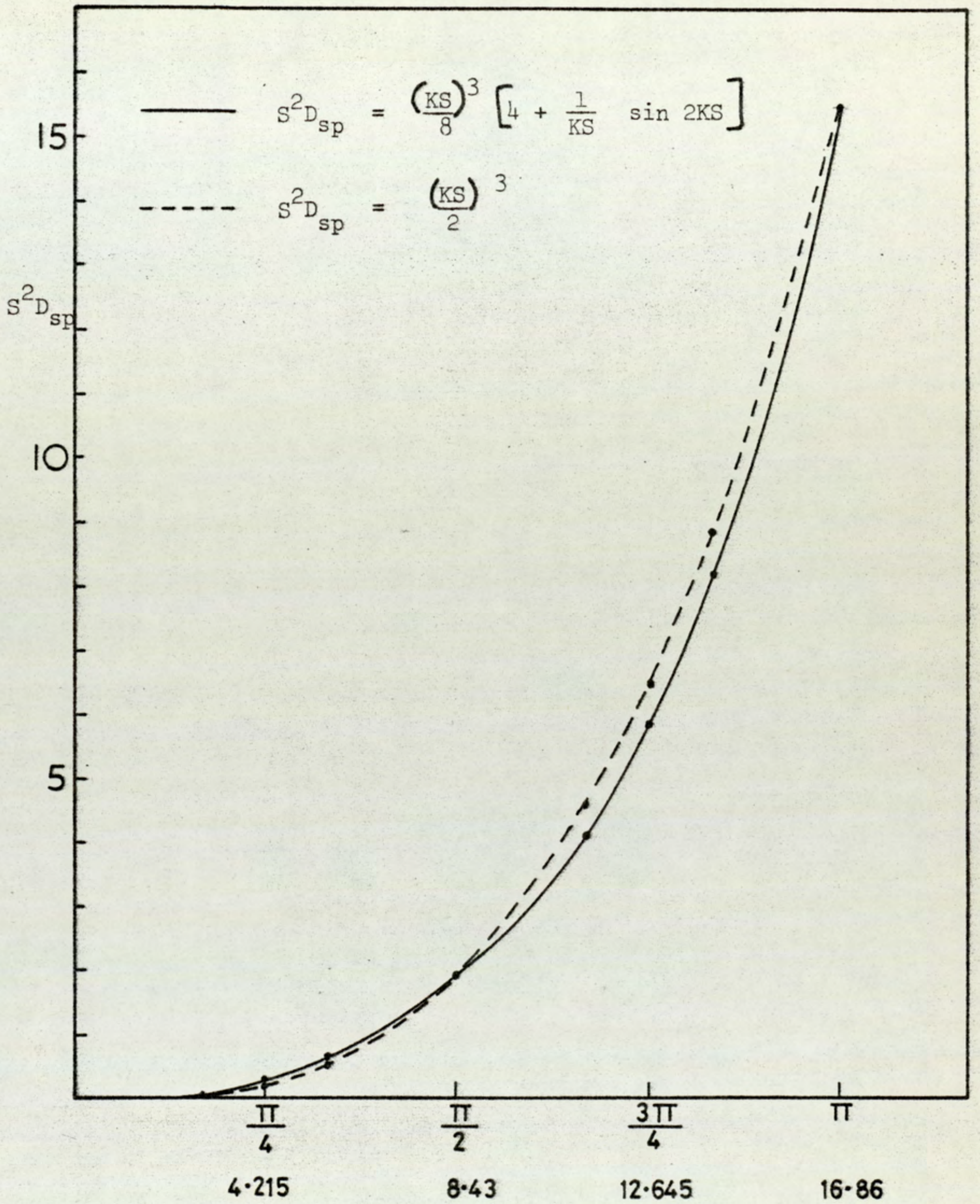

Fig. 2.8 S^2D_{sp} against K values for the square-topped field

Equation 2.31 gives the spiral distortion coefficient for any square-top field in terms of S, the width of the field, and K, the excitation parameter. Equation 2.31 shows that the spiral distortion coefficient expression has two terms; the first is directly proportional to S; and the second is an oscillating term varying as sin (2KS). Figure 2.8 shows the variation of S^2D_{sp} values with excitation parameter K for the square top field. The variation of the spiral distortion coefficients, with excitation parameter K, is of the same form as that of conventional magnetic electron lenses. It starts from zero when K = 0, increases slowly at weak excitations, then increases rapidly with increasing K. In the region of minimum projector focal length, it is the dominant aberration.

In the numerical integration process for calculating the spiral distortion coefficient for any axial field distribution, we simply calculate the contribution to the aberration as given by equation 2.17 for each element of the field. The total distortion of the image plane is then the sum of these individual contributions from the object plane to the image plane. Since, we usually approximate the field in each element by a constant field, this suggests that equation 2.30 can be applied to an individual element. In particular we can apply the general solution of the paraxial ray equation for the square-top field, equations (2.22) to a single element and hence to a series of such elements. In this case we will call the ray height at the i^{th} element, Y_i, and the initial height and slope of the ray for this field element Y_{io} and Y'_{io} respectively. This is illustrated in Figure 2.9 a.

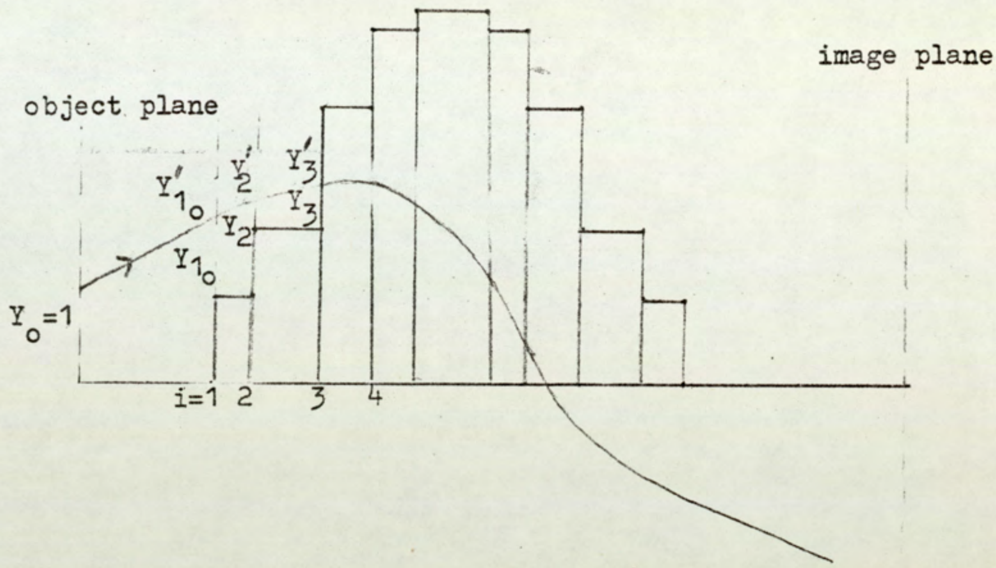

Figure (2.9a). The height Y_i and slope Y_i' of a ray through each element in the field.

An expression for the contribution to spiral distortion coefficient from each element i can be obtained by replacing Y and Y' in equation 2.30 by Y_i and Y_i' and using equations 2.22 for the solution of the paraxial ray equation with Y_{io} and Y_{io}' as the initial condition for each element. Thus, we obtain

$$D_{sp} = \frac{3}{4} K^3 \int_0^S \left(Y_i \cos(KS) + \frac{Y_{io}'}{K} \sin(KS)\right)^2 dS +$$

$$\frac{1}{4} K \int_0^S \left(Y_{io}' \cos(KS) - Y_{io} K \sin(KS)\right)^2 dS \qquad \ldots\ldots 2.32$$

Equation 2.28 readily reduces to

$$\overline{D}_{sp} = \frac{K^3}{8} \left[4 \left(Y_{io}^2 + \left(\frac{Y_{io}'}{K}\right)^2 \right) S + \frac{\sin(2KS)}{K} \left[\left(\frac{Y_{io}'}{K}\right) - Y_{io}^2 \right] - \frac{2\, Y_{io}\, Y_{io}'}{K^2} \cos(2KS) \right] \qquad \ldots\ldots 2.33$$

The bar on the left hand side of expression 2.33 indicates that this expression applies to an intermediate stage of computation in the calculation of the distortion coefficient. It can also be applied to the calculation of distortion in two successive square-top field lenses. Here the ray enters the second lens with a height Y_{io} and slope Y'_{io}. This procedure will be used in Chapter 6 to calculate a system of successive lenses, as in the electron microscope.

Equation 2.33 reduces, as it should, to equation 2.31 if we put $Y_{io} = 1$ and $Y'_{io} = 0$ corresponding to a parallel incoming ray.

2.2.2 c The effect of the finite conjugates on the spiral distortion coefficient of the square-top field

In operating the projector system of the electron microscope, the object distance is not always at an infinite distance from the corresponding magnetic projector lens, and so the finite conjugates of the lens must be taken into consideration when calculating the distortion. In order to assess the magnitude of this effect analytically, it is convenient to study the spiral distortion coefficient of the square-top field for the case of finite conjugates (Figure 2.9b).

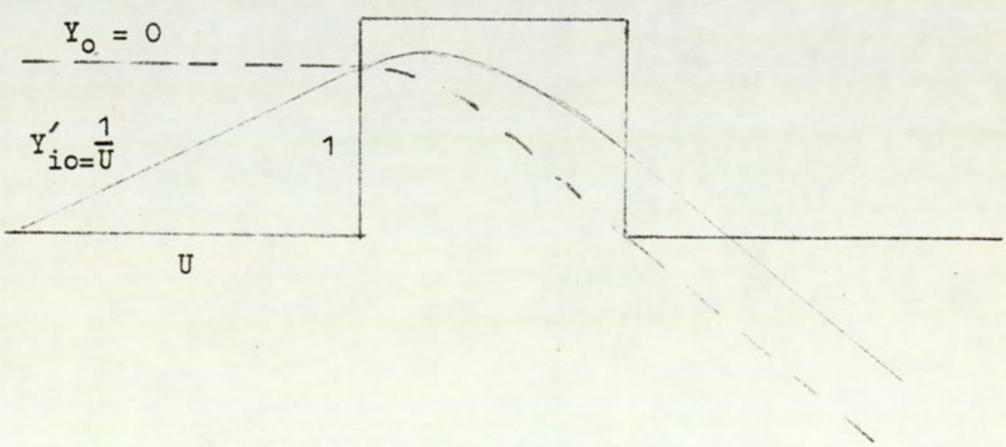

Figure (2.9b). Finite conjugate of a ray with the square-top field.

Equation 2.33 can be written in the form

$$\overline{D}_{sp} = \frac{K^3}{8} Y_{io}^2 \left[4S - \frac{1}{K} \sin (2KS) \right] + \frac{K^3}{8} Y_{io}^2 \cdot \frac{1}{K^2} \left(\frac{Y_{io}}{Y_{io}} \right)^2$$

$$\times \left[4S + \frac{\sin (2KS)}{K} \right] - \frac{K}{4} Y_{io} Y_{io}' \cos (2KS) \quad .. \ 2.34 \text{ a}$$

Considering equation 2.31 we get

$$\overline{D}_{sp} = Y_{io}^2 D_{sp} \left[1 + \frac{1}{K^2} \left(\frac{Y_{io}'}{Y_{io}} \right)^2 \right] - \frac{K}{4} Y_{io}^2 \left(\frac{Y_{io}'}{Y_{io}} \right) \cos (2KS)$$

$$+ \frac{Y_{io}^2}{4} \left(\frac{Y_{io}}{Y_{io}} \right)^2 \sin (2KS) \quad .. \ 2.34 \text{ b}$$

If U is the axial distance from the source to the nearest edge of the field distribution (figure 2.9b), we have

$$\frac{Y_{io}}{U} = Y_{io}' \qquad \text{i.e.} \quad \frac{Y_{io}'}{Y_{io}} = \frac{1}{U}$$

hence

$$Y_{io} Y_{io}' = \frac{Y_{io}^2}{U} \quad .. \ 2.35$$

Substitution from 2.35 into 2.34b with the initial condition $Y_{io} = 1$ gives

$$\overline{D}_{sp} = D_{sp} \left[1 + \frac{1}{K^2 U^2} \right] - \frac{K}{4U} \cos (2KS) + \frac{\sin (2KS)}{4 U^2} \quad .. \ 2.36$$

Equation 2.36 gives the variation of spiral distortion coefficient of the square-top field with $Y_{io} = 1$.

For example, consider the case where the excitation parameter $KS = \pi/2$ corresponding to the minimum focal length position; where the radial distortion is approximately zero. In this case $K = \pi/2S$

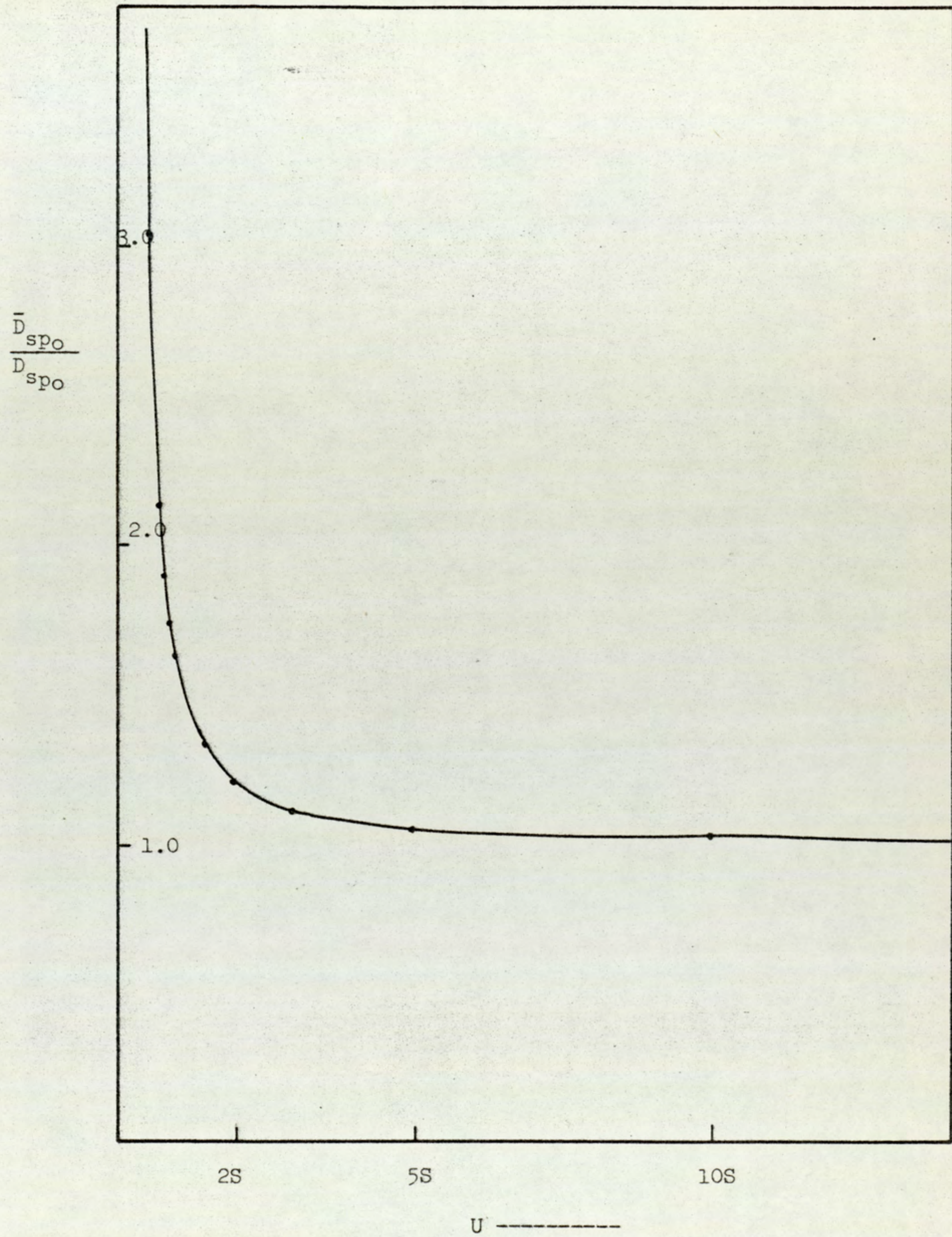

Fig. 2.10 Variation of $\bar{D}_{spo}$ with the distance U of the source

and $D_{sp} = D_{sp_o} = \pi^3/16S$. Equation 2.36 becomes

$$\bar{D}_{sp_o} = \frac{\pi^3}{16S^2}\left[1 + \frac{4}{\pi^2}\left(\frac{S}{U}\right)^2 + \frac{2}{\pi^2}\left(\frac{S}{U}\right)\right]$$

$$= \left[1 + \frac{4}{\pi 2}\left(\frac{S}{U}\right)^2 + \frac{2}{\pi 2}\left(\frac{S}{U}\right)\right] D_{sp_o} \qquad \text{..... 2.36 b}$$

Figure 2.10 shows the form of the relation between $\bar{D}_{sp_o}$ and U. If U is greater than 2S, $\bar{D}_{sp_o}$ is approximately constant and equal to $\bar{D}_{sp_o}$. For U smaller than 2S, $\bar{D}_{sp_o}$ is approximately inversely proportional to U^2.

Furthermore, if U is the distance from the source to the nearest boundary of the field and v is the distance from the far boundary of the field to the point at which $y_i = 0$ (figure 2.11), then we have, at $KS = \pi/2$,

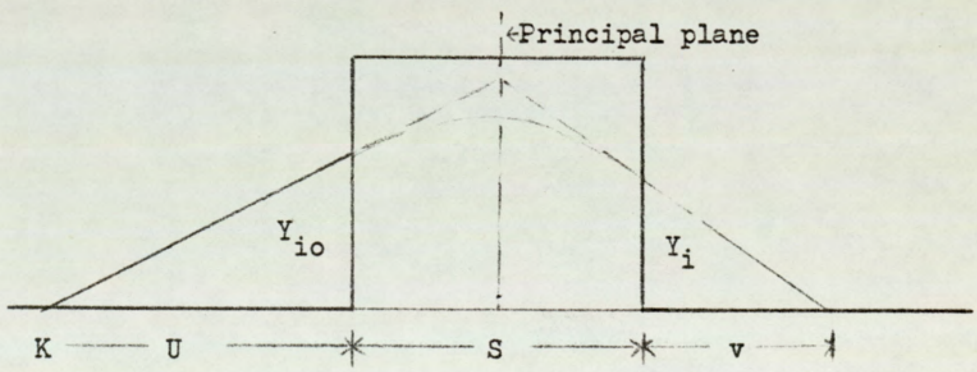

Figure (2.11). Definition of the distances U, S, and v for the square-top field.

$$Y_i = \frac{Y_{io}}{K}, \quad Y_i' = -K \qquad \text{..... 2.37}$$

But $$v = \left| \frac{Y_i}{Y'_i} \right| = \frac{Y'_{io}}{K^2} \qquad \ldots\ldots 2.38$$

from 2.35 $$Y'_{io} = \frac{1}{U}$$

so $$v = \frac{1}{UK^2} \qquad \ldots\ldots 2.39$$

The magnification of the lens in this case

$$M = \frac{v + 0.5\,S}{U + 0.5\,S} \qquad \ldots\ldots 2.40$$

where the value of 0.5 S represents the position of the principal plane of the lens which in this case ($KS = \pi/2$) approximately at the middle of the lens.

From equation 2.40 we can calculate M when U takes a different value. The aim is to get a similar expression to that of weak glass lenses, where

$$D_{sp_1} = D_{sp} \, (1 + M)^2 \qquad \ldots\ldots 2.41$$

But, of course, the power of the term (1 + M) could be different. However, plotting log D_{sp_o} values of the square-top field against log (1 + M), where M is given by 2.40, gives us two regions, the first from M = 0 to 0.44 in which the power of (1 + M), is about 0.7 and the second from M = 0.44 to ∞ in which the power of (1 + M) is approximately two, like the case of glass system. The resultant curves are shown in figure 2.12.

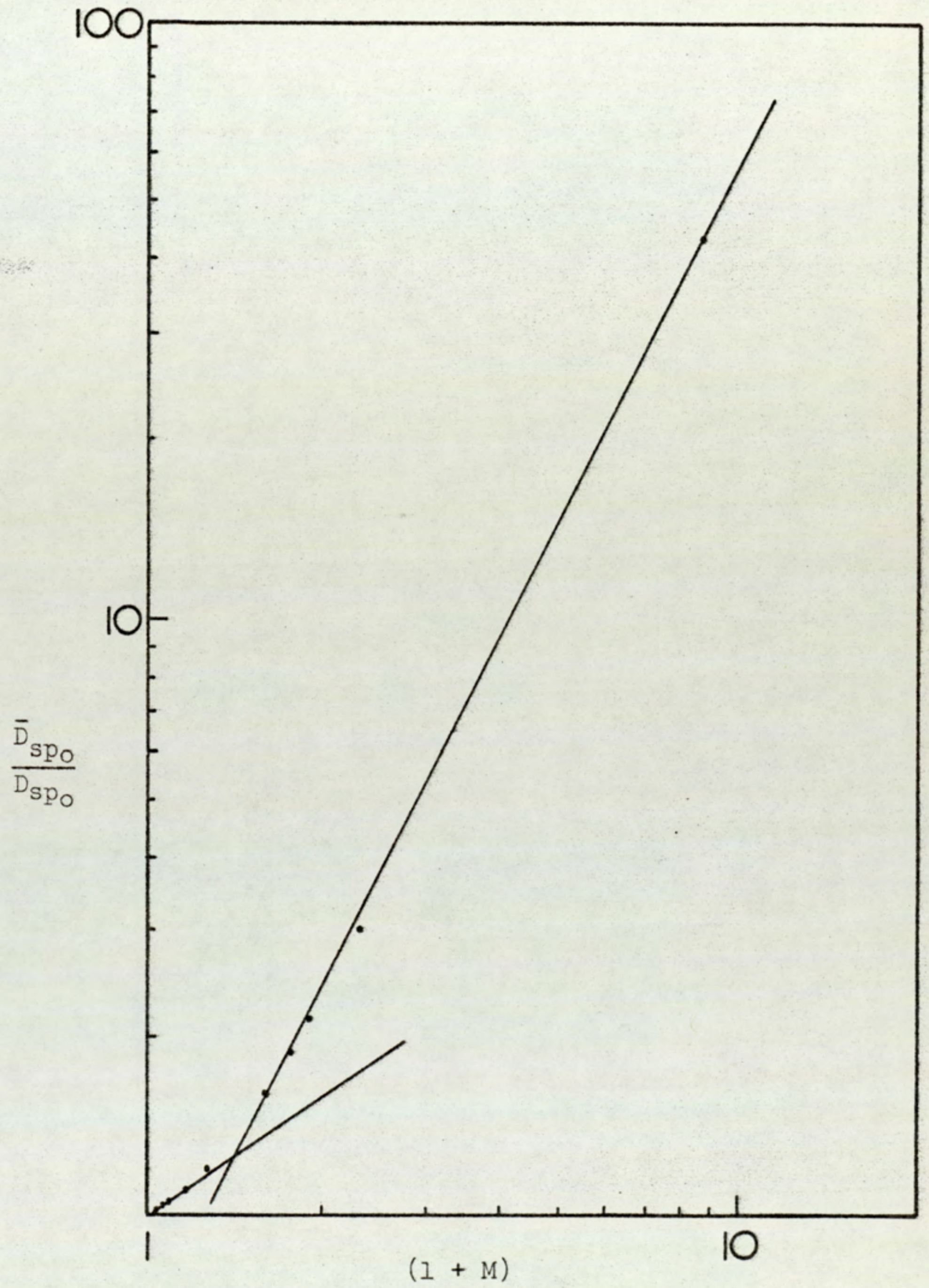

Fig. 2.12 $(\bar{D}_{sp_o}/D_{sp_o})$ against (1 + M) for the square-top field

2.3 A magnetic field model for 'Single-Polepiece' lenses

(The 'exponential-field' model)

Although the magnetic field models described in §2.2 give a remarkably good representation of the properties of double polepiece magnetic electron lenses, it is found (Mulvey and Newman, 1973) to be very difficult to apply them to single-polepiece lenses. In fact, the axial field distribution from this type of lens is approximately exponential in character. This gives importance to the further study of the little-known and neglected exponential field model of Glaser (appendix 1) and its electron optical properties.

The axial field distribution in the exponential field model takes the form

$$B(Z) = Bm(Z) \cdot e^{\frac{-z \ln 2}{d}} \qquad \text{..... 2.42}$$

where d is the width of the field at its half height (figure 2.13). The corresponding paraxial ray equation, as given by Glaser (1952), may be written:

$$\frac{d^2Y}{dX^2} + K^2 e^{-2X \ln 2} Y = 0 \qquad \text{..... 2.43}$$

where

$$Y = \frac{r}{d}, \; X = \frac{z}{d}, \; K^2 = \frac{e B_m^2(Z) d^2}{8mV_r}$$

Changing the variable from X to ξ, where

$$\xi = \frac{K}{\ln 2} e^{-X \ln 2} \qquad \text{..... 2.44}$$

we obtain

$$\frac{d^2Y}{d\xi^2} + \frac{1}{\xi}\frac{dY}{d} + Y = 0 \qquad \text{..... 2.45}$$

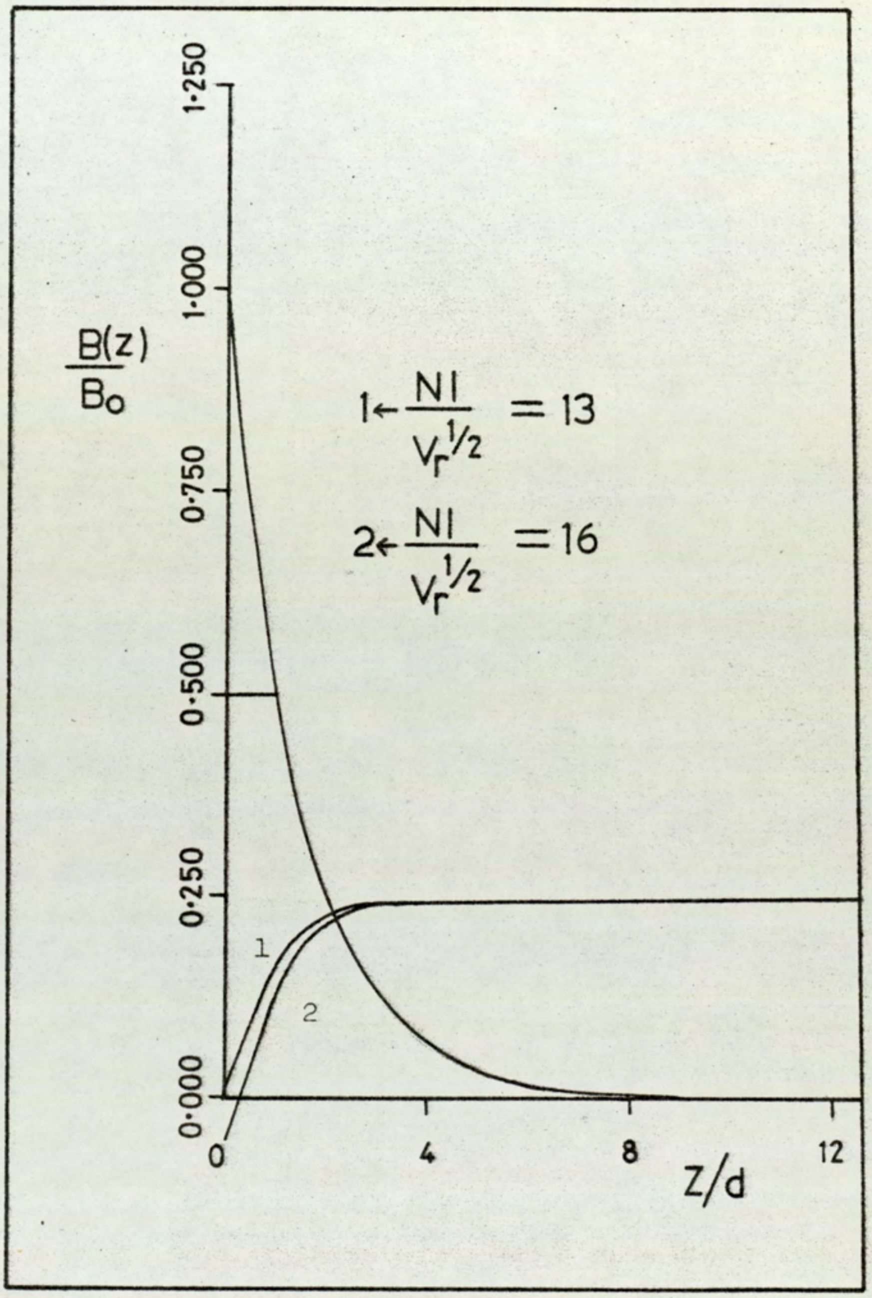

Fig. 2.13 The exponential field model

which is a differential form of the Bessel function of zero order. The solution of equation 2.45 for a ray entering the field at $Z = \infty$ with an initial height $Y = 1$ and initial slope $Y' = 0$, is given by

$$Y(Z) = J_o(\xi) = J_o\left(\frac{K}{\ln 2} \cdot \frac{K}{\ln 2} \cdot e^{-\frac{z}{d} \cdot \ln 2}\right) \qquad \text{..... 2.46}$$

where $J_o(\xi)$ is the Bessel function of zero order.

This ray intersects the axis at points distant Z_n from the origin where

$$Z_n = \frac{d}{\ln 2} \cdot \ln \frac{K}{\xi_n \ln 2} \qquad \text{..... 2.47}$$

where ξ_n is the value at which $J_o(\xi_n) = 0$. These values are $\xi_1 = 2.4048$, $\xi_2 = 5.5201$, ξ_3 . . .

$n = 1$ means that there is one focus only at distance Z_F from the origin, given by

$$Z_F = \frac{d}{\ln 2} \cdot \ln \frac{K}{1.667} \qquad \text{..... 2.48}$$

Since $\int_0^\infty B(Z)\, dZ = \mu_o NI$

$$\int_0^\infty B_m(Z) \cdot d = \mu_o NI \cdot \ln 2 \qquad \text{..... 2.49}$$

And we have

$$K = \left(\frac{e}{8m}\right)^{\frac{1}{2}} \frac{B_m d}{V_r^{\frac{1}{2}}} = 0.1287 \frac{NI}{V_r^{\frac{1}{2}}} \qquad \text{..... 2.50}$$

Substitution from 2.50 in 2.48 gives

$$\frac{Z_f}{d} = 1.44 \ln \frac{NI}{V_r^{\frac{1}{2}}} - 3.69 \qquad \text{..... 2.51}$$

Equation 2.47 is applicable only when Z_F is in the region $Z = 0$ to $Z = \infty$. Also $\frac{Z_F}{d} = 0$ when $\frac{NI}{V_r^{\frac{1}{2}}} \simeq 13$. This means equation 2.51 applies for excitation parameters $\frac{NI}{V_r^{\frac{1}{2}}}$ greater than 13.

The slope $Y'(Z)$ of the ray at a distance Z from the origin is given by

$$Y'(Z) = \frac{dY(Z)}{dZ} = \frac{d}{dZ}\left(J_o(\xi)\right)$$

$$= \frac{d}{d\xi} J_o(\xi)\frac{d\xi}{dZ} = -\frac{\ln 2}{d}\xi J_1(\xi) \qquad \text{..... 2.52}$$

For an excitation parameter $NI/V_r^{\frac{1}{2}}$ less than 13, the objective and the projector focal length for the exponential field are the same and equal to the reciprocal of the slope of the ray at $Z = 0$. For larger excitation parameters Z_f is positive (equation 2.51), and the objective focal length F_{obj} is given by

$$\frac{F_{obj}}{d} = \frac{1}{\ln 2\,\xi_1 J_1(\xi_1)} = 1.156 \qquad \text{..... 2.53}$$

The objective focal length is consequently constant for excitation parameters $NI/V_r^{\frac{1}{2}} \geqslant 13$. The chromatic and spherical aberrations are also constant over this region. This is a consequence of the fact that, for an exponential curve, the shape of the trajectory does not vary with excitation.

2.3.1 Electron-optical properties of the exponential field model

For the exponential field the projector focal length is given by the reciprocal of the slope of the ray at the distance $Z = 0$. At $Z = 0$, we have

$$\xi_o = \frac{K}{\ln 2} = \frac{0.1287}{\ln 2}\frac{NI}{V_r^{\frac{1}{2}}} \qquad \text{..... 2.54}$$

since

$$Y'(Z) = \frac{\ln 2}{d}\,\xi_Z \cdot J_1(\xi_Z)\ ,$$

then

$$Y'(0) = \frac{\ln 2}{d}\,\xi_0\, J_1(\xi_0)$$

$$= \frac{0.1287}{d}\,\frac{NI}{V_r^{\frac{1}{2}}}\, J_1(\xi_0)$$

and therefore

$$\frac{f_p}{d} = \frac{1}{0.1287}\,\frac{NI}{V_r^{\frac{1}{2}}}\, J_1(\xi_0)$$

$$= 7.77\,\frac{NI}{V_r^{\frac{1}{2}}} \cdot J_1\left(0.1857\,\frac{NI}{V_r^{\frac{1}{2}}}\right)$$

The calculation of $\frac{f_p}{d}$ values over a wide range of excitation parameter $\frac{NI}{V_r^{\frac{1}{2}}}$ is therefore straightforward. The corresponding values of $J_o(\xi)$ and $J_1(\xi)$ are taken directly from tables of Bessel functions, or they can be calculated numerically.

Figure 2.14 shows the variation of f_p/d, f_{obj}/d and Z_F/d as a function of the excitation parameter $\frac{NI}{V_r^{\frac{1}{2}}}$ over a wide range of $\frac{NI}{V_r^{\frac{1}{2}}}$ covering the first three zones of operation. In the first zone of operation in which the excitation parameter $NI/V_r^{\frac{1}{2}} \leqslant 13$ the projector and objective focal lengths are equal. Minimum focal length of the lens occurs at $NI/V_r^{\frac{1}{2}} = 13$. The objective focal length is constant for excitation parameters greater than 13; its value is 1.156d which is the same as that of the minimum projector focal length $f_{p\ min}$. Figure 2.14 shows that the objective distance Z_F is zero at the position of minimum focal length. The second and third minimum projector focal lengths

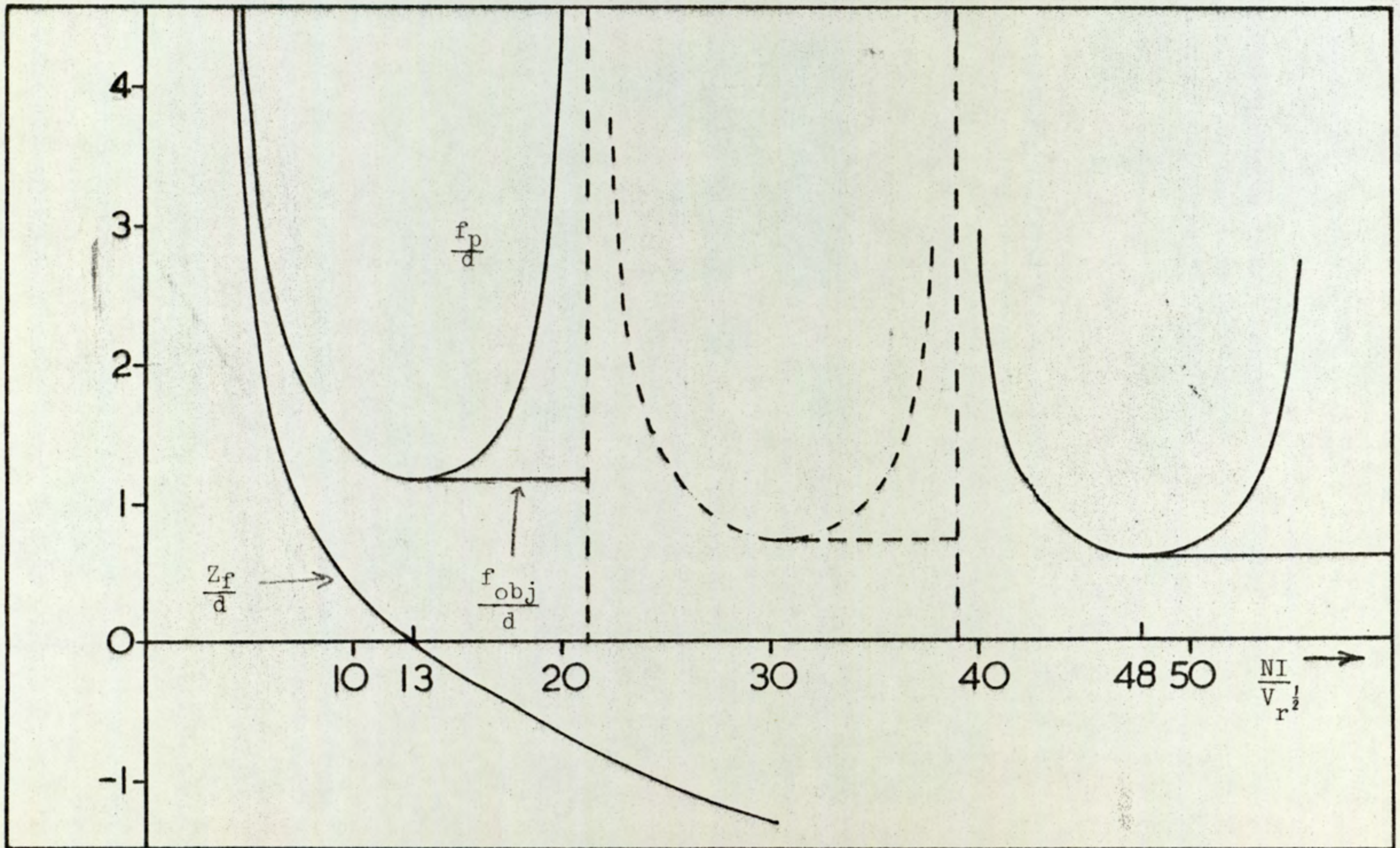

Fig. 2.14 The focal properties of the exponential field distribution

(zones 2 and 3) have values of 0.77 d and 0.614 d respectively and occur at excitation parameters $NI/V_r^{\frac{1}{2}} = 33$ and 48 respectively.

The lens becomes afocal at $NI/V_r^{\frac{1}{2}}$ values of 20.6, 38.5 and 56.5 respectively. At an excitation parameter $NI/V_r^{\frac{1}{2}} = 20.6$, the telescopic ray path through the exponential field occurs as illustrated in figure 2.15. By placing a specimen at a distance Z = 0.7 d along the axis, a strong pre-field is created followed by an imaging field of low aberrations (as will be shown later) in a similar manner to that achieved by the condenser-objective lens of Riecke and Ruska (1966) The figure also shows two possible directions for the illuminating beam, the preferred direction being determined by the operational requirements of a particular microscope.

2.3.2 Chromatic and spherical aberration of the exponential field model

As the chromatic and spherical aberrations of a lens are strongly related to the objective focal length, one can expect that these aberration coefficients of the exponential field models will be constant over the range of excitation for which the objective focal length is constant. Indeed Glaser (1952) showed analytically that the chromatic aberration coefficient for the exponential field, in the range of excitation mentioned above, is constant and equal to 0.721 d.

The present author has calculated the chromatic and spherical aberration coefficients C_c and C_s numerically by Scherzer's formulae, using a digital computer, for the exponential field model (with the aid of the computer program described in section 3.3). To give an idea of the accuracy of the computer program, the calculated value of C_c was found to be 0.722 d, in good agreement with the

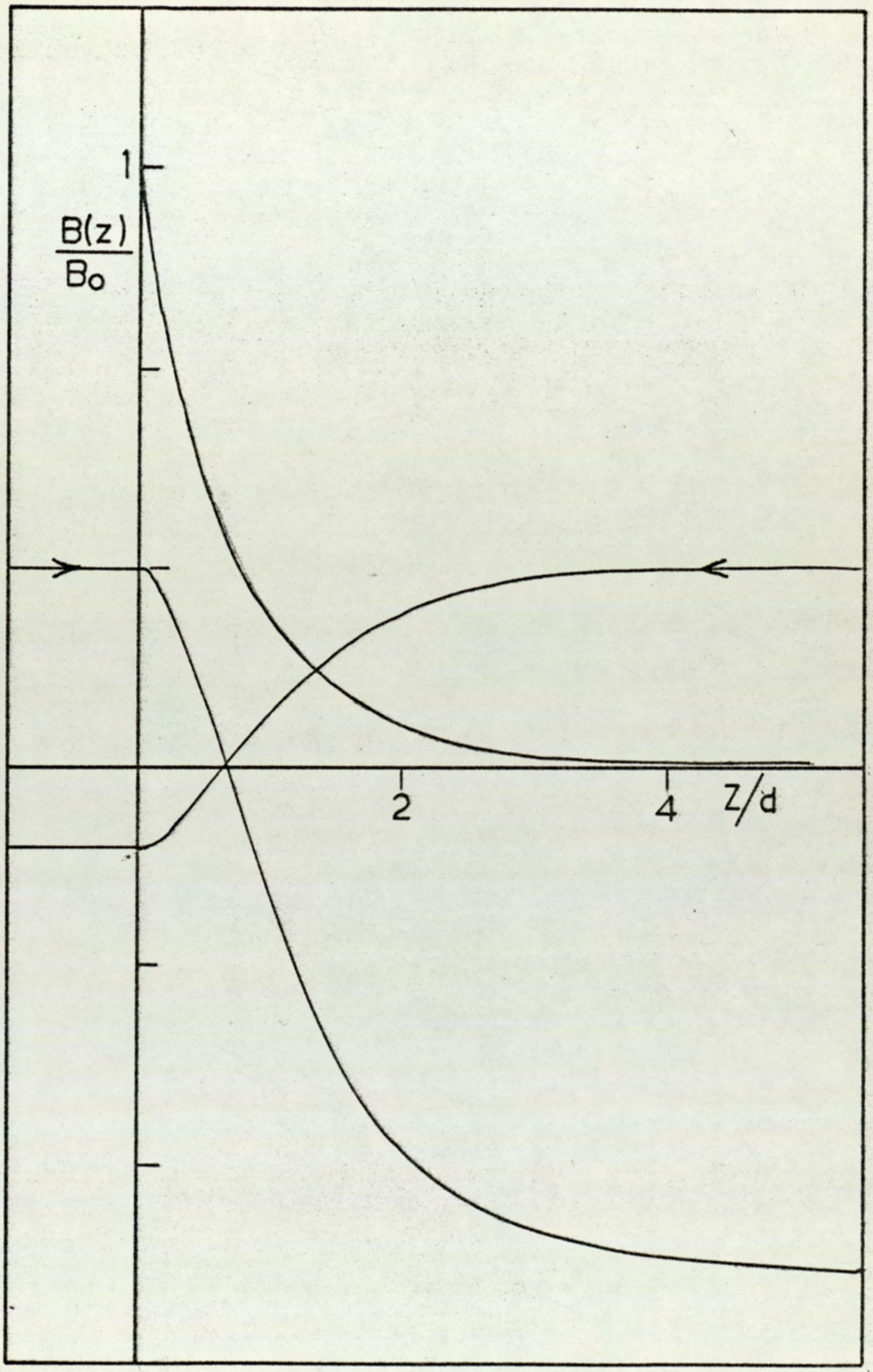

Fig. 2.15 The telescopic ray path through the exponential field

analytical solution. Thus C_c/f is equal to 0.632. The calculated value of C_s, which was not calculated by Glaser in his brief treatment of the exponential field, was found to be 0.363 d, i.e. $C_s/f = 0.315$, a plausible result, not too different from the values obtained with other types of lenses. The calculated C_c/d and C_s/d values together with the objective and projector focal lengths of the exponential field over the first zone of operation, are illustrated in figure 2.16.

2.3.3 Radial and spiral distortion coefficients of the exponential field model

The determination of the distortion coefficients of the exponential field is very important, since it may be used to characterise asymmetric field distribution (Appendix 2), in the same way as the square-top field may be used to characterise conventional two-pole lenses. The coefficients D_{rad} of radial and D_{sp} of spiral distortion have been calculated numerically for the exponential field model, using a digital computer to evaluate equations 2.16 and 2.17. Because of the asymmetry of the field distribution, there are two possibilities for the direction of entry for the beam. The calculation was therefore done for the two directions of the entering beam, and the results are shown in figure 2.17. The solid lines represent the case where the entering beam comes from the negative Z direction, and the dotted lines represent the beam entering from the positive Z direction. Figure 2.17 shows that for the radial distortion coefficients, in both cases the d^2D_{rad} value starts at excitation parameter $\frac{NI}{V_r^{\frac{1}{2}}} = 0$, with a value of 0.25 as was the case for the bell-shaped field model. As the excitation of the lens increases, the value of d^2D_{rad} for the case

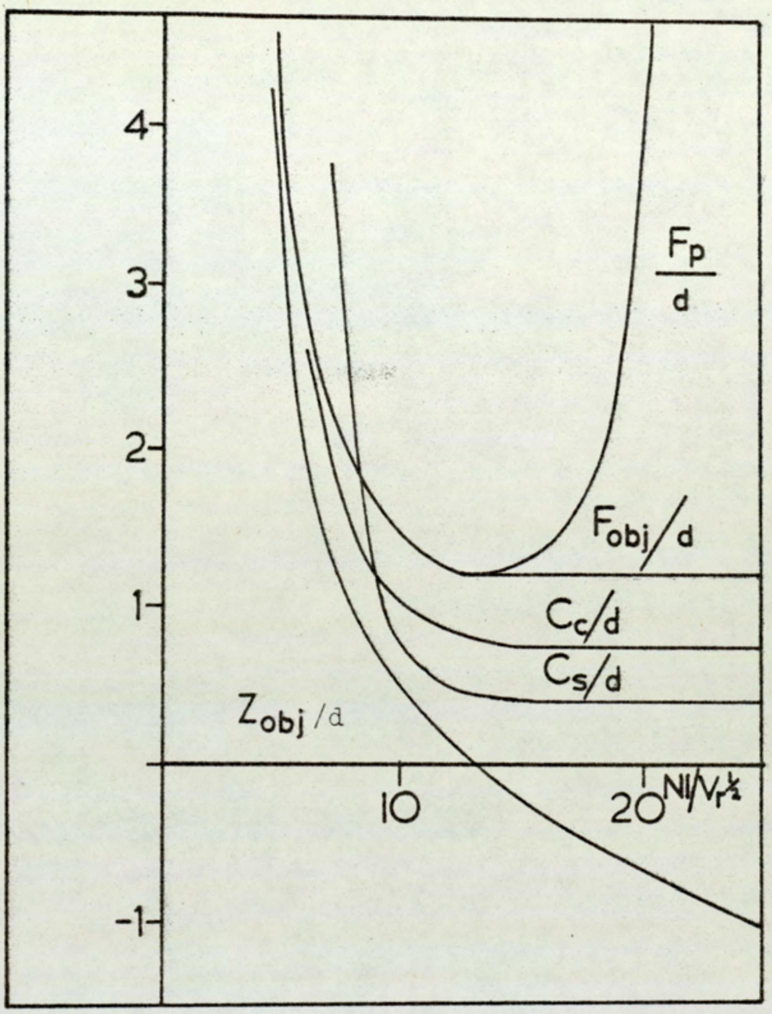

Fig. 2.16 Chromatic and spherical aberration coefficients of the exponential field model

of the beam coming from - Z direction, increases more rapidly than the one in the opposite direction and reaches a maximum value about 0.87 at $NI/V_r^{\frac{1}{2}}$ value equal approximately 10, and then falls more rapidly to zero at $NI/V_r^{\frac{1}{2}} = 14$. The maximum value of d^2D_{rad} for the beam coming from the positive side of Z direction is about 0.46 at $NI/V_r^{\frac{1}{2}} = 7$, and then falls steadily to reach zero at $NI/V_r^{\frac{1}{2}} \simeq 15$. This shows that the radial distortion of the exponential field for the beam coming from the exponential side of the field is only about half that for the beam entering the field the other way round.

The same is true for the spiral distortion coefficient. The most favourable arrangement for low spiral distortion is for the beam to enter the field from the exponential side. In this case the ratio between the two values of d^2D_{sp}, for the two directions of the entering beam, is one third at $NI/V_r^{\frac{1}{2}} = 13$. This ratio increases at $NI/V_r^{\frac{1}{2}}$ is increased. Also, we see that there is a little fluctuation in the value of d^2D_{sp} in the case of the favourable direction, this is similar to the relation found for the spiral distortion coefficient of the square-top field as represented by the 'sine' term of equation 2.31.

The determination of the most favourable arrangement for low distortion is relevant to the design of single-pole projector lenses which can have appreciably lower distortion coefficients than those of the best double pole-piece lenses.

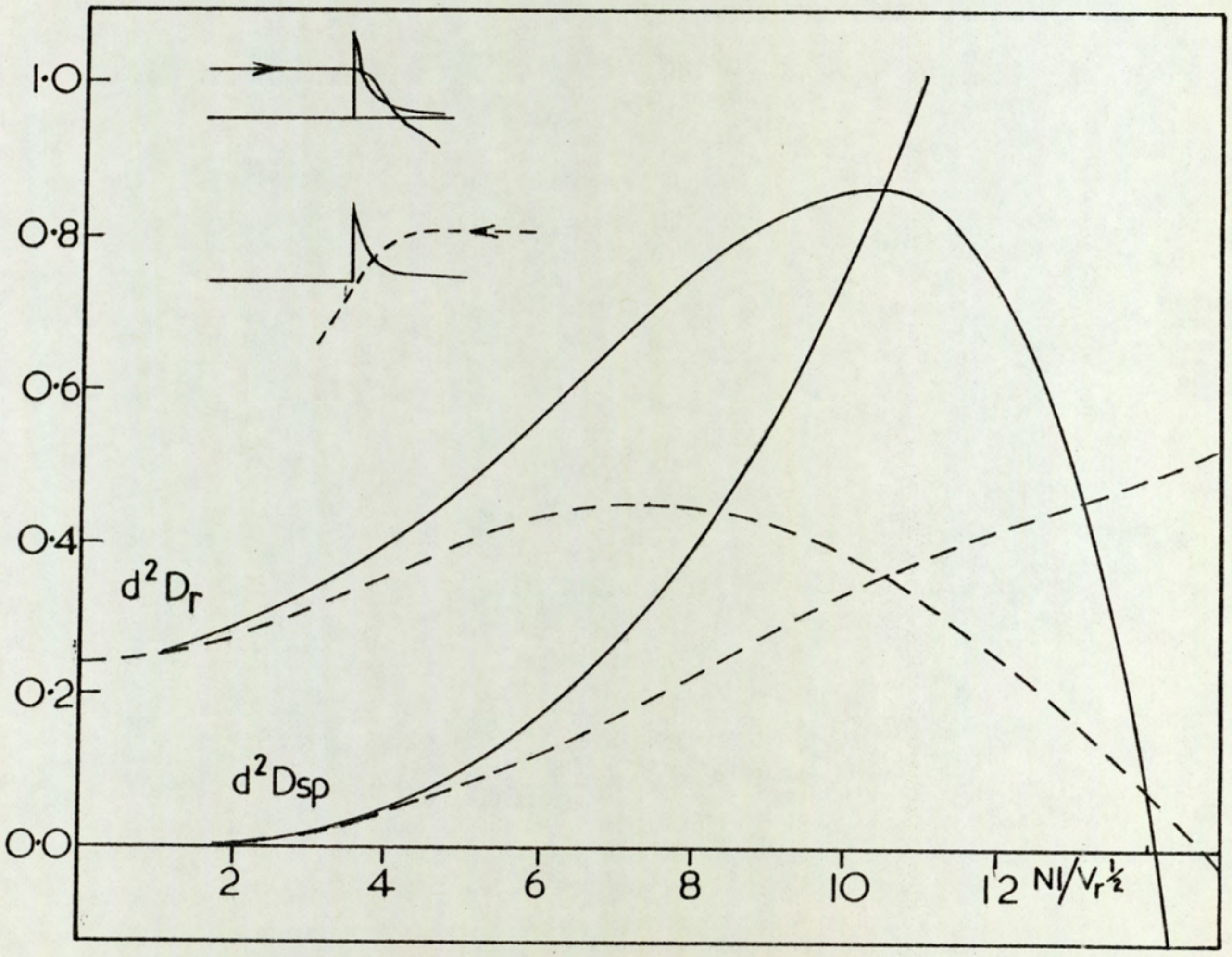

Fig. 2.17 Radial and spiral distortion coefficients of the exponential field distribution

3. COMPUTER PROGRAMS FOR CALCULATING ELECTRON-OPTICAL PROPERTIES AND ABERRATIONS

Digital computers are now used widely in numerical analysis in electron optics. The use of digital computers enables us to get rapid and accurate results for the focal properties and aberrations of magnetic electron lenses; computing the axial field distribution is especially useful for the practical design of such lenses.

Starting with a program for calculating the electron trajectories through an axial field distribution of an iron-free lens, (Marai, 1973), three main programs have been written for calculating electron optical properties, chromatic and spherical aberration coefficients and radial and spiral distortion coefficients for any magnetic field distribution.

3.1 A program for calculating the electron-optical properties of magnetic electron lenses

This program calculates the electron-optical properties of a given magnetic field distribution by solving the paraxial ray equation for a ray passing through that field. Once the trajectory of the ray is known, the electron-optical parameters, such as the objective focal length f_{obj}, the projector focal length f_p, and the objective distance Z_f, can be deduced.

The axial field distribution can be obtained from calculated or measured data, or can be calculated analytically from a field model, or calculated from the Biot-Savart Law for the iron-free lenses, or directly using one of the well-known methods, such as the relaxation method (Liebmann and Grad, 1951) or the finite element method (Munro, 1972). From a knowledge of the axial field distribution B(Z) and the ampere-turns NI, the program computes a quantity A(Z), known as the 'distance function', where

$$A(Z) = \frac{B(Z)}{NI} \qquad \ldots\ldots 3.1$$

on the assumption that we are dealing with unsaturated iron. The function A(Z) is independent of the excitation NI of the lens, and hence the program calculates it once only. The magnetic field at any point Z on the axis is given by multiplying the number of ampere-turns by the function A(Z) at that point.

The second step in the program is to calculate the electron trajectory at any value of NI. To do so, we first divide the field, given in the first stage of the program, into a number of successive intervals, over each we average the value of the function A(Z). The original field given is thereby converted into a 'staircase' field (figure 3.1). For each interval, equations 2.22 are applied; this gives the solution of the paraxial ray equation for a constant magnetic field. We then perform a series of successive operations through the field in which r and r' of one section are taken as r_o and r'_o for the next.

The number of intervals and the interval width are suitably chosen in order to ensure the required accuracy without excessive computer time.

Finally, the required electron-optical parameters F_{obj} and Z_r are calculated as follows:

$$F_{obj} = \frac{1}{r'_{(r = 0)}} \qquad \ldots\ldots 3.2$$

$$Z_f = Z_{(r = 0)} \qquad \ldots\ldots 3.3$$

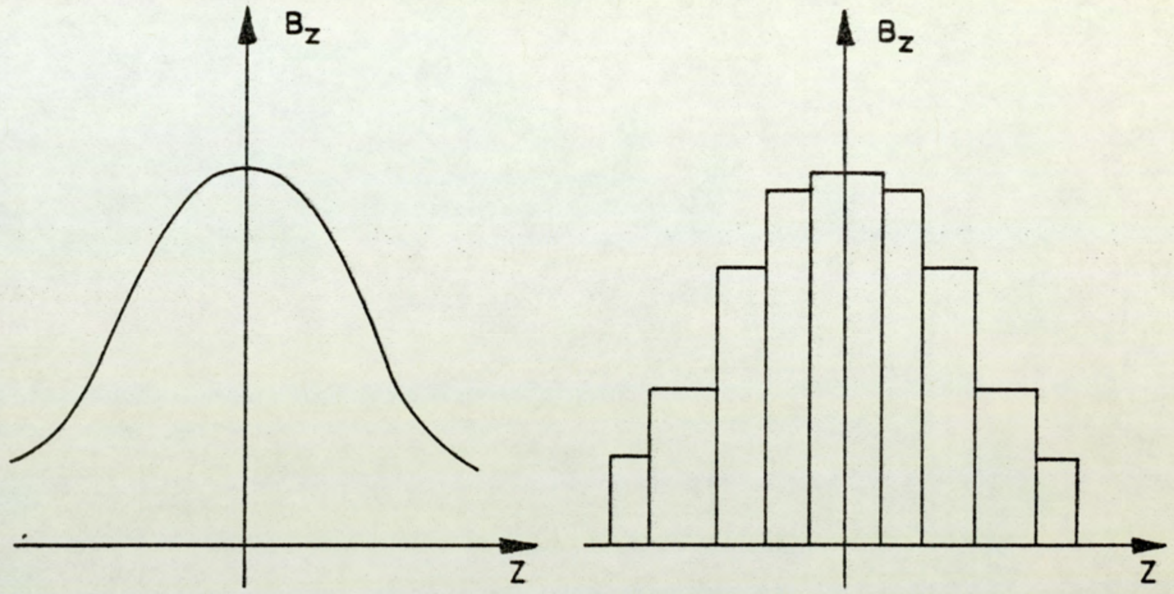

Figure 3.1 The flux density distribution converted into a 'staircase' field

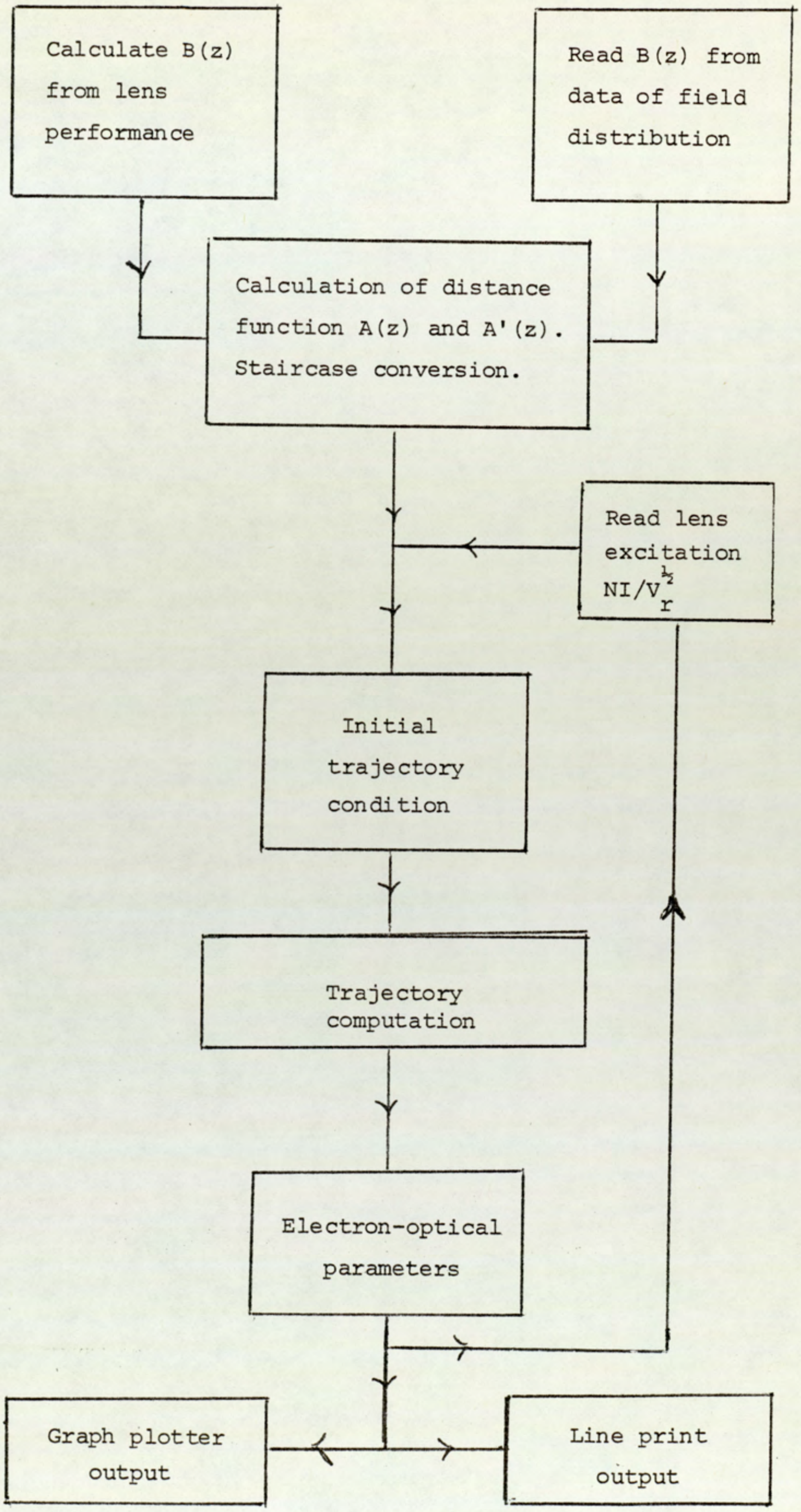

Fig.(3.2) A flow diagram of the computer program (Data BZ).

For a paraxial ray entering the field with initial radial height $r_o = 1$ and initial slope $r_o' = 0$, the projector focal length f_p is given by the reciprocal of the slope of the above ray at the point where the ray leaves the lens field. The output of the computer can, if needed, be fed to a graph-plotter giving directly the ray pattern through the field distribution. This program (Appendix 3), called 'DATA BZ', uses FORTRAN 4. A flow diagram is given in figure 3.2.

3.2 A program for calculating chromatic and spherical aberration coefficients of magnetic electron lenses

The computation of chromatic and spherical aberration coefficients C_c and C_s is carried out using the expressions given by Glaser (1933) and Scherzer (1936),

$$C_c = -\frac{e}{8mV_r} \int_{Z_o}^{Z_i} B^2(Z)\, \chi^2 \, dZ \qquad \text{..... 3.4}$$

$$C_s = \frac{e}{128\ mV_r} \int_{Z_o}^{Z_i} \chi^4 \left[\frac{3e}{mV_r} B^4(Z) + 8\ B'(Z)^2 - 8B^2(Z) \left(\frac{\chi'}{\chi} \right)^2 \right] dz \qquad \text{... 3.5}$$

in which B(Z) is the axial field along the Z-axis, B' is the derivative of the field with respect to Z, and χ is a ray satisfying the condition that at the object position $\chi_o = 0$ and the slope $\chi_o' = 1$.

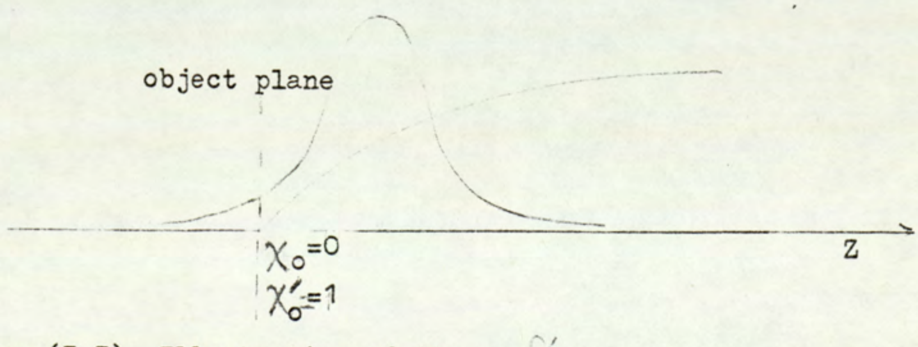

Figure (3.3) Illustration of the ray χ.

For both chromatic and spherical aberration coefficients we chose the image plane Z_i to be at infinity, i.e., the ray χ leaves the lens field parallel to the axis Z (figure 3.3). In practice the process of numerical integration is carried out in reverse direction, i.e. one starts with a ray which enters the lens field parallel to the Z-axis and the integration stopped at the point where the ray intersects the axis, i.e., at the object plane Z_o. The initial height of the ray used in the calculation was 1, so the computed trajectory was normalised so that the slope at the object point Z_o was equal to unity. This was done by multiplying the ray trajectory by f_{obj} $\left[\text{since } f_{obj} = 1/r'(Z_o)\right]$.

The computer program, called 'DABERRATION' (Appendix 4), for calculating the aberration coefficients, was constructed for use with any magnetic field distribution, e.g. from published or calculated data, as well as analytical field models. The first part of the program is very similar to the program 'DATA-BZ', and in which the calculations of the parameters B(Z), $B'(Z)$, χ, and χ' take place. In this part of the program the quantities f_{obj}, Z_F and the coefficients of the terms in equations 3.4 and 3.5 are also calculated.

In the second part of the program, the summation operation, for the individual contribution to equations 3.4 and 3.5 from every interval of the magnetic field distribution, takes place. The output of the program gives the relevant electron-optical quantities C_c, C_s, $NI/V_r^{\frac{1}{2}}$, Z_F, f_{obj}, $C_s\,(B_m/V_r^{\frac{1}{2}})\,10^6$, and $f_{obj}\,(B_m/V_r^{\frac{1}{2}})\,10^6$. The last two parameters are sensitive indicators (Mulvey and Wallington, 1973) of magnetic electron lens optimisation.

As a check on the program, the value of C_c/d was calculated for the exponential field distribution, where d is the 'half-width' of the exponential field. This was found to be 0.722 compared with the calculated value of 0.721, obtained analytically (Glaser 1952).

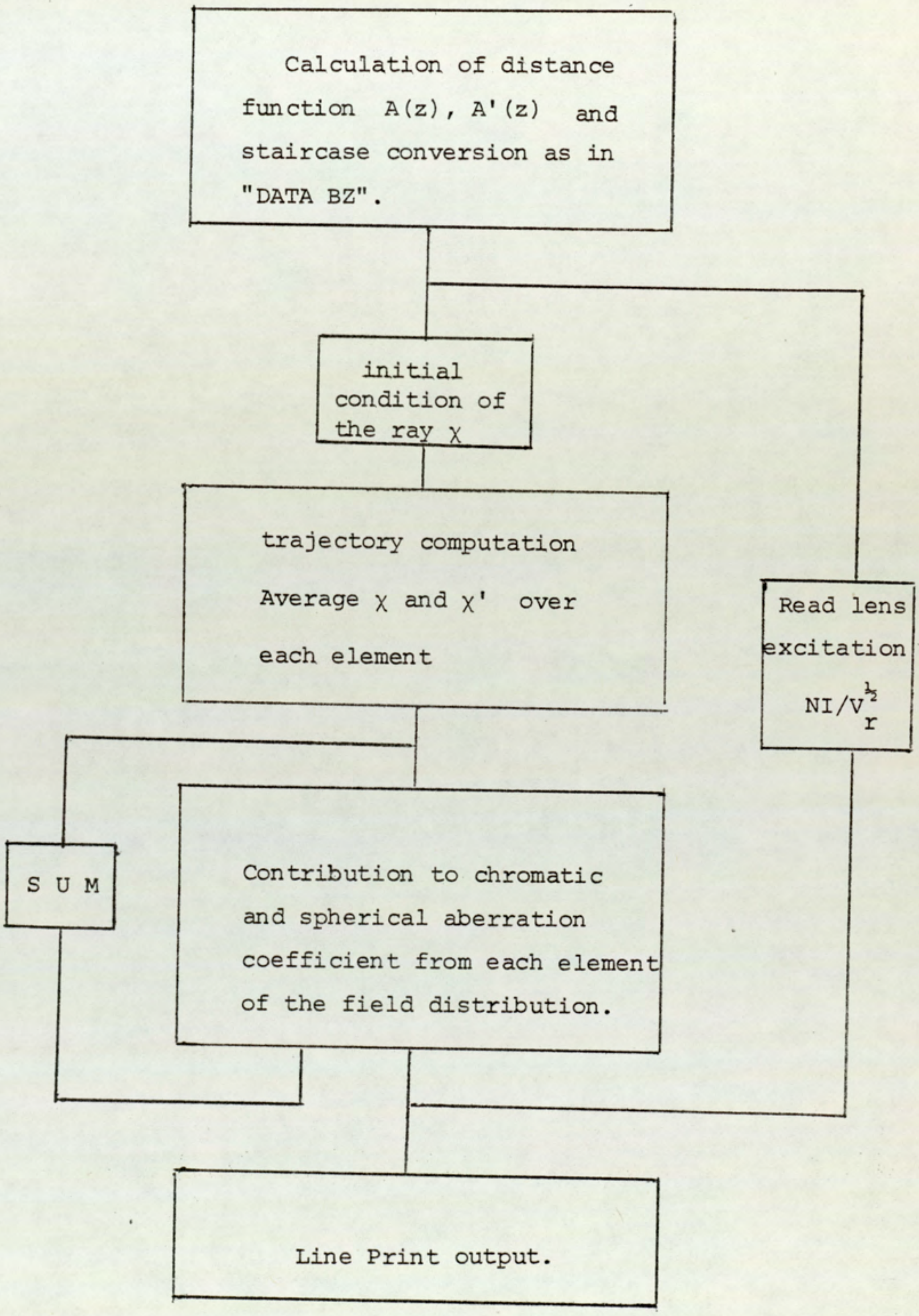

Fig. (3.4) A flow diagram of the computer program "D ABERRATION".

A flow diagram for the computer program 'DABERRATION' is given in figure 3.4.

3.3 A program for the calculation of radial and spiral distortion coefficients of magnetic electron lenses

The calculation of the distortion coefficients D_{rad} and D_{sp}, from equations 2.16 and 2.17, follows a similar procedure to that of calculating the aberration coefficients C_c and C_s. In calculating the distortion coefficients, the integration must be carried out over the entire field distribution. In calculating the radial distortion coefficient D_{rad}, two particular solutions of the trajectory equations are needed, namely, Y and X as defined in equation 2.18. This makes the computation of D_{rad} more complicated. The two rays Y and X are shown in figure 3.5.

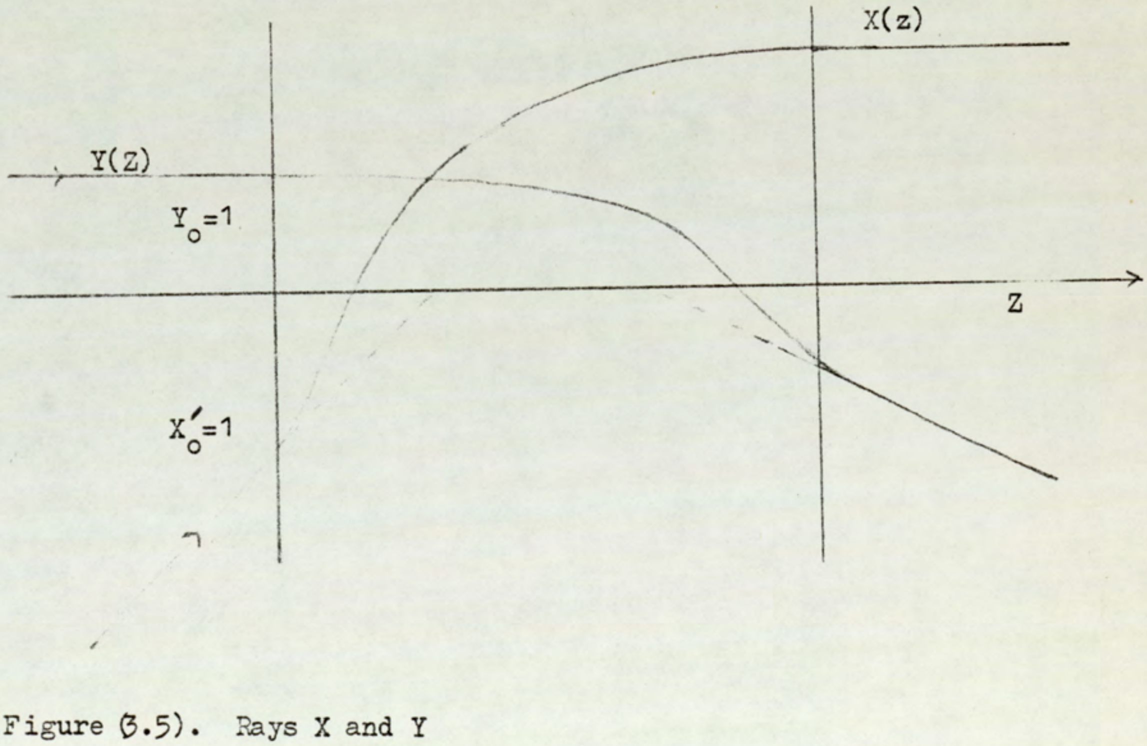

Figure (3.5). Rays X and Y

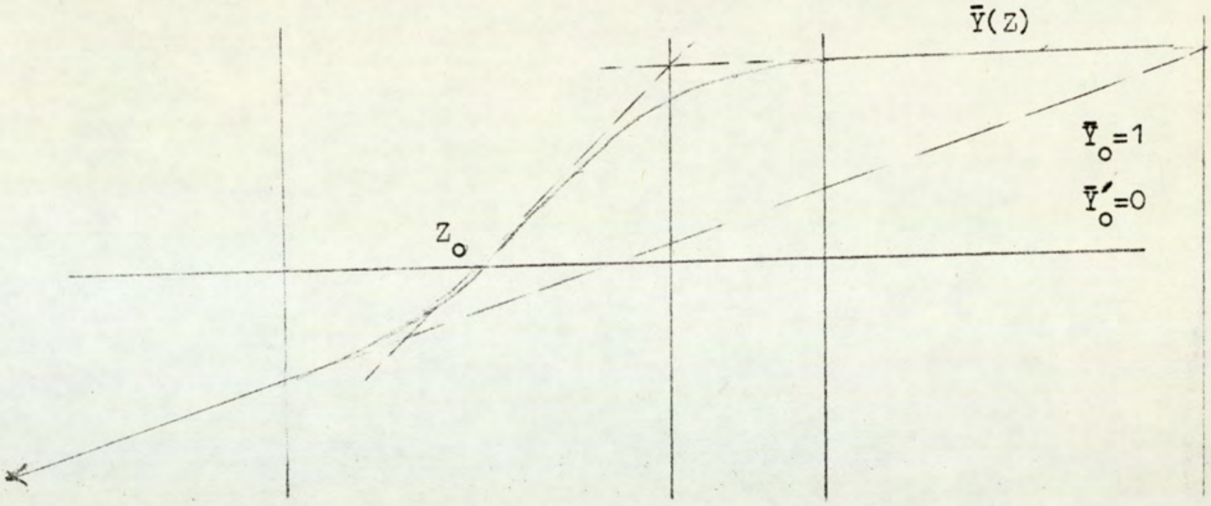

Figure (3.6). Definition of $\bar{Y}$

In order to calculate the trajectory of the ray X, we first calculate the trajectory for the ray $\bar{\bar{Y}}$ (figure 3.6). $\bar{\bar{Y}}$ is a ray for which $\bar{Y}_i = 1$ and $\bar{Y}_i' = 0$ at the image plane. The trajectory is calculated with a ray of unit height and zero slope starting at the image plane; the trajectory is then calculated throughout the field distribution up to the point from which we start the calculation for the ray Y. In order to find the ray X, we then normalise the ray path of the ray $\bar{Y}$, as explained previously, by mutliplying it by the value $-f_{proj}$ or $- 1/Y_i'$.

The program for calculating the distortion coefficients, called 'D DISTORTION', is also constructed so that the relevant coefficients can be obtained for any magnetic field distribution, including those of field models. The full program is given in Appendix 5 and a flow diagram is shown in figure 3.7.

The first part of the program calculates the parameters B(Z), $B'(Z)$, Y, Y', X and the average value of each parameter over each interval of the magnetic field distribution. In this part of the program, f_{proj} is calculated for the corresponding $\frac{NI}{V_r^{\frac{1}{2}}}$; the

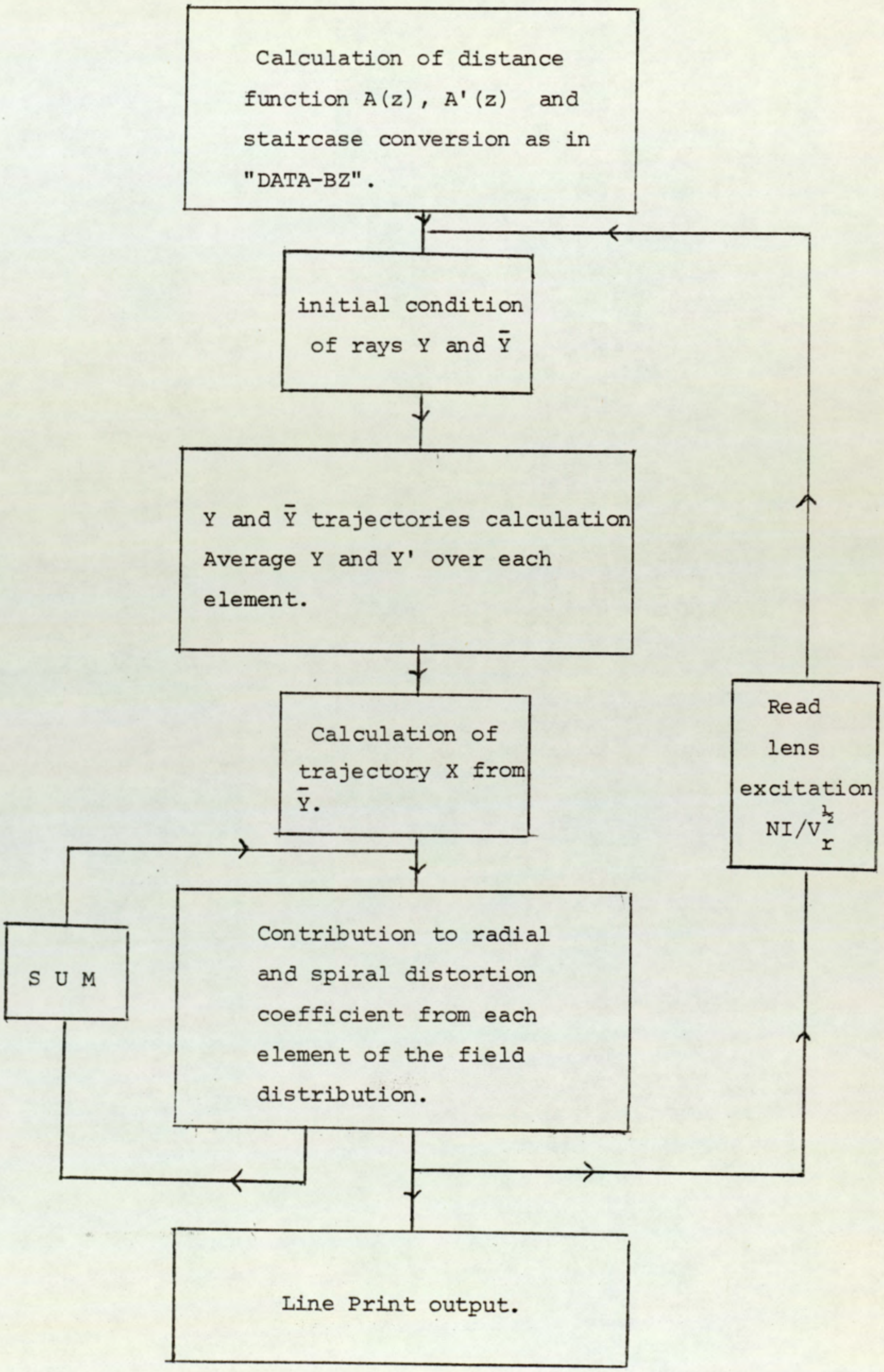

Fig.(3.7) A flow diagram of the computer program "D DISTORTION".

excitation of the magnetic lens.

In the second part of the program, the contribution to equations 2.16 and 2.17 from each interval of the magnetic field distribution is calculated; these contributions are then summed to give the values of the coefficients D_{rad} and D_{sp} corresponding to the excitation parameter $NI/V_r^{\frac{1}{2}}$. For field models it is convenient to express the distortion coefficients in the form a^2D, where a is the half-width of the field distribution. The output from this program gives the quantities $NI/V_r^{\frac{1}{2}}$, f_{proj}, D_{rad} and D_{sp} respectively. The coefficients D_{rad} and D_{sp} can be related to Liebmann's (1952) coefficients of radial and spiral distortion C_d and C_{sp} respectively by the relations

$$C_d = D_{rad}\, R^2 \quad \text{and} \quad C_{sp} = D_{sp}\, R^2 \qquad \text{..... 3.6}$$

where R is the radius of the lens bore.

3.4 The effect of the slope $B'(Z)$ of the field distribution on the calculation of the aberration coefficients

In calculating some of the aberration coefficients, such as the spherical aberration coefficient C_s (equation 3.5) and the radial distortion coefficient D_{rad} (equation 2.16) which depend directly on the slope $B'(Z)$ of the magnetic field, a mathematical difficulty arises in a field distribution that has an infinite slope at one or more points. An example is the exponential field model (figure 2.13). Figure 3.8 shows the slope $B'(Z)$ as a function of Z for the exponential field model. At the singular point Z = 0, there are two slopes, the first is given from the analytical expression

$$\frac{dB(Z)}{dz} = \frac{d}{dZ}\; B_m\, e^{-\ln 2\; Z/d}$$

$$= -\,\frac{\ln 2}{d}\, B\,(Z) = -\,\frac{\ln 2}{d}\, B_m \qquad \text{..... 3.7}$$

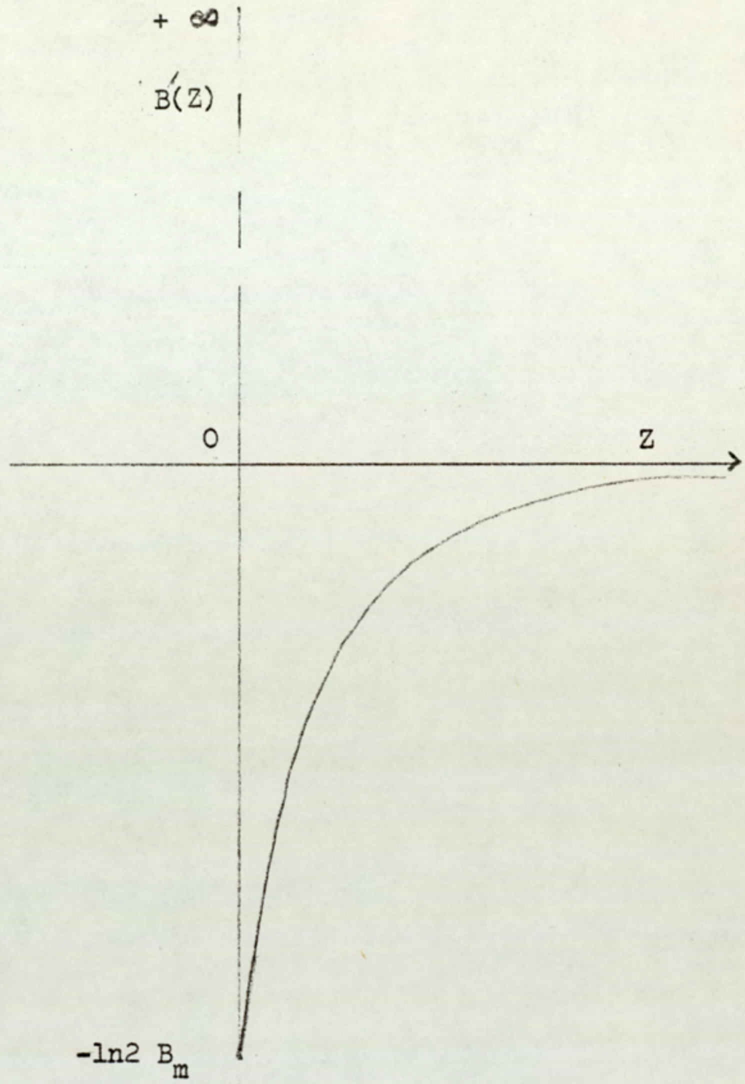

Figure (3.8). $B'(Z)$ as a function of Z

where B_m is the maximum field at Z = O, and d is the half-width of the exponential field.

The second slope at Z = O is infinite; this arises from the fact that the field strength at Z = O drops suddently from its maximum value B_m to zero. From the strictly mathematical point of view the coefficients C_s and D_{rad} for this field will become infinite if the numerical calculation is allowed to proceed in the normal way at this point. This seems to be a difficult problem facing the electron optics researcher when trying to calculate the aberrations of a field distribution like the square-top magnetic field distribution.

For this reason it was important to calculate several field distributions from actual single polepiece lenses in order to compare the results with those calculated from the exponential field.

4. ABERRATIONS OF MAGNETIC ELECTRON LENSES

4.1 Aberrations of iron-free coils

The improvement of the resolution of the TEM and STEM can be achieved mainly by reducing the aberration of the objective lens. The reduction of spherical aberration requires a high magnetic flux density; this is limited by the saturation of the lens material or by the 'critical current' if a superconducting winding is used. Thus to improve the iron-free electron-optical performance, super-conducting coil lenses could be employed. Many publications (Der Schwartz and Makarova, 1968) have appeared concerning the electron-optical properties and aberrations of iron-free coils, but none of them, in fact, found an optimum lens design for the use as objectives or projectors. Moreover in the paper by Der Schwartz and Makarova cited above, the authors did not present their results in a convenient form for finding such an optimum design if it in fact exists. Furthermore, the practice of relating the electron optical properties to an arbitrary scale of length, e.g. the inner diameter D_1, (Figure 4.1), makes it extremely difficult to compare the results obtained from lenses of different shape and size. On the other hand, if a parameter such as D_m, the mean diameter of the coil = $(D_1 + D_2)/2$, figure 4.1, where D_2 is the outer diameter, is taken as the unique geometrical parameter for a set of coils with different D_2/D_1 values and different widths, then relating the electron-optical properties of these lenses to that mean diameter will give a reasonable and acceptable way of comparison.

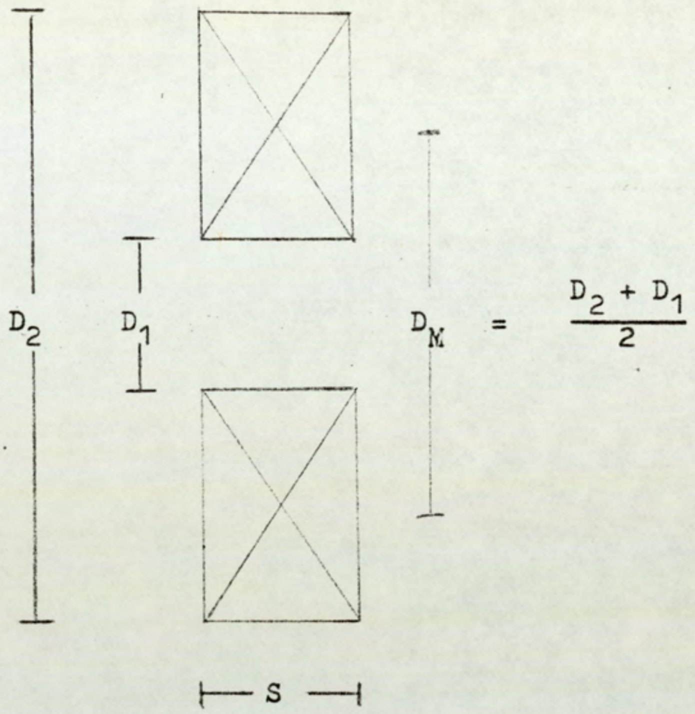

Figure (4.1). Iron-free coil with rectangular cross section.

In calculating the aberrations of magnetic electron lenses, sensitive parameters for the minimisation of lens aberrations like $C_s\, B_{max}/V_r^{\frac{1}{2}}$ and $f_{obj}\, B_{max}/V_r^{\frac{1}{2}}$ (Mulvey and Wallington, 1973) were calculated for a wide range of iron-free coils with outer to inner diameter ratio D_2/D_1 ranging between 3 and 999 and width to mean diameter ratio S/D_m ranging from 0.001 to 0.5. The computer program 'DABERRATION', described in Chapter 3, was used for this calculation, and as a check on the program, the results of spherical aberration coefficient C_s/D_1 obtained for the coil with $D_2/D_1 = 19$ were compared with those obtained by Bassett and Mulvey (1969) for the same lens. The results are in good agreement and are shown in figure 4.2.

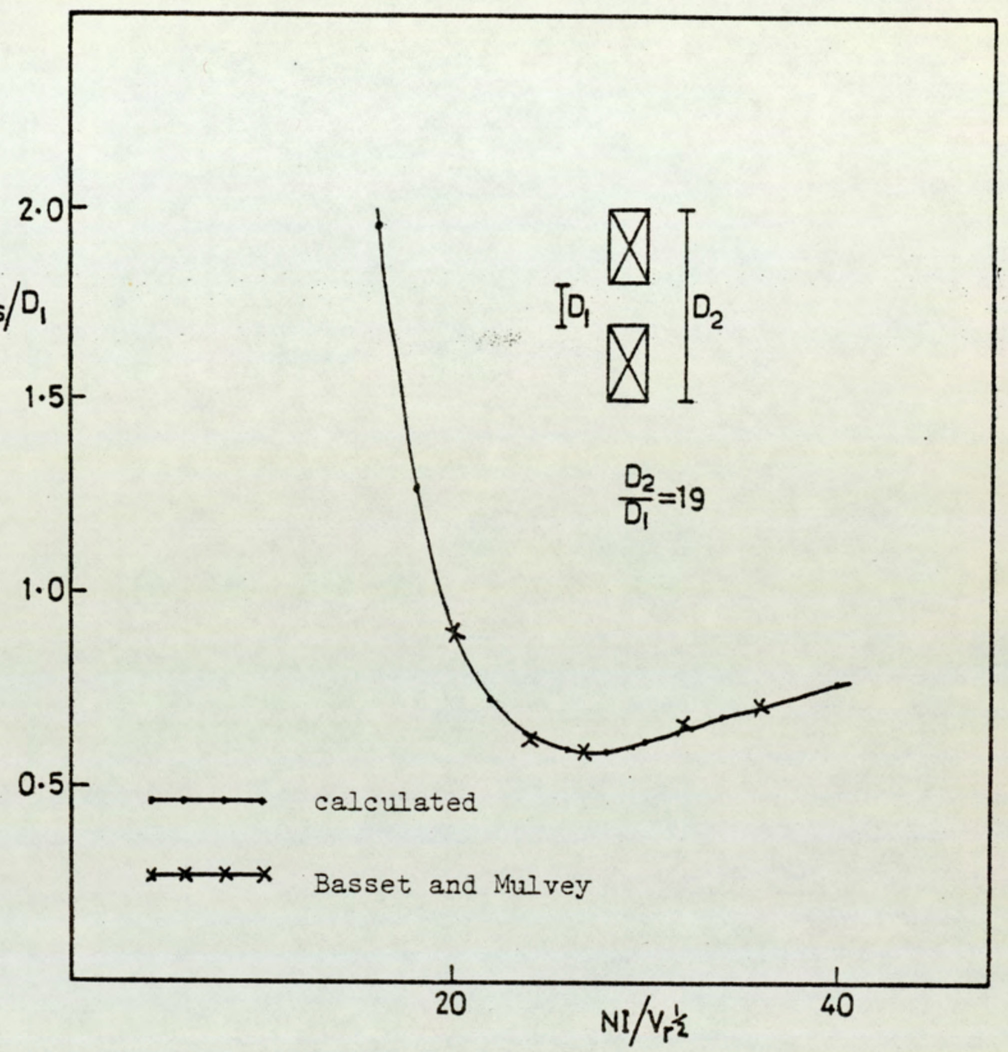

Figure 4.2 Spherical aberration ratio C_s/D_1 for iron-free coil with $D_2/D_1 = 19$

4.1.1 Iron-free coils with minimum spherical aberration

a) Optimum S/D_m value for iron-free coils

It was previously thought that a very thin coil would be the best in order to get the smallest spherical aberration coefficient (Bassett and Mulvey, 1969, Mulvey and Wallington, 1973). However, calculation of the parameter $C_s\ B_{max}/V_r^{\frac{1}{2}}$ for different shapes of iron-free coils shows that there is an optimum size of such lenses, corresponding to a width to mean diameter ratio S/D_m of 0.1. Figure 4.3 shows the variation of the minimum $C_s\ B_{max}/V_r^{\frac{1}{2}}$ value for coils with D_2/D_1 = 19, 24 and 32, respectively, as a function of S/D_m. The results show an optimum value of S/D_m = 0.1 for all these lenses.

b) Optimum ratio D_2/D_1 for iron-free coils

It was also thought that as the outer to inner diameter ratio of the iron-free coil lenses is increased, the spherical aberration coefficient of the lens would get smaller. This would imply that the 'best' lens would be one with D_2/D_1 equal to infinity. Calculation of the parameter $C_S\ B_{max}/V_r^{\frac{1}{2}}$ for excitation parameters $NI/V_r^{\frac{1}{2}}$ up to 40 were made for different iron-free coil lenses with different shape and size. For lenses with S/D_m different from 0.1 the graph of the minimum values of $C_s\ B_m/V_r^{\frac{1}{2}}$ against D_2/D_1 shows that there are real optimum values for D_2/D_1 within range ($3 < D_2/D_1 < 999$), (figure 4.4). For example, with lenses with S/D_m = 0.005, i.e. thin coils have an optimum D_2/D_1 value nearly equal to 28. The minimum $C_s\ B_{max}/V_r^{\frac{1}{2}}$ corresponding to this ratio is 3.06 mm mT.$V^{-1/2}$. After this minimum as we increase the ratio D_2/D_1, the value of $C_s\ B_{max}/V_r^{\frac{1}{2}}$ increases more rapidly until D_2/D_1 is about 250, the increase in $C_s\ B_{max}/V_r^{\frac{1}{2}}$ becomes slower and slower until it reaches a saturation value just over 4.22 mm.mT.$V^{-1/2}$ for D_2/D_1 ratios greater than 1000. For lenses with S/D_m = 0.1, the figure shows different behaviour of the minimum

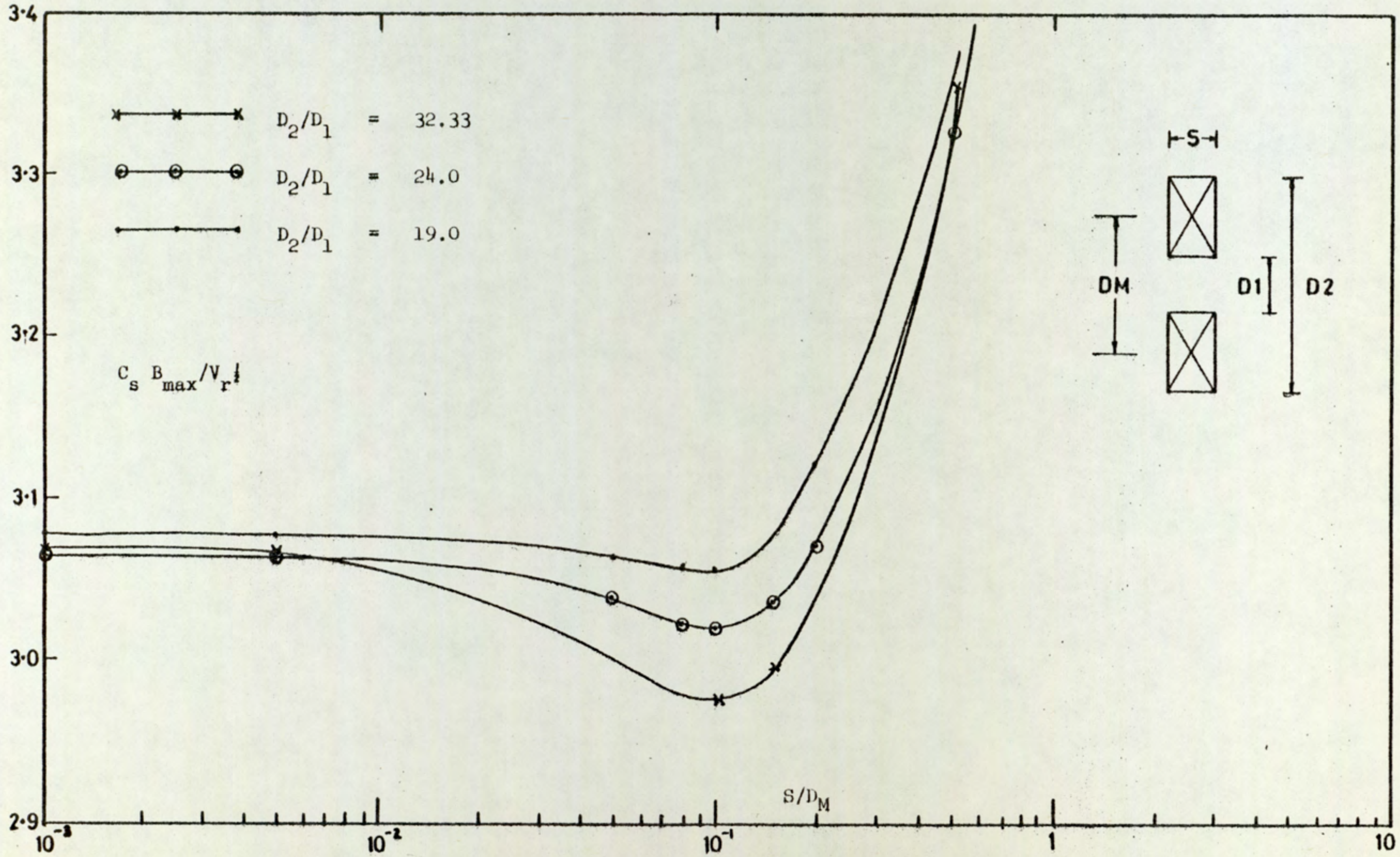

Fig. 4.3 Optimum width to mean diameter ratio for iron-free coils

$C_s\ B_{max}/V_r^{\frac{1}{2}}$ values. It starts with a value equal to 3.575 mm.mT.$V^{-1/2}$ at $D_2/D_1 = 3$, and falls very rapidly as the D_2/D_1 ratio increases until the ratio is about 40. The decrease of $C_s\ B_{max}/V_r^{\frac{1}{2}}$ becomes much slower as D_2/D_1 exceeds 40, and for $D_2/D_1 = 100$ or more the change of $C_s\ B_{max}/V_r^{\frac{1}{2}}$ is very small and reaches approximately a constant value equal to 2.87 mm.mT.$V^{-\frac{1}{2}}$ at $D_2/D_1 = 999$. This value of $(C_s\ B_{max}/V_r^{\frac{1}{2}})_{min}$ is the smallest value, to my knowledge, that has been calculated for any iron-free coil up to the present. These results, again, confirm that the optimum size of the lens occurs at $S/D_m = 0.1$.

c) <u>The minimum $C_s B_m/V_r^{\frac{1}{2}}$ values of iron-free coils and the theoretical limits of magnetic lenses</u>

The theoretical limit of $C_s\ B_{max}/V_r^{\frac{1}{2}} = 2.225$ mm.mT.$V^{-\frac{1}{2}}$ for the field distribution of magnetic lenses was first given by Tretner (1959). Recently Moses (1972) gave a revised value for that limit equal to 2.338 mm.mT.$V^{-\frac{1}{2}}$. Any lens with a value of $C_s\ B_{max}/V_r^{\frac{1}{2}}$ close to these limits can be regarded as ideal as far as a spherical aberration is concerned and hence will be suitable as an objective lens in a high resolution electron microscope. A comparison of the iron-free coil lenses described above with the theoretical values of Tretner and Moses shows that the minimum value of $C_s\ B_{max}/V_r^{\frac{1}{2}}$ found for the lens with $S/D_m = 0.1$ and $D_2/D_1 = 999$ is the lowest value calculated for any objective lens up to now. Figure 4.5 shows the variation of $C_s\ B_{max}/V_r^{\frac{1}{2}}$ against $f_{obj}\ B_{max}/V_r^{\frac{1}{2}}$ for the iron free lenses $D_2/D_1 = 19$, 24 and 999. The first two lenses with S/D_m ratio = 0.005 but S/D_m for the last one is 0.1. The figure also shows the limits given by Tretner and Moses.

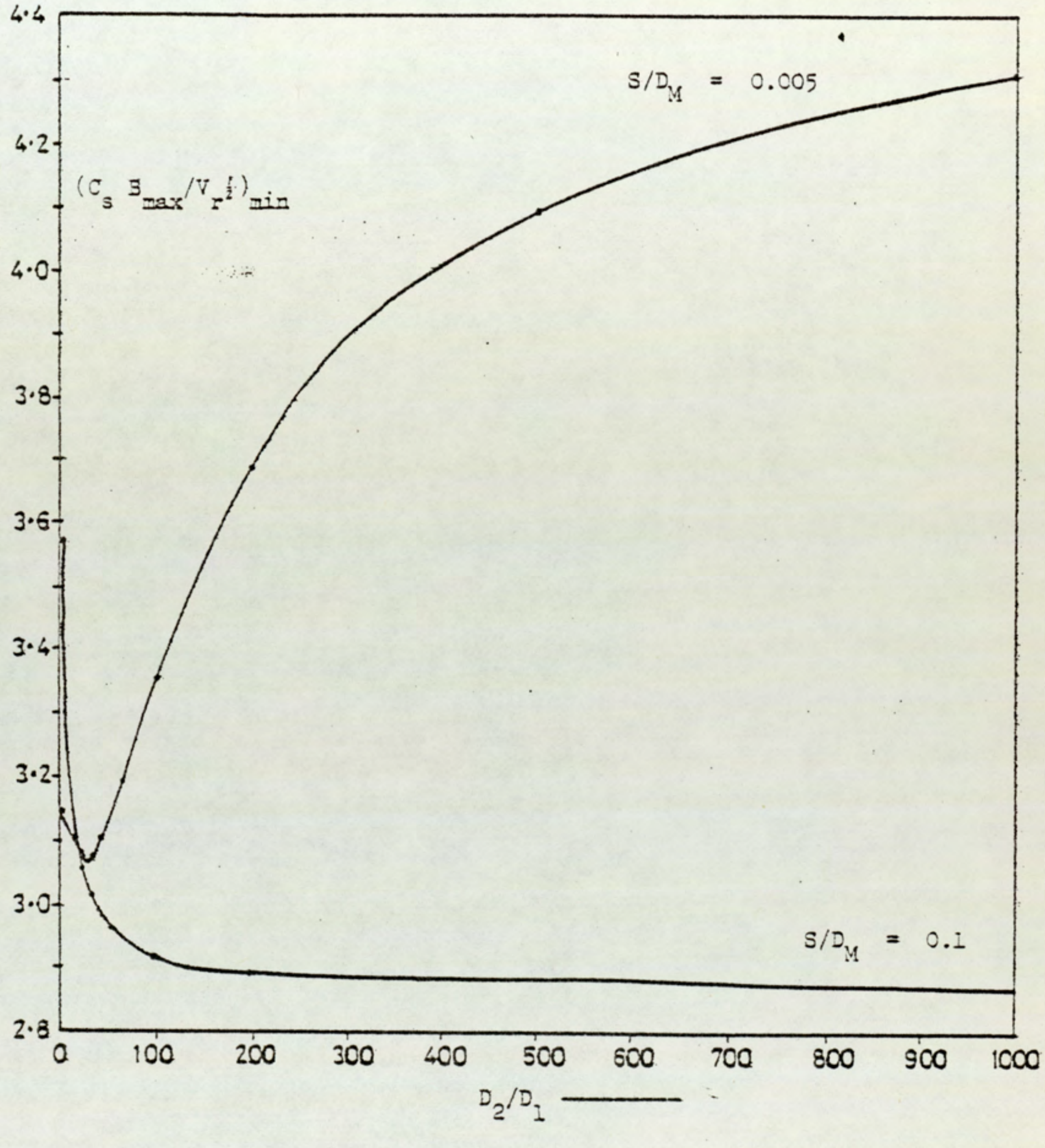

Fig. 4.4 Optimum outer to inner diameter ratio D_2/D_1 for iron-free coils

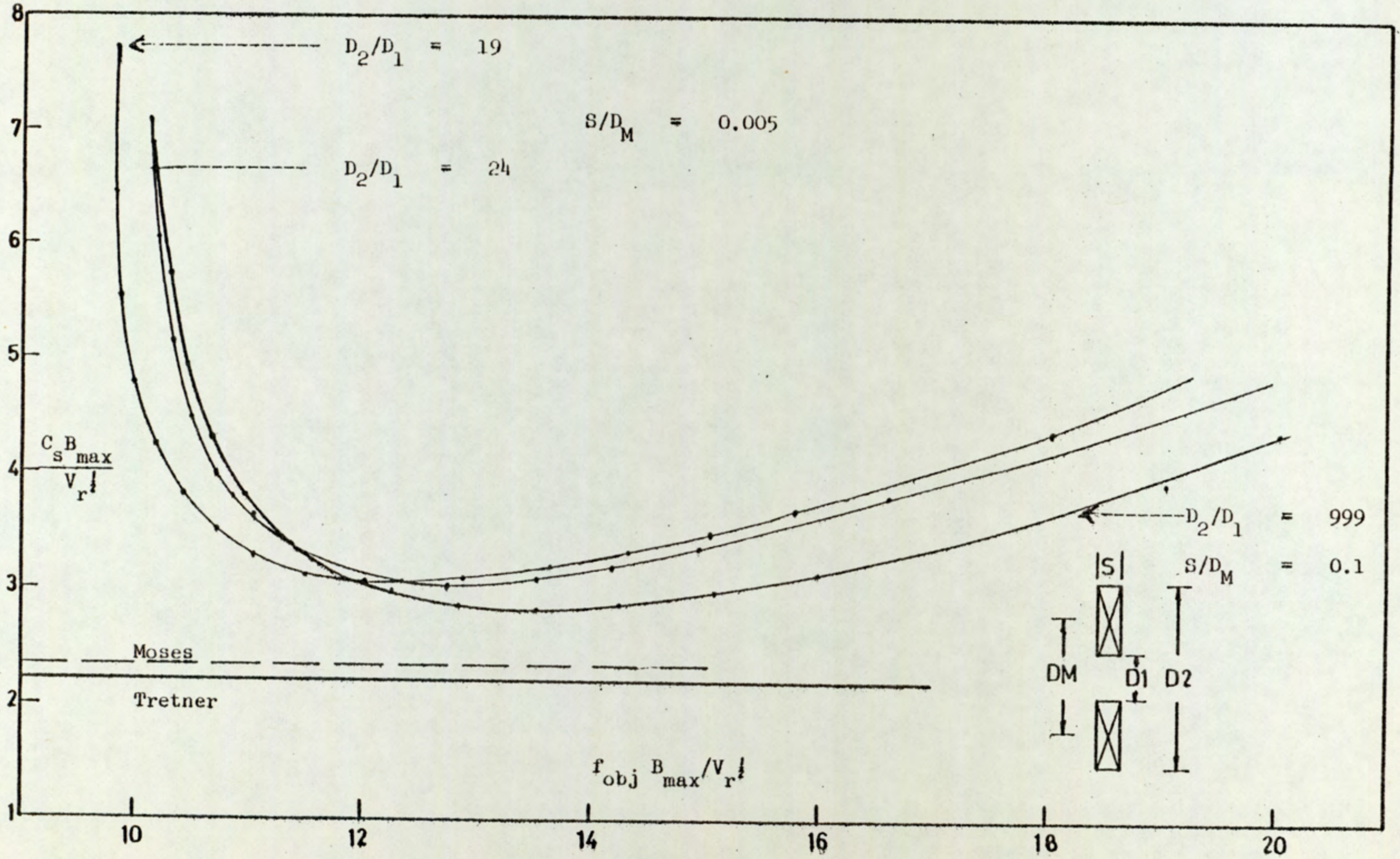

Fig. 4.5 $(C_s\ B_{max}/V_r^{\frac{1}{2}})$ versus $f_{obj}B_{max}/V_r^{\frac{1}{2}}$ for iron-free coils

4.1.2 Distortion coefficients of iron-free coil lenses

When we talk about projector lenses in the electron microscope, the important parameters will be the radial and spiral distortion coefficients of these lenses, as well as the minimum projector focal length. In order to employ iron-free coil lenses as projectors, it would be useful if we could find an optimum design for this purpose, as was the case with the objectives. The computer program 'D DISTORTION', described in Chapter 3, was used to calculate the distortion coefficients for a wide range of iron-free coils, with different S/D_m and D_2/D_1 values. The results are illustrated in figures 4.6 and 4.7.

a) In figure 4.6, the radial and spiral distortion coefficients $C_d = R^2 D_{rad}$, and $C_{sp} = R^2 D_{sp}$, are shown for a range of iron-free lenses of constant ratio $D_2/D_1 = 19$ but having $S/D_m = 0.005$, 0.05, 0.1, 0.5 and 1.0 respectively are shown as a function of NI/NI_o. Here R denotes the inner bore radius. The figure shows that both C_d and C_{sp} decrease as the ratio S/D_m increases. This behaviour is similar to that of the calculations of Liebmann (1952) for double-pole lenses (Liebmann, 1952). For the very thin coils the radial distortion changes from pincushion to barrel at $NI/NI_o = 1.2$, while the change for the very wide coils occurs at $NI/NI_o = 1.05$. The changing point for the lenses with different S/D_m ratios lies between the two values mentioned above. The difference in the value of C_{d_o} (C_d at $NI/NI_o = 0$) between very wide lenses and the very thin ones is of the order 10. So from the point of view of the distortion coefficient only, the lenses with high S/D_m ratio seem better, but a check of the important parameter $Q_{sp} = f_p \, (D_{sp})^{\frac{1}{2}}$ (see Appendix 6) of these lenses shows only a slight difference in the actual distortion, for a given screen diameter and projection length, since

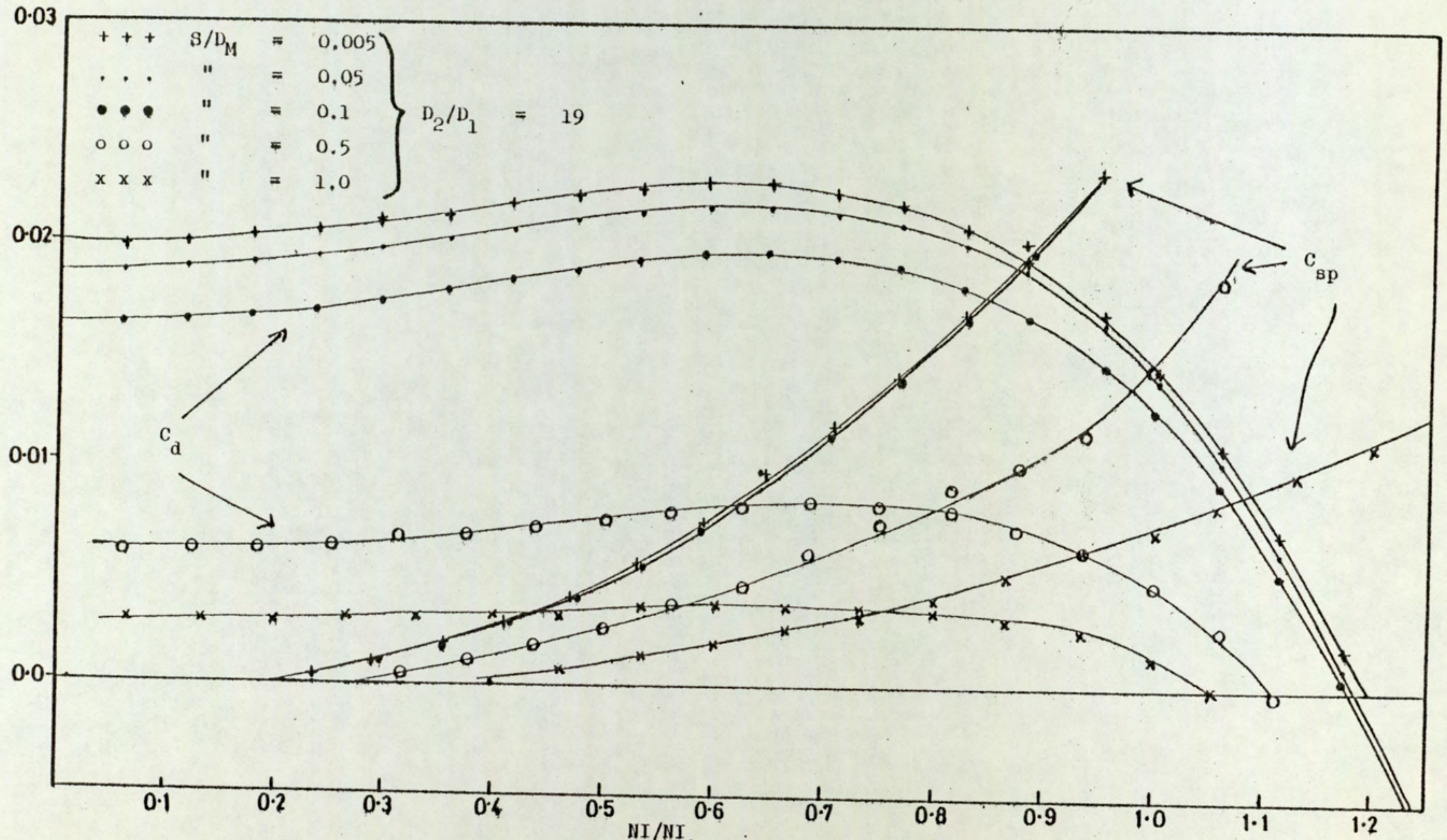

Fig. 4.6 Radial and spiral distortion coefficients of the iron-free coils as a function of NI/NI_o

the Q value for all these lenses is about the same (Q_{sp} = 1.1 at NI/NI_o = 1). So for iron-free coil lenses there is no preferred S/D_m value for use as a projector lens.

b) In figure 4.7 the spiral distortion parameter $Q_{sp} = f_p \, (D_{sp})^{\frac{1}{2}}$ of coils with radius of outer to inner diameter D_2/D_1 = 3, 19, 99 and all having the same width to mean diameter ratio S/D_m = 0.1, are shown as a function of the relative excitation parameter of the lenses NI/NI_o. The figure shows that the lens with D_2/D_1 = 3 has a slightly smaller minimum value of Q_{sp} = 0.91 compared with 0.96 for the lens with D_2/D_1 = 99 at NI/NI_o = 0.65. But at the minimum focal length position (NI/NI_o = 1) where the lens is usually operated, the Q_{sp} value of all these lenses are about the same and equal 1.1. This result is very similar to that of the double-polepiece lenses (Appendix 6) except that the value of Q_{sp} of the latter is around 1.

From the properties of the iron-free coil lenses we conclude

1. When the iron-free coils are used as objectives there is a preferred width for the coil, in order to achieve better resolution, namely S/D_m = 0.1. With that ratio of S/D_m = 0.1, the coils with higher D_2/D_1 ratio will be better.

2. When iron-free coils are used as projectors, there is no practical optimum shape or size for the coil used, since all give essentially the same amount of distortion.

4.2 Aberration of double-polepiece lenses

4.2.1 Liebmann's (1952) calculation of the radial and spiral distortion coefficients of double-pole lenses

The radial and spiral distortion coefficients $C_d = D_r R^2$ and $C_{sp} = D_{sp} R^2$, where R is the radius of the lens bore, were calculated by Liebmann (1952), for four conventional double-pole lenses with

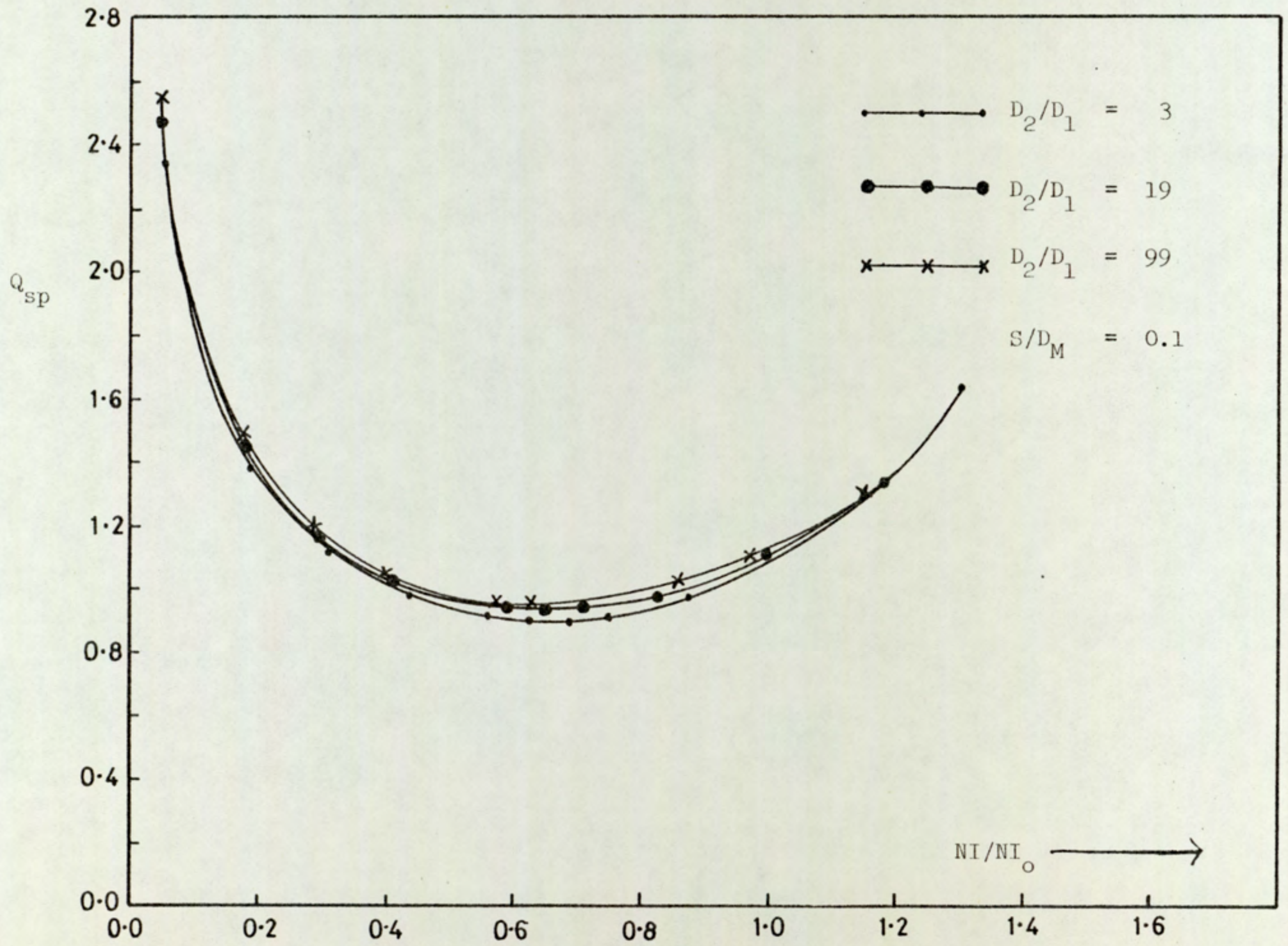

Fig. 4.7 Distortion parameter Q_{sp} of iron-free coils having the same S/D_M as a function of NI/NI_o

gap to diameter ratios S/D equal to 0.2, 0.6, 1 and 2 respectively. His results for radial distortion show that for any lens, an excitation can be found at which the resulting image is free from radial distortion. Liebmann's results also show that, for a given excitation, as S/D increases the value of C_d decreases.

For spiral distortion, Liebmann found a similar behaviour to that for the radial distortion coefficient insofar as the spiral distortion coefficient C_{sp} decreases as the ratio S/D increases. The coefficient C_{sp} is very small at low lens excitation and then increases continuously as the excitation of the lens increases. Figure 4.8 shows the variation of the coefficients C_{d_o} and C_{sp_o} against S/D values, on log-log paper, as found by Liebmann. Here, C_{d_o} denotes the value of C_d at very low excitation, and C_{sp_o} denotes the value of C_{sp} at $(NI/NI_o) = 1$. When the relative value C_{sp}/C_{sp_o} is drawn as a function of the relative excitation parameter $K^2/K^2_{min} = (NI/NI_o)^2$ on log-log paper, Liebmann obtained a single straight line as shown in figure 4.9, on which the calculated values for all lenses with different S/D values lie. This line has a slope 1.36, which means that C_{sp}/C_{sp_o} varies as $(NI/NI_o)^{2.72}$. More recently, from a study of the spiral distortion of the square-top field distribution (see Appendix 6), it was found that the relative spiral distortion coefficient D_{sp}/D_{sp_o} varies as the cube of the relative excitation NI/NI_o, but there is an additional oscillatory term which is a function of $(NI/NI_o)^2$ and the total spiral distortion coefficient is the sum of the two terms.

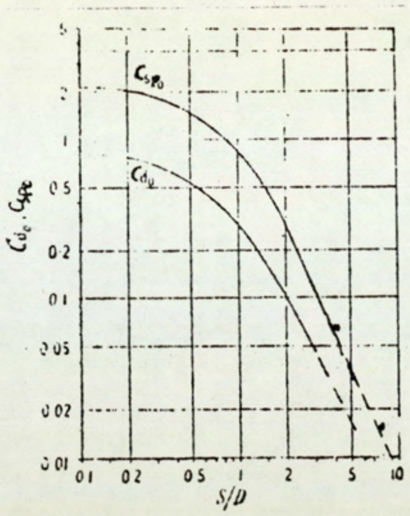

Figure 4.8 C_{d_0} and C_{sp_0} as a function of S/D as given by Liebmann

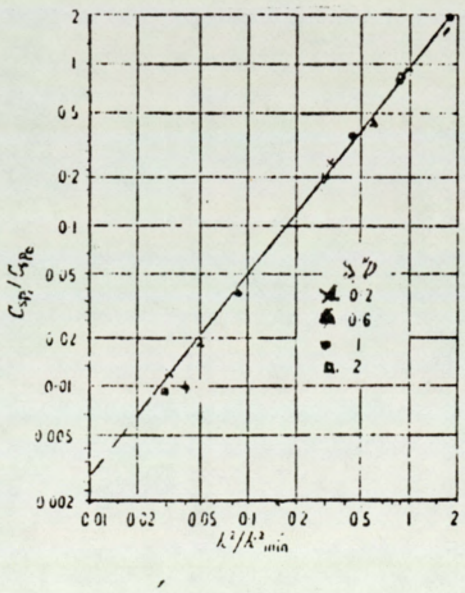

Figure 4.9 C_{sp}/C_{sp_0} versus $(K/K_{min})^2$ calculated by Liebmann

4.2.2 Recalculation and extended computation for the radial and spiral distortion coefficients of double-pole lenses from improved data of the axial field distributions

The radial and spiral distortion coefficients of a wide range of double-pole lenses were calculated by the author using the computer program 'D DISTORTION' described in Chapter 3. The range of gap to bore S/D went from 0.2 to 8. The best available data for the field distribution were used in these calculations; it is likely to be slightly more accurate than those used by Liebmann. The aims of repeating Liebmann's calculations were as follows:

1. To test for the computer program used in the present calculation.

2. To extend the work to cover a larger range of lenses with S/D up to 8, which is close, electron-optically, to S/D = ∞ .

3. To see if there were any significant differences between Liebmann's direct method to calculate image distortion by calculating a third-order ray, and the present method, which relies on Scherzer's equation.

The re-calculation of the radial and spiral distortion coefficients of the lenses with S/D 0.2, 0.6, 1 and 2, shows that C_{d_o} for the first three lenses are essentially the same as those obtained by Liebmann. For the lens S/D = 2, the calculated C_{d_o} was about 0.12, compared with 0.1 in Liebmann's calculation. For all four lenses, there is a difference between the maximum C_d value obtained by Liebmann and those computed by the 'D DISTORTION' program. The latter is lower by an average of 20 percent. For lenses with S/D = 2 and higher, the curve for C_d decreases continuously with increasing excitation parameter $NI/V_r^{\frac{1}{2}}$, at first slowly and then more rapidly as the

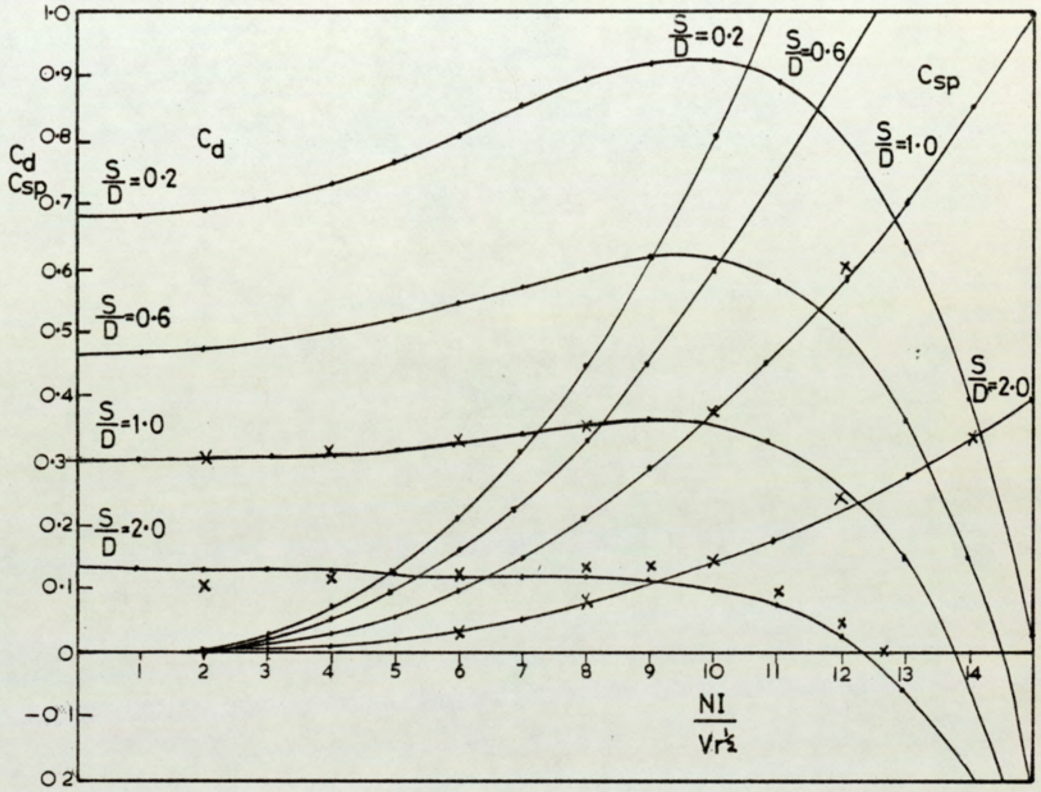

Figure 4.10 Radial C_d and spiral C_{sp} distortion coefficients of double-pole lenses with gap width to inner diameter ratios S/D = 0.2, 0.6, 1 and 2, calculated from the improved data for the axial field distribution. The crosses represent Liebmann's values

excitation $NI/V_r^{\frac{1}{2}}$ of the lens approaches the excitation $NI/V_r^{\frac{1}{2}}$ corresponding to minimum focal length. The excitations for radial distortion-free operation ($C_d = 0$) agree in all cases with the values obtained by Liebmann. Figure 4.10 shows the values of C_d and C_{sp}, calculated by the program 'D DISTORTION' (solid line) together with Liebmann's values for C_d and C_{sp} (crosses) for comparison reasons. This shows excellent agreement as to the shape of the function, but there is a systematic difference in the absolute values of C_{sp}, ours being some 4% less than those of Liebmann. We can therefore be reasonably confident in applying this program to novel situations.

A further check on the program consisted in calculating the radial and spiral distortion coefficients of the miniature double-pole objective lens for the EM6 transmission electron microscope, extensively studied by Juma (1975). This lens has an S/D value equal to 1. The axial field distribution of the lens was measured by means of a Hall probe Gauss meter. The corresponding distortion coefficients were then calculated by the computer program 'D DISTORTION', the results of which are shown in figure 4.11. The calculated values, for the same lens, from the improved data of the field distribution and Liebmann's values are given on the graph, from which we see that the values of C_d and C_{sp} calculated from the measured field and the improved field distribution data are identical and the agreement between these and Liebmann's value is very good, except at the peak value of the radial distortion coefficient curve.

Figure 4.12 shows the variation of the coefficients C_d and C_{sp} for two lens geometries that were not calculated by Liebmann, (S/D=4, S/D = 8). The motive for studying these two lenses was to complete our information about the distortion characteristics of all double-pole lenses distortion, since the lens with S/D = 8 is, to a large extent, representative of the case S/D = ∞, which presents some

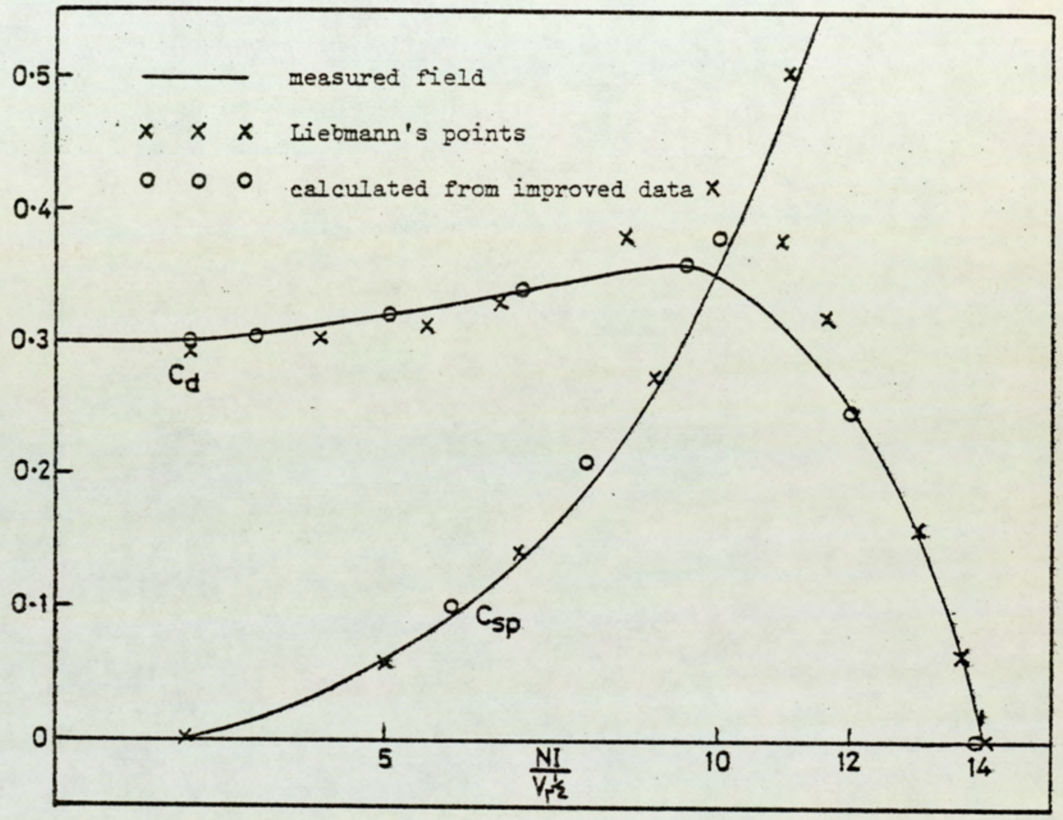

Figure 4.11 C_d and C_{sp} for the lens S/D = 1, calculated from a measured field distribution

mathematical difficulties in computing its aberration as mentioned previously. From figure 4.12 we see that the radial distortion coefficient C_d starts at a low value, $C_{do} = 0.059$ for $S/D = 4$ and 0.028 for $S/D = 8$; it decreases steadily with increasing excitation and reaches zero at $NI/V_r^{\frac{1}{2}} = 11$ for $S/D = 4$ and 9.9 for $S/D = 8$. Figure 4.10 shows that in the range $0 < S/D < 2$ the point of zero radial distortion, $C_d = 0$, occurs at an excitation $NI/V_r^{\frac{1}{2}}$ higher than that for minimum focal length. At the ratio $S/D = 2$, the point of zero radial distortion occurs before the excitation for minimum focal length (figure 4.12); for larger S/D values, the points of zero radial distortion fall increasingly below that for minimum focal length. From figure 4.12, we can see that the spiral distortion coefficient C_{sp} for each lens has essentially the same shape as those of lower S/D, but with reduced magnitude by a factor of about 10. These new results enable one to see more clearly that the spiral distortion coefficient varies as the cube of the excitation parameter $NI/V_r^{\frac{1}{2}}$.

4.3 Aberrations of single-polepiece magnetic electron lenses

As a single-polepiece magnetic electron lens produces an asymmetrical axial magnetic field distribution of distinctive shape, its first-order focal properties and aberrations can, to very good approximation, be represented by those of the exponential field distribution of Glaser (1952), (see Appendices 1 and 2). Indeed, the lens aberrations of single-polepiece lenses are very similar to those of the exponential field distribution. In Chapter 5, the electron optical properties and aberrations of two practical single-pole lenses will be discussed in more detail. But, in general, we can say that for any single-pole lens there are two modes of operation according to the direction of the incident electron beam. The first

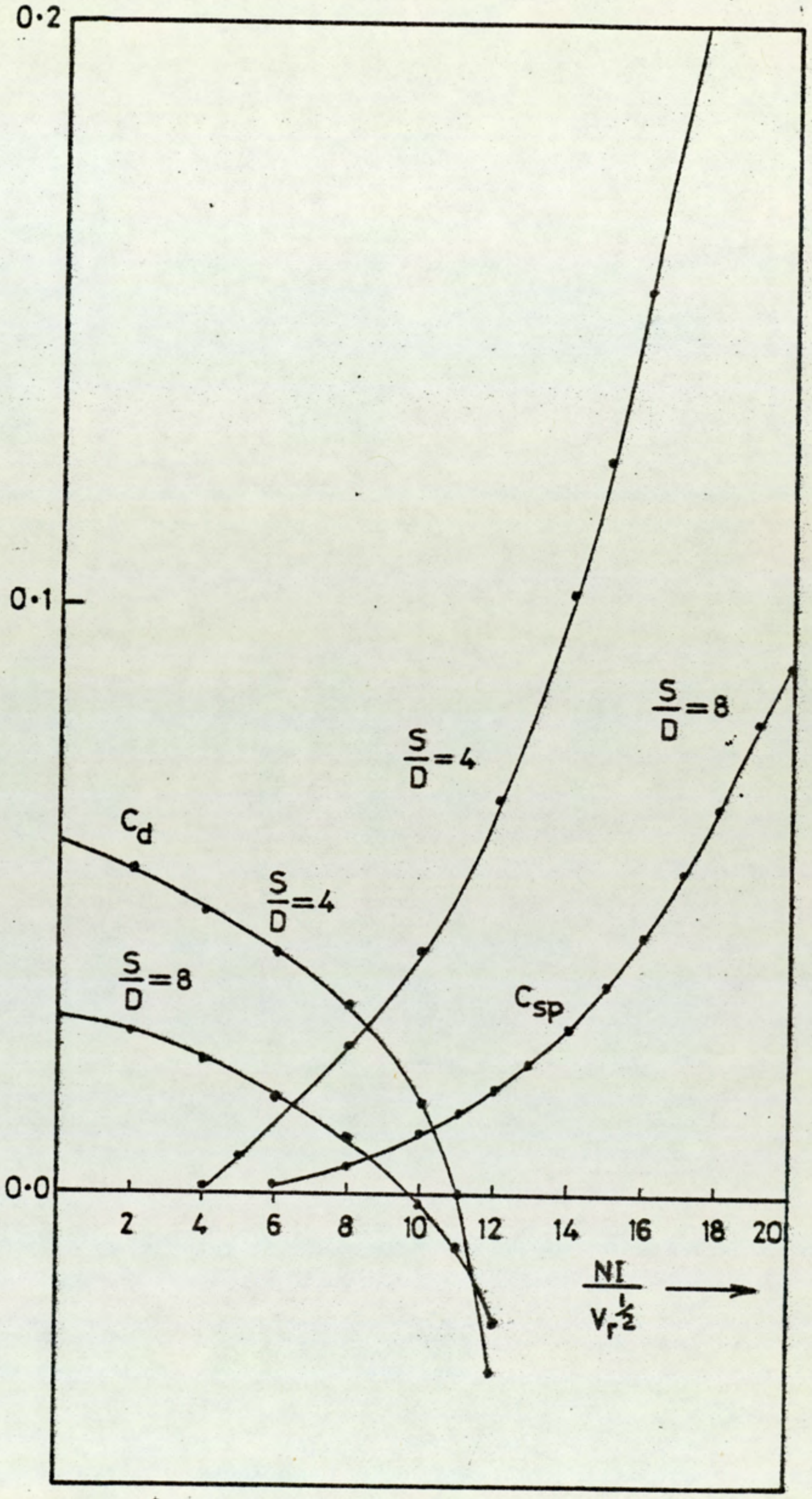

Figure 4.12 Radial C_d and spiral C_{sp} distortion coefficients for lenses with S/D = 4 and 8 calculated from the improved data of the axial field distribution

corresponds to its entering the field of the lens from the 'smooth' side of the field distribution, the second corresponds to entry from the side where the axial field changes abruptly. Accordingly, there is always a preferred direction for a single-pole lens depending on the particular application. For example, when a single-pole lens is used as a projector in an electron microscope, the preferred direction is that with its poleface (snout) facing the incoming electron beam. This way round, the distortion of the image is reduced by a factor of 3 compared with that obtained when the lens snout faces the fluorescent screen.

4.4 The final projector stage of the electron microscope

The projector stage of an electron microscope should provide a distortion-free image, at a suitable magnification, on a fluorescent screen or photographic plate. Other lens defects in this stage are not in general of importance in limiting the performance of the image. The projector stage originally consisted of one lens, but in modern instruments consists of several projector lenses. However, only the final projector lens contributes significantly to image distortion. This is generally kept within prescribed limits by placing the photographic plate at a considerable distance, typically 50 cm from the final projector lens. It therefore seemed useful to investigate whether it would be possible to reduce the length of the viewing chamber by an appreciable amount while maintaining image distortion below the prescribed amount on a standard size screen or photographic plate. In the following section some important parameters in the design of the final stage of the microscope will be discussed.

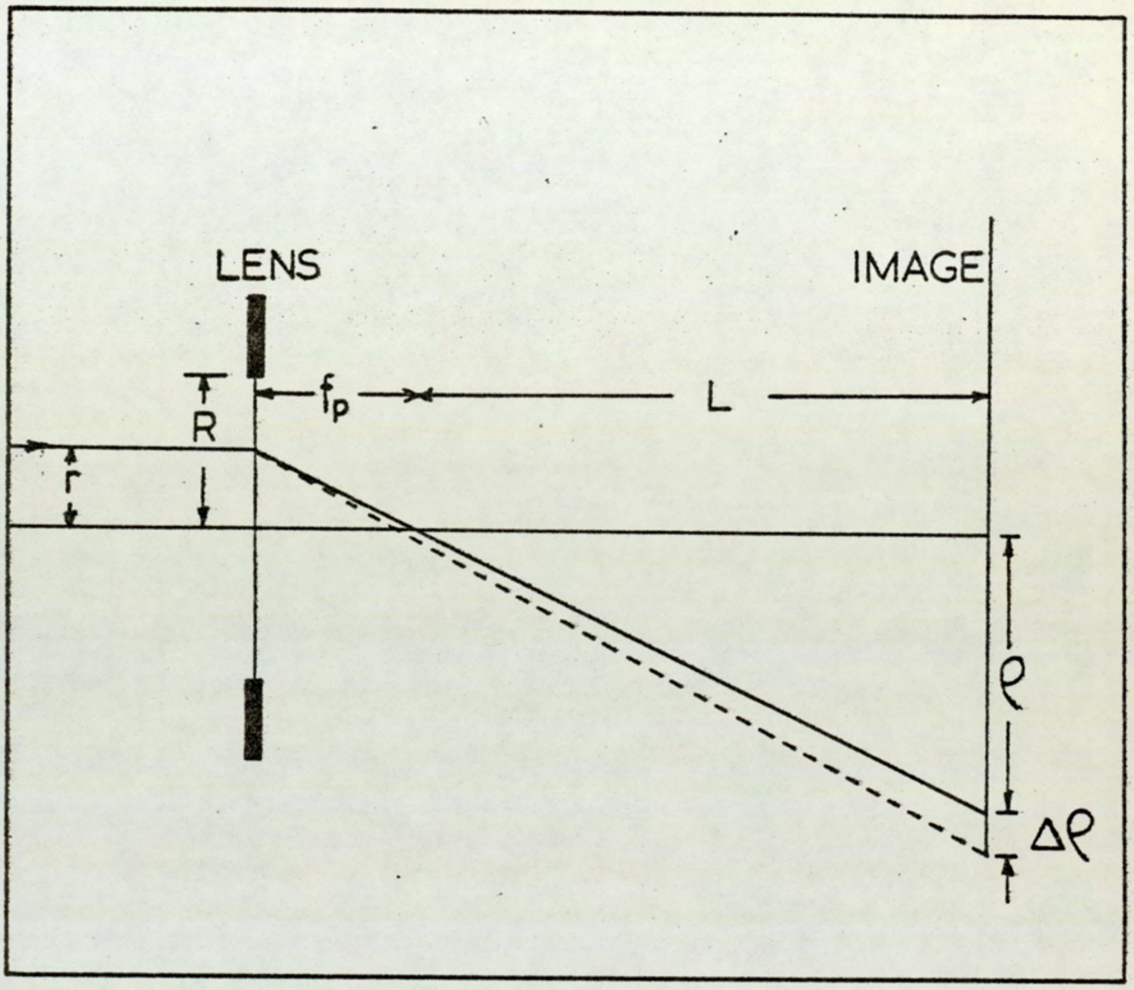

Figure 4.13 A diagram showing electron trajectory in the final projector stage

4.4.1 Important parameters in the design of the final stage of the electron microscope

Considering figure 4.13, the distortion ($\Delta\rho / \rho$) of the image is given by

$$\frac{\Delta\rho}{\rho} = D \cdot r^2 \qquad \text{...... 4.1}$$

where ρ is the radial height of the Gaussian ray in the image, D is the distortion coefficient (radial or spiral) and r is the height of the incident beam. If L is the projection distance and f_p the projector focal length, equation 4.1 may be written as:

$$\frac{\Delta\rho}{\rho} = D\left(\frac{\rho}{L}\right)^2 .f_p{}^2 \qquad \text{...... 4.2}$$

or

$$\frac{\Delta\rho}{\rho} = Q^2 \left(\frac{\rho}{L}\right)^2$$

where $Q = (D)^{\frac{1}{2}} f_p$ will be called the distortion parameter. It will be shown that this parameter is much more relevant than the distortion coefficient D in isolation. From equation 4.2, there will be a minimum value of L for a given image radius ρ and a given amount of distortion. This is given by:

$$L = Q \frac{\rho}{(\Delta\rho / \rho)^{\frac{1}{2}}} \qquad \text{...... 4.3}$$

Q is thus a crucial parameter in the design of the final stage of the microscope, a lower Q value corresponding to lower distortion, other things being equal. A comparison of different kinds of projector lenses based on the parameter Q will give a correct idea about the best lens for the final projector lens. The value of $Q_{sp} = \left(D_{sp}\right)^{\frac{1}{2}} f_p$ for double-polepiece lenses with gap width ratio S/D between 0.2 and infinity are shown in figure 4.14 as a function of lens excitation parameter NI/NI_o. In addition, the Q values for the exponential field distribution in its two modes of operation are given for comparison purposes. From the figure for double-polepiece lenses, it is clear that there is very little difference in the Q_{sp} values over this wide range of S/D of double-pole lenses, in spite of an order of magnitude difference in the distortion coefficients. Higher S/D values lead to slightly lower Q value but from a practical point of view, all double-polepiece lenses may be taken to have the same Q value and hence produce the same distortion for a given image size and projection distance. At minimum focal length ($NI/NI_o = 1$), where the radial distortion is nearly zero the Q_{sp} value of all double-pole lenses is in the region of 1. The exponential field, which is a good approximation to that of single-pole lenses, has an appreciably lower Q_{sp} value for the preferred direction of entry to the field. Not only is Q_{sp} low (about 0.78), but also it is nearly constant over a wide range of NI/NI_o (0.7 to 1.05). In the same range of excitation, the Q_{sp} value for the non-preferred direction of entry into the exponential field is nearly doubled at corresponding excitation values. This suggests the possibility of using single-pole lenses in a correcting system for spiral distortion. In order to fix ideas, consider a spiral distortion of 2% and a radial distortion of 1% with image radius $\rho = 50$ mm. Table 4.1 gives the L values for the different double-pole lenses (providing there is no restriction from the lens bore) together with the corresponding value of L for the preferred direction of the exponential field, L of the preferred direction of a practical design of single-polepiece lens (miniature HV single-pole lens, discussed in the next chapter), and the L value for the bell-shaped field distribution.

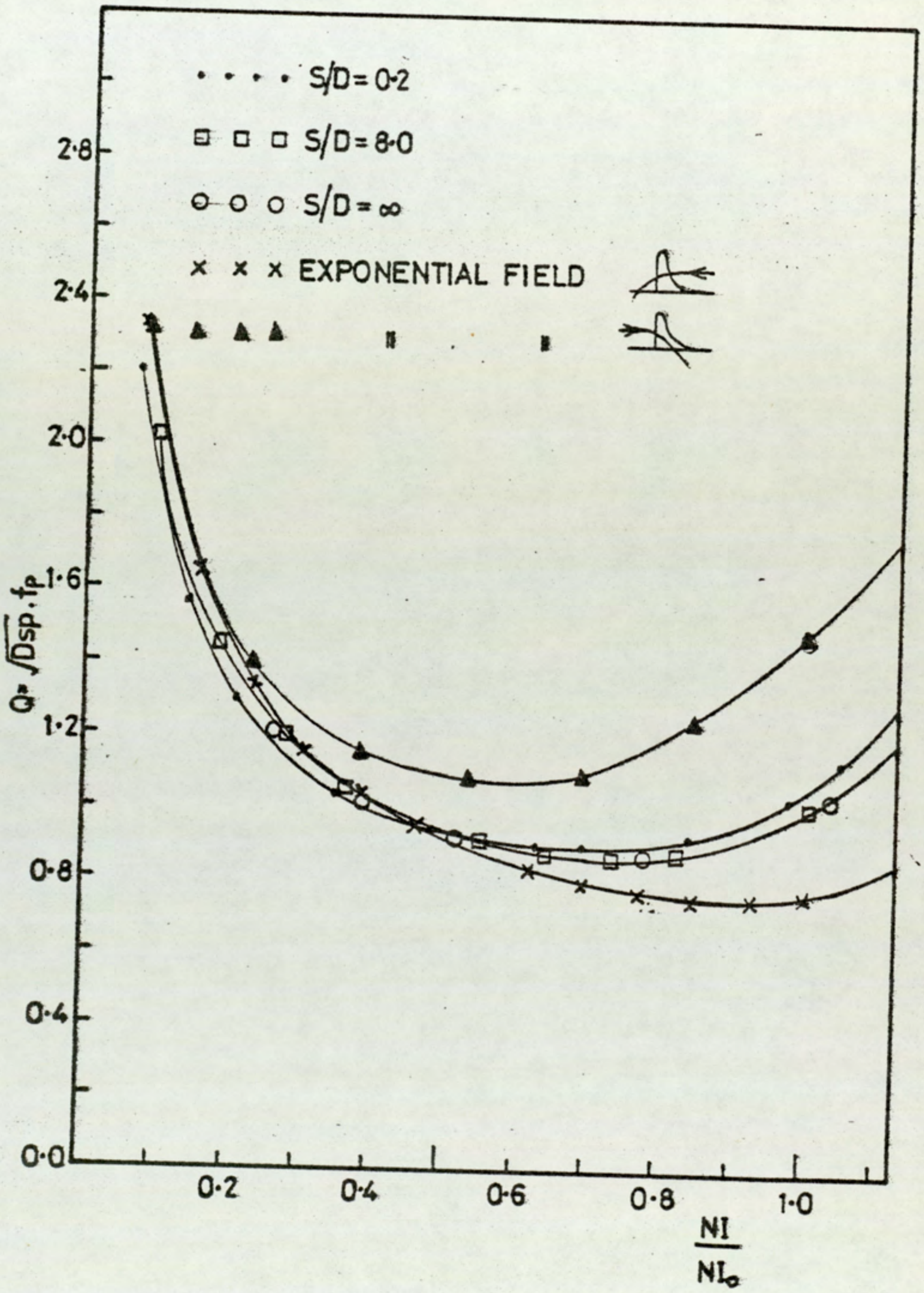

Figure 4.14 The projector distortion parameter Q_{sp} as a function of the relative excitation parameter NI/NI_o for double-pole lenses and the exponential field

Lens	L cm	NI/NI_o	F_p/f_{p_o}
Exponential field model (preferred direction)	27.25	0.972	1.0052
Miniature H.V. single-pole lens	28.96	0.94	1.0064
Double-pole lenses			
S/D = 2	33.22	0.862	1.044
S/D = 1	34.7	0.843	1.056
S/D = 0.2	35.68	0.997	1.042
Bell-shaped field	38.6	0.898	1.0067

Table (4.1). The minimum projection distance L for various double-pole lenses compared with that of the exponential field (preferred direction) and bell-shaped field when $\left(\frac{\Delta\rho}{\rho}\right)_{sp} = 2\left(\frac{\Delta\rho}{\rho}\right)_{rad} = 0.02$, $\rho = 5$cm.

Another useful parameter when optimising the design of the final projector stage is the value of Q^2. For a fixed value of ρ and L, the distortion is directly proportional to Q^2. For the same lenses shown in figure 4.14, figure 4.15 shows the variation of Q^2_{sp} as a function of the relative excitation parameter NI/NI_o. From the figure we see that the spiral distortion resulting from the preferred direction of the exponential field is about 40% less than that of the double-pole lenses in the useful region of excitation around the position of minimum focal length. This again indicates that single-pole lenses could advantageously be used as projectors.

A third parameter is important in designing the final projector stage of the microscope, that is the field of view of the projector

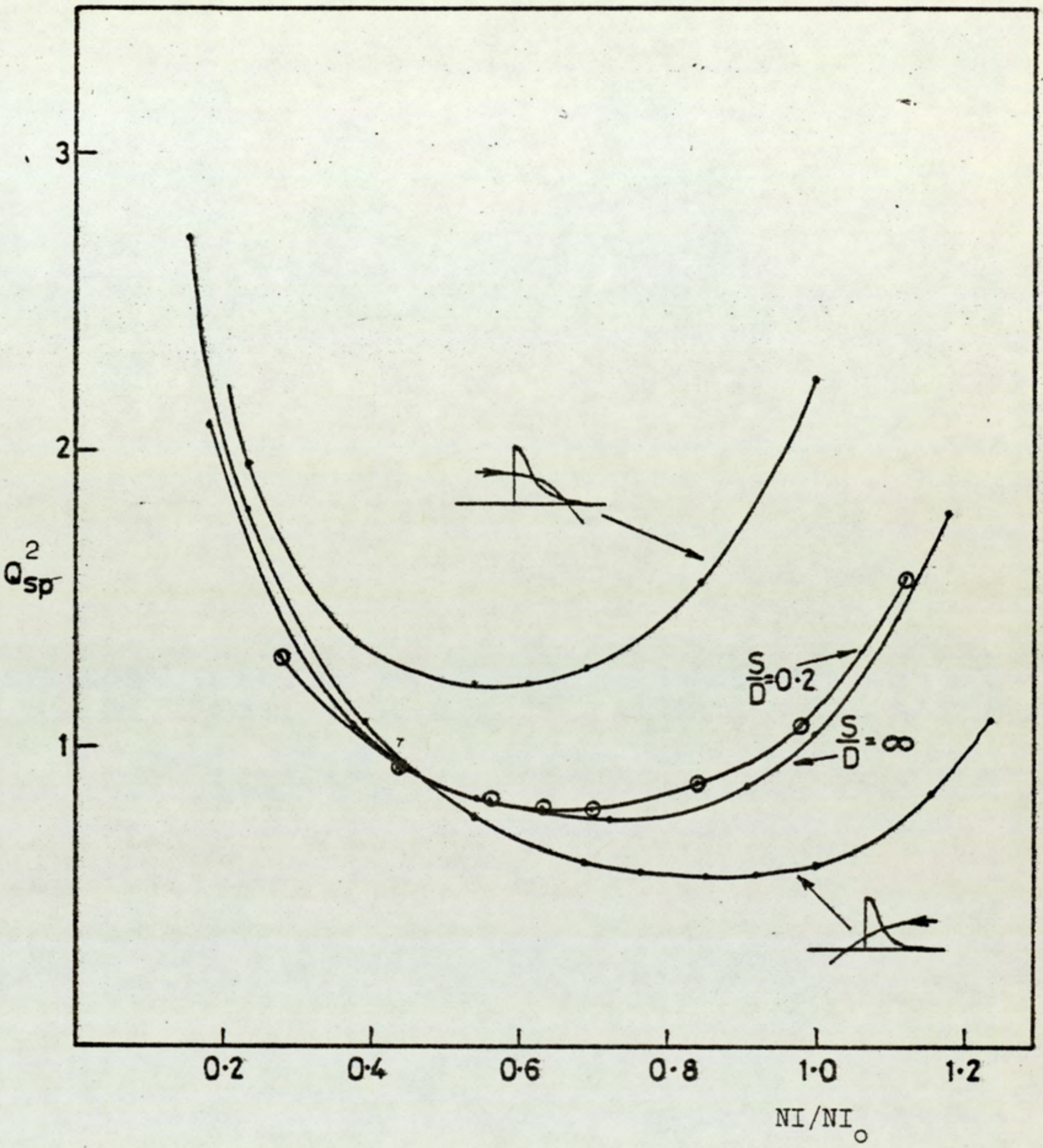

Figure 4.15 Q^2_{sp} as a function of NI/NI_o for double-pole lenses and the exponential field

lens. The larger the field of view, the more area of the object that can be seen and investigated. The field of view of double-pole lenses is limited by the lens bore. In a single-pole lens with the preferred direction of operation, the principal plane of the lens is located outside the body of the lens itself, while the focal point is located very close to the tip of the poleface of the snout, especially when the lens is operated near its maximum magnification. That means a large field of view can be obtained with the single-pole lenses; this can be increased by boring the back plate of the lens in a conical shape with an angle chosen to suit the required viewing arrangements. Such a design is described in Chapter 5.

4.4.2 Optimum design of the final projector lens

The optimum design of the final projector lens depends on the parameters mentioned in section 4.4.1. To sum up, a good projector lens should have the following characteristics:

1. Low Q value
2. Large field of view
3. Adequate magnification

The first two requirements are not influenced by lens size or working flux density. From the investigation of the important parameters in designing the final projector stage of the electron microscope, one can readily conclude that a single-pole piece lens, with its axial field distribution as close as possible to the exponential field distribution, and used in the preferred direction, is probably the best arrangement for the final projector lens of the electron microscope. The employment of miniature lenses enables us to use more intermediate lenses, in order to obtain a given total magnification for the microscope. It is not therefore necessary to concentrate the magnification into a few steps involving the use of lenses of very short focal length. In fact, the employment of an intermediate single-pole lens in such an arrangement as suggested in Chapter 6 of this thesis should minimise both the rotational distortion and the length of the viewing chamber without any sacrifice of total magnification.

5. APPLICATION TO PRACTICAL LENS DESIGN

Single-pole magnetic lenses have different axial field distributions from those of double-polepiece lenses. For this reason, their electron-optical properties are different and cannot be predicted from the data of conventional lenses (Marai and Mulvey, 1974). The axial field distribution of single-polepiece lenses is approximately exponential in nature, being closely related to those partially iron-shrouded helical coils described by Mulvey and Wallington (1973). To see how far the electron-optical properties of the exponential field distribution could be useful in predicting single-polepiece lens properties, two practical single-pole lenses were investigated in detail and their electron-optical properties were calculated or measured making use of calculated or measured axial field distributions.

5.1 A simple single-pole 100 KV objective lens

A twice full size model of the 100 KV objective lens described by Marai and Mulvey (1974) was constructed (Figure 5.1), in which a flat helical winding of mean diameter 75 mm is placed inside a short hollow iron cylinder closed off at one end by an iron plate provided with an axial hole of 10 mm diameter and a 2 mm snout of 40mm diameter. The axial field distribution was measured by means of Hall-effect probe. The axial field distribution was also calculated from the Biot-Savart law. Figure 5.1 shows a schematic diagram of the lens. Using the computer program described in Chapter 3, the focal properties, chromatic and spherical aberration coefficients and the radial and spiral distortion coefficients of the lens were calculated. The results, which are similar to those of the exponential field model, are given below.

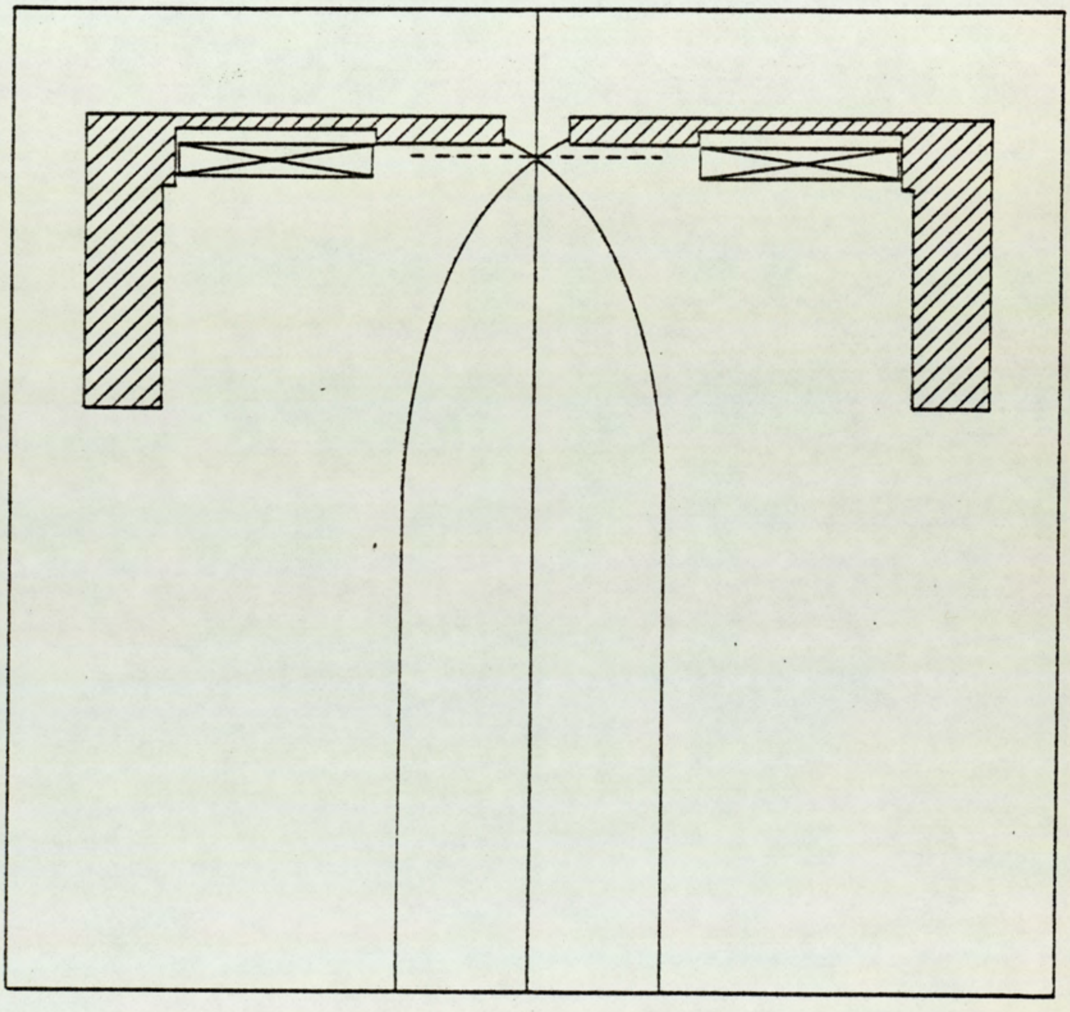

Figure 5.1 Schematic diagram of the 100 KV objective lens

5.1.1. Axial field distribution and focal properties

Figure 5.2 shows four curves for the axial field distribution. Curve 1 represents the axial field distribution calculated using the Biot-Savart law. The magnetic effect of the iron back-plate of the lens may be calculated by 'the method of images'. A back plate of infinite radius would act as a 'mirror' producing an equi-distant 'image' of the lens coil; the combination of the field from the original coil and its image will then produce the same field distribution as the coil and the back-plate. The finite radius of the back-plate was ignored in this calculation as it was considered that the error involved would be small. The field distribution represented by curve 1 in figure 5.2, then, is the resultant of the field produced by the two coils described above. Curve 2 in figure 5.2 represents the axial flux density of the lens measured by the Hall-effect probe. The peak of this curve is pushed forward into the lens compared with that calculated. This is caused by the effect of the iron 'snout' or single-polepiece of the lens (40 mm in diameter and 2 mm depth into the lens).

To study the effect of the hole on the axial flux density distribution, a cylindrical piece of iron of outside diameter 10 mm was placed in the hole of the lens with its front face at the same plane of the snout face. The resultant measured flux density in this case was identical with that of curve 2 of figure 4.2 apart from the snout and up to a point at about 10 mm from the snout, and then the flux density went higher as the distance from the snout was reduced; the maximum value of the flux density was about twice the value of the flux density when measured in the case of a hole of 10 mm diameter in the lens at the plane of the snout face. This case of the flux density distribution is represented by curve 3 in figure

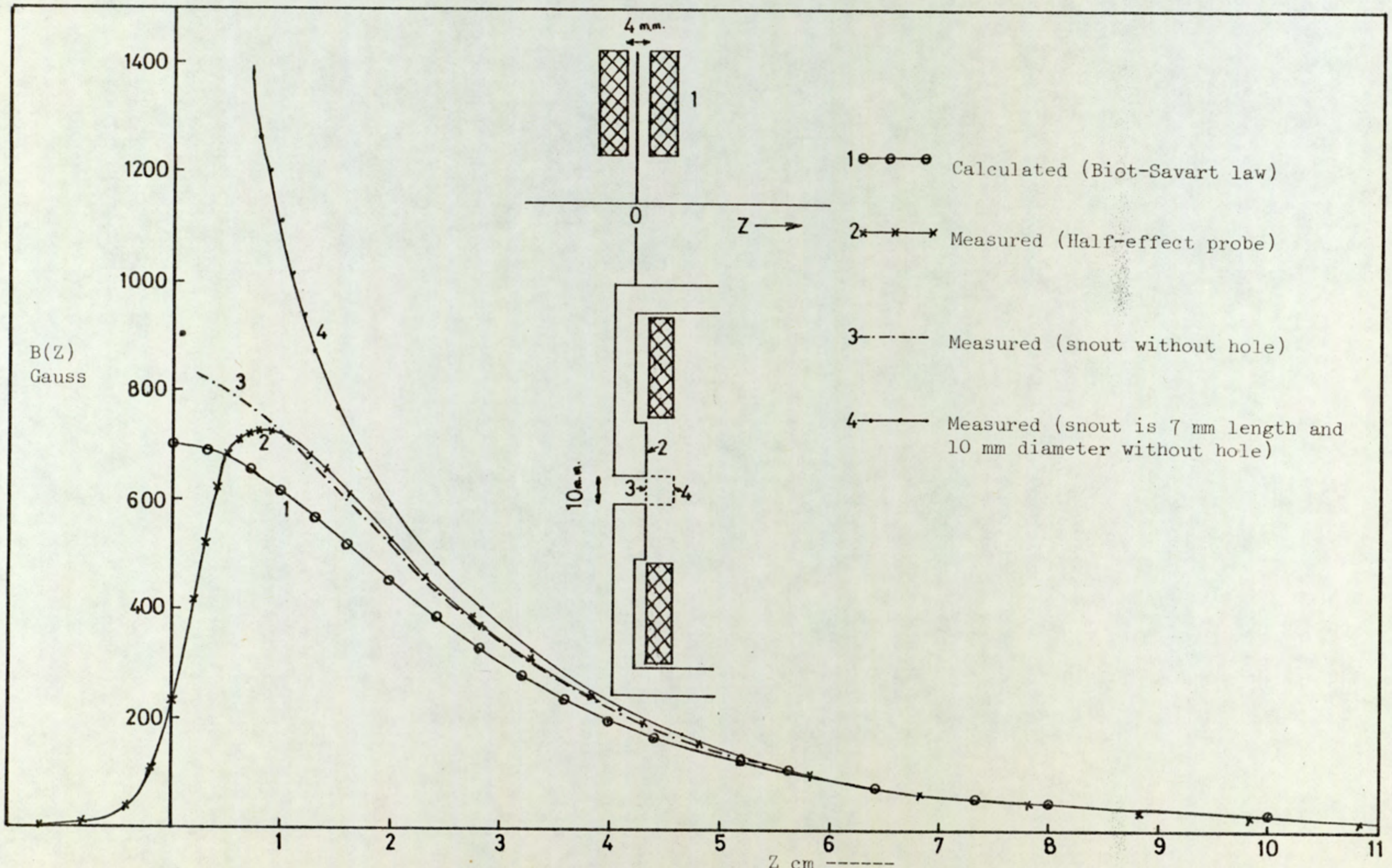

Figure 5.2 The axial flux density distribution of the 100 KV single pole objective lens

5.2. Furthermore, to see the effect of extending the snout length on the axial flux density distribution of the lens, the piece of iron used in case 3 was pushed forward into the lens so its front face was located at 5 mm from the old snout position. In this case, we formed a new snout or a single-polepiece of 10 mm diameter and 7 mm penetration into the lens and without a bore. The resultant axial flux density distribution of this case is represented by curve 4 of figure 5.2. The maximum field position is moved forward in the lens by a 5 mm distance from that of case 3, and the maximum field is about twice the peak value of curve 2 when the snout was only 2 mm in extent with a 10 mm hole.

Figure 5.3 shows the measured axial flux density of the lens in comparison with the exponential field distribution as a function of Z, the distance from the snout. Figure 5.4 shows the same thing but on log-linear scale. Both figures show that the agreement between the measured axial field distribution and the exponential field is identical in the area between the peak of the measured field and Z = infinity. The maximum value of the exponential field is a bit more than twice the value of the measured axial field distribution at the plane of the snout face. At the peak position of the axial flux density, the flux density was measured for a lens current up to 20 amps. The I-B relation curve is shown in figure 5.5. The relation is perfectly linear up to this value of exciting current of the lens which covers the range of operating the lens.

The focal properties of the lens were calculated for both the calculated axial field distribution from the two-coil model, and the measured axial flux density distribution using the Hall-effect probe method. The results were approximately the same. Figure 5.6 represents the focal quantities F_p, F_{obj} and Z_{obj} as a function of the excitation parameter $NI/V_r^{\frac{1}{2}}$. The circles represent results

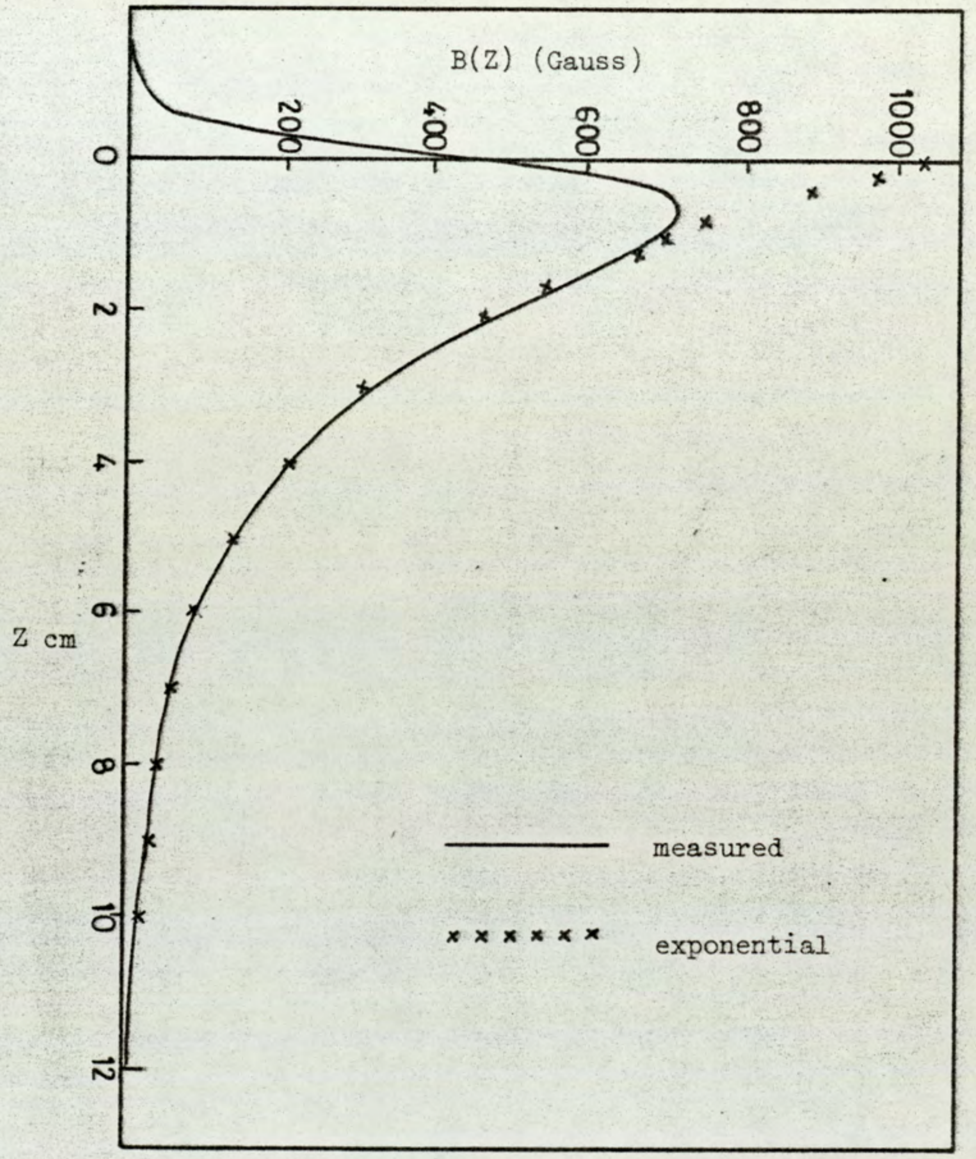

Figure 5.3 The axial flux density distribution of the 100 KV single pole lens compared with the exponential field

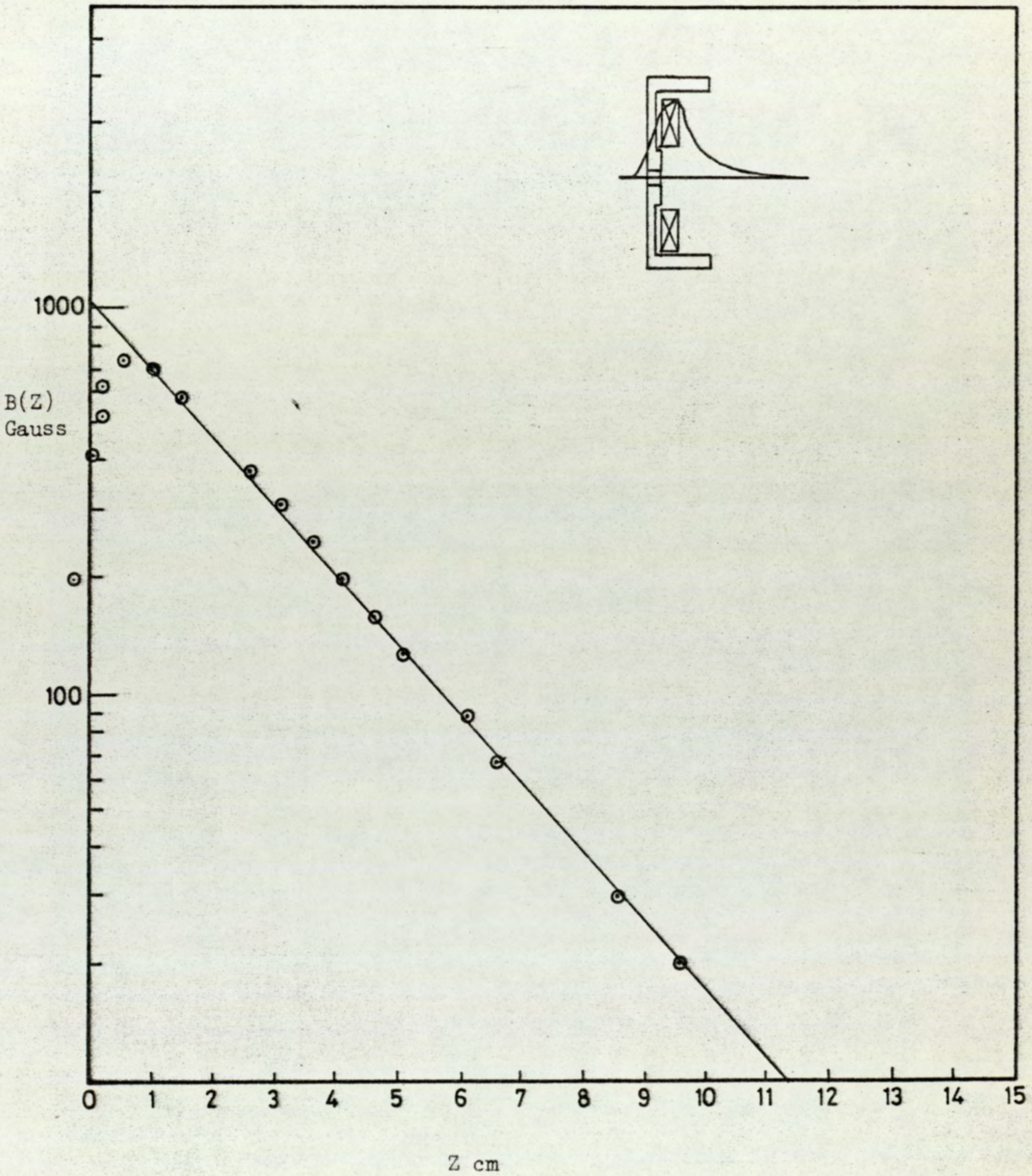

Figure 5.4 The axial flux density of the 100 KV single pole lens

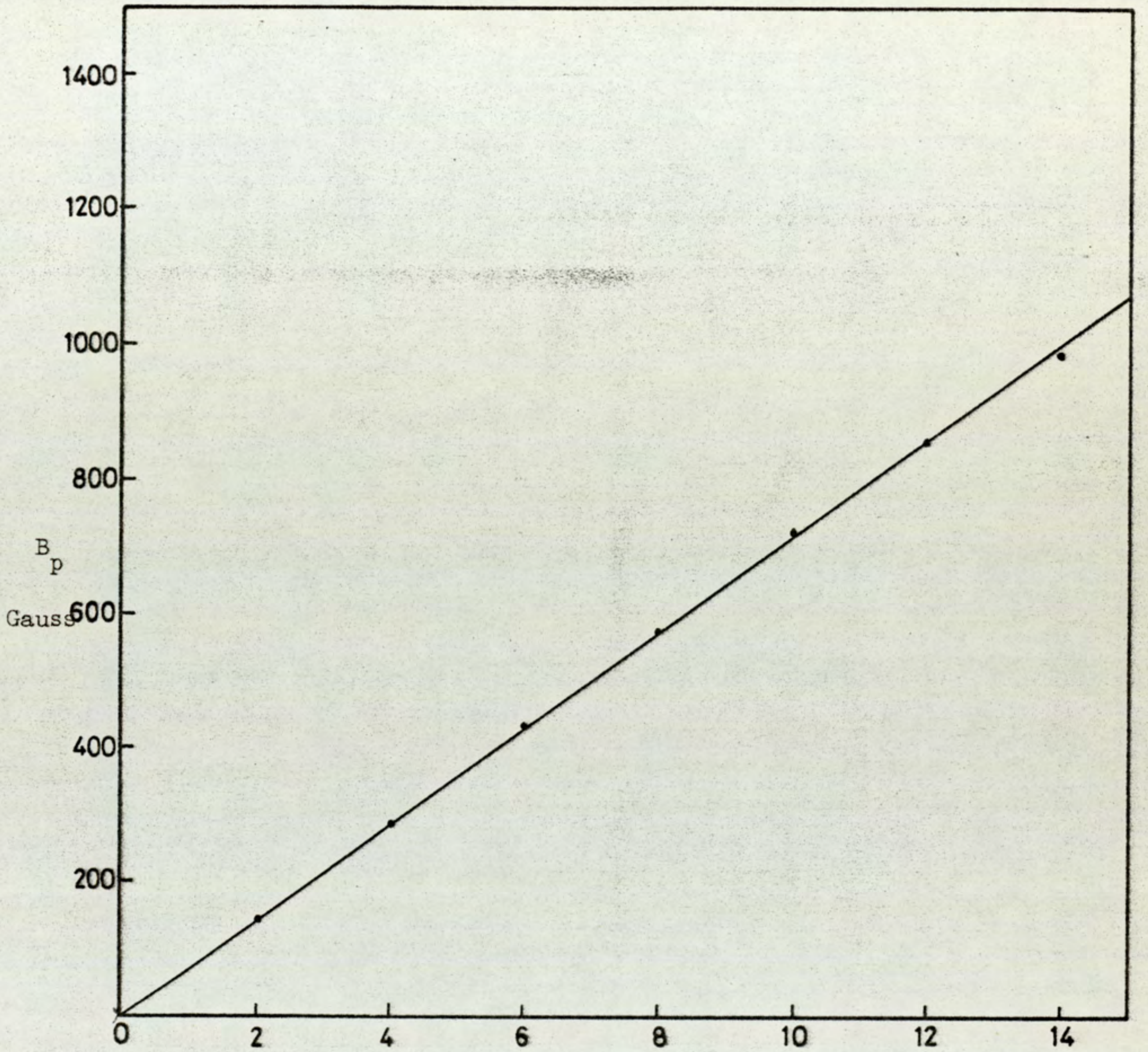

Figure 5.5 The I - B_p curve for the 100 KV single-pole lens

from the calculated field distribution while the crosses represent results calculated from the measured field. From the figure we find that $F_{p\ min}$ is equal to 20 mm and occurs at an excitation parameter $NI/V_r^{\frac{1}{2}} = 13$, exactly as the case of the exponential field distribution. F_{obj} and F_p are the same up to the minimum projector focal length position and then F_{obj} remains constant for excitations $NI/V_r^{\frac{1}{2}}$ higher than 13, again the same property as in the case of the exponential field distribution. Furthermore, the object distance Z_{obj} varies in a similar way as that of the exponential field distribution and crosses the snout plane at an excitation $NI/V_r^{\frac{1}{2}} = 13$ corresponding to the minimum focal length of the lens. A direct comparison between the focal properties of the lens and the focal properties of the exponential field distribution in the first zone of operation is shown in figure 5.7, in which all the quantities F_p, F_{obj} and Z_{obj} are given in terms of the half-width of the field distribution.

5.1.2 Chromatic and spherical aberrations

The chromatic and spherical aberration coefficients of the lens were calculated, using the computer program 'D ABBERATION' described in Chapter 3, for both the calculated and the measured axial field distributions. The results are in very good agreement with those of the exponential field distribution. At the excitation for minimum focal length, the ratios $C_s/F_{obj} = 0.325$ and $C_c/F_{obj} = 0.625$ compared with the $C_s/F_{obj} = 0.315$ and $C_c/F_{obj} = 0.632$ for the exponential field distribution. Both C_s and C_c are constant for excitation parameters $NI/V_r^{\frac{1}{2}}$ greater than 13. The results of the aberration coefficients C_c and C_s, together with the projector focal length f_p, objective focal length f_{obj} and the object distance Z_{obj} are given in figures 5.8 and 5.9 as a function of the excitation parameter $NI/V_r^{\frac{1}{2}}$, for both the calculated and measured field distribution of

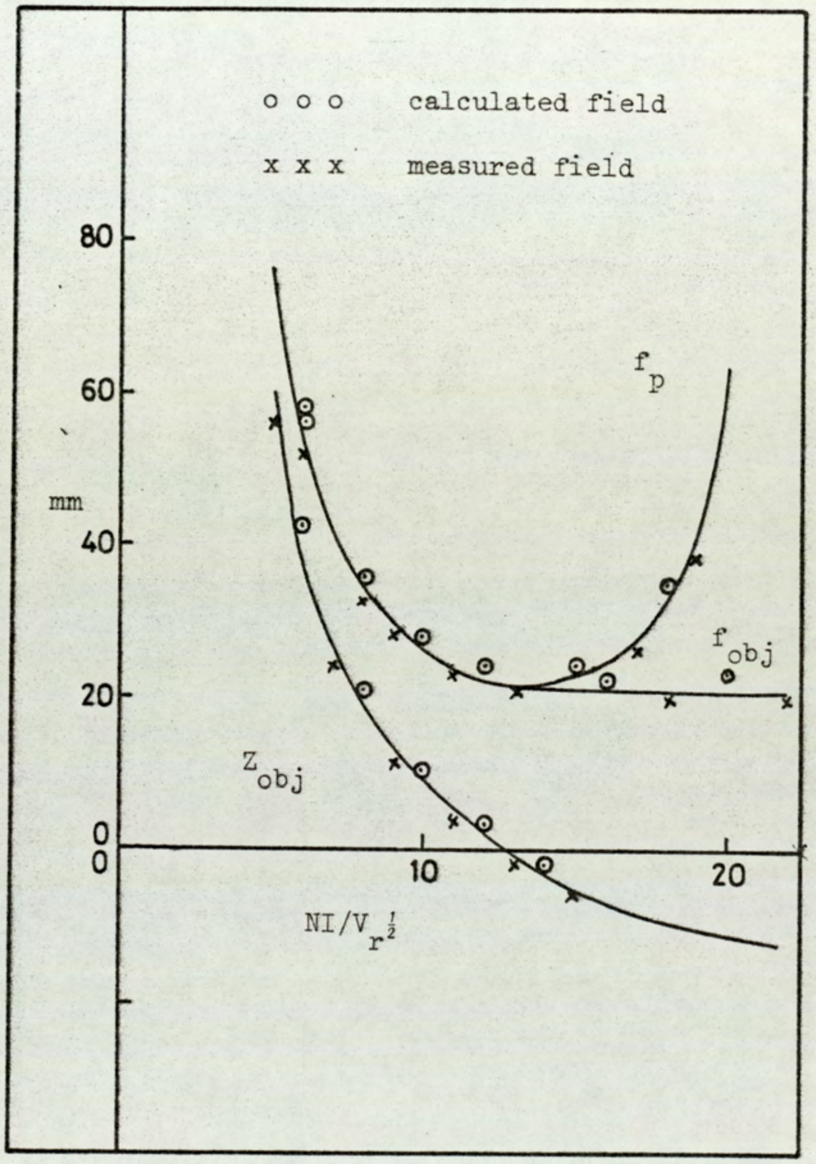

Figure 5.6 Focal properties of the 100 KV single pole objective lens

Figure (5.7). The relative focal properties $f_{p/d}$, $f_{obj/d}$, $Z_{obj/d}$ for both the single-pole lens and the exponential field.

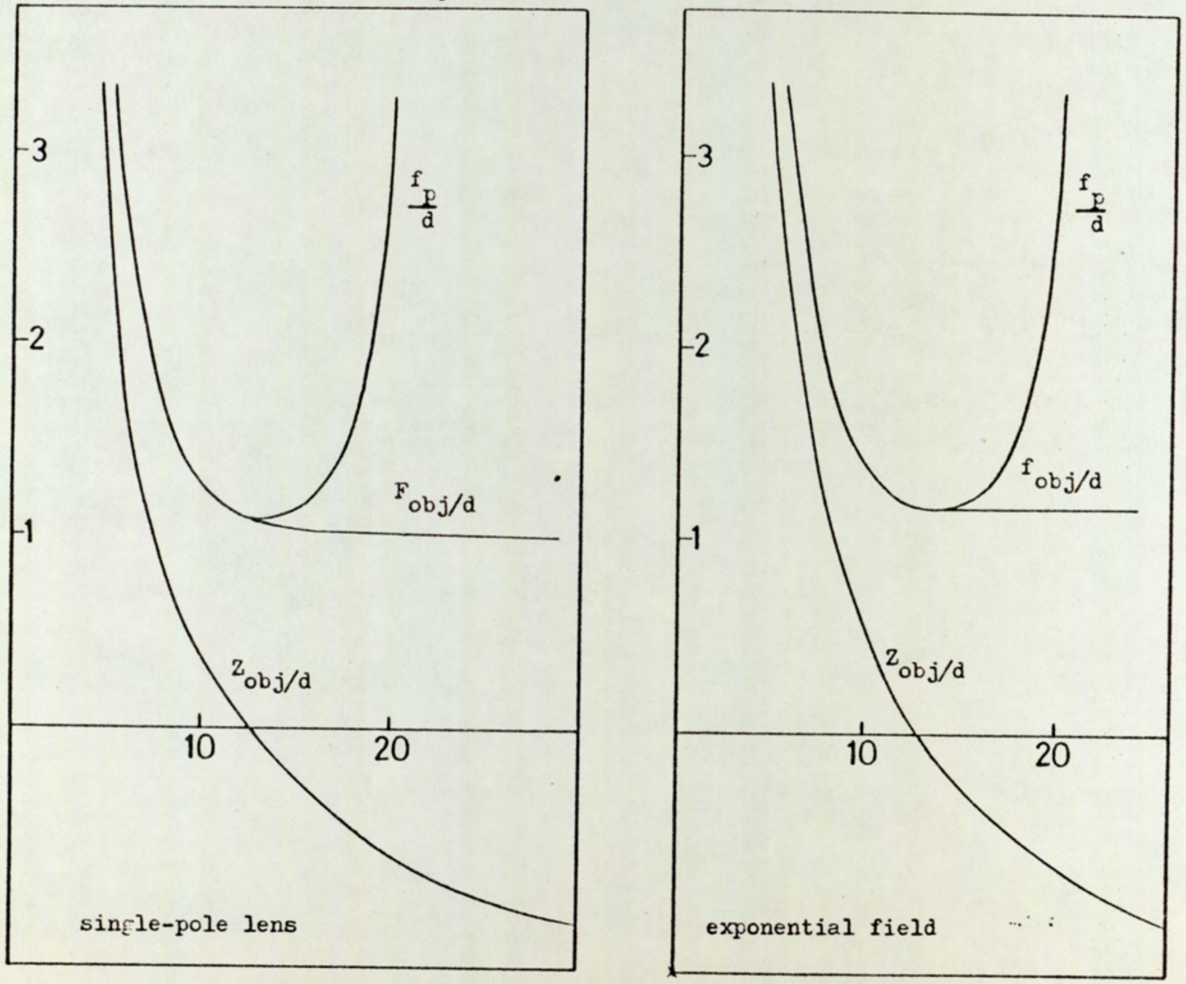

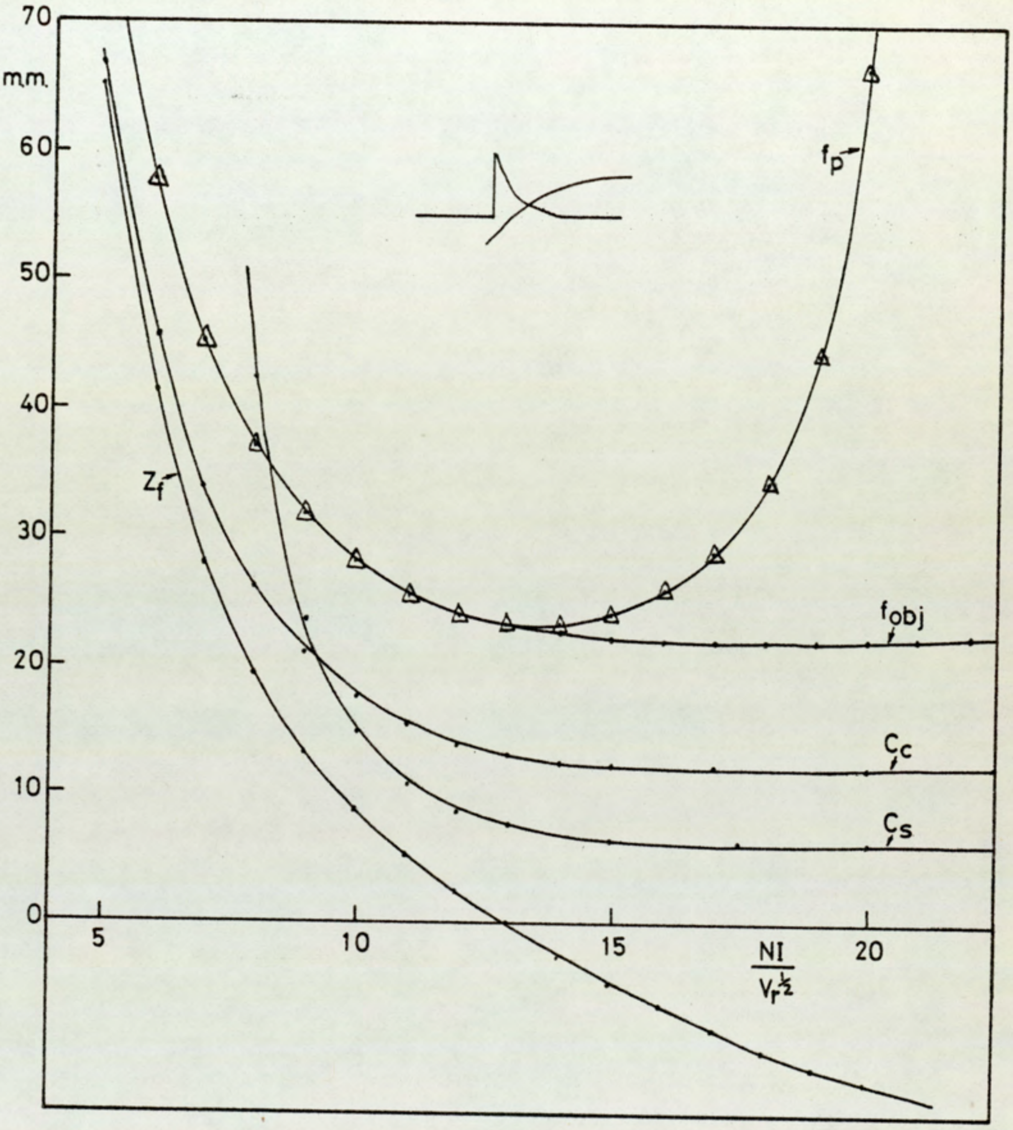

Figure 5.8 Chromatic and spherical aberration coefficients of the 100 KV objective lens calculated from the calculated field distribution (two coil model)

the lens.

The results for the spherical aberration coefficient is very important since it depends on the derivative $\frac{dB}{dZ}$ of the axial magnetic field distribution. The agreement between the results for the spherical aberration coefficients of the single-pole lens described above and that of the exponential field distribution strongly supports the idea explained in Chapter 3, that ignoring the infinite slope of the steeply rising part of the field distribution of the exponential field model leads to results in very good agreement to that obtained for field distributions of practical single-pole lenses.

5.1.3 Radial and spiral distortion coefficients of the objective single-pole lens

The radial and spiral distortion coefficients of the single-pole lens described above were calculated using the computer program 'D DISTORTION' for the two directions of beam entry to the lens field. Figure 5.10 shows the variation of the calculated coefficients $C_d = R^2D_r$ and $C_{sp} = R^2D_{sp}$ as a function of the excitation parameter $NI/V_r^{\frac{1}{2}}$, where R is the radius of the lens bore. The figure shows the considerable difference between the values of the radial and spiral distortion coefficients in the two ways of operation. The preferred direction of operating the lens, in order to get smaller distortion, is that for which the incoming electron beam enters the field of the lens from the gently sloping part to the field distribution, i.e. on the 'open' side of the lens. The radial distortion coefficient is zero for $NI/V_r^{\frac{1}{2}} = 15$. For the opposite direction $\frac{NI}{V_r^{\frac{1}{2}}} = 14$, which is again in very good agreement with the case of the exponential field distribution, (figure 2.17). The curves of figure 5.10 for the spiral distortion coefficients show, as in the exponential field distribution, a reduction of the coefficient by a factor 3 near the

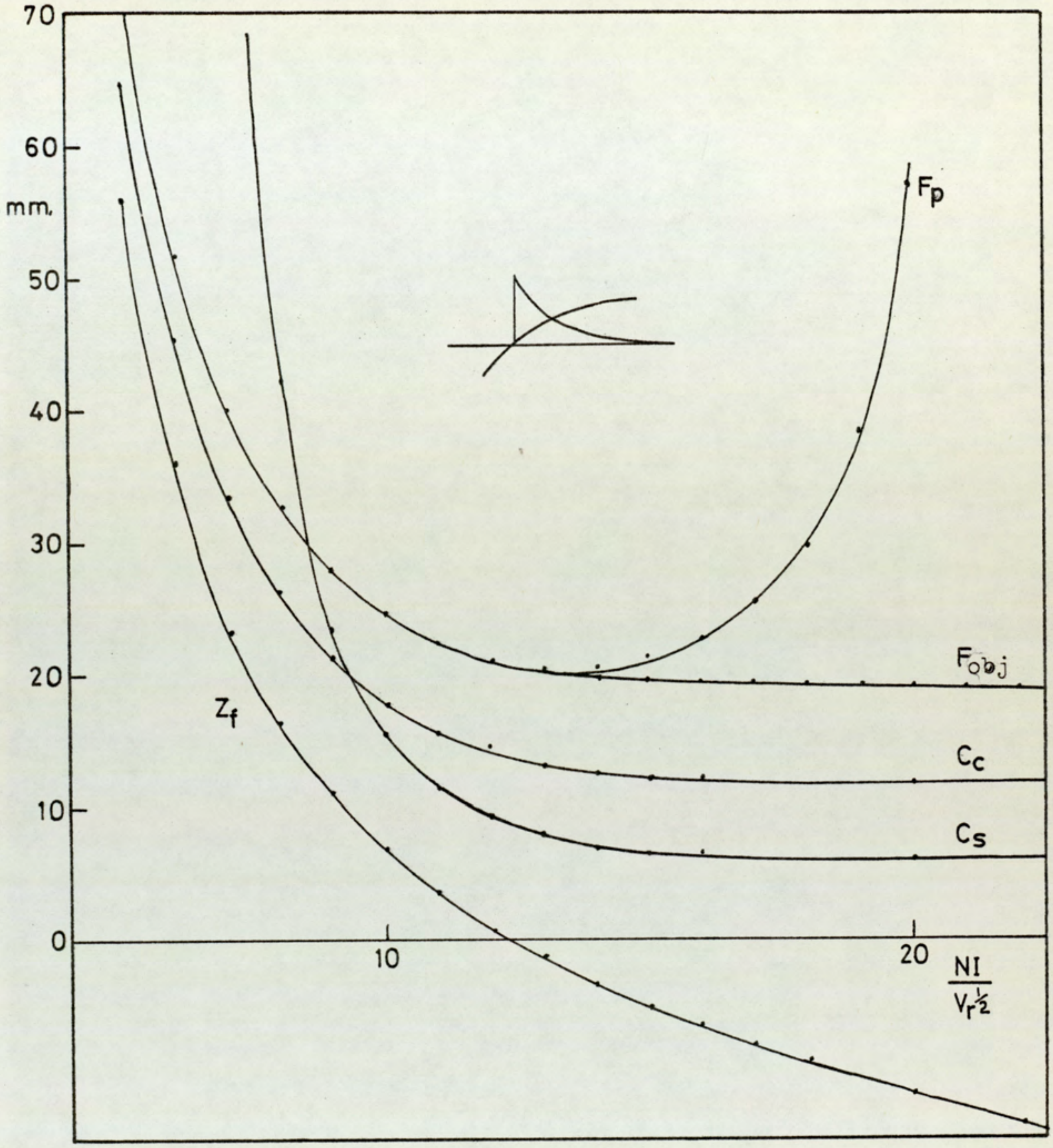

Figure 5.9 Chromatic and spherical aberration coefficients of the 100 KV objective lens calculated from the measured field distribution

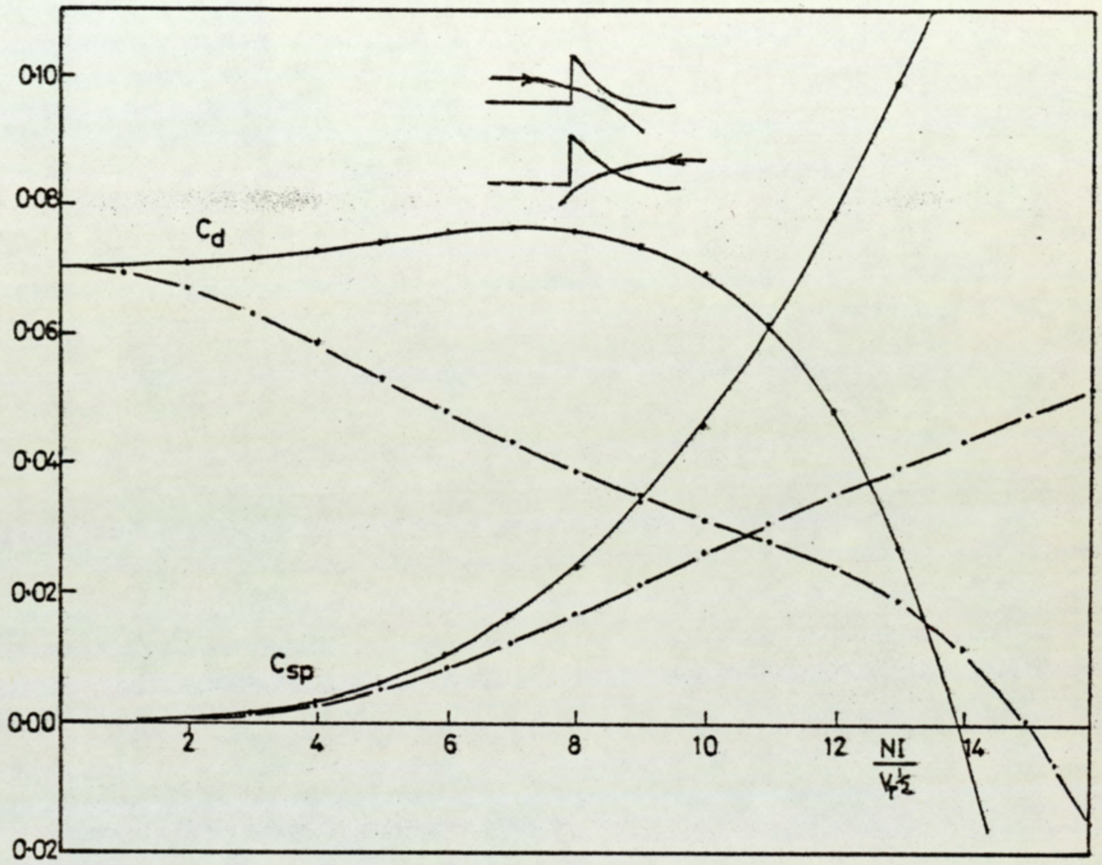

Figure 5.10 Radial C_d and spiral C_{sp} distortion coefficients of the 100 KV single-pole objective lens

excitation for minimum focal length when operating the lens in the preferred direction compared with that of the opposite direction.

The distortion quality factor $Q = D^{\frac{1}{2}} f_p$ was also calculated for the lens in the two modes of operation as a function of the relative excitation parameter NI/NI_o. The results are shown in figure 5.11.

The results of the radial and spiral distortion coefficients and the distortion quality factors Q_{rad} and Q_{sp} confirm again that the approximation made with the exponential field distribution, in order to avoid the mathematical difficulty of an infinite slope of the field $B'(Z)$ at $Z = 0$, was reasonable in the light of its application to practical cases.

5.2 A miniature single-polepiece projector lens for the high voltage electron microscope

Another practical single-polepiece lens successfully tested in the high voltage electron microscope is the miniature single-polepiece lens described by Mulvey and Newman (1973). Figure 5.12 shows the cross section of Hitachi HU 1000 KV volt electron microscope installed at the C.E.G.B. Research Laboratories at Berkeley, Gloucestershire, where the miniature single-pole lens was inserted in a Faraday cage port above the normal final projector lens of the microscope. The lens power available at the time was not enough to operate the lens down to its minimum focal length, but sufficient to produce good micrographs comparable in quality with those of the normal projector. Figure 5.13 shows a micrograph of a diffraction grating replica taken at one million volts in the HU 1000 using the miniature lens as the final projector lens. The lens excitation was about 12500 A-t, producing a focal length about 16 mm. The micrograph shows a radial distortion of about 6%. We now know that the reason for this is that the lens

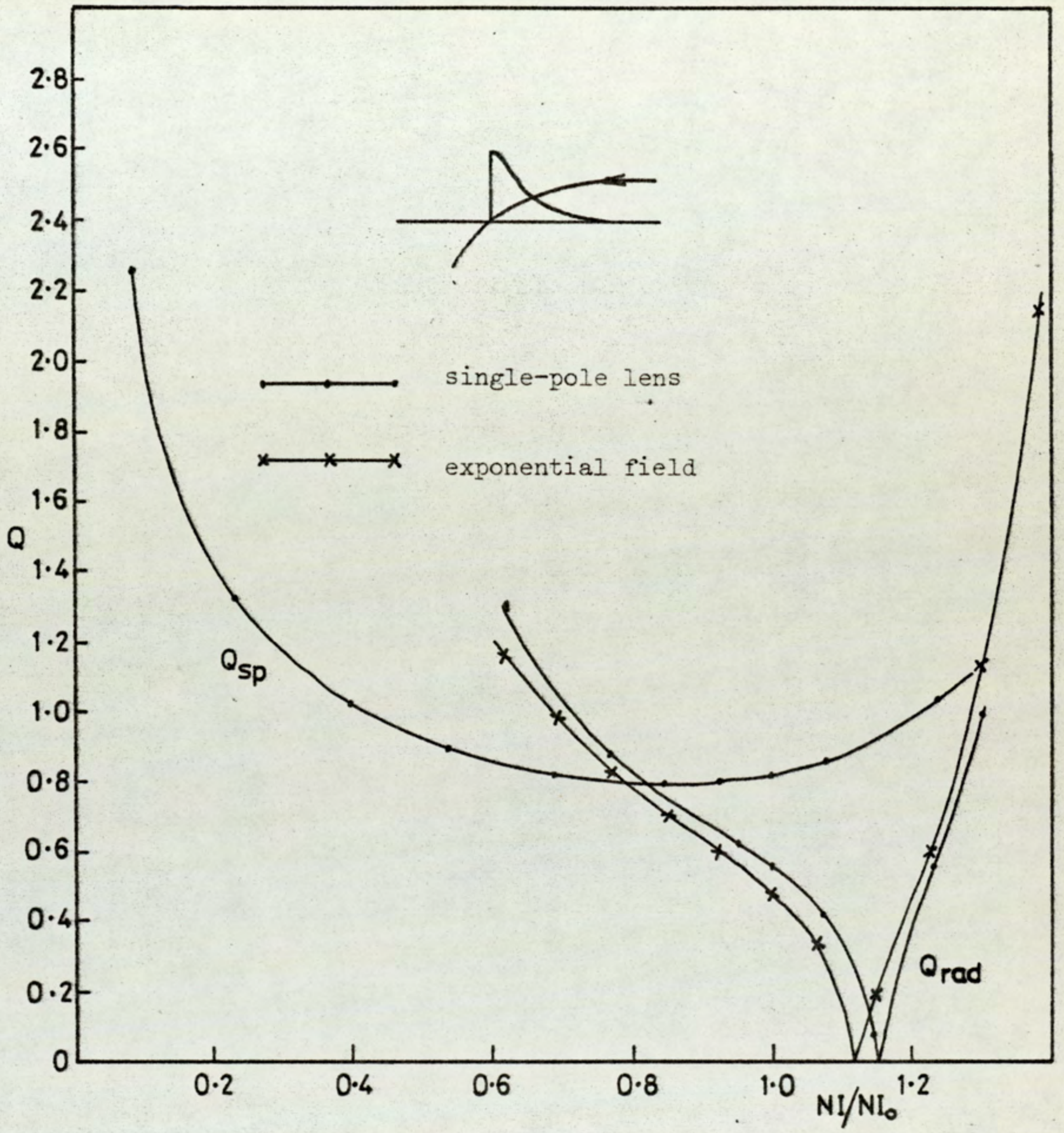

Figure 5.11 Q_{sp} and Q_{rad} of the 100 KV single-pole lens in comparison with the exponential field

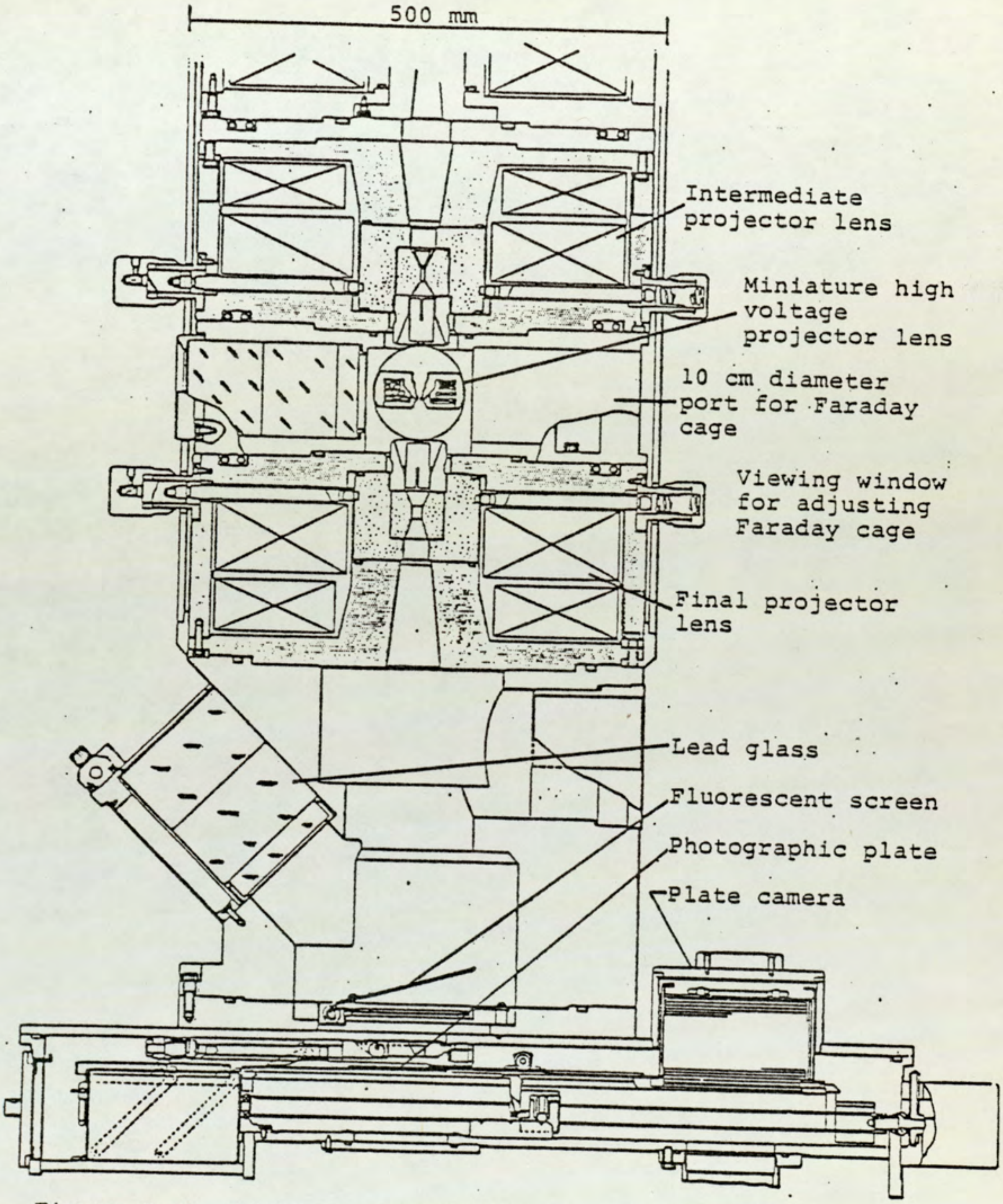

Figure 5.12 Cross-section of Hitachi HU 1000 million volt electron microscope showing intermediate and final projector lens. Miniature projector lens inserted in Faraday cage port above the final projector lens.

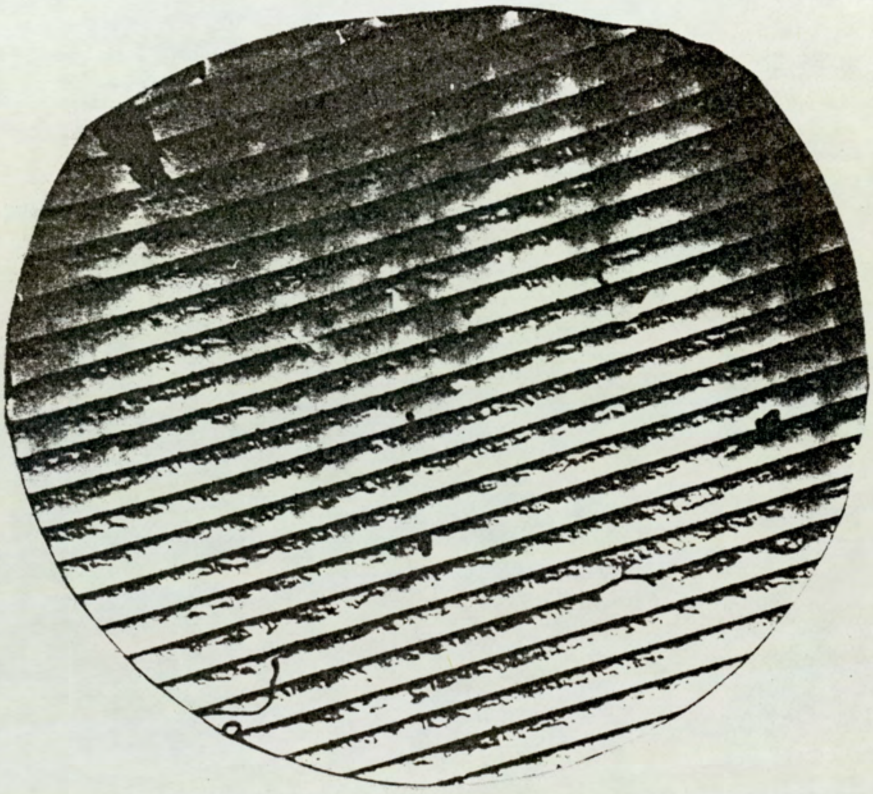

Figure 5.13 A micrograph of a diffraction grating replica taken in the HU 1000 electron microscope with the single-pole lens operating as final projector

was used with its snout facing the screen, i.e. opposite to the preferred direction of using single-pole lenses mentioned above. The calculation of the focal properties and aberrations of the lens was in fact carried out by the author after this experiment, in order to determine the optimum arrangement of using the miniature high voltage lens.

Figure 5.14 represents a full-scale cross-section of the miniature high voltage single-pole lens. The exciting coils, consisting of wire windings, comprised four coils with 126, 126, 158 and 187 turns respectively, a total of 597 turns. Figure 5.15 shows a front view of the same lens with the water and electric connections.

5.2.1 Calculated focal properties of the miniature high voltage single-pole lens

The electron-optical properties of the high voltage single-pole lens were calculated, making use of both the calculated and the measured axial magnetic flux density distributions of the lens. These calculations included the use of the lens both as an objective and as a projector in a high voltage electron microscope.

a) The calculated field properties

The axial magnetic flux density distribution of this lens was kindly calculated by the Rutherford laboratory making use of the computer program of W. Trowbridge et al (1972). This method divides the iron circuit of the lens and the exciting coil into small elements, the number and shape of which are chosen according to the accuracy required. The magnetic field from the coil is calculated by the Biot-Savart Law. The magnetic flux in each element is calculated by an integral method taking into account the magnetic field of the coil and the magnetising effect of the other iron elements. The total field at any point is the sum of the field produced by the coil and that produced by the

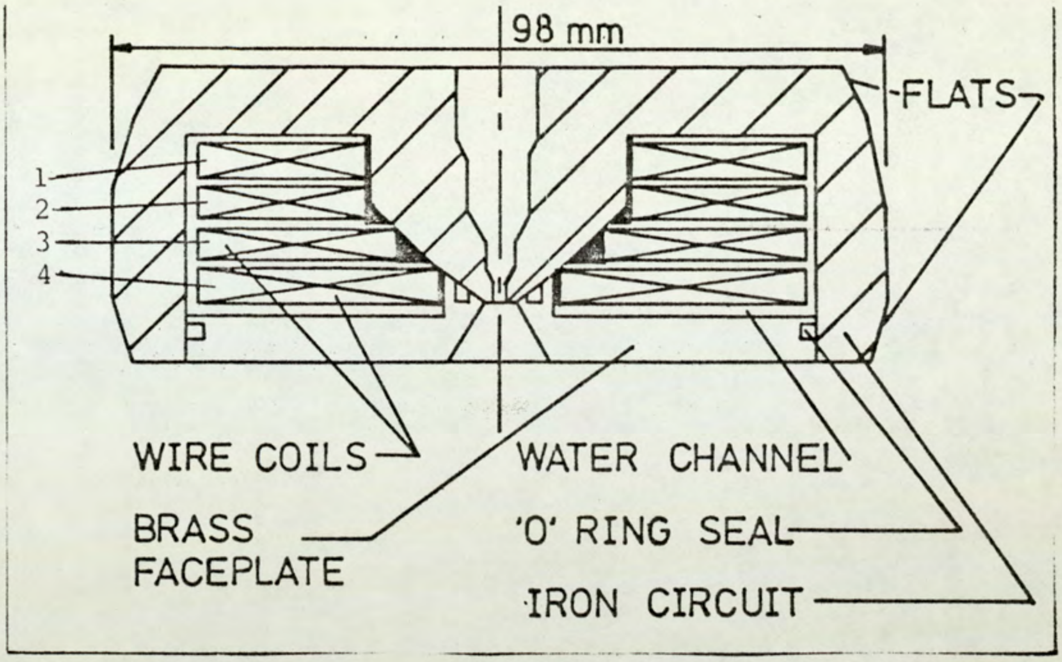

Figure 5.14 Cross-section of the high voltage single-pole lens scale 1 : 1

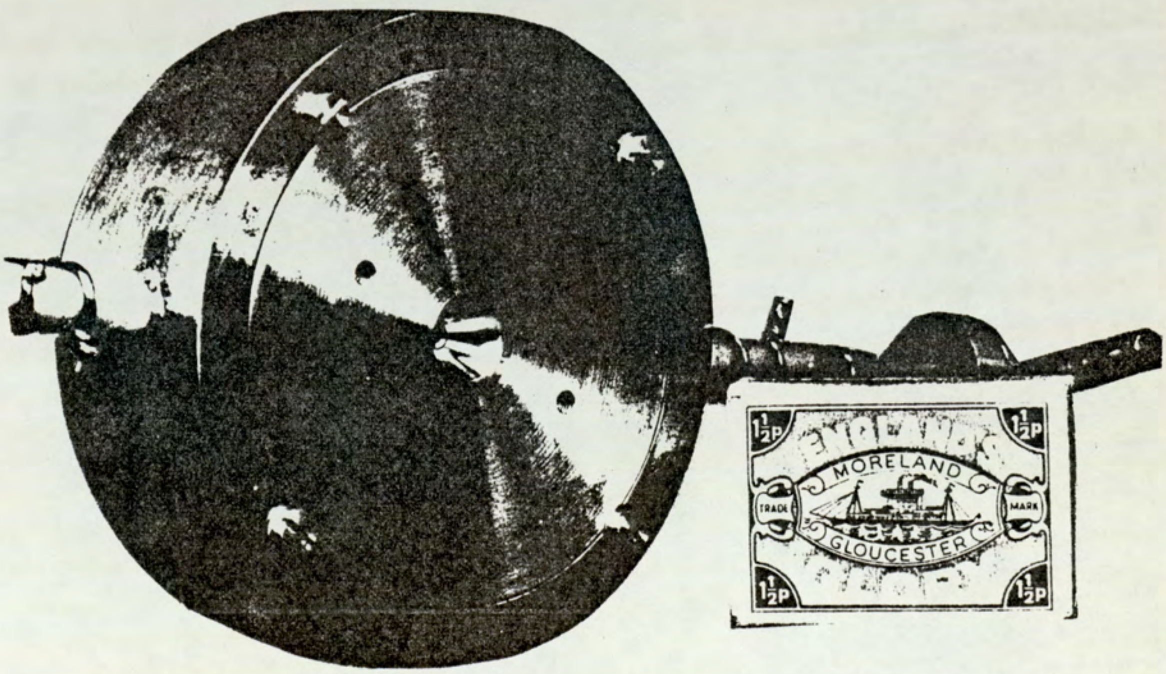

Figure 5.15 Front view of the high voltage single-pole lens showing the water and electrical connections

iron circuit. In particular the axial flux density distribution can be plotted directly by the graph-plotter output facilities of the computer. Figure 5.16 shows the computed axial flux density at a lens excitation of 12086 A-t. The circles on the graph represent points measured by means of a Hall effect probe Gaussmeter. The peak value of the measured flux density is about 20% greater than that calculated. This is partly due to the approximation made in calculating the field distribution. For simplicity the snout surface was represented not by a smooth cone but by a stepped structure. Furthermore actual internal steps in the bore itself were omitted from the computer calculation for simplicity. It should also be mentioned that the measured field distributions shown here were made after a minor re-machining of the lens bore and face, which tended to produce a slight increase in flux density at the poleface. Taking everything into consideration, the 20% discrepancy between calculated and measured field distribution can readily be accounted for, and did not warrant a subsequent re-calculation.

The computer program 'DATA - BZ' and 'D ABERRATION', described in Chapter 3, were used to calculate the focal properties and the chromatic and spherical aberration coefficients from the calculated axial flux density distribution of the high voltage single-pole lens. Figure 5.17 shows the variation of projector and objective focal lengths, the object points Z_{obj}, and the position of the principal plane, all as a function of the excitation parameter $NI/V_r^{\frac{1}{2}}$ for an electron beam entering the lens field from the iron-plate side of the lens. The figure shows a minimum projector focal length of = 10.7 mm at an excitation parameter $NI/V_r^{\frac{1}{2}} = 15.5$.

The objective focal length is approximately equal to the projector focal length up to an excitation parameter $NI/V_r^{\frac{1}{2}} = 10$ but then decreases more rapidly as the excitation parameter increases.

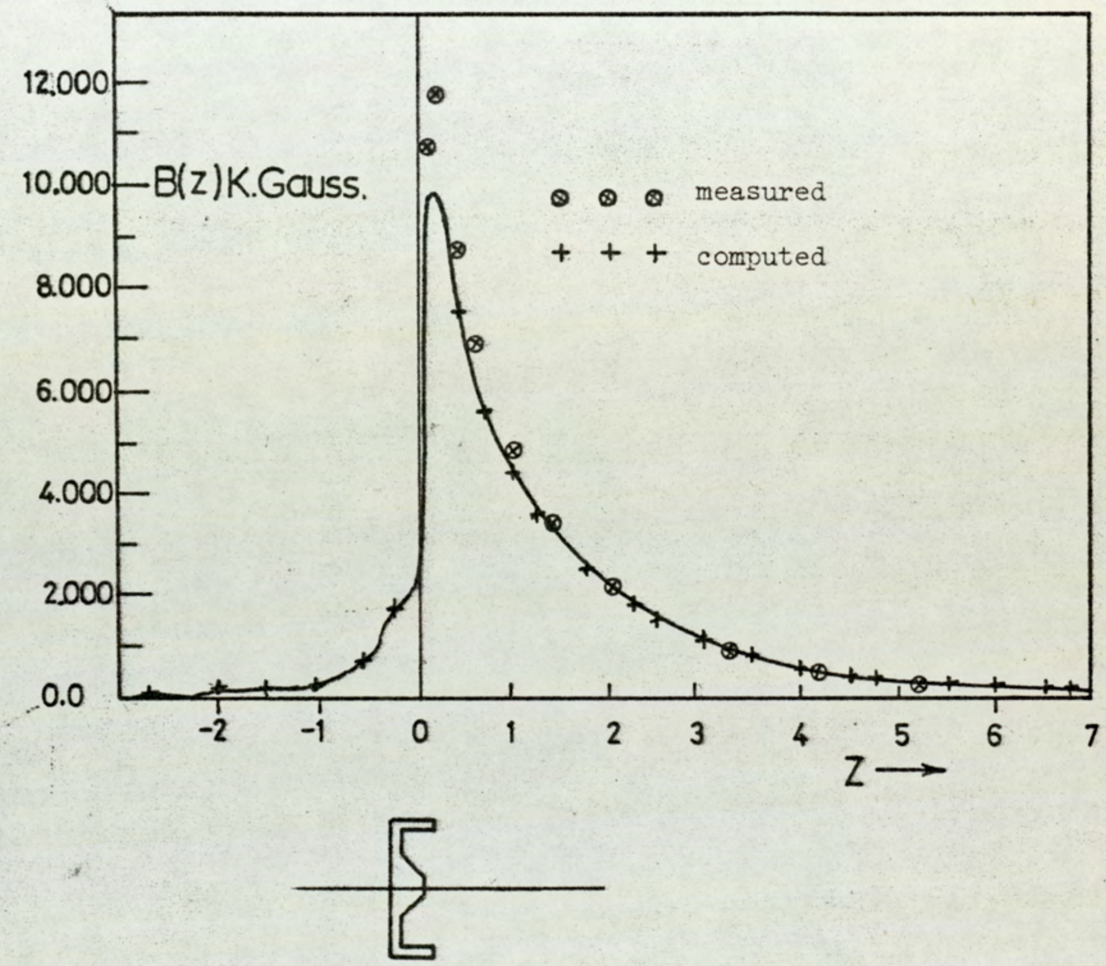

Figure 5.16 Axial flux density distribution of the high voltage single-pole lens computed by laboratory computer aids. NI = 12086 A-t

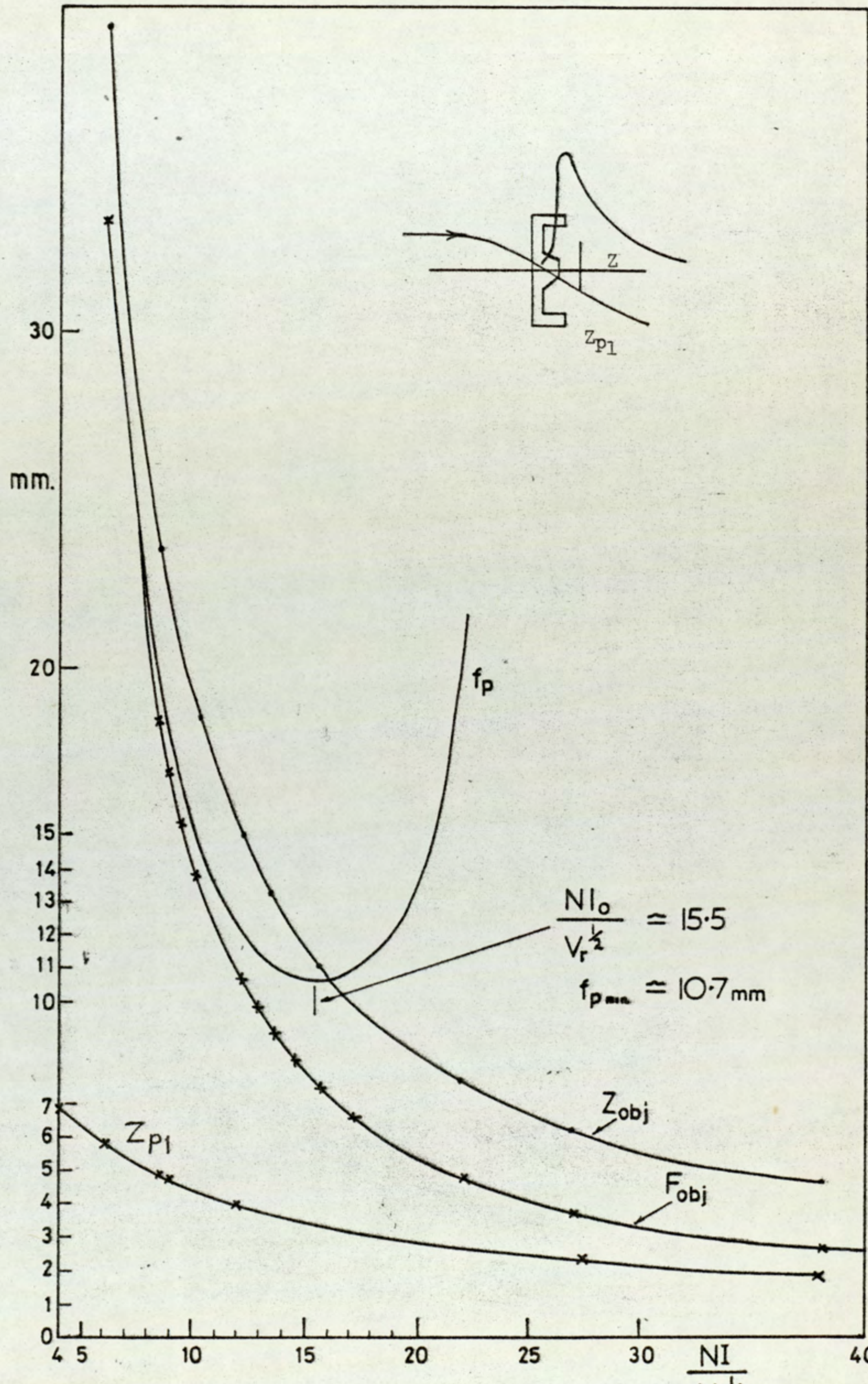

Figure 5.17 Focal properties of the high voltage single-pole lens calculated from the calculated flux density distribution

The objective distance Z_{obj} falls in the same manner as the objective focal length. The principal plane Z_{p1} is at a far distance away from the snout at very low excitation but quickly reaches an approximately constant value of 2.5 mm from the snout for excitations $NI/V_r^{\frac{1}{2}}$ more than 25.

Figure 5.18 shows the variation of projector focal length with relativistically corrected accelerating voltage V_r for a fixed excitation NI = 12086 A-t. The value of V_r required for the minimum projector focal length as shown in the figure is about 650 KV. The increase of the projector focal length for accelerating voltages higher than this value is approximately linear.

Figure 5.19 represents the chromatic aberration coefficient C_c and the spherical aberration coefficient C_s of the lens, when the direction of the trajectory is as shown in the figure, together with the projector and objective focal lengths, for comparison purposes, as a function of the excitation parameter $NI/V_r^{\frac{1}{2}}$. The figure shows that the chromatic aberration coefficient is about three quarters of the objective focal length for excitations greater than corresponding to the minimum projector focal length and about the same as f_{obj}, for low excitations, as for conventional lenses. The third-order spherical aberration coefficient C_s, is high compared with C_s values for an electron beam entering the lens from the opposite direction. The reason for this is the effect of the shape of the field.

Figure 5.20 shows the variation of C_c, C_s, f_{obj} and f_p values as a function of the excitation parameter $NI/V_r^{\frac{1}{2}}$ in the case where the electron beam trajectory is parallel to the axis at a long distance from the snout. The minimum projector focal length of 10.7 mm occurs as expected at a value of $NI/V_r^{\frac{1}{2}}$ equal to 15.5 in agreement with previous calculations. It is to be expected that the objective focal length, chromatic and spherical aberration coefficients would

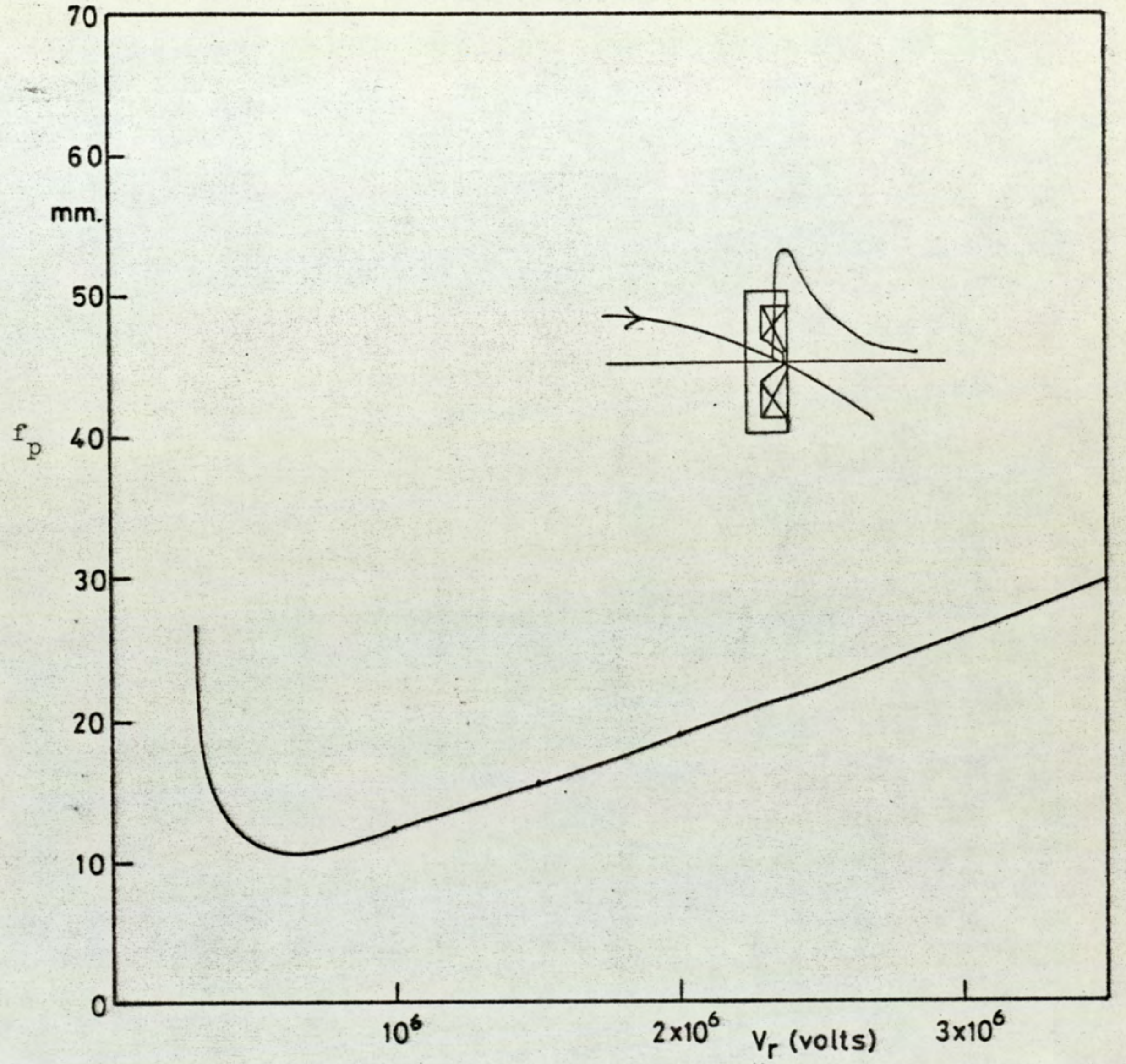

Figure 5.18 The variation of projector focal length f_p as a function of V_r, the relativistically corrected accelerating voltage, for the HV single-pole lens

NI = 12088 A-t

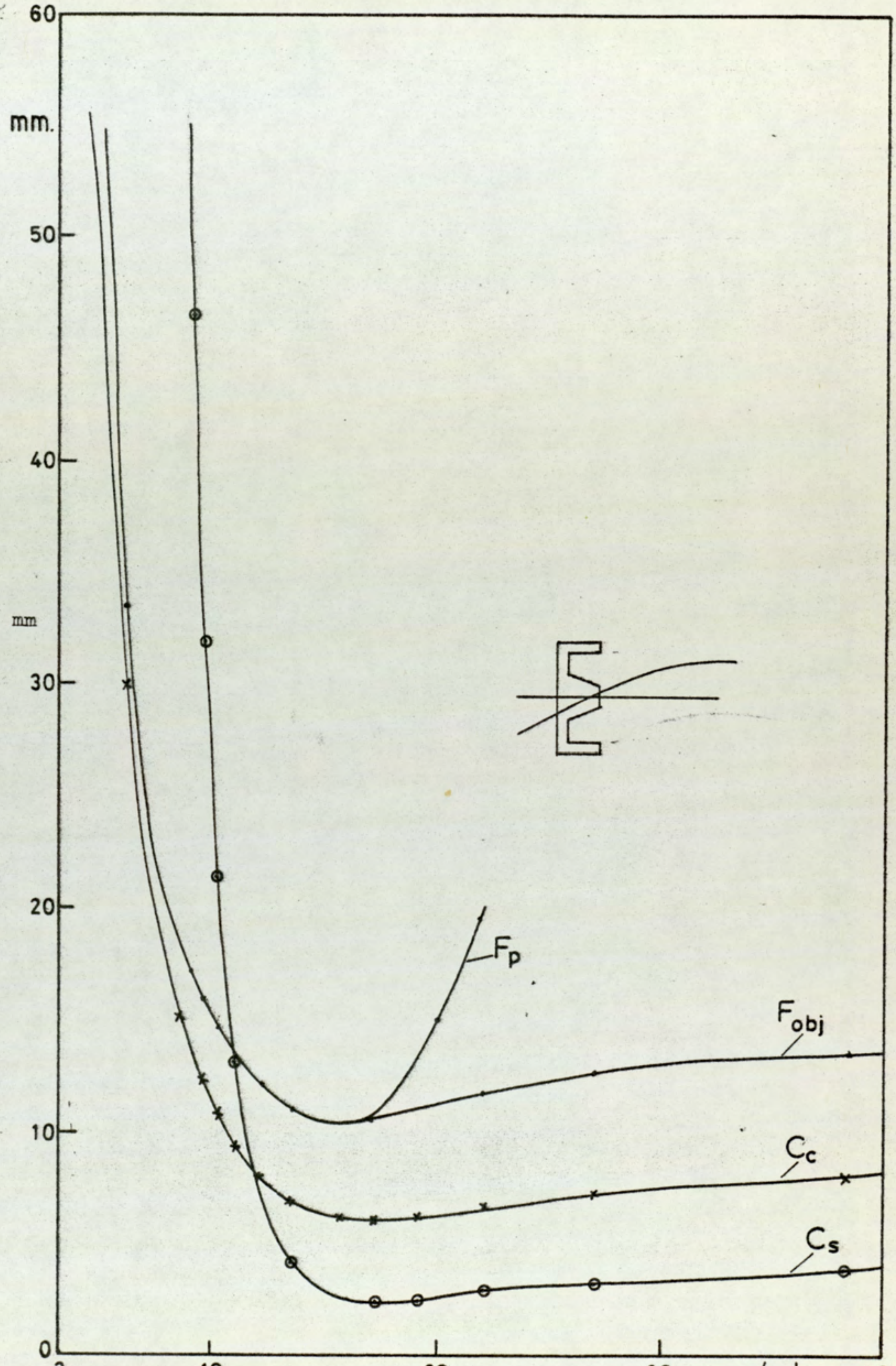

Figure 5.20 Focal properties and chromatic and spherical aberration coefficients of the miniature HV single-pole lens calculated from the calculated field distribution (preferred direction)

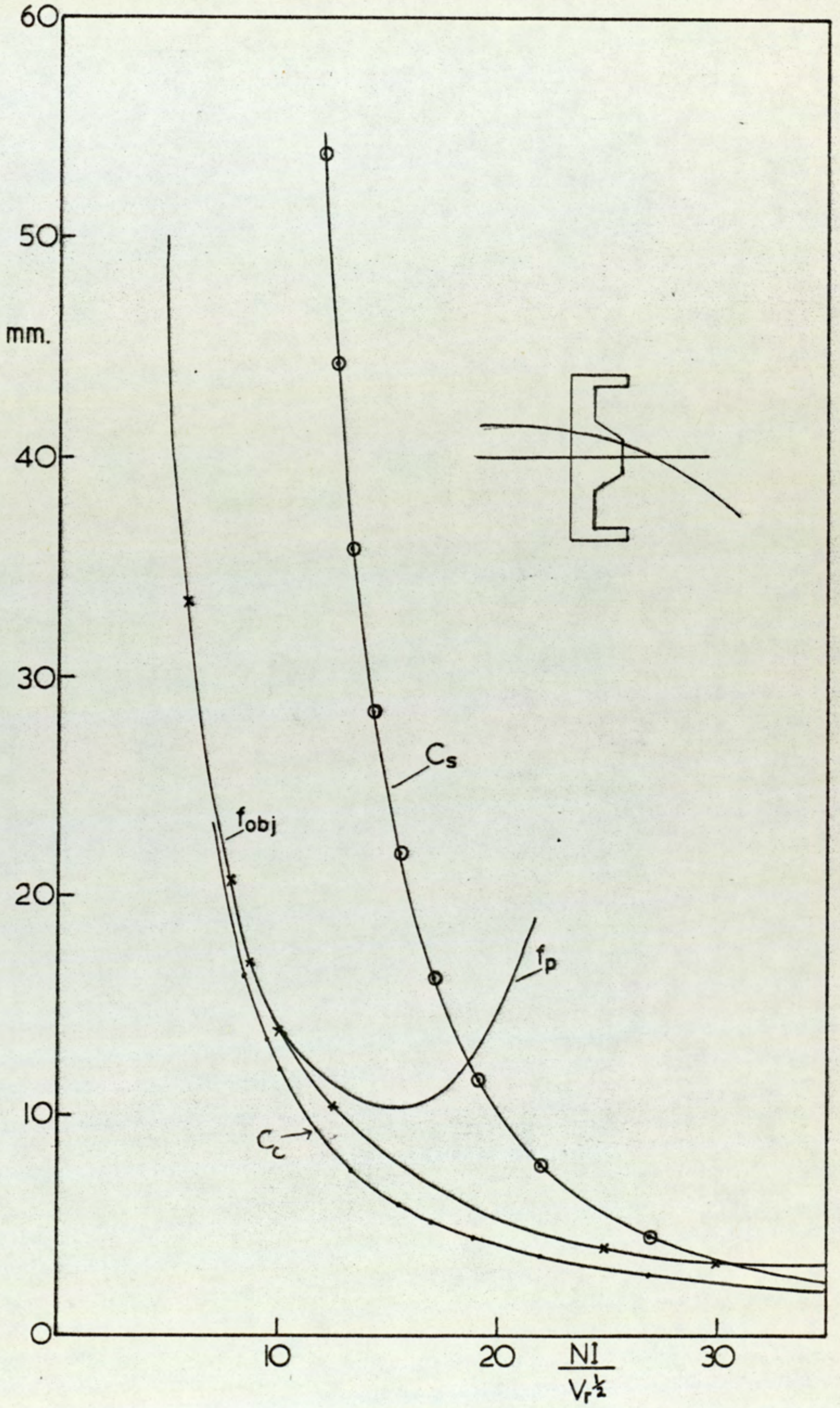

Figure 5.19 Chromatic and spherical aberration coefficients of the HV single-pole lens calculated from the calculated field distribution. The parallel trajectory is at the iron side of the lens

be different. The minimum f_{obj} = 10.4 mm, occurring at $NI/V_r^{\frac{1}{2}}$ = 15.6, $C_{c\ min}$ = 6 mm at $NI/V_r^{\frac{1}{2}}$ = 17 and $C_{s\ min}$ = 2.4 mm at $NI/V_r^{\frac{1}{2}}$ = 17.

b) <u>The electron-optical properties and aberrations of the high-voltage single-pole lens calculated from the measured field distributions</u>

The axial magnetic flux density distribution for the high voltage single-pole lens was measured using a Hall-effect probe gaussmeter. The flux density distribution, for a lens excitation NI = 2985 A-t is shown in figure 5.21. Because the bore diameter was too small to allow the probe to go through, the part of the flux density distribution on the negative Z side of figure 5.21 was estimated. This field distribution was used to calculate the focal properties and aberration coefficients of the lens by means of the computer program described in Chapter 3. Figure 5.22 shows the variation of the focal quantities f_p, f_{obj}, Z_{obj} and the chromatic C_c and spherical C_s aberration coefficients of the high voltage single-pole lens as a function of the excitation parameter $NI/V_r^{\frac{1}{2}}$ for the case where the parallel trajectory enters at the iron side of the lens. The figure shows a similar behaviour to that calculated from the calculated flux density distribution, except that the minimum projector focal length is 9.4 mm compared with 10.7 mm in the calculated field case. This is caused by the peak values of the measured field being about 20% higher than those calculated, for the reasons explained above. Figure 5.23 shows the variation of f_p, f_{obj}, Z_{obj}, C_c and C_s as a function of $NI/V_r^{\frac{1}{2}}$ calculated from the measured axial flux density distribution in the case where the parallel electron trajectory enters the 'open' side of the lens. The minimum projector focal length $f_{p\ min}$ is 9.4 mm and occurs at $NI/V_r^{\frac{1}{2}}$ = 15.5. The objective and projector focal lengths are equal at an excitation $NI/V_r^{\frac{1}{2}}$ = 15.5 and smaller values,

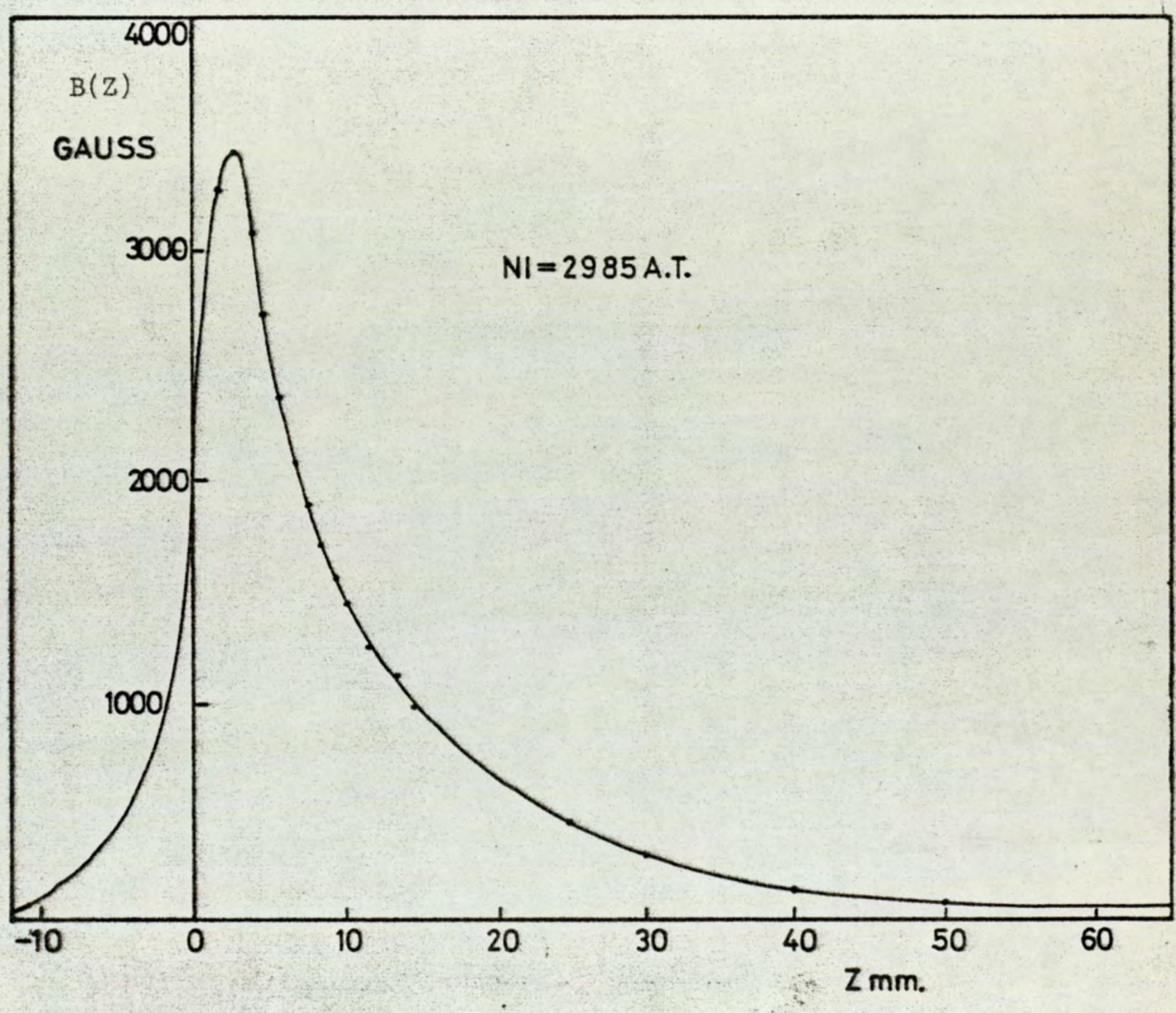

Figure 5.21 . The axial flux density distribution of the high voltage single-pole lens measured by a Hall-effect probe

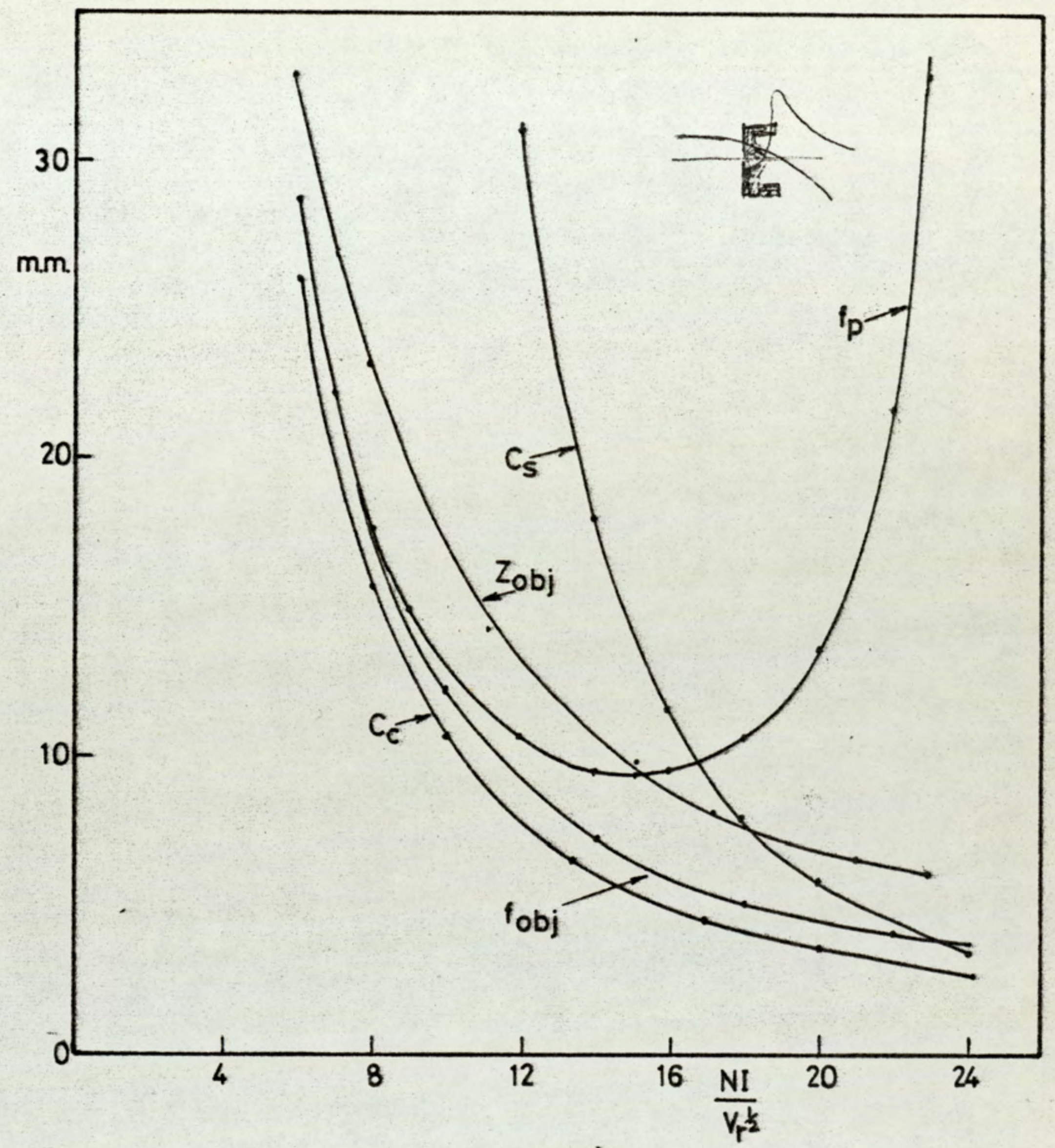

Figure 5.22 Focal properties and aberration coefficients of the high voltage single-pole lens calculated from the measured field distribution

but for excitations greater than that for minimum focal length, f_{obj} reaches a minimum of 9.3 mm at $NI/V_r^{\frac{1}{2}} = 16$ and then increases steadily and slowly with increasing $NI/V_r^{\frac{1}{2}}$. The same behaviour occurs for both C_c and C_s. The minimum value for $C_c = 5.3$ mm, occurs at ($NI/V_r^{\frac{1}{2}} = 17$) and $C_{s\ min} = 2$ mm at $NI/V_r^{\frac{1}{2}} = 17$.

5.2.2 Radial and spiral distortion coefficients of the high voltage single-pole lens

As the high voltage single-pole lens was originally intended to work as a projector lens in the high voltage electron microscope, the investigation of its image distortions, mainly radial and spiral distortions, could lead to the determination of the optimum operational arrangement. The radial and spiral distortion coefficients of the lens were therefore calculated from the data of the measured field distribution by the computer program 'D DISTORTION' described in Chapter 3. The values of radial distortion coefficient $C_d = \frac{D_r}{R^2}$ and the spiral distortion coefficient $C_{sp} = \frac{D_{sp}}{R^2}$ were, therefore, calculated for a lens with a bore radius R = 1 mm. The variation of C_d and C_{sp} with the excitation parameter $NI/V_r^{\frac{1}{2}}$ is shown in figure 5.24. The solid lines represent the case which was used in the Hitachi H U 1000 microscope where the parallel incoming electron beam entered the lens field at the iron backplate of the lens, i.e. the lens snout faced the screen. Consequently, the bore of the lens sets an upper limit on the height of the incoming rays. The curves for C_d and C_{sp} in this case have the same general shape as those of conventional double-pole lenses. The dashed lines in figure 5.24 represent the case when the incoming electron beam enters the lens field from the opposite side of the lens, i.e. when the snout faces the incoming beam. In this case the field of view or the initial height of the incident beam is not limited by the size of the hole

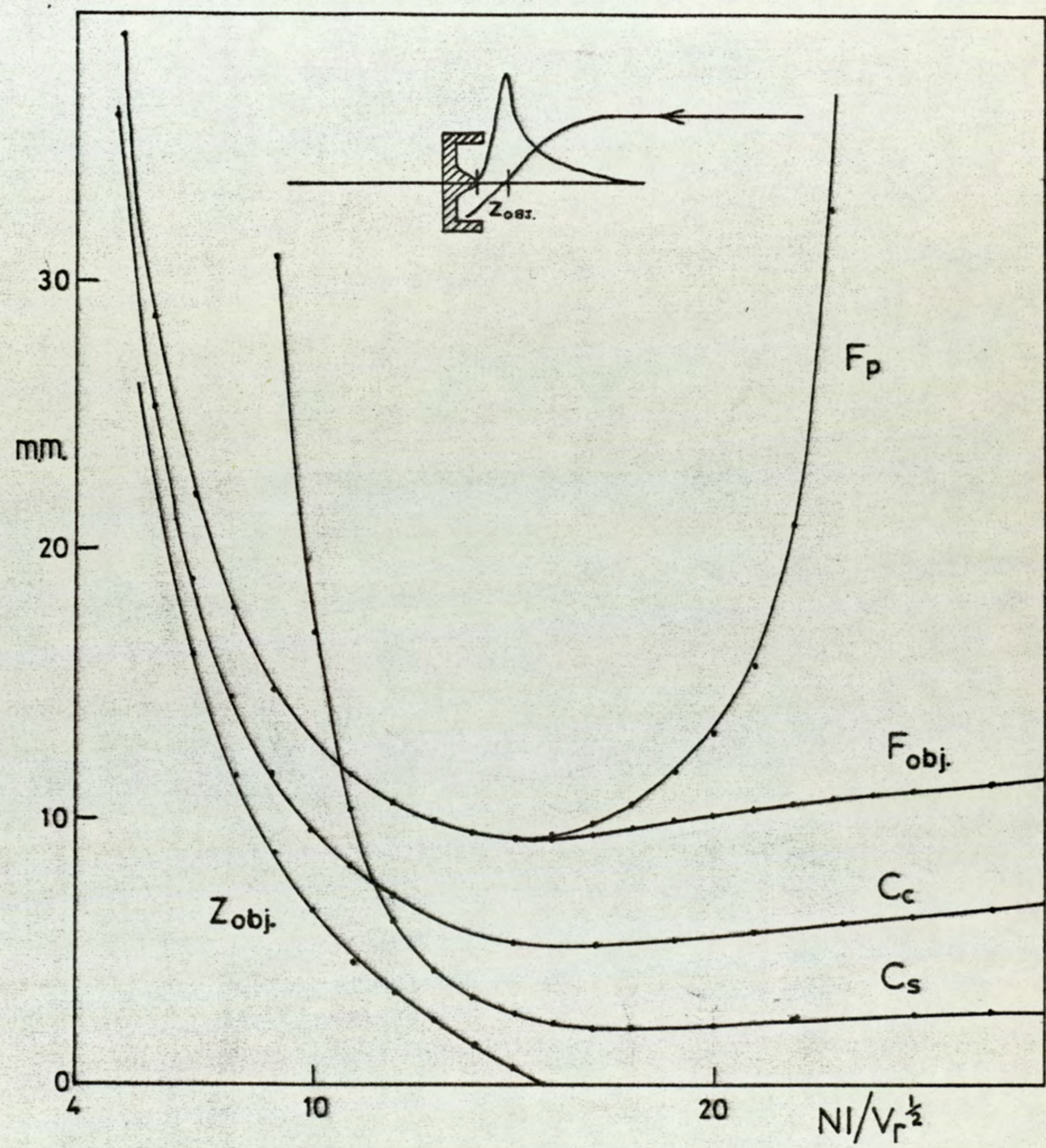

Figure 5.23 Focal properties and chromatic and spherical aberration coefficients of the miniature HV single-pole lens, calculated from the measured field distribution (preferred direction)

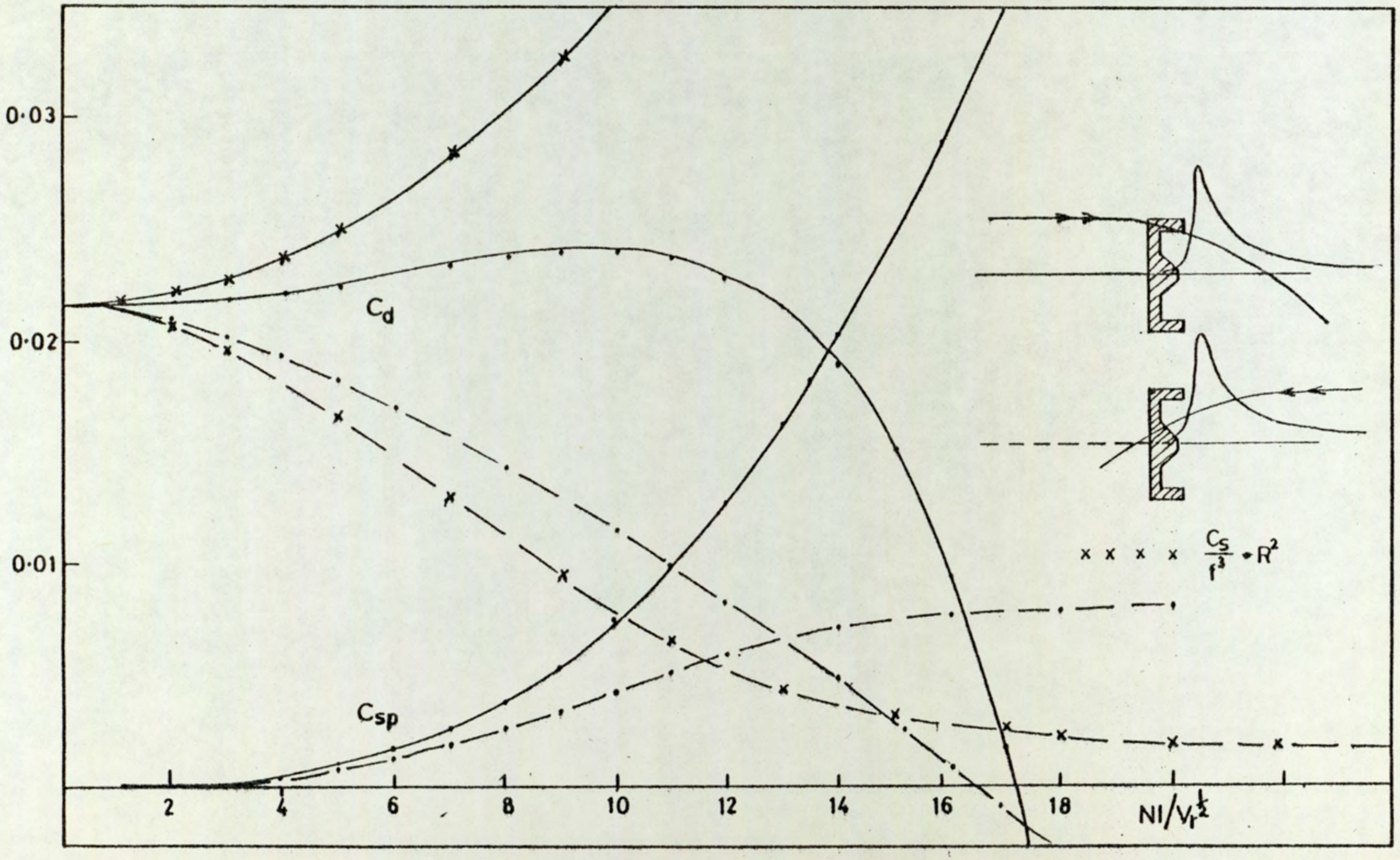

Figure 5.24 Radial C_d and spiral C_{sp} distortion coefficients of the miniature HV single-pole lens, calculated from the data of the measured field distribution

in the snout, but is limited by the exit angle of the conical part of the lens. However, the radial and spiral distortion coefficients in this case behave in a different way from those when the incoming beam enters from the opposite direction. The radial distortion coefficient C_d starts from the same value C_{do} and decreases continuously as the excitation parameter increases and reaches zero at $NI/V_r^{\frac{1}{2}} = 16.6$, i.e. nearer to the minimum focal length position than that for a beam entering from the unfavourable direction. In the range of excitation $NI/V_r^{\frac{1}{2}}$ between 10 and 16, C_d for the favourable direction is less than 50 per cent of its value for a beam coming from the opposite direction. The spiral distortion coefficient C_{sp} also shows a big difference in this favourable case. Indeed, at minimum focal length, C_{sp} in this case is only one third of the value for the unfavourable direction. The variation of C_{sp} is very slow for excitations $NI/V_r^{\frac{1}{2}}$ greater than 16. These results therefore suggest that one can obtain a better image performance and micrographs in an instrument such as the Hitachi HU 1000 electron microscope of Berkley, if the mini-projector is turned through an angle of 180^o so as to make the snout face the incoming beam. This would enable the projection distance to be reduced substantially.

As a check on the order of magnitude of the values of C_d of the high voltage single-pole lens, we made use of the approximation $C_d = \frac{C_s}{f^3} R^2$ (see Appendix 7) valid when the lens excitation is low. The values of $\frac{C_s}{f^3} R^2$ for the two modes of operating the lens are represented by the crosses in figure 5.24. The approximation is very good at low excitations and gives a good indication of the general shape to be expected for C_d for each mode of operating the lens at low excitation. These results tend to confirm the validity of the more rigorous calculations. It should be borne in mind, however, that by itself, the magnitude of the quantity C_d or C_{sp} is not a sufficient indication of the lens quality. As was shown in Chapter 4, the distortion produced by the lens in the image is determined by the distortion factor $Q = D^{\frac{1}{2}}f_p$, where D is the distortion coefficient ($D = C/R^2$). Hence, it is useful to determine the values of Q_{rad} (for radial distortion) and Q_{sp} (for spiral distortion) as a function of lens excitation. Figure 5.25 shows the variation of Q_{rad} and Q_{sp} of the high voltage single-pole lens for the preferred direction of operation as calculated from the measured field distribution, as a function of the relative excitation parameter NI/NI_o, where NI_o corresponds to the minimum focal length. In addition, the magnification parameter $M = \frac{f_{po}}{f_p}$ of the lens is given for the purpose of indicating at what magnification the lens gives its best performance. From the figure we see that the minimum value of Q_{sp} is 0.8 at $NI/NI_o = 0.86$. Q_{sp} hardly varies over the range $0.7 < NI/NI_o < 1$. This behaviour is very similar even down to numerical values, to that predicted from the exponential field distribution. Also, from figure 5.25 we see that $Q_{rad} = 0$ at $NI/NI_o = 1.07$ corresponding to a relative magnification $M = 0.98$, and the values of $Q_{rad} \leqslant 0.71\ Q_{sp}$ in the region $0.96 < NI/NI_o < 1.15$ corresponding to a relative magnification starting at 0.98, passing through the maximum value 1.00 and then down again to 0.925. In this range of magnification the radial distortion will not exceed 50% of the value of spiral distortion. If, for example, the lens is operated at its maximum magnification and it is required to produce an image with spiral distortion less than 2% and radial distortion less than 1%, on a screen of radius $\rho = 50$ mm, the projector distance L is given by

$$L = Q_{sp} \cdot \frac{\rho}{0.02} = 0.82 \times \frac{50}{0.1415} = 289 \text{ mm}$$

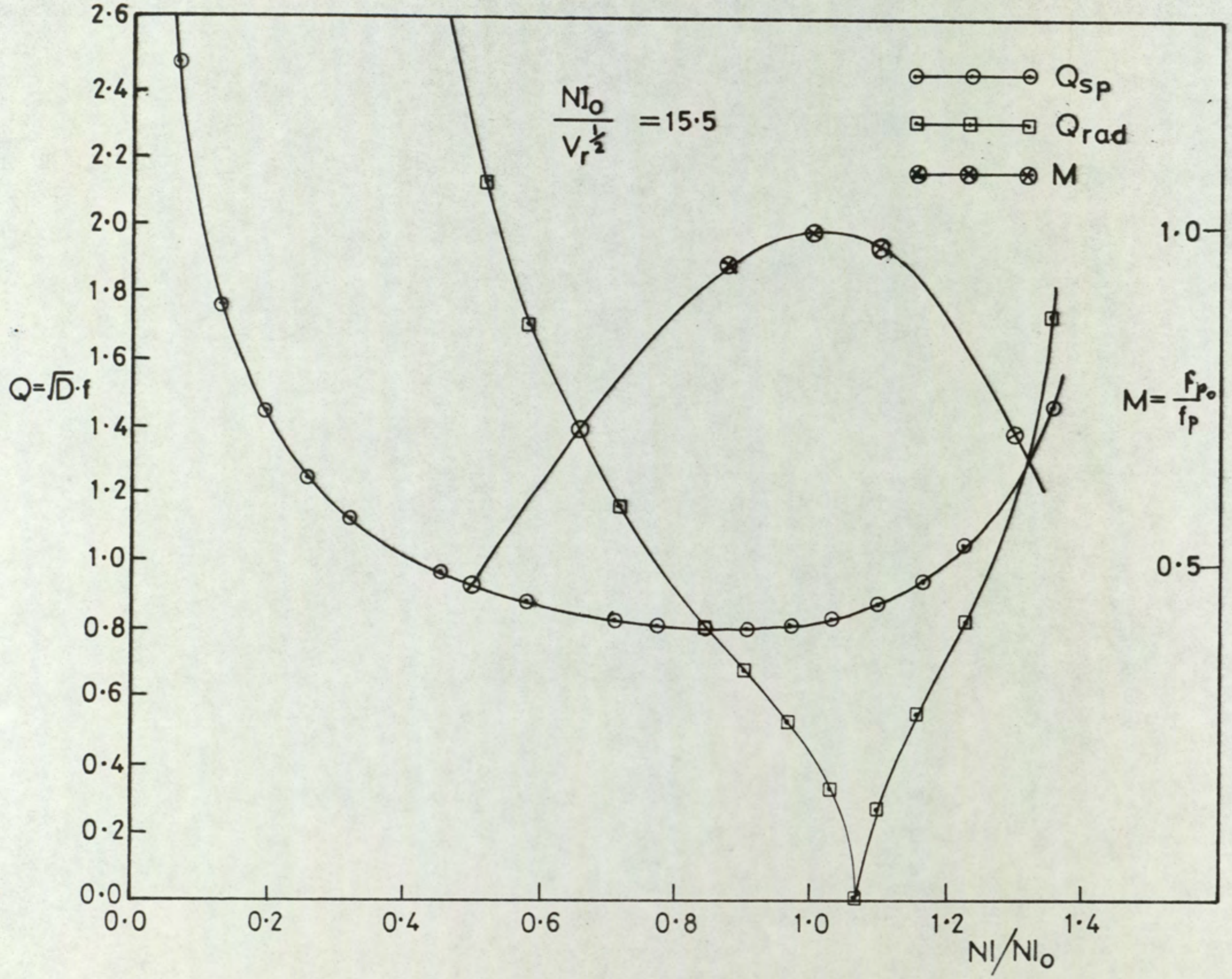

Figure 5.25 The distortion factor Q of the miniature HV single-pole lens calculated from the data of the measured field distribution

Comparing this distance with the projector distance of a typical high voltage electron microscope which is about 500mm, we can see the advantage of using the single-pole lens, in its preferred direction of operation, as a final projector lens in the high voltage electron microscope.

We can therefore conclude from the results of the electron-optical properties of the two single-pole lenses described in sections 5.1 and 5.2 that the exponential field distribution is adequate for predicting to a first approximation the focal properties of a single-pole magnetic lens once the axial field distribution of such a lens is known. It is also encouraging to note that the approximation made in calculating the aberration and distortion coefficients of the exponential field distribution, namely neglecting the infinite slope of the field distribution at $Z = 0$, does not appear to introduce an appreciable error into the calculations of lens aberrations.

5.2.3 Experimental measurement of the focal properties and aberrations of the high voltage miniature single-pole lens

a) The projector focal length, radial and spiral distortion

In order to check the theoretical calculations of the properties of the miniature high voltage single-pole lens, the lens properties were determined experimentally on an Intercol Electron Optical bench at an accelerating voltage of 10 KV. A series of micrographs was taken of the shadow image of an electron microscope grid, formed by the miniature high voltage lens in the two modes of operating the lens corresponding to different excitation parameters $NI/V_r^{\frac{1}{2}}$. The experimental arrangement is shown in figure 5.26, in which the grid was at a distance of 34 mm from the source and the distance between the grid and the lens was 43 mm. A fluorescent screen was placed

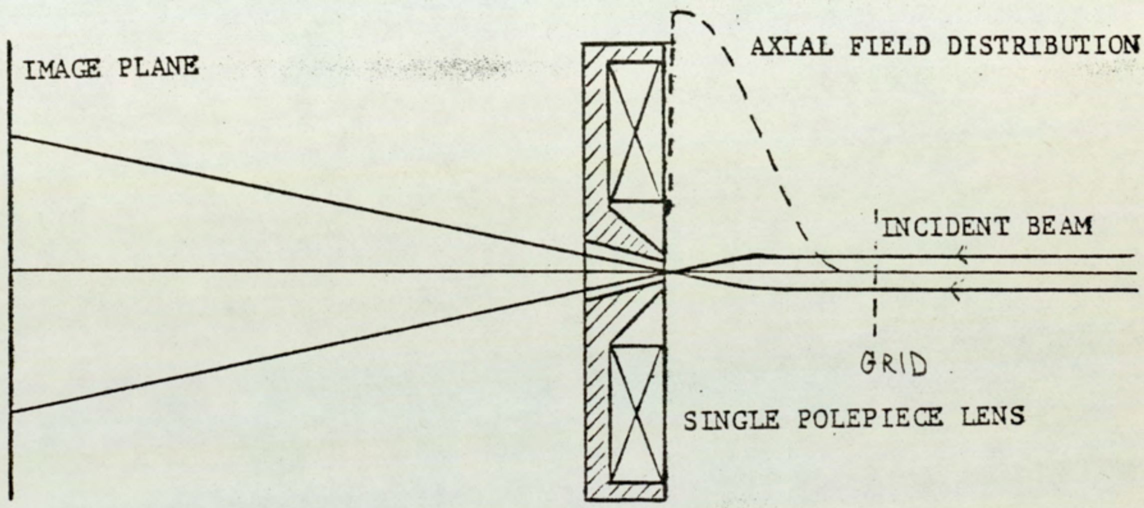

Figure (5.26). Experimental arrangement for measuring the focal properties and distortions of the high voltage lens.

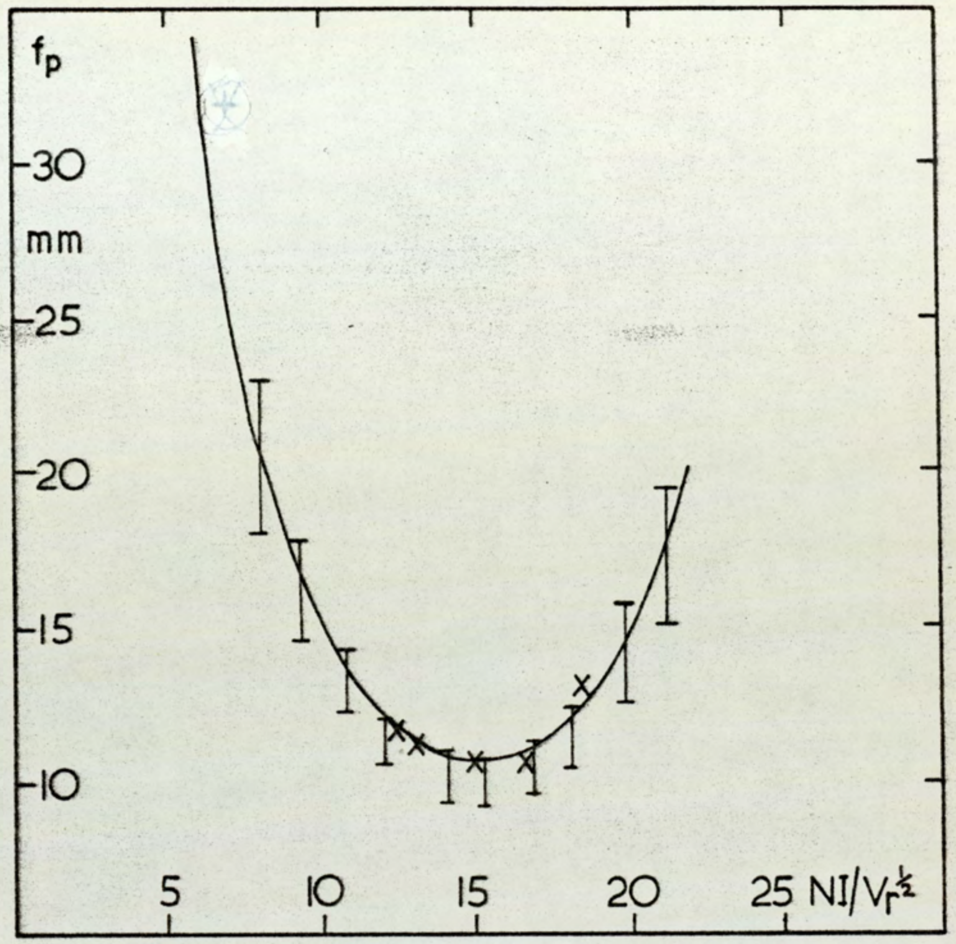

Figure 5.27 Projector focal properties of the high voltage single-pole lens. Solid line, calculated from the calculated field distribution, I, experimental points measured by Newman at 30 KV. X, experimental points measured by the present author at 10 KV

above the lens but separated from it by a short brass cylinder. The primary aim of the experiment was to measure the distortion of the image for the two possible directions of the incident beam, since the projector focal length had been previously measured by Newman (1976). Newman had already found good agreement between his measured results and the projector focal lengths calculated by the present author. Figure 5.27 shows the projector focal length re-measured by the present author (crosses) and those obtained by Newman, compared with the calculated values using the calculated axial field distribution. The figure shows good agreement between the three results especially near the minimum focal length position. Figures 5.28 and 5.29 show a selection of micrographs for the grid image formed by the lens (a) with the lens snout facing the screen and (b) with the snout of the lens facing the incoming incident electron beam (the preferred direction of operating the lens). From the micrographs a considerable difference in the image distortions may be seen in the two cases. With the lens in the preferred direction of operation, the spiral distortion is small, hardly measurable even with a high lens excitation, whereas the distortion is very noticeable with the lens in the unfavourable direction. Figure 5.30 shows the measured radial and spiral distortion coefficients C_d and C_{sp} respectively, measured from the micrographs, compared with the calculated values from the measured axial field distribution. The curves refer to the first zone of operating the lens for the two possible ways of the incident electron beam. The measured values of spiral and radial distortion are in good agreement with those calculated. In addition to the reduction in distortion when using the single-pole lens with its snout facing the incoming electron beam, the micrographs in figures 5.28 and 5.29 show that the favourable direction of the lens permits

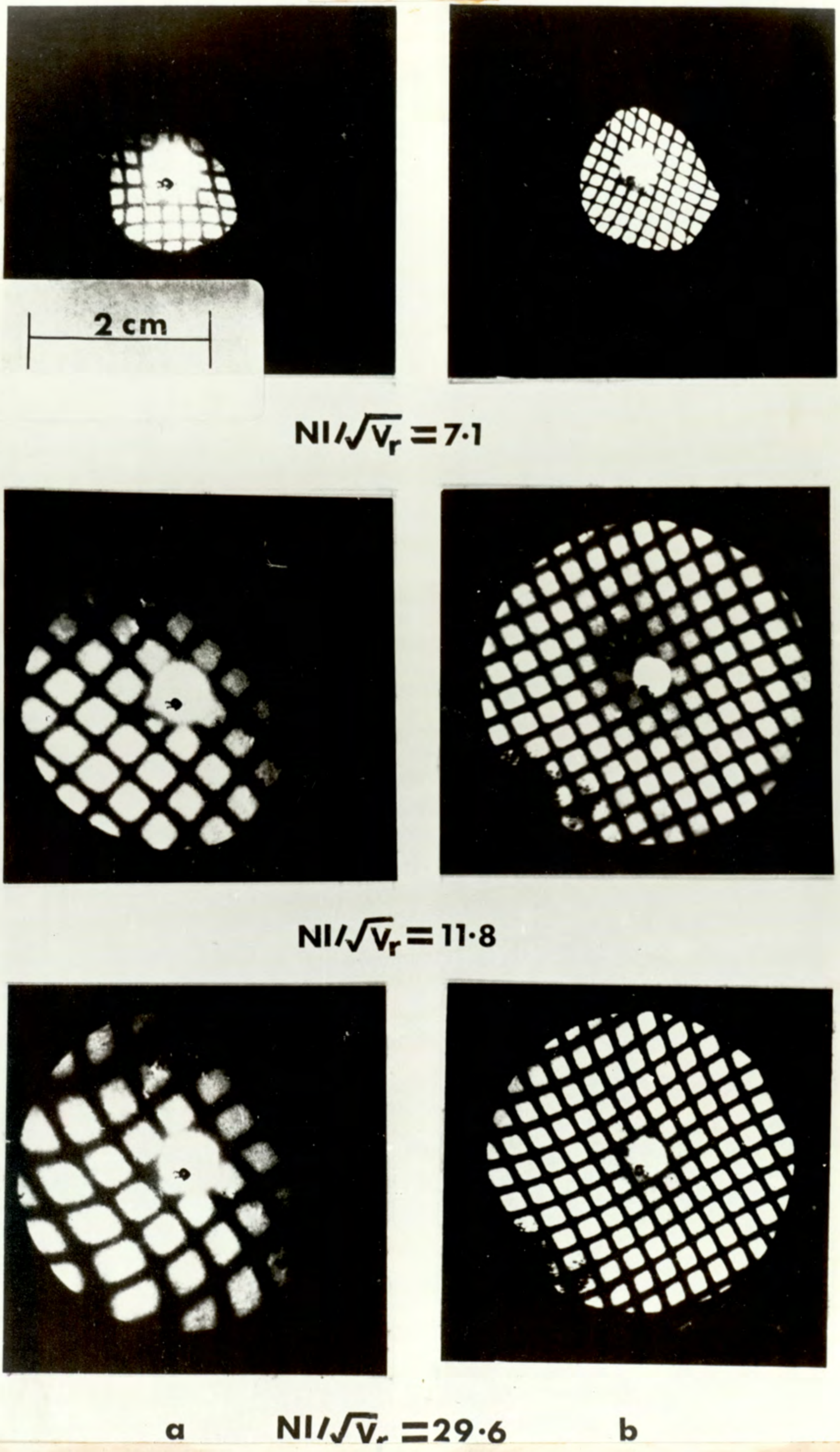

Fig. (5.28) Micrographs formed by the HV single-pole lens : a) snout facing the screen, b) snout facing the incoming beam.

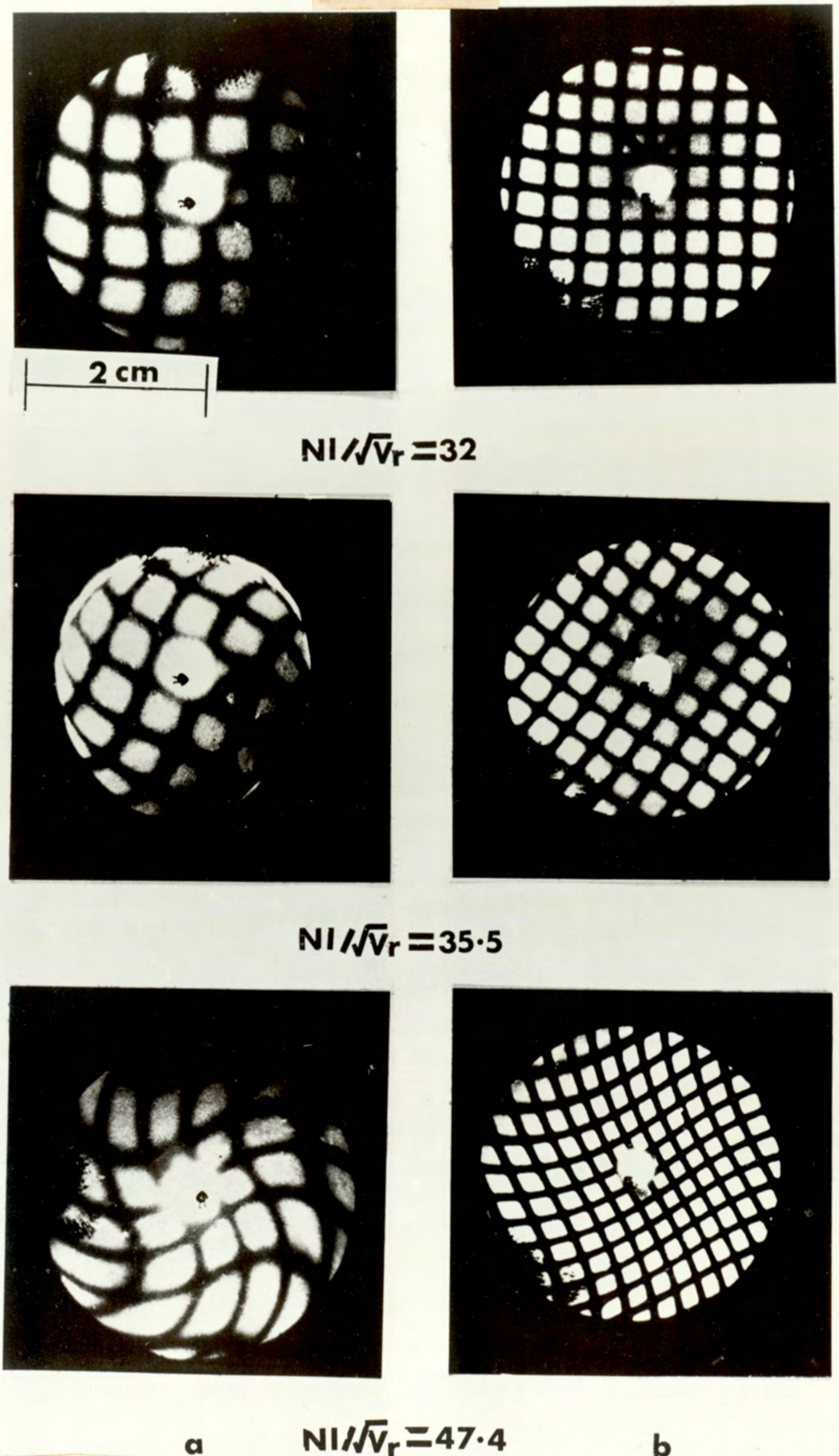

Fig. (5.29) Micrographs formed by the HV single-pole lens : a) snout facing the screen, b) snout facing the incoming beam.

a larger field of view as suggested above. This is shown both by the larger number of grid meshes visible and the larger image diameter.

b) The effect on the focal properties of an iron plate facing the snout of a single-pole lens

1) The axial field distribution

Measurement of the focal length of the high voltage single-pole lens carried out in the EM6 electron microscope by Juma, (1974) showed that the measured focal lengths were shorter than expected both from calculations and experiments carried out on the Intercol electron-optical bench. For example, the minimum focal length was found to be 8 mm compared with the calculated value of 10 mm. In trying to discover the cause of this discrepancy, it was noticed that in tests carried out in the EM6 electron microscope, the lens had been mounted directly on top of the iron flange of the viewing chamber of the electron microscope with its snout facing the screen. This suggested that the iron flange was possibly modifying the lens properties. It therefore seemed useful to perform an experiment to investigate the effect of an iron plate on the axial field distribution of a single-pole lens, and hence on its focal properties. A circular iron plate, 1 cm thick and 10 cm in diameter, i.e. equal to the outer diameter of the high voltage single-pole lens, and provided with a central hole of 10 mm diameter, was placed coaxially in front of the high voltage miniature single-pole lens, first at a distance of 11.3 mm from the snout, and then at 7.8 mm from the snout of the lens. The axial flux density distribution corresponding to an excitation NI = 2985 A-t was measured for the two cases, by means of a Hall-effect probe gaussmeter. The resultant field distributions together with the original distribution with no iron plate in place are shown in figure 5.31. Curve 1 shows the original distribution in the absence

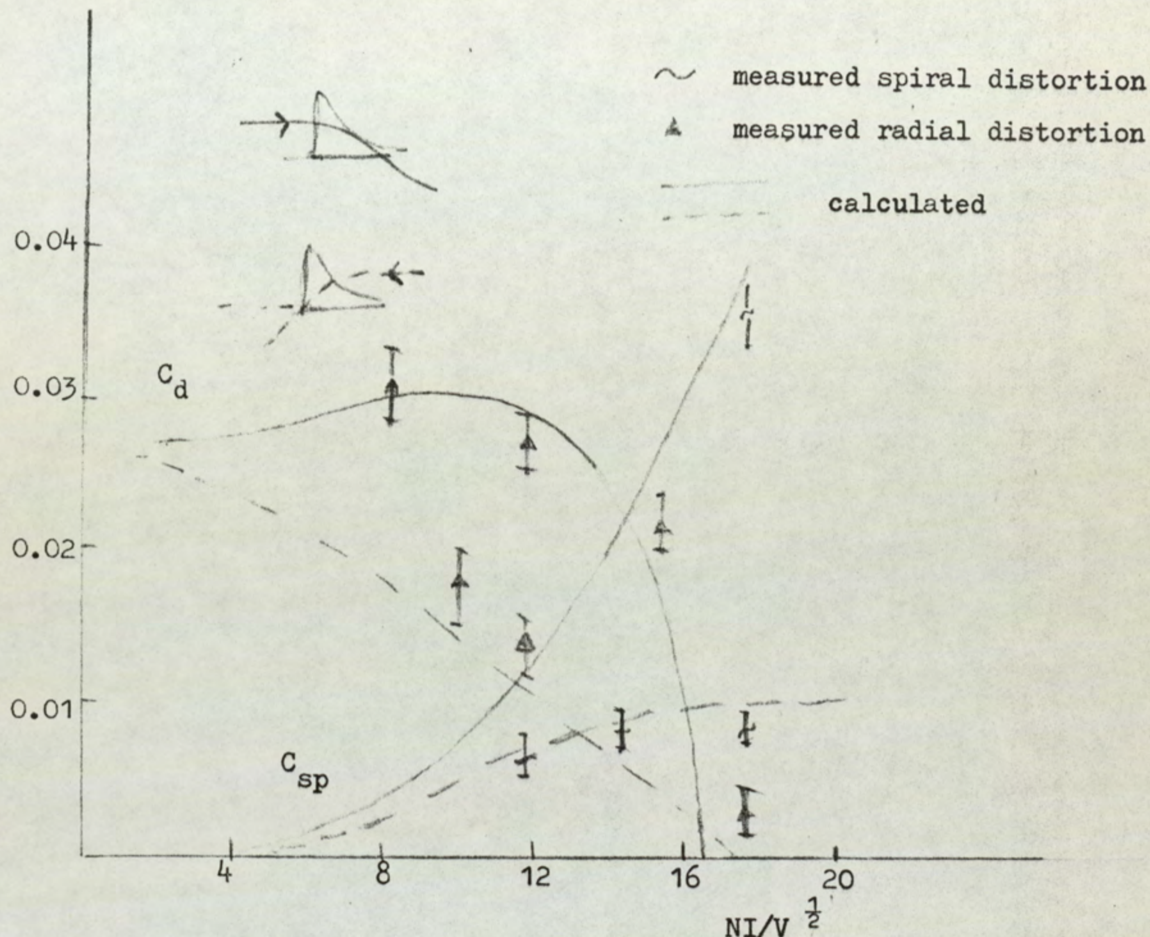

Figure 5.30. Measured and calculated radial and spiral distortion coefficients of the high voltage single-pole lens as a function of the excitation parameter $NI/V_r^{\frac{1}{2}}$.

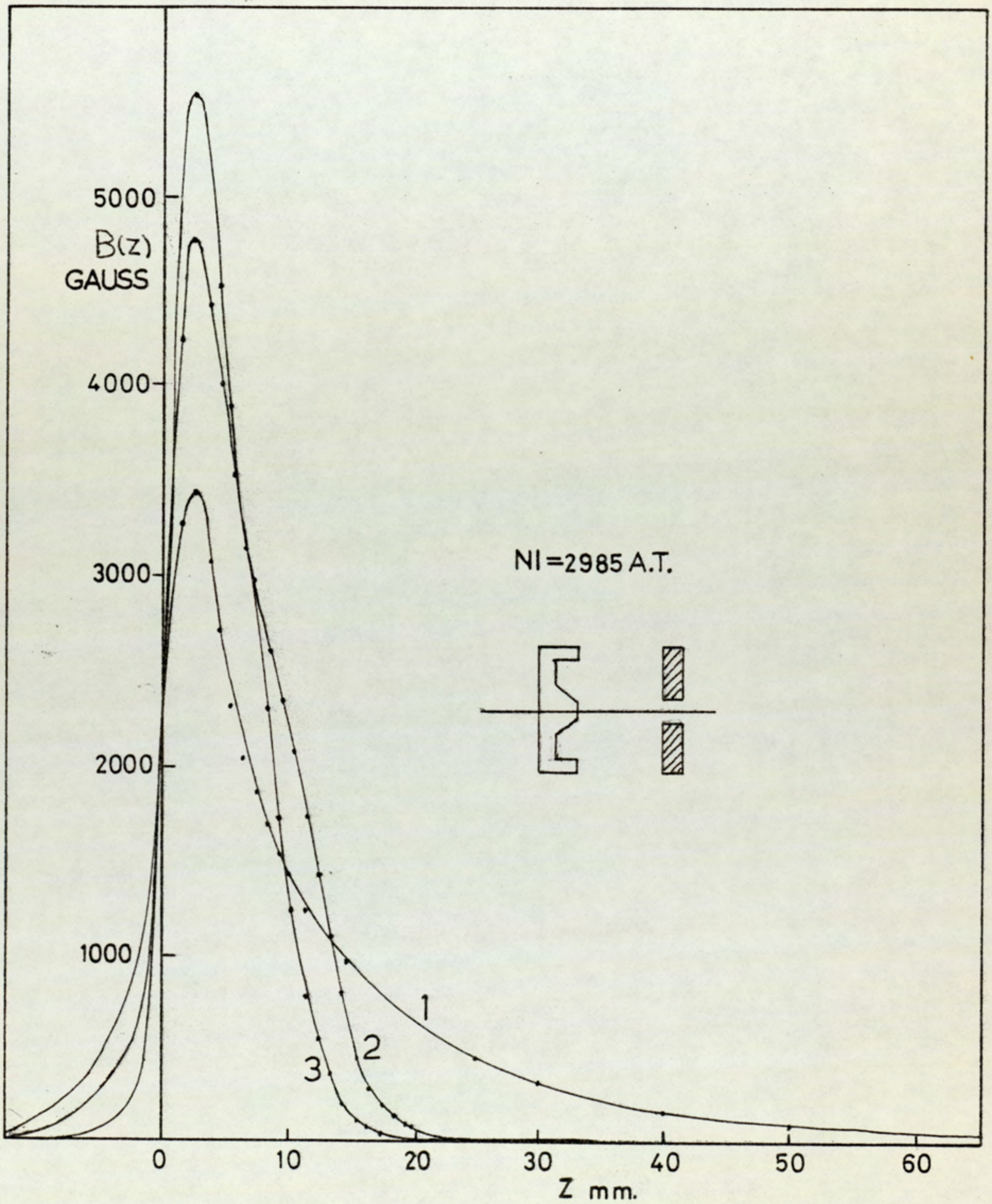

Figure 5.31 Measured field distribution of the high voltage single-pole lens, (1) in the absence of an iron plate, (2) the iron plate facing the lens at 11.3 mm from the snout, (3) the iron plate facing the lens at 7.8 mm from the snout

of the plate, and curve 2 gives the axial field distribution of the single-pole lens with the iron plate at 11.3 mm from the snout. Figure 5.31 shows the effect of the iron plate is to cut off the axial field distribution at a distance of about 20 mm from the snout and to push up the peak field from 3440 Gauss in the original distribution to 4770 Gauss, an increase of about 38%. The "half-width" of the field distribution however remains approximately the same. The prescence of such a plate tends to change the axial field distribution, so that it begins to resemble more closely that of a conventional double-pole lens.

Curve 3 in figure 5.31 shows the axial field distribution for the iron plate at 7.8 mm from the snout. The shape of the field distribution in this case becomes quite similar to that of a double-pole lens. The peak value was pushed up to 5340 Gauss, an increase of 55% from the original peak value without the iron plate. Here the "half-width" of the field is about 15% less than that of the distributions 1 and 2. The peak positions of all the three field distributions occur at the same axial distance from the snout, namely 2.5 mm.

2) <u>The focal properties and aberration coefficients</u>

The change in the axial flux density distribution by the iron plate is accompanied, as one might expect, by a change in the electron-optical properties of the lens. Figure 5.32 shows the calculated focal properties and chromatic and spherical aberration coefficients of the field distribution 2 of figure 5.31, corresponding to a separation of 11.3 mm between iron plate and snout, for the preferred direction of the incoming electron beam. The minimum focal length is 6.4 mm, about 30% less than that in the absence of the iron plate. The decrease in focal length is thus mainly caused by the increase

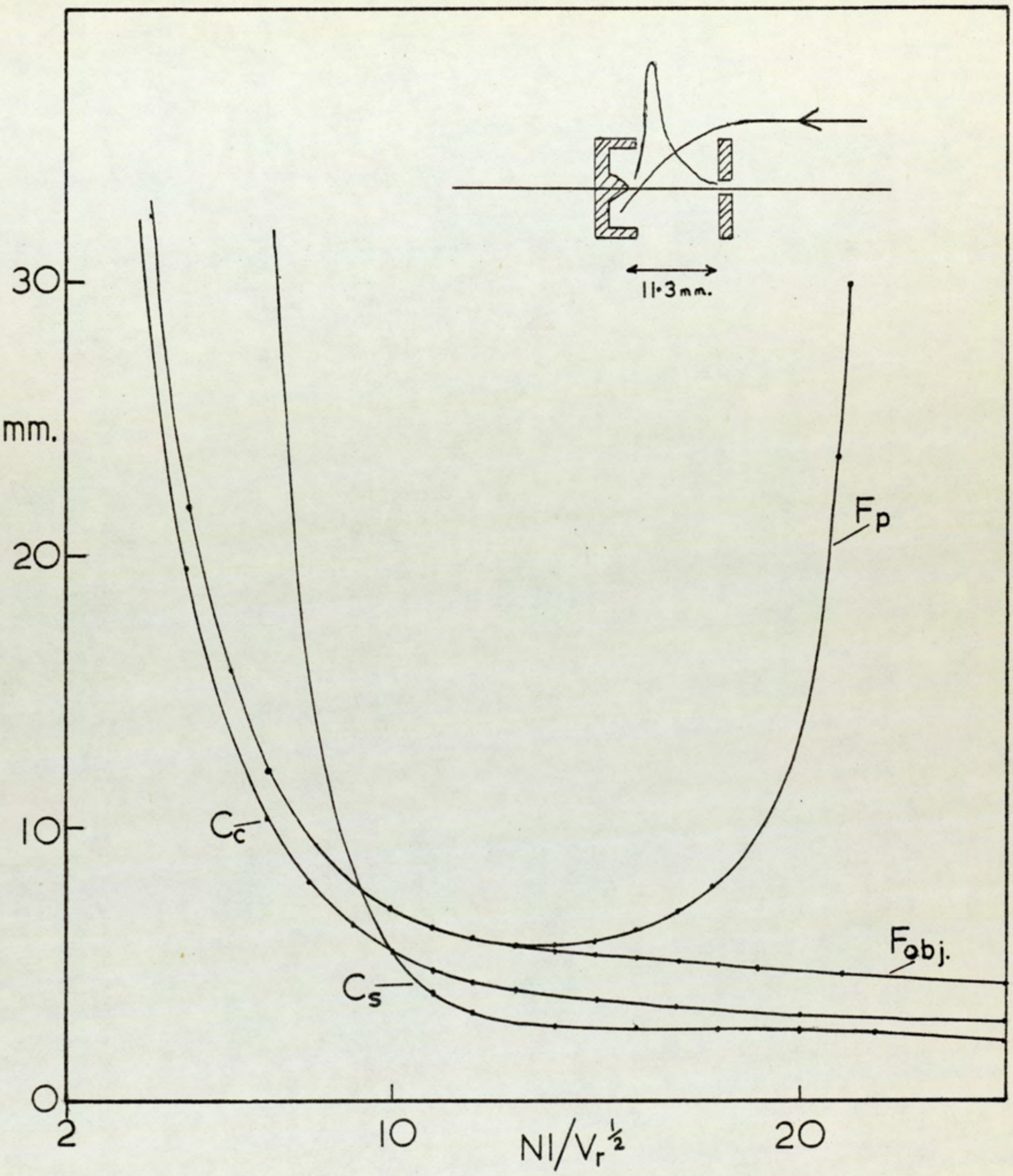

Figure 5.32 Focal properties and chromatic and spherical aberration coefficients of the miniature HV single-pole lens as a function of $NI/V_r^{\frac{1}{2}}$ when an iron plate of diameter 100 mm and a central hole 10 mm faces the lens at 11.3 mm from the snout

in the value of the peak flux axial density. The objective focal length f_{obj} has the same value as the projector focal length f_p for excitations up to that of minimum focal length ($NI/V_r^{\frac{1}{2}} = 14$). For higher excitations the objective focal length decreases slowly and steadily as $NI/V_r^{\frac{1}{2}}$ increases further. The same behaviour occurs for the C_c values which decrease to about 3.75 mm at the minimum focal length position, taking on the value of 0.66 f_{obj} for high excitations. The spherical aberration coefficient C_s starts with very high values at low excitations but decreases rapidly as $NI/V_r^{\frac{1}{2}}$ increases. The change in the value of C_s slows down as $NI/V_r^{\frac{1}{2}}$ reaches 10. At the minimum focal length position, $C_s = 2.7$ mm and then it becomes approximately constant for $NI/V_r^{\frac{1}{2}}$ values greater than 15. The ratio C_s/f_{obj} is approximately equal to one half.

3) Radial and spiral distortion

Radial and spiral distortion coefficients were calculated for the field distribution of figure 5.31 (curve 2) with the iron plate facing the lens at a distance 11.3 mm from the snout. The resultant C_d and C_{sp} values are shown in figure 5.33 as a function of excitation parameter $NI/V_r^{\frac{1}{2}}$ for the two modes of operating the lens. The value of the radial distortion coefficient C_{do} at very low excitation is 0.0346 compared with 0.0216 for the case when the iron plate is absent, i.e. an increase of about 60%. The coefficient C_d, for the two possible ways of entry of the beam has the same form as that described previously for single-pole lenses. For the spiral distortion coefficient C_{sp} the divergence of the two curves, corresponding to the two possible ways of beam entering the lens field, decreased as a result of changing the field distribution to a shape nearer to that of a conventional double-pole lens, although it still showed some asymmetry. We see from the figure the numerical

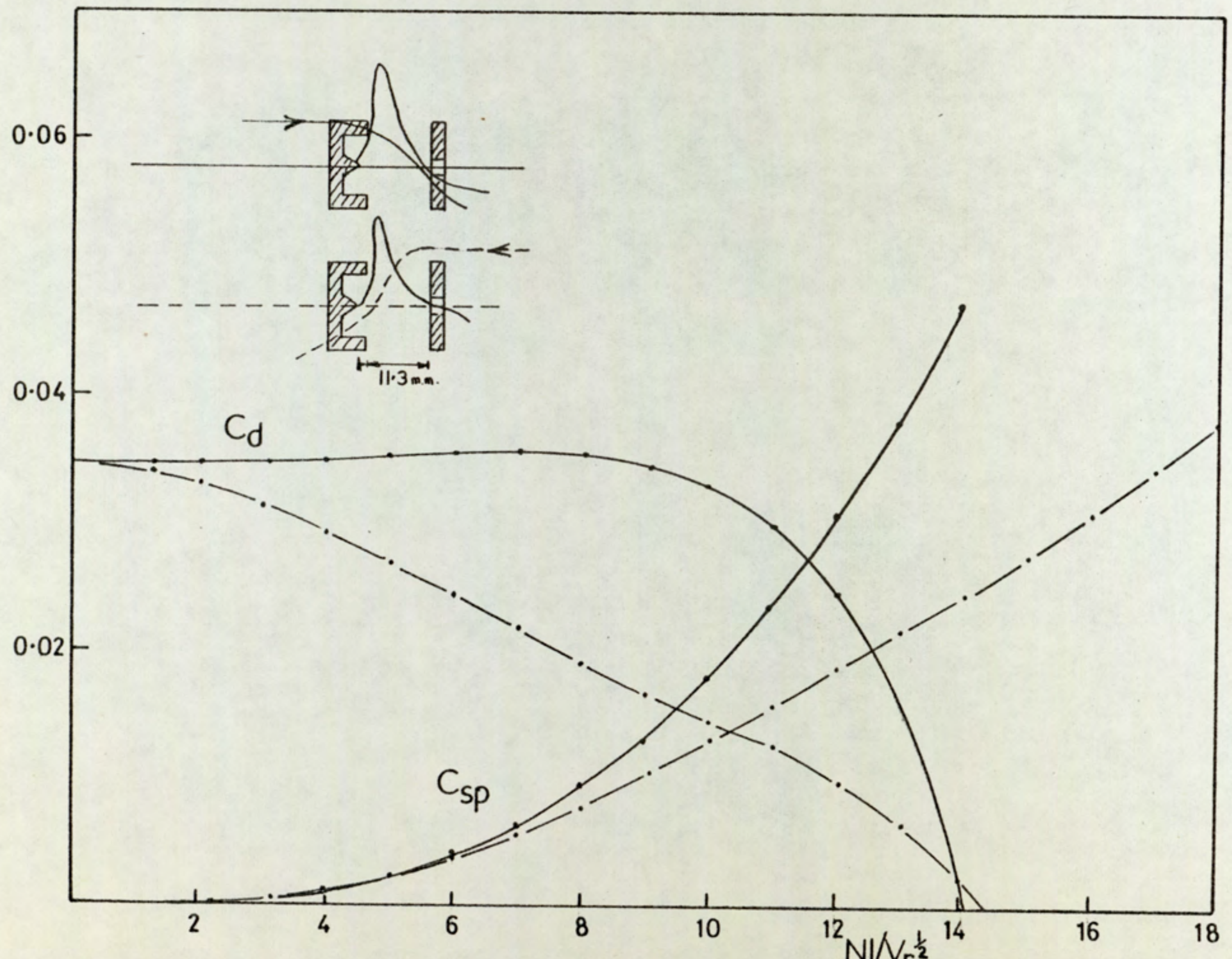

Figure 5.33 Radial C_d and spiral C_{sp} distortion coefficients of the miniature HV single-pole lens when an iron plate faced the lens at a distance 11.3 mm

value of C_{sp} when the iron plate is in place is about three times its value in the absence of the iron plate. The distortion factor Q_{sp} of the lens which, as was discussed in Chapter 4, is an important parameter in the design of projector lenses, is about 0.91 at $NI/NI_0 = 1$, for the preferred direction of operating the lens. This means that the situation has become worse, from the point of view of spiral distortion and projection distance, if we employ such a design making use of the effect of an iron plate, even though it offers shorter focal length (by about 30%). But for an objective lens, we can make use of such a device, since we will get shorter focal length; the spherical aberration coefficient will remain about the same, but the chromatic aberration coefficient will be reduced in proportion to the reduction in objective focal length.

5.3 Optimum arrangement of the high voltage single-pole projector lens

From the results we have discussed in section 5.2, and those in Chapter 4 about the important parameters in designing projector lenses, we can achieve an optimum arrangement for using the high voltage single-pole lens in high energy electron microscope.

1. In order to get lower distortion in the final image, the lens should be used with its snout facing the incoming electron beam, since in that position we get a lower Q value and hence lower Q^2, the factor that determines directly the distortion in the final image. Lower Q values also mean shorter projection distances L, which lead to a reduction in the length of the viewing chamber.

2. The field of view is another important parameter in finding the optimum arrangement of the high voltage single-pole projector lens. Compared with the 2 mm field of view

allowed by the bore of the snout when the lens is used with its snout facing the viewing screen, the field of view increases to 3.5 mm when turning the lens upside down, i.e. the snout facing the incoming beam. This value of the field of view is limited only by the back bore of the lens.

An improvement of the lens to get bigger image size at shorter projection distance, and to increase the field of view at the same time, was made by re-boring the lens in a conical shape with semi-angle 22^{0}. The tip of the conical bore is located at the focal point of the lens. For a lens excitation corresponding to the minimum focal length, that is 0.5 mm inside the bore of the snout. The diameter of the back bore of the lens, in this case, becomes 23 mm. This means at maximum magnification of the lens, for a beam filling the cone of the lens, the field of view at the principal plane of the lens increases to 8.1 mm. At the same time the size of the image 105 mm and is located at a distance 100 mm from the back face of the lens. The radial distortion of this image will be 3.2%, and the spiral distortion 12.8%, which are remarkably low values of distortion considering the projection distance and the image size. However, we can remove the radial distortion by operating the lens at an excitation $NI/V_r^{\frac{1}{2}}$ slightly higher than the maximum magnification value. The spiral distortion in this case (about 12%) can be eliminated by using an intermediate lens of the same type (single-pole lens as a correcting lens for the spiral distortion, in an arrangement such as described in Chapter 6. Figure 5.34 shows an enlarged cross-section of the original inside bore of the lens. Line 1 on the diagram shows the maximum field of view obtainable with the original bore of the lens. Line 2 shows the new field of view after re-boring the back of the lens through an angle of 22^{o}.

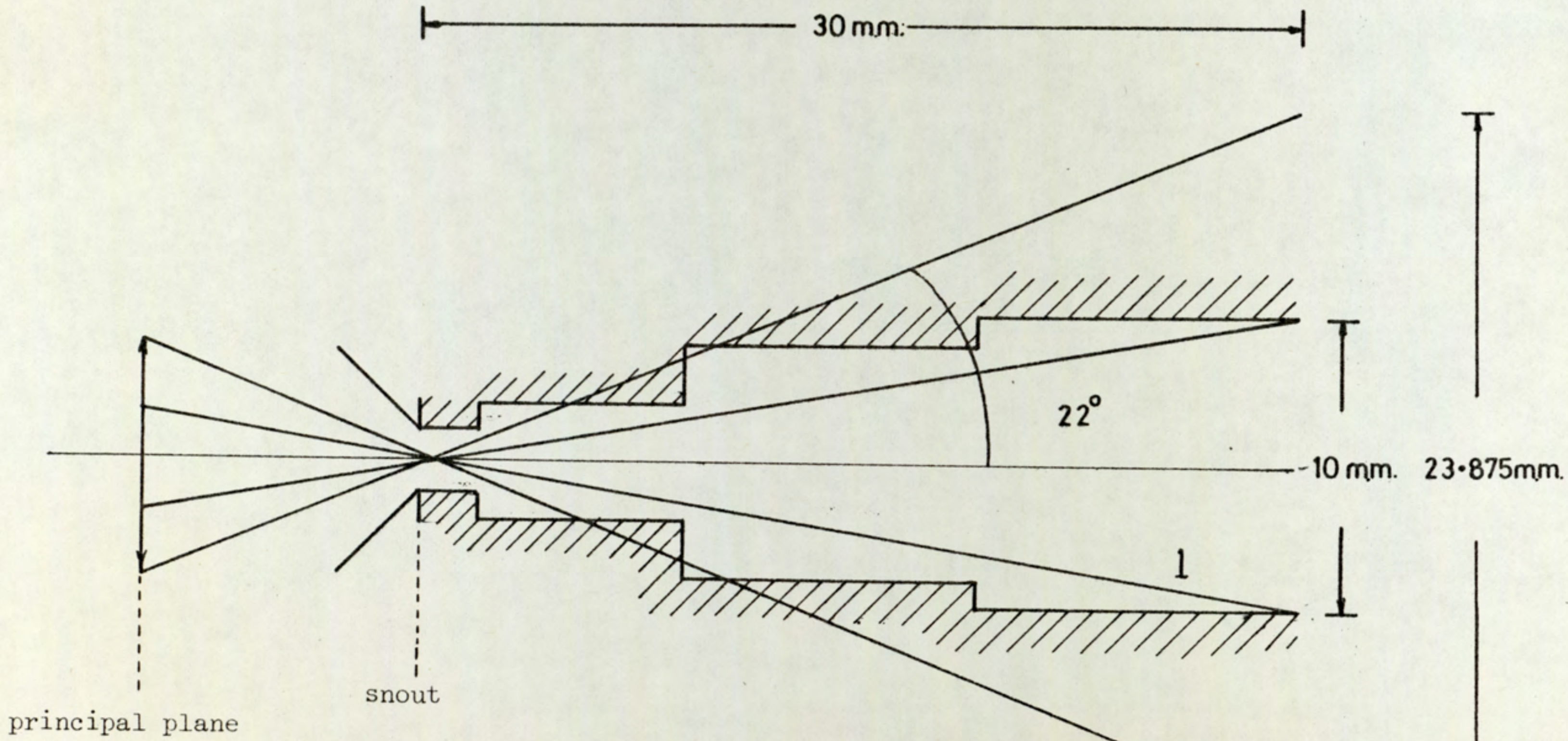

Figure 5.34 Cross-section of the inside bore of the high voltage single-pole projector lens (1) the original bore, (2) after reboring the lens through a cone semi-angle 22°

6. CORRECTION OF ANISOTROPIC (SPIRAL) DISTORTION IN THE ELECTRON MICROSCOPE

6.1 The use of an intermediate lens in a system for correcting distortion

An intermediate lens placed before the final projector lens in the electron microscope has the advantage of increasing the total magnification and the number of modes of operation of the instrument. Such an intermediate lens contributes an amount of spiral distortion to the final image that is inversely proportional to the square of the image magnification provided by the intermediate lens. This distortion can either add to or subtract from the distortion caused by the final projector lens, depending on the direction of the current in the two projector lenses. At first sight, the possibility of correcting the spiral distortion of the final projector lens seems straightforward; one simply reverses the current in the preceding intermediate lens. However, with conventional lenses the magnification of the intermediate lenses would have to be very close to unity in order to get an effective correction. The two projector lenses must therefore be set very close to each other, if not impossible to arrange, which is very difficult in practice, especially with conventional lenses (see Appendix 6).

However, the investigation of the properties of the single-pole lens has made it clear that this kind of lens has two modes of operation (Appendix 2). When the incident beam enters the lens in the direction in which the magnetic field is rising slowly, the spiral distortion is much lower than for a beam entering in the opposite direction. This suggests the possibility of correcting spiral distortion by using two single-pole lenses with their snouts facing each other, as a projector system for the electron microscope. However, for the purpose of understanding the behaviour of a two-lens correcting system, it is more convenient to consider the case of two square-topped field distributions, which can be treated analytically.

6.2 The square-topped field distribution and the correction of spiral distortion

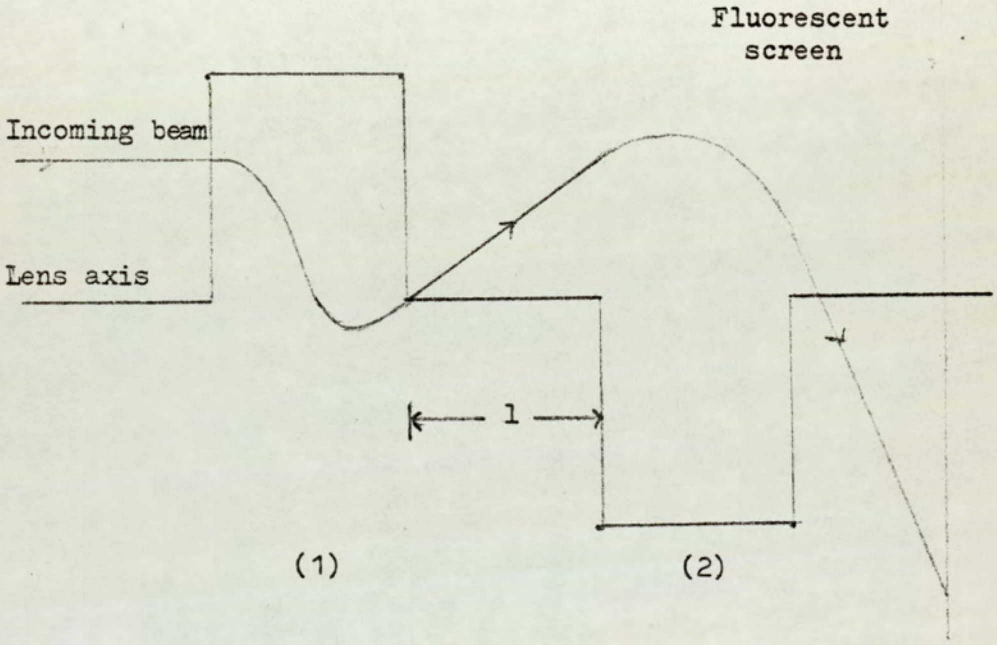

Figure (6.1). Two Square-top fields arranged for the correction of spiral distortion.

Consider two rectangular field distributions 1 and 2, each of axial extent S separated from each other by a distance l, as shown in figure 6.1. The directions of the two magnetic field distributions are opposite to each other. It is also preferred to operate the second lens at an excitation parameter $NI/V_r^{\frac{1}{2}}$ in the region of minimum focal length and hence at maximum magnification. Thus the second lens has an excitation parameter $NI/V_r^{\frac{1}{2}} = 8.43$ corresponding to $(KS)_2 = \frac{\pi}{2}$ (the first focal zone). For simplicity of analysis, the excitation of the correcting lens will be taken as

$(KS)_1 = n\frac{\pi}{2}$, where n = 1, 3, 5, 7, ...

Applying equation 2.31 to the first field distribution gives

$$D_{sp}(1) = K_1^3 \frac{S}{2} = \frac{n^3\pi^3}{16\,S^2} \qquad \text{...... 6.1}$$

since $$K_1 = \frac{n\pi}{2S} \qquad \text{...... 6.2}$$

The magnification of the first lens at the second lens is given by

$$M_1 = \frac{l}{f_{pl}} \qquad \text{...... 6.3}$$

where $f_{p1} = -\frac{1}{K_1}$ is the projector focal length of the first lens.

Hence $$M_1 = -\frac{l\pi n}{2S} \qquad \text{...... 6.4}$$

The contribution to the spiral distortion coefficient of the second lens is given by applying equation 2.36 where U = l.

Thus $$\bar{D}_{sp_o}(2) = \left[1 + \frac{4}{\pi^2}\left(\frac{S}{l}\right)^2 + \frac{2}{\pi^2}\left(\frac{S}{l}\right)\right]\frac{\pi^3}{16S^2} \qquad \text{...... 6.5}$$

Now, to correct the spiral distortion in the image the spiral distortion produced by each lens at the image must cancel exactly

i.e. $$D_{sp}(1)/M_1^2 = \bar{D}_{sp_o}(2) \qquad \text{...... 6.6}$$

i.e. $$n^3\left(\frac{2S}{ln\pi}\right)^2 \cdot \frac{\pi^3}{16S^2} = \left[1 + \frac{4}{\pi^2}\,\frac{S}{l}^2 + \frac{2}{\pi^2}\,\frac{S}{l}\right]\frac{\pi^3}{16S^2} \qquad \text{...... 6.7}$$

i.e. $$\frac{4}{\pi^2}(n-1)\left(\frac{S}{l}\right)^2 - \frac{2}{\pi^2}\left(\frac{S}{l}\right) - 1 = 0$$

...... 6.8

or $$4(n-1)\left(\frac{S}{l}\right)^2 - 2\left(\frac{S}{l}\right) - \pi^2 = 0$$

Equation 6.8 is a general expression giving the separation l between two square-top field lenses in terms of the width of the lens, when using the second lens at constant excitation $K_2 = \frac{\pi}{2S}$. This is a quadratic equation, the solution of which is:

$$\frac{S}{l} = \frac{2 \pm \sqrt{4 + 16\,(n - 1)\pi^2}}{8(n - 1)} \qquad \ldots\ldots\ 6.9$$

From 6.9, we get two values for $\frac{S}{l}$, one of which, when using the negative sign, is imaginary. So, the true solution will be

$$\frac{S}{l} = \frac{2 + \sqrt{4 + 16\,(n - 1)\pi^2}}{8(n - 1)}$$

$$= \frac{1 + \sqrt{1 + 4\,(n - 1)\pi^2}}{4(n - 1)} \qquad \ldots\ldots\ 6.10$$

Examples for the use of equation 6.10

1. To take a simple example, if the **lenses** have the same excitation, n = 1 and S/l is infinite, i.e. l = 0. Thus to correct spiral distortion, the two lenses must be placed in contact, so that the total magnification of the system is 1. This is clearly of no practical use in electron microscopy although it is a useful check on Equation 6.10.

2. $n = 3$

$$\frac{S}{l} = \frac{1 + \sqrt{1 + 8\pi^2}}{8}$$

or $l = 0.8045\ S$

The projector focal length of the system in this case is

$$f_p = 0.169\ S$$

3. If $n = 5, \frac{S}{l} = \frac{1 + \sqrt{1 + 16\pi^2}}{16}$

$l = 1.176\ S$

4. If $n = 7, \frac{S}{l} = \frac{1 + \sqrt{1 + 24\pi^2}}{24}$

$l = 1.461\ S$

Thus, the separation l between the two lenses 1 and 2 for a distortion-free image under these circumstances is comparatively small, even when a very high excitation is employed for the correcting lens. This indicates again the practical difficulty of using a spiral distortion correcting system with conventional double-pole lenses. Figure 6.2 shows the variation of the separation distance $\frac{l}{S}$ as a function of the correcting lens excitation parameter K_1S, when the corrected lens 2 is kept at constant excitation $K_2S = \frac{\pi}{2}$.

6.3 Design and construction of a correcting system for spiral distortion using two single-pole projector lenses

The approach to a distortion-free projector system requires the use of an intermediate lens with a high spiral distortion coefficient compared with that of the final projector lens. This case is very difficult to achieve using the conventional double-pole lenses, since all have approximately the same value of $Q = D_{sp}^{\frac{1}{2}} f_p$ (Appendix 6). The use of single-polepiece magnetic electron lenses shows that in one mode of operating the lens we can reduce the spiral distortion coefficient by a factor of 3 compared with that using the lens the other way round, in the vicinity of the minimum focal length position (Marai and Mulvey, 1975). The corresponding values of $Q = D_{sp}^{\frac{1}{2}} f_p$ differ approximately by a factor of 2 (Appendix 6). This suggests that the use of two single-pole magnetic electron lenses

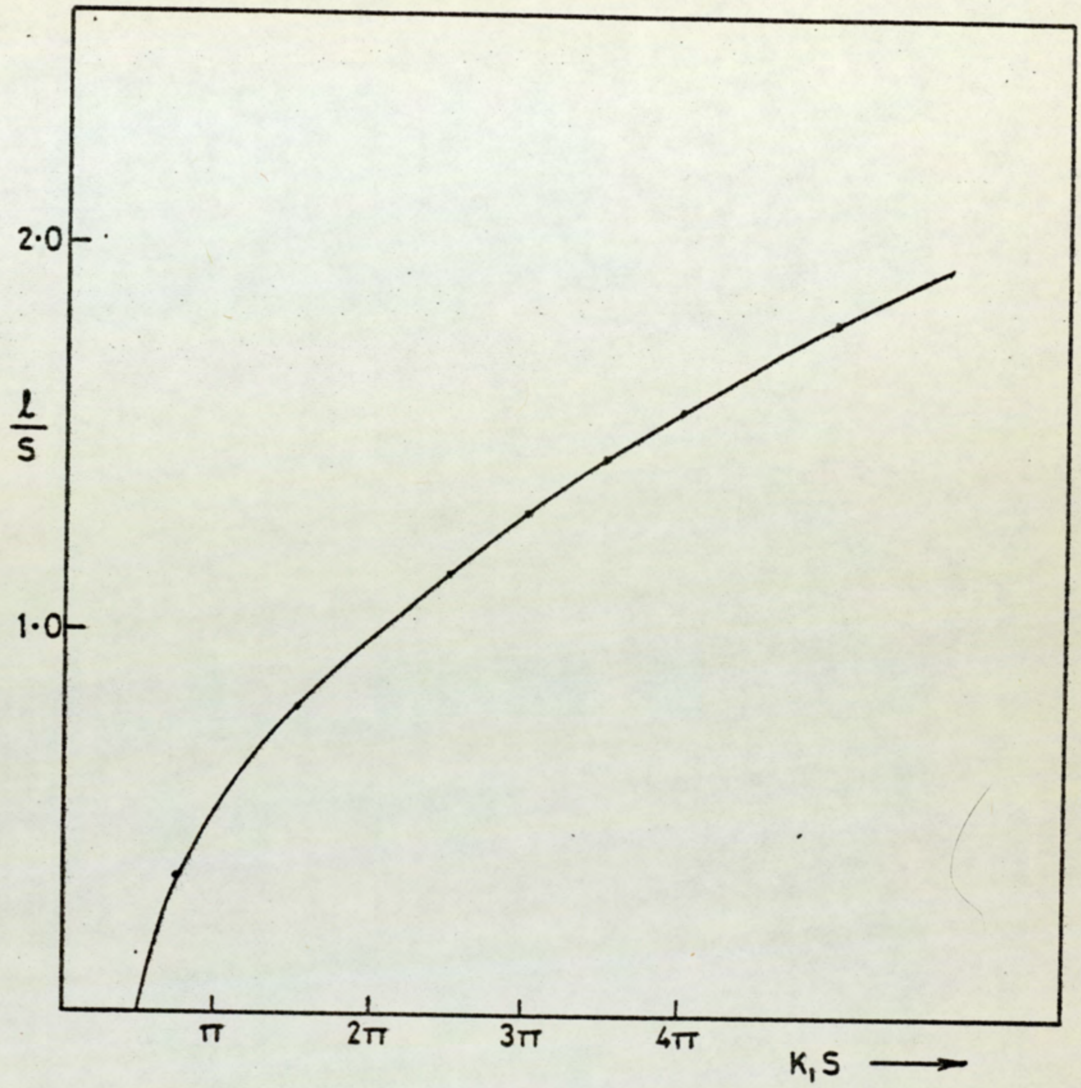

Figure 6.2 The separation distance l as a function of the correcting lens excitation parameter K_1S for a square-top field spiral distortion correction arrangement

facing each other with suitable separation between them would be the most likely system for correcting the spiral distortion.

The investigation of the characteristics of miniature high voltage single-pole projector lenses (Chapter 5) shows that the lens is very close to the optimum design when using it with the snout facing the incident electron beam. This suggests the use of this type of lens as the final projector lens in the spiral distortion correcting system. The correcting intermediate lens on the other hand is required to have a large bore to allow a larger field of view. This also allows an axial tube to contain the vacuum, so it is possible to adjust the position of the intermediate lens and its

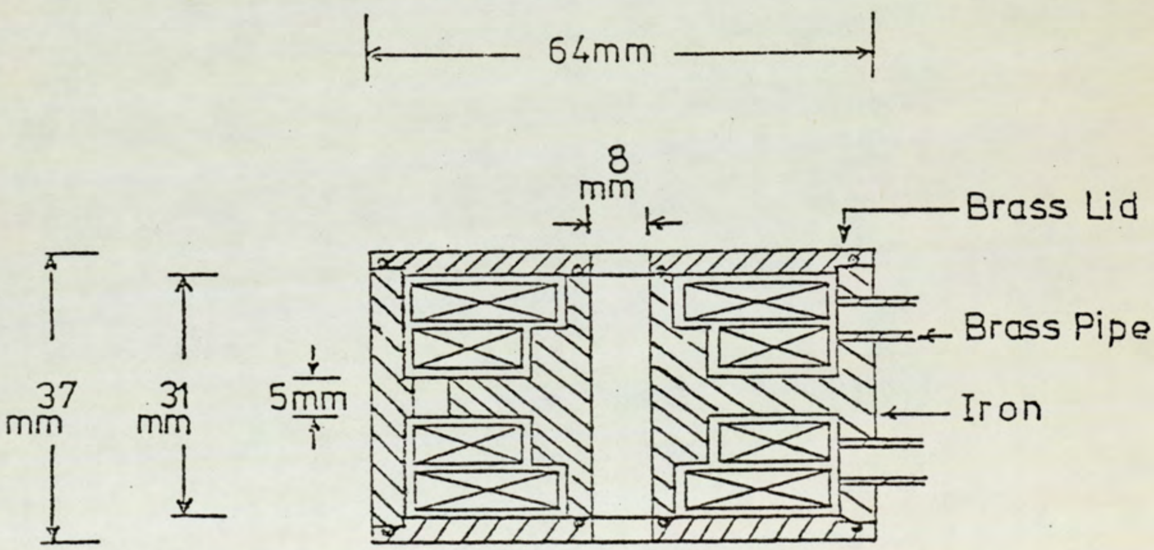

Figure (6.3). Cross-section of the miniature 100 kV double snorkel lens. Scale: full-size.

separation from the final projector lens. We found that a lens such as the 8 mm bore single-pole projector lens, designed by Juma, 1975, for the 100 KV EM6 electron microscope rotation free projector system, and shown in figure 6.3, could be used for this purpose.

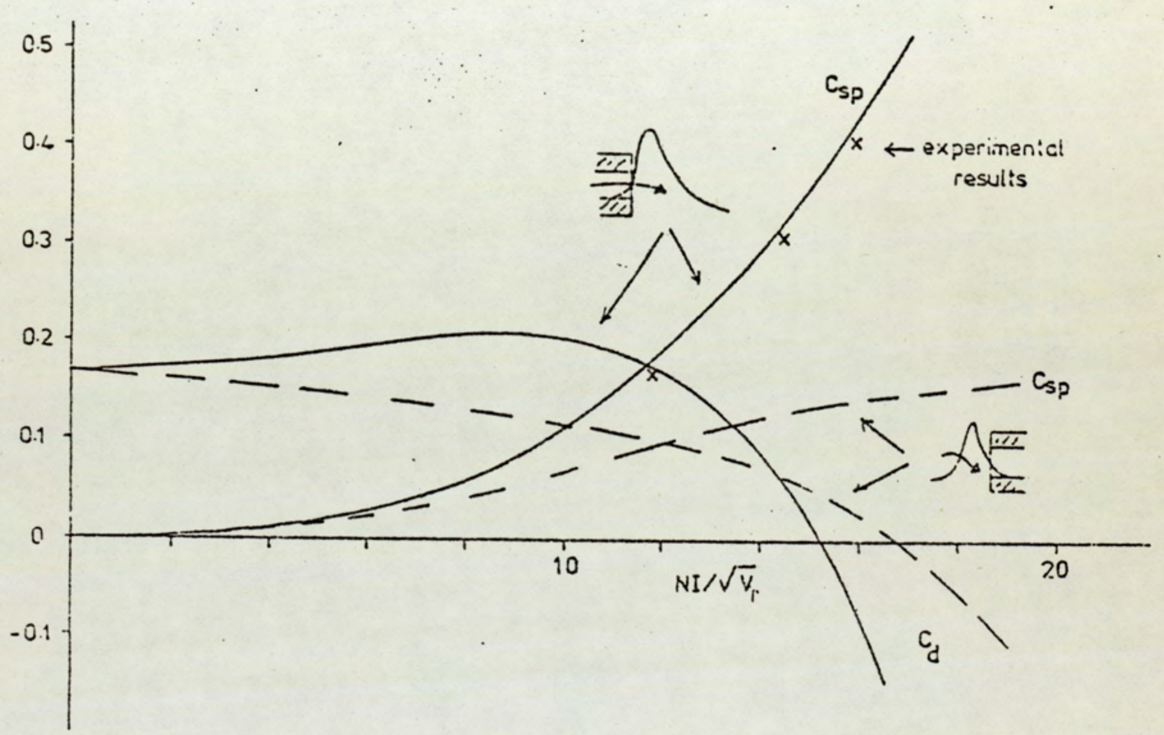

Figure 6.4. Radial and spiral distortion coefficients of the 8 mm bore single-pole lens as a function of excitation parameter $NI/V_r^{\frac{1}{2}}$, for the two modes of operation.

Figure 6.4 shows the radial and spiral distortion coefficients of this lens.

An experimental arrangement for the correcting system was designed for use on the 30 KV 'Intercol' electron optical bench, as shown in figure 6.5. A brass disc of radius 5 cm fits onto the existing specimen stage and the electron beam is allowed to go through a central brass tube, one end of which is secured to the centre of the brass disc. The inside diameter of the tube is 5 mm, and the outside one is a sliding fit in the correcting lens. A second brass disc, 1.2 cm thickness, is placed on the upper part of the tube, resting on three pillars fixed symmetrically around the centre of the lower brass disc at a diameter that allowed the correcting lens to move freely along the vertical axis of the system. The distance between the lower and the upper discs is 11 cm and the width of the correcting lens is 3.8 cm. This allows a maximum separation of 7.2 cm between the correcting lens and the upper disc. On the top of the upper disc a brass ring, thickness 1.2 cm and a 2.5 cm inner diameter, was placed to maximise the field of view to the upper projector lens. The projector lens, whose spiral distortion is to be corrected, was placed on top of the brass ring with its snout facing the correcting lens. A further brass ring of inner diameter 6 cm and width 2.5 cm was placed on top of the iron base of the projector lens. The separation between the fluorescent screen and the face of the snout of the projector lens was 5.6 cm. Four adjusting screws were provided for the alignment of the projector lens. The correcting lens could be positioned at a known distance from the projector lens.

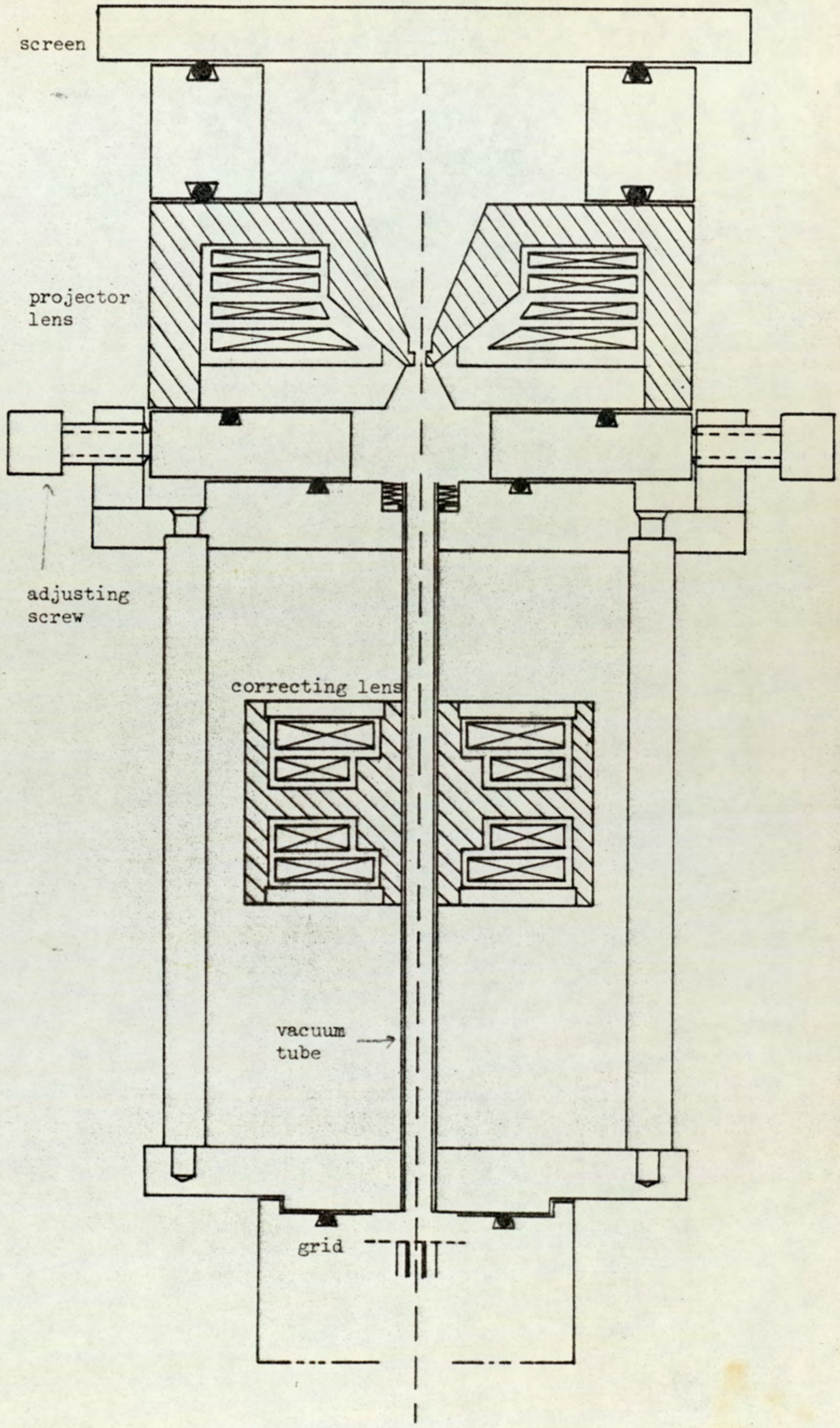

Figure 6.5 Correcting system for spiral distortion mounted on the 30 KV Intercol electron-optical bench

6.4 Experimental test of the correcting system using the 30 KV Intercol electron-optical bench

The spiral distortion correcting system described in section 6.4 was tested using the 30 KV Intercol electron-optical bench. Although the experimental arrangement was not ideal, for reasons to be mentioned later, it was sufficient to show that the correction of the spiral distortion of a projector is possible. Figure 6.6 shows a general view of the system under working conditions. The procedure was as follows:

1. The excitation of the projector lens was excited for minimum focal length ($NI/V_r^{\frac{1}{2}} = 15.5$) in order to minimise the radial distortion of the lens. The accelerating voltage was set at 10 KV for all experiments. The spiral distortion of the lens in this case is expected to be 12% at the edge of the field of view, which is limited by the back bore of the lens (see Chapter 5).

2. With the current in the correcting lens opposite to that in the projector lens, the correcting lens was gradually excited starting from a very low current up to an excitation parameter $NI/V_r^{\frac{1}{2}} = 36$. A series of photographs was taken of the image on the screen. The results will be discussed in the next section.

3. The current in the projector lens was then reversed and the same value of $NI/V_r^{\frac{1}{2}}$ as before. The correcting lens was once more excited from a low value and up to $NI/V_r^{\frac{1}{2}} = 30$. This case will give the distortion on the screen due to the sum of the distortion produced by each lens. A series of photographs was taken for comparison with the results obtained with the current in opposition.

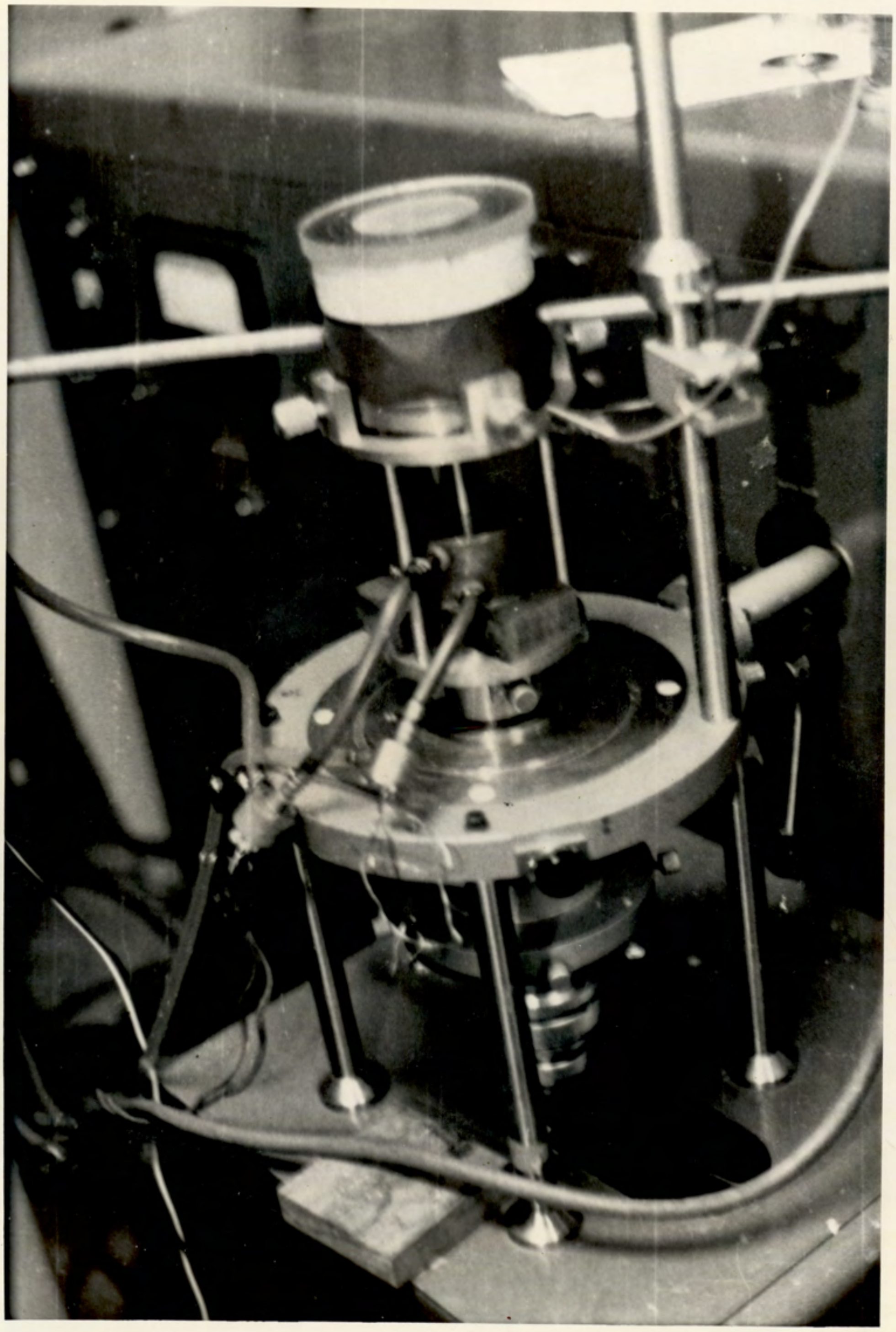

Fig.(6.6) The Intercol electron-optical bench with the spiral distortion correcting projector system.

4. A further experiment was made in which the current in the correcting lens was fixed and was opposite to that in the projector lens, but the separation of the lenses was varied, in order to find the best value for the separation.

All the experiments were made with a G 150 grid (bar thickness 60 μm, and pitch 100 μm).

The grid was located at a distance of 34 mm from the source, which was about 50 μm in diameter.

The difficulty in the experiment was: the source size (50 μm set a limit of 50 μm) to the sharpness of the image and it made it impossible to benefit from the use of grids of finer mesh.

6.5 Results and discussions of the spiral distortion correction experiment

In order to choose the best separation between correcting lens and projector lens for the correction of distortion, some preliminary calculations were carried out. The results suggest the optimum separation to be of the order of twice the minimum focal length of the correcting lens, since the ratio between the two coefficients, $D_{sp(c)}/D_{sp(p)}$ when we use the lens in the way described in section 6.4, is 3.26. Since the minimum focal length of the correcting lens is 7 mm, the required distance should be 12.6 mm; this is not easy to realise in practice, since the fields of the two magnetic lenses will cancel each other. Inspection of the two field distributions in question (figures 5.9 and 6.7) indicates that the minimum distance between the peak fields in the two lenses is 60 mm to avoid appreciable interaction. In order to make use of this separation, we must use the correcting lens at an excitation higher than that for minimum focal length, in order to make the distortion coefficient

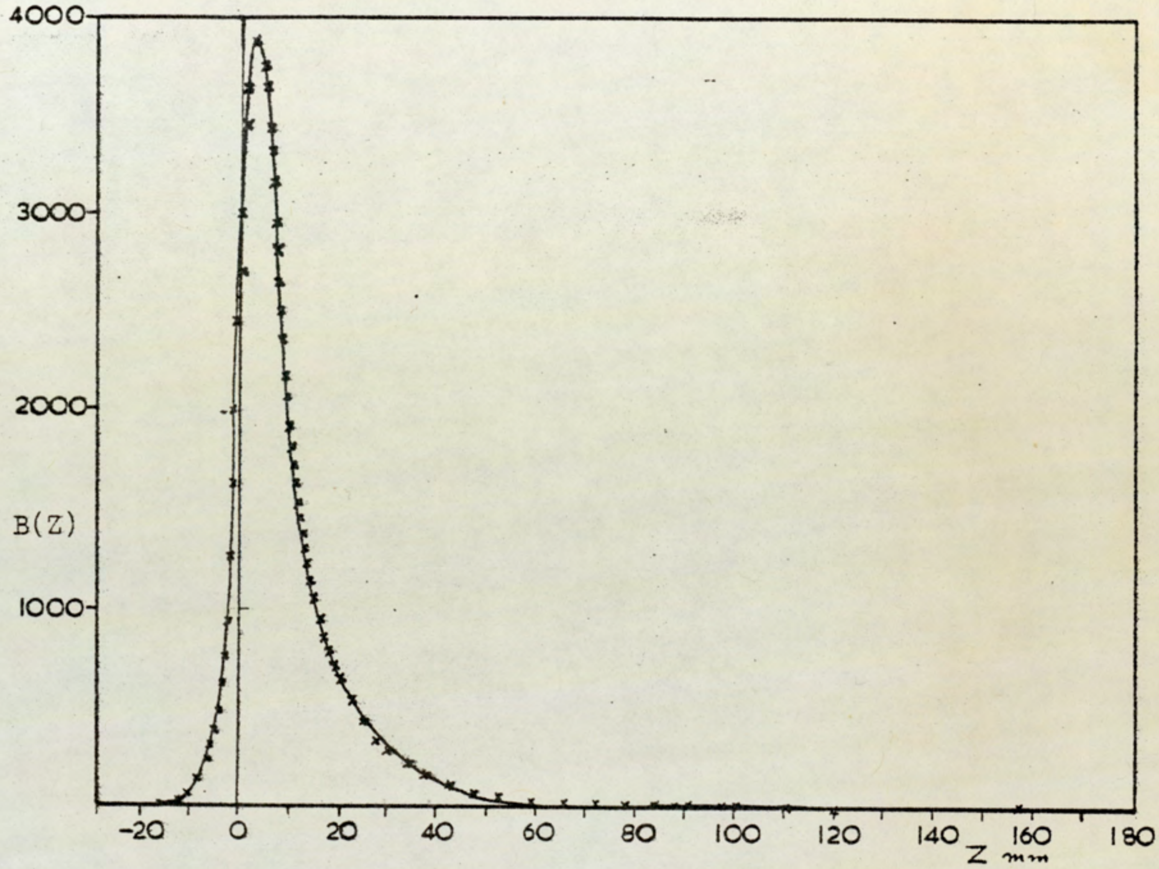

Figure 6.7 The 8 mm bore single-pole lens axial flux density distribution

of the correcting lens sufficiently high. The correcting lens must, in fact, be used in the second zone of operation in a region where the focal length is longer than the minimum value. This will make the correcting ratio factor D/M^2 larger and hence improve the possibility for correction.

Figures 6.8, 6.9 and 6.10 show a series of images for: (a) the current in the correcting lens opposite to that in the projector lens and (b) the current in both lenses in the same direction. The magnification between the prints and the screen is 1. All the results were obtained with the projector lens excitation fixed at $NI/V_r^{\frac{1}{2}} = 15.5$. In figure 6.8 the excitation parameter of the correcting lens was 0, 12 and 14 respectively. When the current is zero in the correcting lens, we get an image formed by the projector lens only at its maximum magnification. The spiral distortion measured in this case is 7.2%. This is because at the principal plane of the lens, the maximum height of the electron beam is only 3 mm, due to the limitation of the inside diameter (5 mm) of the vacuum tube. This explains why the size of the image on the screen in this case is only 41 mm in diameter, while the maximum diameter, as limited by the conical back bore of the lens, is 52.2 mm. This is clear from the second photograph in figure 6.8 in which the correcting lens was excited at $NI/V_r^{\frac{1}{2}} = 12$, enlarging the field of view of the projector lens, so we see the maximum size of the image mentioned above. Figures 6.8a and 6.8b show no great difference in spiral distortion, since the correcting lens is operating in the first zone, so it makes only a small contribution to the final image distortion.

As the excitation of the correcting lens moves from the first zone into the second zone, one can observe without too much difficulty the effect of the correcting lens itself on the spiral distortion coefficient of the projector lens. Figure 6.9 shows three exposures

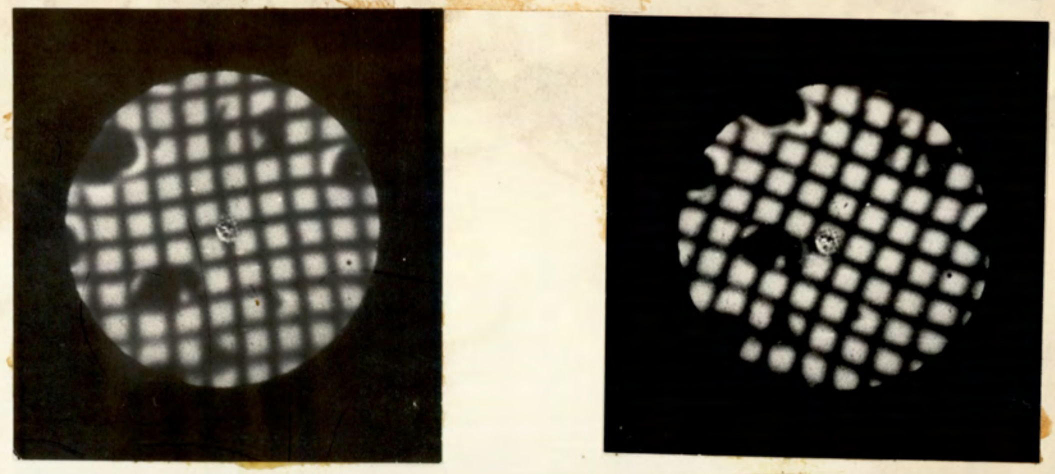

Correcting lens excitation $NI/V_r^{\frac{1}{2}} = 0$

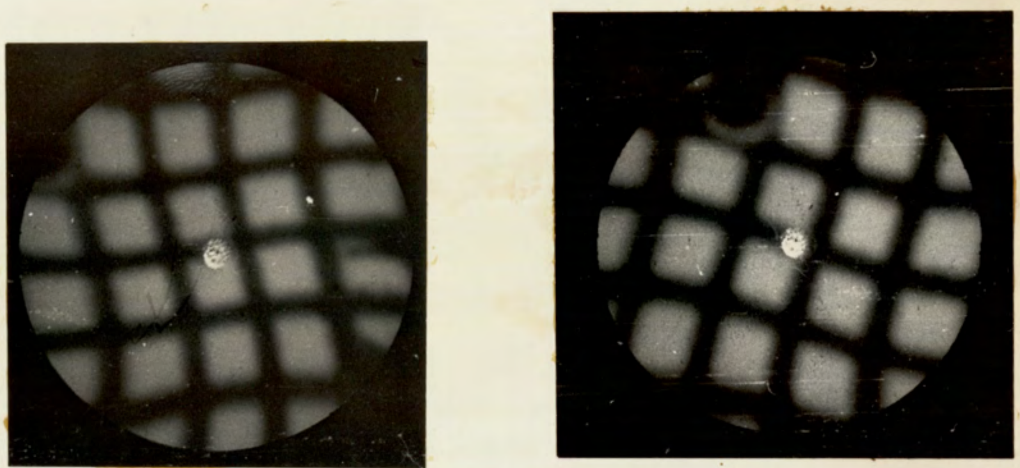

" " " $NI/V_r^{\frac{1}{2}} = 12$

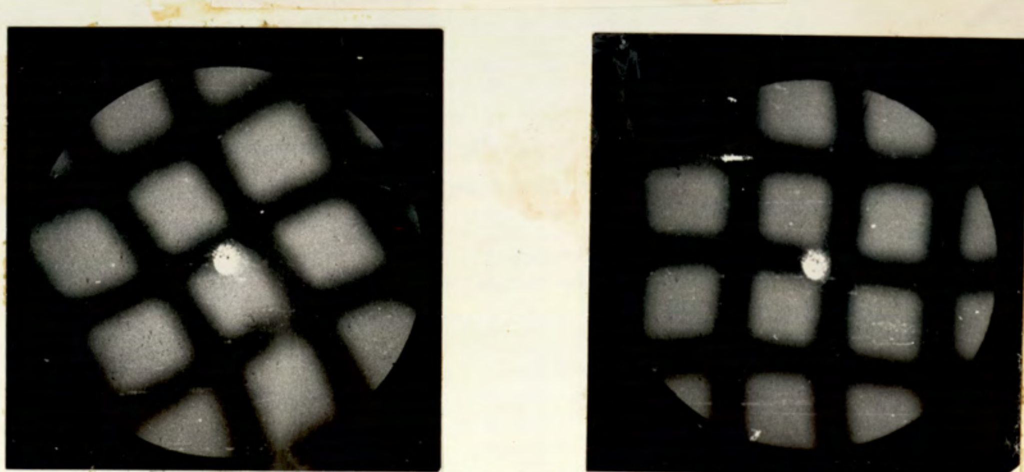

" " " $NI/V_r^{\frac{1}{2}} = 14$

a b

Fig.(6.8) Micrographs of a grid image formed by the correcting system of spiral distortion, a) the currents in the two lenses are in opposition, b) the currents are in the same direction.

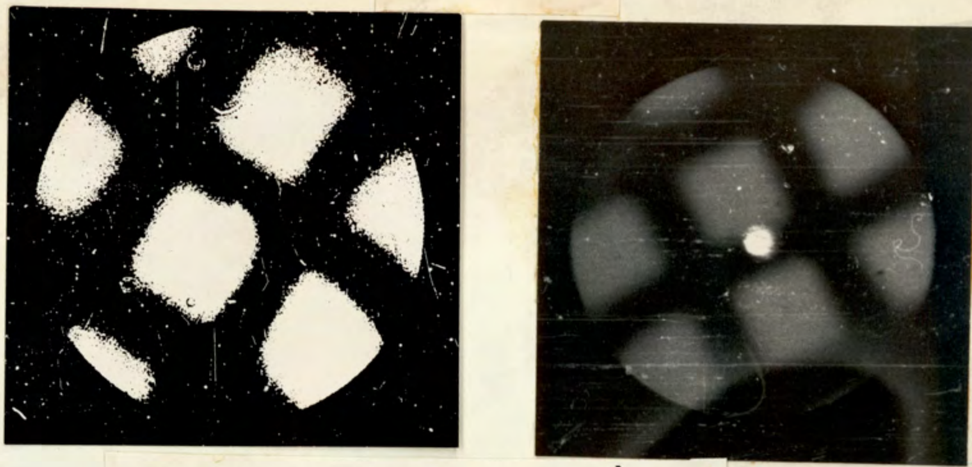

Correcting lens excitation $NI/V_r^{\frac{1}{2}} = 18$

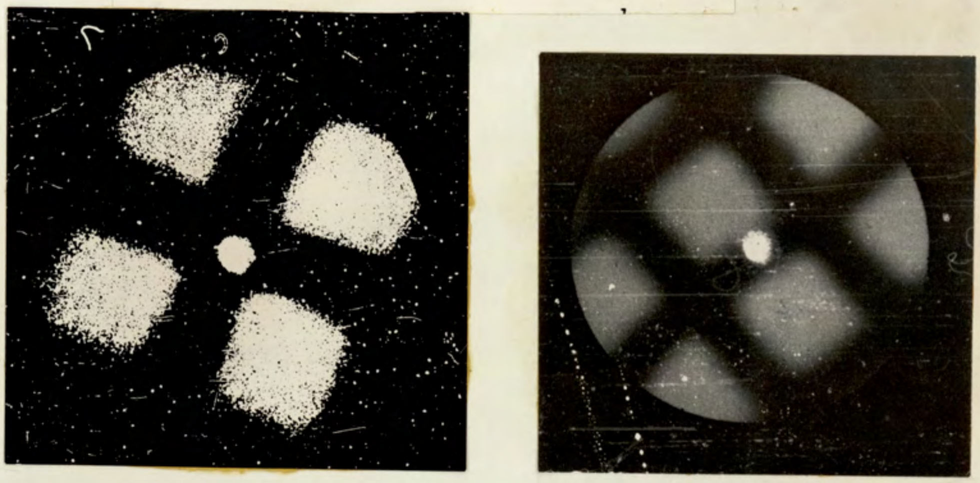

" " " $NI/V_r^{\frac{1}{2}} = 20$

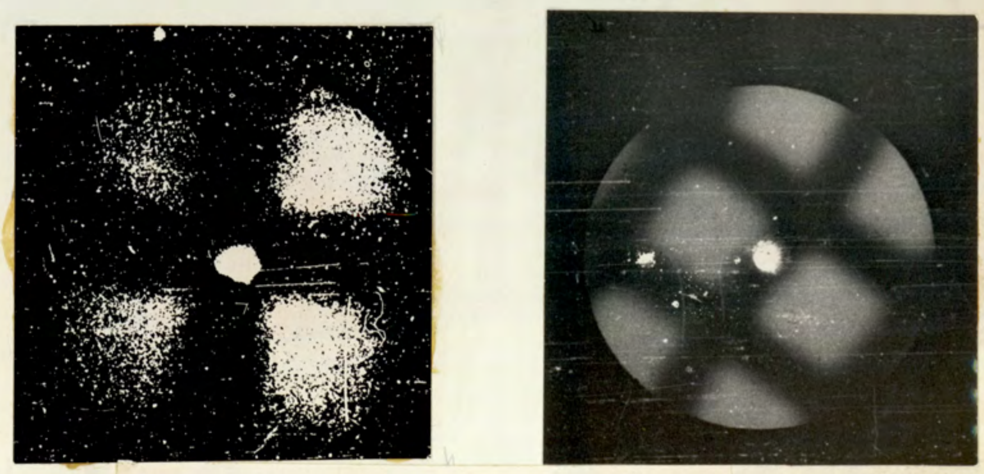

" " " $NI/V_r^{\frac{1}{2}} = 22$

a b

Fig.(6.9) Micrographs of a grid image formed by the correcting system of spiral distortion, a) the currents in the two lenses are in opposition, b) the currents are in the same direction.

corresponding to excitation parameters $NI/V_r^{\frac{1}{2}}$ = 18, 20 and 22 respectively, (a) when the current in the correcting lens is opposite to that in the projector lens, and (b) when the current in the two lenses is in the same direction. In group (a) of the photographs, it is clear that the spiral distortion is largely corrected, while in group (b), where distortion of the two lenses is additive, observable spiral distortion is appreciable. It can be seen that the magnification in the two sets of figures 6.9a and 6.9b are different, even though they correspond to the same excitation parameter $NI/V_r^{\frac{1}{2}}$. The reason for this lies in the fact that the principal plane of the correcting lens is located at different positions in the two cases, although the focal length is the same.

Figure 6.10 shows similar behaviour to that in figure 6.9. The exposures in this figure correspond to excitation parameters $NI/V_r^{\frac{1}{2}}$ = 24, 26 and 30 respectively. From figures 6.9 and 6.10, it is clear that the correction of the spiral distortion takes place over a wide range of excitation of the correcting lens and hence a wide range of magnification of the system. That means we can achieve both higher magnification and lower distortion with this system. It is noticeable also from the figures that the radial distortion in the region of low spiral distortion is also very low, because of the choice of projector lens excitation which minimises radial distortion.

Figures 6.11.1 and 6.11.2 are another two cases of correction for spiral distortion when the currents in the two lenses oppose each other. The two cases correspond to excitation parameters of the correcting lens $NI/V_r^{\frac{1}{2}}$ = 32 and 34 respectively. It is true that some radial distortion is visible, but spiral distortion is clearly corrected. For an excitation $NI/V_r^{\frac{1}{2}}$ of the correcting lens greater than 34, the spiral distortion appears to be reversed in sign, but

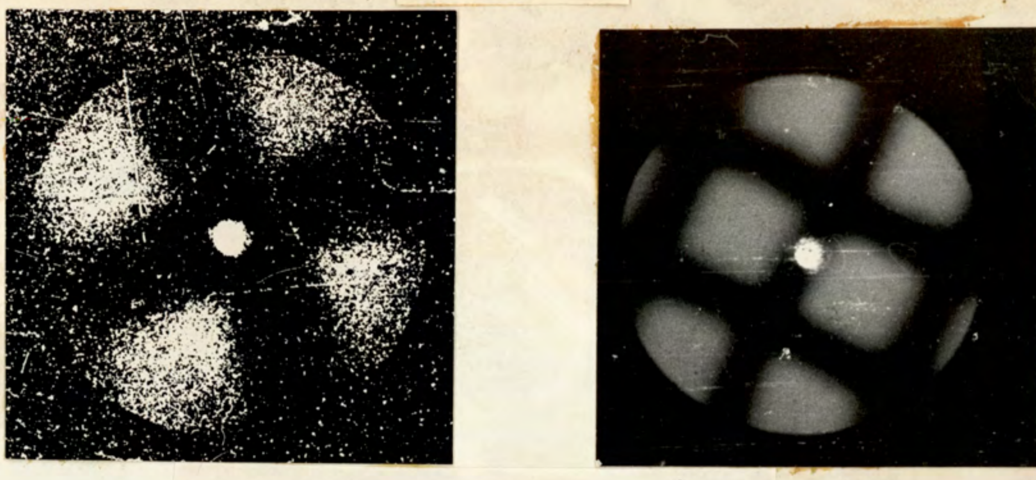

Correcting lens excitation $NI/V_r^{\frac{1}{2}} = 24$

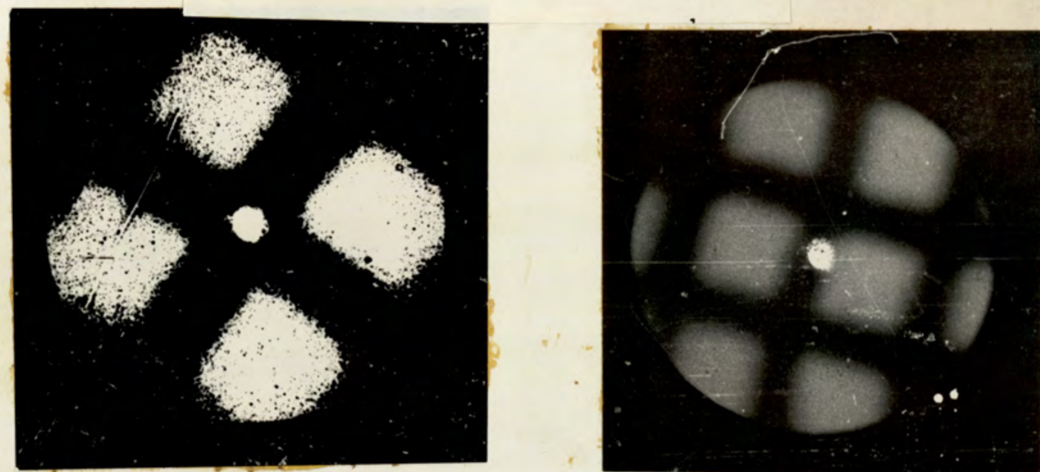

" " " $NI/V_r^{\frac{1}{2}} = 26$

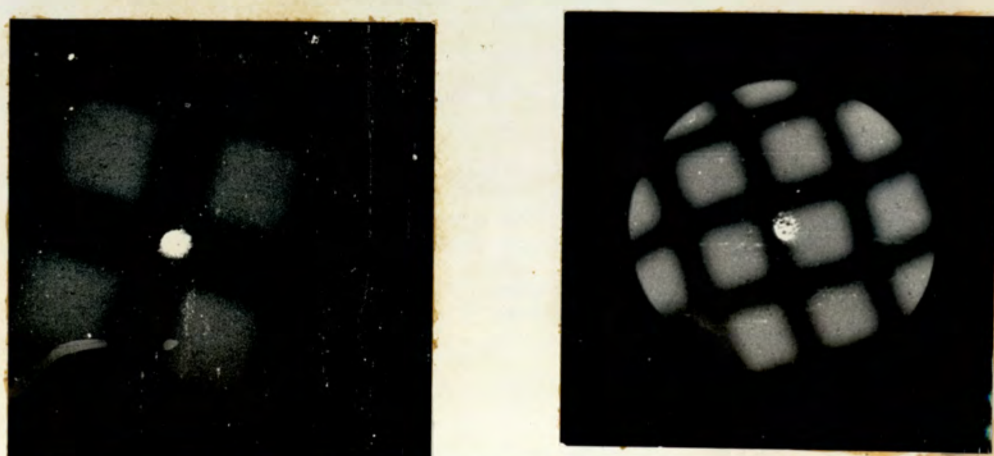

" " " $NI/V_r^{\frac{1}{2}} = 30$

a b

Fig. (6.10) Micrographs of a grid image formed by the correcting system of spiral distortion, a) the currents in the two lenses are in opposition, b) the currents are in the same direction.

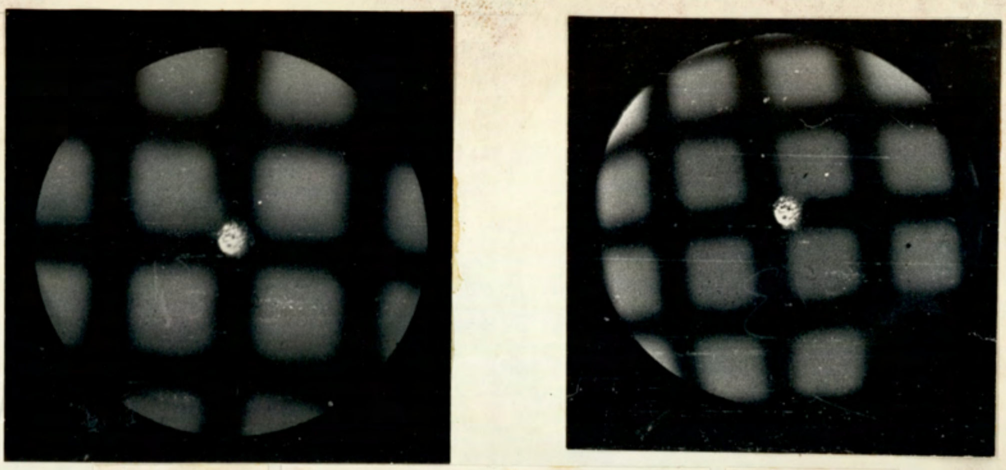

$NI/V_r^{\frac{1}{2}} = 32$ Correcting lens excitation $NI/V_r^{\frac{1}{2}} = 34$

Fig.(6.11) Micrographs of a grid image formed by the correcting system of spiral distortion, currents are in opposition.

unfortunately we could not take a satisfactory photograph, because the image was very small and the barrel distortion was very large.

The above results, although of a preliminary character, are sufficient to indicate the feasibility of correcting spiral distortion in the electron microscope by using a similar projector system to that described. The study of the different lenses available indicates that the use of two single-pole lenses is the most favourable choice for the correction process. A full-scale trial on an electron microscope is now required to determine the best arrangement.

However, the arrangement we used in this experiment, namely the placing of the correcting lens before the lens to be corrected, seems to be much better than that suggested by Hillier (1945) for the correction of radial distortion, in which the correcting lens is placed at the focal point of the lens to be corrected, which is excited by the same number of ampere-turns. As well as the loss of refracting power in this method, the spiral distortion cannot be reduced by more than 50% as we can see by applying this method to the rectangular field distribution.

Another important thing in this experiment is the short projector distance used with this system. By a similar arrangement in the TEM we should be able to obtain an image size 12 cm in diameter at a projection distance about 15 cm from the snout of the projector lens or 12 cm from the back face of the lens near to the screen. This is of great importance, especially for the high voltage electron microscope in which this distance is at present about 50 cm. This would mean a five-fold reduction in the length of the viewing chamber.

7. CONCLUSION

The calculations contained in this thesis for conventional double-pole lenses show that there is no optimum design for projector lenses. Moreover, the analysis made for the square-top field distribution explains why it is difficult to use such lenses, in a system for correcting the spiral distortion of the final image in electron microscope.

For iron-free coils which are related to superconducting lenses, similar calculations show that there is no optimum shape of the coil when used as a projector even though an optimum design exists for such lenses as objectives. On the other hand, the calculations and experiments indicate that single-polepiece lenses have unique advantages as projector lenses. The present investigation has shown that it is possible to provide a theoretical basis for understanding such lenses. Both calculations and experiments show that single-pole lenses can be used with advantage either as projectors or objectives. They can even be used as condenser-objective lenses as described by Riecke and Ruska in 1966.

The calculations indicate that the properties of single-pole lenses can be predicted to a first approximation, making use of the properties of the mathematical exponential field distribution studied extensively in this thesis.

As a result, the correction of spiral distortion in the electron microscope now appears feasible with an arrangement of the final projector stage in which two single-pole lenses face each other. The experiments carried out on the Intercol electron optical bench, showed clearly the feasibility of correcting spiral distortion of the final projector lens, but has not answered all the relevant questions, since the results were limited by the time and facilities available. A full-scale experiment in the electron microscope itself is, therefore, needed for the determination of the optimum arrangement for correcting spiral distortion.

8. REFERENCES

Basset, R. and Mulvey, T. (1969) Zeitschrift für angewandte Physik, 27 Band, 3 Heft, 1969, S.142-145.

Der-Schwartz, G.V. and Makarova, I.S. (1968), Radio Engineering and Electronic Physics, Vol.13, No.7, 1100-1103.

Durandeau, P and Fert C. (1957), Rev.Opt.Theor.Instrum. 36, 205-234.

Glaser, W. (1933), Z.Physik 81, 647.

Glaser, W. (1941b), Z.Physik, 118, 264

Glaser, W. (1952), Grundlagen der Elektronenoptik, pp.306-307, Springer.

Grivet, P. (1972), Electron Optics, pp. 164-170, Pergamon Press.

Hawkes, P.W. (1972), Electron Optics and Electron Microscopy, pp. 70-71, Taylor and Francis Ltd.

Herrman, K.H., Ihmann, K. and Krahl, D. (1974), Eighth International Congress on Electron Microscopy, Canberra, Vol.1, pp.132-133.

Hillier, J. (1946), J.App.Phys. 17, 411-419.

Juma, S.M. (1974), Private Communications, Aston University.

Juma, S.M. and Mulvey, T. (1974), Eight International Congress on electron Microscopy, Canberra, Vol.1, 134-135.

Juma, S.M. (1975), Ph.D. Thesis, The University of Aston in Birmingham.

Juma, S.M. and Mulvey, T. (1975), EMAG 75, Bristol, 45-48

Kamminga, W., Verster, J.L. and Franken, J.C. (1968), Optik 28, 442-461.

Kynaston, D. and Mulvey, T. (1963), Journal of Applied Physics, 14, 199-206

Liebmann, G. (1952). Proc.Phys.Soc. B 65, 94-108

Liebmann, G. and Grad, E.M. (1951), Proc.Phys.Soc. B 64, 956-971.

Marai, F.Z. (1973), M.Sc. thesis, Physics Dept., The University of Aston in Birmingham.

Marai, F.Z. and Mulvey, T. (1974), Eighth International Congress on Electron Microscopy, Canberra, Vol.1, 130-131.

Marai, F.Z. and Mulvey, T. (1975), EMAG 75, Bristol, 43-44.

Marai, F.Z. and Mulvey, T. (1977), Ultramicroscopy, North Holland (In the press)

Moses, R.W. (1972), Proc.Fifth European Congress in Electron Microscopy, 1972.

Mulvey, T. (1967), Focusing of charged particles, Vol.1, Chapter 26, Academic Press Inc., New York.

Mulvey, T. (1971), Electron Microscopy and Analysis, Proc.25th Anniversary Meeting of EMAG.

Mulvey, T. (1974), Proc.Seventh Annual Scanning Electron Microscopy Symposium, Chicago, Illinois, U.S.A., pp. 43-49.

Mulvey, T. and Newman, C. (1972), Fifth European Congress on Electron Microscopy, pp. 116-117.

Mulvey, T. and Newman, C.D. (1973a), Scanning electron microscopy: System and Applications, pp.16-21, Institute of Physics.

Mulvey, T. and Newman, C.D. (1973b), Proc.Third Int.Conf.H.V. Microscopy, Oxford 1973, Academic Press 1974.

Mulvey, T. and Wallington, M. (1969), J.Sci.Inst. (J.of Physics E) Vol.2.

Mulvey, T. and Wallington, M.J. (1973), Rep.Prog.Phys. 36, 347-421.

Munro, E. (1972), Ph.D. Thesis, Cambridge.

Newman, C.D., (1976), Ph.D. Thesis, The University of Aston in Birmingham.

Riecke, W.D. and Ruska, E. (1966), Sixth Int.Cong. for Electron Microscopy, Kyoto, 19-20.

Scherzer, O. (1936), Z.Phys. 101, 593-603.

Scherzer, O. (1937) in "Beiträge zur Elektronenoptik" ed. H. Busch and E. Brüche, J.A. Barth, Leipzig, pp. 33-41.

Tretner, W. (1959), Optik, 16, 155.

Trowbridge, C.W. (1972) with Newman, M.J., Turner, L.R., Proc. 4th Int.Conf. on Magnet Technology, Brookhaven.

Yada, K. and Kawakatsu, H. (1976), J.Elec.Microsc. 25, 1, pp. 1-9.

APPENDICES

Appendix 1 : 'Electron optical characteristics of single-pole magnetic lenses' (A paper published in the Eight International Congress on Electron Microscopy, Canberra, 1974

ELECTRON OPTICAL CHARACTERISTICS OF SINGLE-POLE MAGNETIC LENSES

F.Z. Marai and T. Mulvey

Department of Physics, The University of Aston
in Birmingham B4 7ET (UK)

Single-pole magnetic lenses may be employed advantageously both as objectives[1] or projectors[2] in the electron microscope. The advantages of such lenses arise from their essentially different axial flux density distribution from those of normal twin-polepiece lenses. For this reason their electron-optical properties cannot be predicted from the data of conventional lenses, the focal properties of single-pole lenses being more closely related to those of partially shrouded helical coils[3]. As an illustration, consider the simple 100kV objective lens of this type shown in Figure 1(a), in which a flat, helical winding of mean diameter 37.5mm is placed inside a short iron cylinder closed off at one end by an iron plate, in which an axial hole of 5mm diameter allows passage of the illuminating beam and manipulation of the specimen placed in close proximity to the surface of the iron. Under these conditions a lens excitation of 4,300A-t is required at 100kV to form an image of the specimen at high magnification. The corresponding axial flux density distribution is shown in Figure 1(b). The full line shows the axial flux density distribution as measured by a Hall-effect probe on a twice-full size model of the lens. The chain-dotted line shows the flux density distribution calculated from the Biot-Savart Law, assuming that the iron screen consists of a plane sheet of infinite permeability. The validity of this assumption has been established by experiments which show that the presence of the iron cylinder has a negligible effect on the axial flux density distribution. A close inspection of the measured and calculated field distribution shows that the measured flux density in the region of the specimen is higher than that calculated, in spite of the effect of the hole; moreover the peak has been pushed forward into the lens. These effects can be ascribed entirely to the effect of the iron 'snout' or single polepiece, 20mm in diameter, which protrudes 1mm into the lens. If the polepiece were of a smaller diameter the peak axial flux density would increase appreciably. A similar result would occur if the hole were made smaller. In Figure 1(b) the crosses indicate a flux density distribution that falls off exponentially with axial distance z according to the Law $B(z) = \exp(-az)$ where a is a constant. This suggests that the little-known exponential field model[4] might be useful in calculating the properties of single-pole lenses. The focal properties of the lens in Figure 1(a) were therefore calculated using both the measured and the calculated field distributions. The results, which were approximately the same for either distribution are shown in Figure 2. The focal properties differ from those of conventional lenses. For example, the minimum objective and projector focal lengths are the same, namely 10mm and occur at z=0, corresponding to an excitation parameter $NI/V_r^{1/2}$ of 13, where NI is the ampere-turns and V_r the relativistically corrected accelerating voltage. For greater excitations the objective focal length is constant. This also applies to the chromatic aberration coefficient C_c =6mm and the spherical aberration coefficient C_s =3mm, remarkably low values considering that the peak flux density is only 0.16 Tesla (1,600 gauss). Glaser in his brief treatment[4] of the exponential field calculated the minimum objective focal length and chromatic aberration but did not derive the general focal properties or the spherical aberration coefficient. This can be done most conveniently by numerical methods using a digital computer. The resulting focal properties are shown in Figure 3. It is convenient to express the axial field distribution as $B(z)=B_{max}\exp-[(\ln 2)/d]z$ where d is the axial distance from the position of the maximum B_{max} to where the field has fallen to half

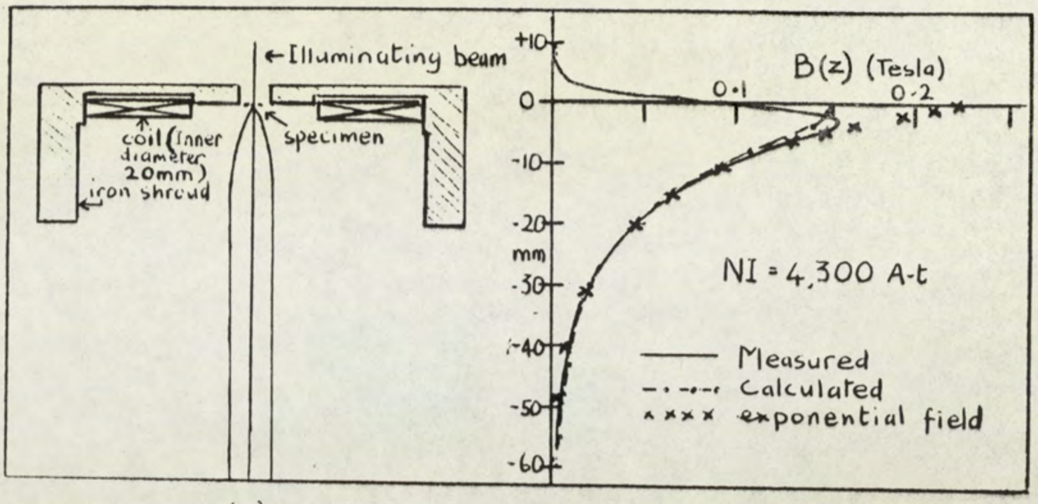

(a) (b)

FIG.1.

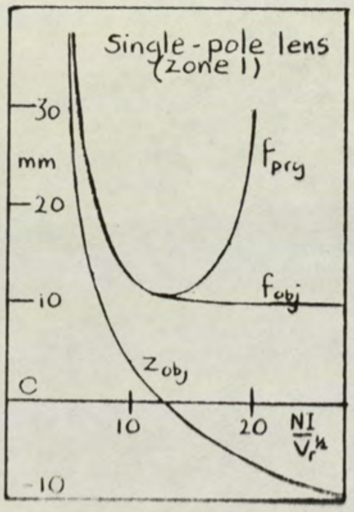

FIG. 2.

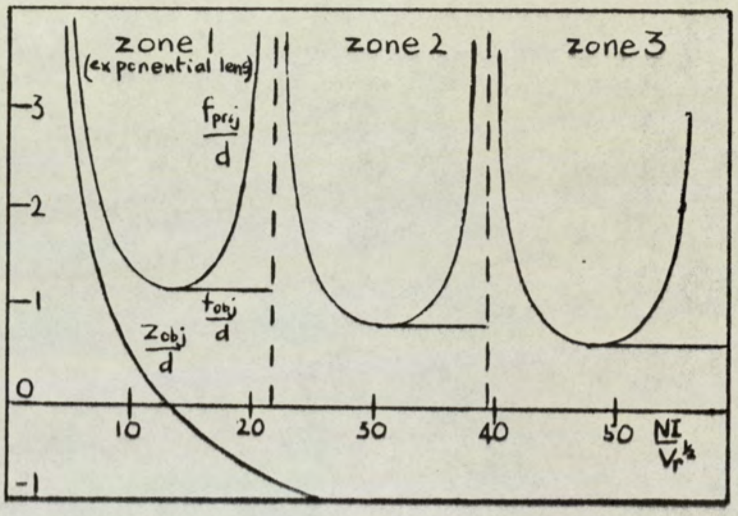

FIG. 3.

this value. Figure 3 shows the objective focal length f_{obj}, the projector focal length f_{prj} and the objective focal distance Z_{obj} as a function of the excitation parameter $NI/V_r^{½}$. The curves show a remarkable similarity to those of Figure 2. In particular, in the first zone, the minimum projector focal length equals 1.156d and occurs at an excitation parameter $NI/V_r^{½}=13$. As a check on the accuracy of the computer program, the value of C_c was calculated numerically. The result, $C_c=0.722d$ is in good agreement with the analytical solution, $C_c=0.721d$. Thus $C_c/f = 0.632$. Numerical calculation of C_s by Scherzer's formula gave $C_s=0.363d$, i.e. $C_s/f = 0.315$, an acceptably low value. Improved lens performance can be obtained in practice by replacing the short flat polepiece by a short cone of large apex angle. If the peak axial flux density and half-width can be measured experimentally, the exponential-field model can be used to provide a useful first approximation to the focal properties.

References.
1. Mulvey, T. These Proceedings
2. Juma, S.M. and Mulvey, T. These Proceedings
3. Mulvey, T. and Wallington, M.J. Rep.Progr.Phys. 36 347-421 (1973)
4. Glaser, W. Grundlagen der Elektronenoptik 306-307 Springer (1952)

APPENDICES

Appendix 2 : 'Electron optical characteristics of single-pole and related magnetic electron lenses' (A paper published in the Electron Microscopy and Analysis Group Conference EMAG 75 held in Bristol 1975)

ELECTRON-OPTICAL CHARACTERISTICS OF SINGLE-POLE AND RELATED MAGNETIC ELECTRON LENSES

F.Z. Marai and T.Mulvey

Department of Physics, The University of Aston in Birmingham, B47ET, England.

In a single-pole magnetic lens the axial magnetic field is strongly concentrated by a single polepiece, rather than by two closely spaced polepieces. Such lenses, especially when used in conjunction with miniaturized coil windings,can be used to advantage in electron microscopes(Juma and Mulvey,1975). These lenses can produce high axial field strengths and small "half-widths" of the field distribution resulting in lower aberrations than those of conventional lenses. In order to make a general appraisal of the electron-optical properties of such lenses,it has been found convenient to make use of the exponential field model (Glaser,1952). A brief treatment of the paraxial properties of this model has already been given (Marai and Mulvey 1974). Here the treatment is extended to include chromatic and spherical aberration and to point out the advantages that may be gained in electron microscopy by exploiting the asymmetry of the field distribution. Figure 1 shows the exponential axial field distribution which is of the form $B_z = B_o \exp -\left(\overline{\ln 2}/d\right) z$ where d is the "half-width" of the field distribution and B_o is the maximum value of the axial field. Two electron trajectories are shown. Trajectory 1 is for an excitation parameter $NI/V_r^{1/2}=13$ which is just sufficient to cause the electron to cross the axis within the field. Figure 2 shows the focal properties, chromatic aberration coefficient C_c and spherical aberration coefficient C_s in terms of the half width d as a function of the excitation parameter $NI/V_r^{1/2}$, for rays entering the field in the way shown in Figure 1, namely from the side of positive z values. For values $NI/V_r^{1/2} > 13$, the focal properties, with the exception of the focal distance Z_{obj}, do not vary with excitation.

Projector Lenses. Because of the asymmetry of the field distribution, the focal properties and aberrations differ if the electron beam enters from the side of negative z values. Figure 3 shows the radial (D_r) and the spiral (D_{sp}) distortion coefficients, as defined for example in Hawkes (1972),for the two directions of entry of a parallel electron beam into the lens. These coefficients are closely related to the corresponding coefficients for conventional polepiece lenses. The curves of Figure 3 show that the most favourable arrangement for low distortion is for the electron beam to enter the field as shown in Figure 1. These principles are relevant to the design of single-pole projector lenses which can have appreciably lower distortion coefficients than those of the best double-polepiece lenses.

Single-pole condenser-objective. Figure 4 shows the telescopic ray path through an exponential field. This occurs when $NI/V_r^{1/2} = 20.6$. By placing a specimen at a distance Z = 0.7d along the axis a strong pre-field is created followed by an imaging field of low aberrations in a similar manner to that achieved by the condenser-objective of Riecke and Ruska. There are two possible directions for the illuminating beam, the preferred direction being determined by the operational requirements of a particular microscope. Tests are now proceeding to evaluate the application of single-polepiece lenses in both STEM and TEM.

References.Glaser,W.(1952) "Grundlagen der Elektronenoptik" pp 306-307 Springer, Berlin. Hawkes, P.(1972) "Electron Optics and Electron Microscopy" pp 67-71. Taylor and Francis, London. Juma,S.M. and Mulvey,T. These Proceedings, p.45. Marai,F.Z. and Mulvey T.(1974)"Electron Microscopy 1974".(Sanders and Goodchild,Eds)Vol.I,pp.130-131. Australian Acad.Sci. Canberra.

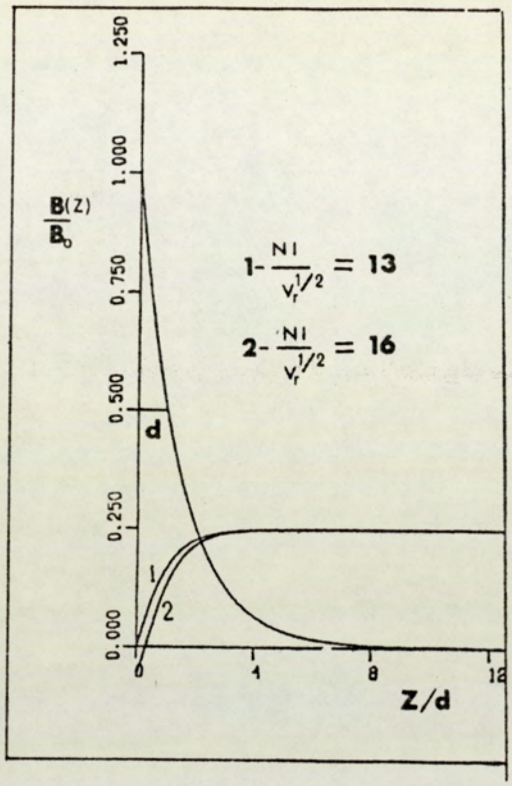

Fig.1. Exponential field model. Maximum field B_o, half-width d.

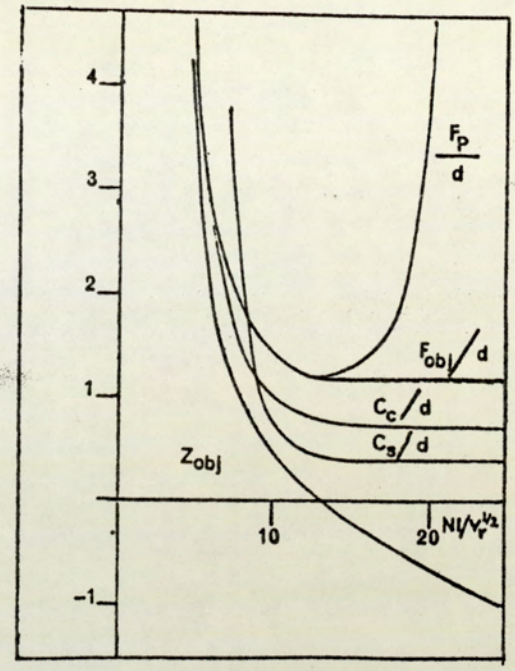

Fig.2. Focal properties and aberrations of exponential field model.

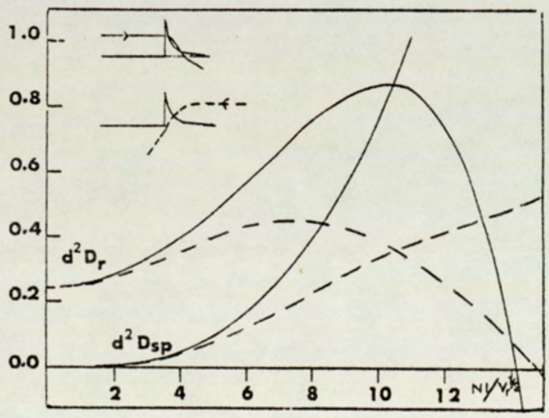

Fig.3. Radial (D_r) and spiral (D_{sp}') distortion coefficients

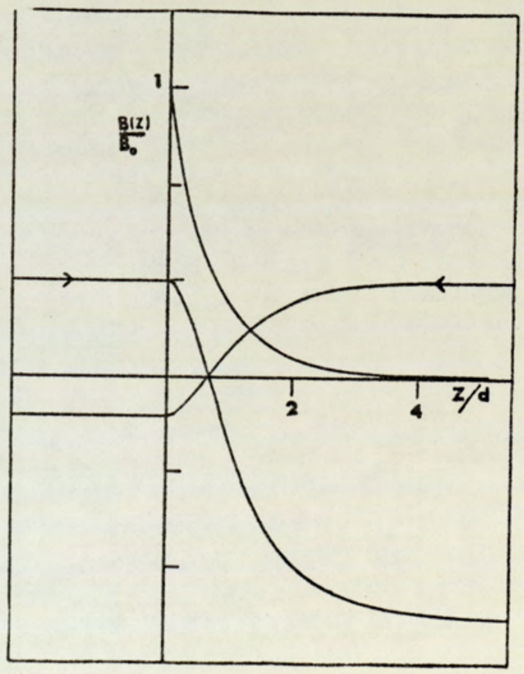

Fig.4. Exponential field model as a condenser-objective.

APPENDICES

Appendix 3 : 'DATA-BZ' computer program

```
      TRACE 1
      READ FROM (CR)
      MASTER
C     THE PROGRAM USES THE MEAN VALUE OF AZ BETWEEN THE TWO Z INTERVALS TO
C     CONSTRUCT THE ELECTRON TRAJECTORY USING THE PARAXIAL RAY EQUATION
      DIMENSION A1(112),A2(112),A10(112),A11(112),A20(112),A22(112),
     1AS(112),AP(112),AZ(112),BZ(112),AZA(112),X(112)
      DIMENSION G1(111),F1(111),F2(111),R(111),R1(111)
      G=SQRT(1.6*10.**(-19.)/(9.1*(10.**(-31.))*8.))
   99 DO 5 K=1,112
      READ(1,3)X(K),BZ(K)
    3 FORMAT(F8.4,F8.2)
      AZ(K)=BZ(K)/(12086.*10**4.)
      IF(K.EQ.1) GO TO 6
      AZA(K)=(AZ(K)+AZ(K-1))/2.0
    6 WRITE(2,20)X(K),AZ(K),BZ(K)
   20 FORMAT(1H ,3X,F8.4,8X,F14.11,8X,F8.2)
    5 CONTINUE


    9 READ(1,11)R0,R01,V
   11 FORMAT(2F4.1,F10.1)
      IF(V)15,0,1
      P1=12086.2/SQRT(V)
      WRITE(2,111)R0,R01,P1,V
  111 FORMAT(1H1,3X,F11.8,8X,F14.8,8X,F7.4,8X,F10.1)
      DO 7 K=2,112
      Z0=(X(K)-X(K-1))/100.0
      G1(K)=G*AZA(K)*P1
      F1(K)=COS(G1(K)*Z0)
      F2(K)=SIN(G1(K)*Z0)
      R(K)=R0*F1(K)+R01*F2(K)/G1(K)
      R1(K)=R01*F1(K)-G1(K)*R0*F2(K)
      WRITE(2,500)X(K),AZA(K),R(K),R1(K)
  500 FORMAT(1H ,3X,F8.4,8X,F14.11,8X,F11.8,8X,F14.8)
      R0=R(K)
      R01=R1(K)
      IF(K.LT.112) GO TO 7
      FPROJ=1./R1(K)
      WRITE(2,900)FPROJ
  900 FORMAT(1H ,20X,F12.7)
    7 CONTINUE
      GO TO 9
   15 STOP
      END
```

APPENDICES

Appendix 4 : 'D ABERRATION' computer program

```
      TRACE 1
      READ FROM (CR)
      MASTER
C     THE PROGRAM USES THE MEAN VALUE OF AZ BETWEEN THE TWO Z INTERVALS TO
C     CONSTRUCT THE ELECTRON TRAJECTORY USING THE PARAXIAL RAY EQUATION
      DIMENSION A1(112),A2(112),A10(112),A11(112),A20(112),A22(112),
     1AS(112),AP(112),AZ(112),BZ(112),AZA(112),X(112)
      DIMENSION G1(111),F1(111),F2(111),R(111),R1(111)
      DIMENSION AZC(112),AZ1(112),AZ1C(112),RA(112),RAC(112),RAS(112),
     1R1AC(112),R1A(112),H(112)
      G=SQRT(1.6*10.**(-19.)/(9.1*(10.**(-31.))*8.))
   99 DO 5 K=1,112
      READ(1,3)X(K),BZ(K)
    3 FORMAT(F8.4,F8.2)
      AZ(K)=BZ(K)/(2985.*10**4.)*0.8525
      IF(X(K).EQ.+00.2250)AZM=AZ(K)
      IF(K.EQ.1)GO TO 5
      AZA(K)=(AZ(K)+AZ(K-1))/2.0
      AZC(K)=AZA(K)**2.
      AZ1(K)=(AZ(K)-AZ(K-1))/(X(K)-X(K-1))*100.0
      AZ1C(K)=AZ1(K)*AZ1(K)


    5 CONTINUE
      WRITE(2,300)AZM
  300 FORMAT(1H0,10X,5H AZM=,F14.11)
      WRITE(2,500)
  500 FORMAT(1H1,8X,3H ZF,5X,9H NI/VT1/2,8X,3H CC,14X,3H CS,13X,5H FOBJ,
     111X,4H CSM,10X,6H FOBJM)
    9 READ(1,11)R0,R01,P1
   11 FORMAT(2F4.1,F5.1)
      IF(P1)13,0,0
      AB1=(G*P1)**2.
      AB2=3.*AB1
      AB3=AB1/2.
```

```
      DO 7 K=2,112
      ZU=(X(K)-X(K-1))/100.0
      G1(K)=G*AZA(K)*P1
      F1(K)=COS(G1(K)*ZU)
      F2(K)=SIN(G1(K)*ZU)
      R(K)=R0*F1(K)+R01*F2(K)/G1(K)
      RA(K)=(R(K)+R(K-1))/2.
      RAC(K)=RA(K)*RA(K)
      RAS(K)=RAC(K)*RAC(K)
      R1(K)=R01*F1(K)-G1(K)*R0*F2(K)
      R1A(K)=(R(K)-R(K-1))/(X(K)-X(K-1))*100.0
      R1AC(K)=R1A(K)*R1A(K)
      H(K)=R1AC(K)/RAC(K)
      IF(R(K))31,31,28
   31 U1C=R1AC(K)
      FOBJ=1./R1A(K)
      ZF=X(K)
      GO TO 29
   28 R0=R(K)
      R01=R1(K)
      IF(K.LT.112) GO TO 7
      U1C=R1AC(K)
      FOBJ=1./R1A(K)
      ZF=X(K)
    7 CONTINUE
   29 U1S=U1C*U1C
      FC=0.0
      FS=0.0
      DO 10 K=2,112
      DX=(X(K)-X(K-1))/100.0
      FC=FC+AZC(K)*RAC(K)*DX
      FS=FS+(AZ1C(K)+AB2*(AZC(K)**2.)-H(K)*AZC(K))*RAS(K)*DX
      IF(R(K))27,27,10
   10 CONTINUE
   27 CC=(AB1*FC)/U1C
      CS=(AB3*FS)/U1S
      CSM=CS*AZM*(10.**6.0)*P1
      FOBJM=FOBJ*AZM*(10.**6.0)*P1
      WRITE(2,112)ZF,P1,CC,CS,FOBJ,CSM,FOBJM
  112 FORMAT(1H ,5X,F8.4,5X,F5.1,5X,F12.7,5X,F12.7,5X,F12.7,5X,F10.5,5X,
     1F10.5)
      GO TO 9
   15 STOP
      END
```

APPENDICES

Appendix 5 : 'D DISTORTION' computer program

```
      TRACE 1
      READ FROM (CR)
      MASTER
      DIMENSION A1(112),A2(112),A10(112),A11(112),A20(112),A22(112),
     1AB(112),AP(112),AZ(112),BZ(112),AZA(112),X(112)
      DIMENSION G1(111),F1(111),F2(111),R(111),R1(111)
      DIMENSION AZC(112),AZ1(112),AZ1C(112),RA(112),RAC(112),RAS(112),
     1R1AC(112),R1A(112),H(112),AZD(112),RAD(112),GA(112),AZM(112)
      DIMENSION XM(112),GM(112),FM1(112),FM2(112),RM(112),RMA(112),RM1(1
     112)
      S=SQRT(1.6*10.**(-19.)/(9.1*(10.**(-31.))*8.))
      SIGMA=0.0
   99 DO 5 K=1,112
      READ(1,3)X(K),BZ(K)
    3 FORMAT(F8.4,F8.2)
      AZ(K)=BZ(K)/(2985.*10**4.)
      IF(K.GT.1) GO TO 14
      R(K)=1.
      R1(K)=0.0
      RM(K)=1.
      GO TO 5


   14 AZA(K)=(AZ(K)+AZ(K-1))/2.0
      DX=(X(K)-X(K-1))/100.
      SIGMA=SIGMA+AZA(K)*DX
      AZC(K)=AZA(K)**2.
      AZD(K)=AZA(K)*AZC(K)
      AZ1(K)=(AZ(K)-AZ(K-1))/(X(K)-X(K-1))*100.0
      AZ1C(K)=AZ1(K)*AZ1(K)
    5 CONTINUE
      ERROR=((SIGMA/(4.*10.**(-7.)))-1.)*100.
      WRITE(2,333)SIGMA,ERROR
  333 FORMAT(1H ,6X,7H SIGMA=,F13.10,8X,7H ERROR=,F6.2)
      DO 20 K=1,112
      AZM(K)=AZA(114-K)
      XM(K)=X(113-K)
   20 CONTINUE
    9 READ(1,11)R0,R01,P1
   11 FORMAT(2F4.1,F5.1)
      IF(P1)13,0,0
      AB1=(S*P1)**2.
      AB2=3.*AB1
      AB3=AB1/2.
      AB4=AB1**(3./2.)/4.
      RM0=1.
      RM01=0.0
```

```
      DO 7 K=2,112
      ZO=(X(K)-X(K-1))/100.0
      G1(K)=S*AZA(K)*P1
      F1(K)=COS(G1(K)*ZO)
      F2(K)=SIN(G1(K)*ZO)
      R(K)=RO*F1(K)+RO1*F2(K)/G1(K)
      RA(K)=(R(K)+R(K-1))/2.
      RAC(K)=RA(K)*RA(K)
      RAD(K)=RAC(K)*RA(K)
      R1(K)=RO1*F1(K)-G1(K)*RO*F2(K)
      R1A(K)=(R(K)-R(K-1))/(X(K)-X(K-1))*100.0
      R1AC(K)=R1A(K)*R1A(K)
      H(K)=R1AC(K)/RAC(K)
      ZM=(XM(K)-XM(K-1))/100.0
      GM(K)=S*AZM(K)*P1
      FM1(K)=COS(GM(K)*ZM)
      FM2(K)=SIN(GM(K)*ZM)
      RM(K)=RMO*FM1(K)+RMO1*FM2(K)/GM(K)
      RMA(K)=(RM(K)+RM(K-1))/2.
      RM1(K)=RMO1*FM1(K)-GM(K)*RMO*FM2(K)
      RMO=RM(K)
      RMO1=RM1(K)
      RO=R(K)
      RO1=R1(K)
      IF(K.LT.112) GO TO 7
      FPROJ=1./R1(K)
    7 CONTINUE
      FS=FPROJ*FPROJ
      DO 40 K=2,112
      GA(K)=-FPROJ*RMA(114-K)
   40 CONTINUE
      FD=0.0
      FSD=0.0
      DO 10 K=2,112
      DX=(X(K)-X(K-1))/100.0
      FD=FD+(AZ1C(K)+AB2*(AZC(K)**2.)-H(K)*AZC(K))*RAD(K)*GA(K)*DX
      FSD=FSD+(3.+H(K)/(AB1*AZC(K)))*AZD(K)*RAC(K)*DX
   10 CONTINUE


      AD=3.0/(8.*FS)+AB3*FD
      SD=AB4*FSD
      WRITE(2,112)P1,FPROJ,AD,SD
  112 FORMAT(1H ,5X,F8.4,8X,F12.7,8X,F12.7,8X,F14.8)
      GO TO 9
   13 STOP
      END
```

APPENDICES

Appendix 6 : Scherzer's formula and the correction of spiral distortion in the electron microscope (A paper accepted for publication in 'Ultramicroscopy', North Holland (1977)

SCHERZER'S FORMULA AND THE CORRECTION OF SPIRAL DISTORTION IN THE ELECTRON MICROSCOPE

by F. Z. Marai and T. Mulvey

Department of Physics, The University of Aston in Birmingham, B4 7ET, U.K.

INTRODUCTION

There are few people working away at the improvement of the electron microscope who have not benefited greatly from the insight into electron optics provided by the writings and the spoken contributions at conferences of OTTO SCHERZER, starting with the "Geometrische Elektronenoptik" of Brüche & Scherzer and continued over the years with remarkable schemes and suggestions for correcting spherical and chromatic aberrations, schemes which are only now becoming fully technologically feasible.

For those who are working to perfect and improve the conventional electron microscope, Scherzer's "formulae" have always been of great value. In spite of the great technical progress that has been made in electron-optical instrumentation, these formulae always appear to be up-to-date, even those that were written forty years ago. This probably comes about because the author always worked from first principles and seemed to go to a lot of trouble to eliminate superfluous mathematical terms that were not really essential to the description of the physics of the process. Thus in the calculation of the spherical aberration coefficient C_s, he was able to eliminate the second differential coefficient of the variation of the magnetic field along the axis, thereby avoiding a great deal of difficulty in measuring or otherwise determining this awkward quantity. Furthermore, in proving conclusively that the spherical aberration coefficient of round lenses could unfortunately nevery be made to vanish he was characteristically not content to remain in a state of disappointment but immediately set about suggesting ways round the problem.

As a lighthearted but nevertheless very sincere tribute to Otto Scherzer in this "Festschrift", we would like to describe a recent application in our laboratory of one of his possibly less well-known calculations to a current problem, namely, that of correcting the anisotropic (spiral) distortion in the electron microscope. The relevant calculation of the coefficient D_{sp} of anisotropic distortion in electric and magnetic lenses was carried out and published by Scherzer forty years ago (Scherzer 1937) but until recently has not received a great deal of attention by electron microscope designers. For combined magnetic and electric fields the coefficient may be written in standard notation as follows:

$$D_{sp} = \frac{1}{16}\left(\frac{2e}{m}\right)^{\frac{1}{2}}\int_{z_o}^{z_i} BY^2V^{-3/2}\left[K - \frac{V'}{2}\frac{Y'}{Y} + V\left(\frac{Y'}{Y}\right)^2\right] dz$$

$$+ \frac{1}{32}\left(\frac{2e}{m}\right)^{\frac{1}{2}}\left[\frac{BY^2}{V^{\frac{1}{2}}}\left(\frac{3}{2}\frac{V'}{V} + 2\frac{Y'}{Y} - \frac{B'}{B}\right)\right]_{z_o}^{z_i} \qquad \text{........ (1)}$$

where $K = \frac{3e}{8m}B^2 + 9\frac{V'^2}{8v} + \frac{V'B'}{B}$, e/m is the ratio of charge to mass, V is the accelerating potential along the z axis, B is the flux density distribution along the z axis, and Y is a paraxial ray of height Y = 1 and slope $Y' = 0$, at $z = -\infty$. Dashes indicate differentiation with respect to z.

The importance of this calculation arises from the fact that spiral distortion is present to some extent in all electron micrographs taken so far in instruments with magnetic lenses, the well-known shape of this distortion being shown in Figure 1. If ρ is the radius of a point in the image, the distortion $\Delta\rho/\rho$ is given by

$$\frac{\Delta\rho}{\rho} = D_{sp} r^2 \qquad \text{....... (2)}$$

where r is the height of the incident electron in the projector lens. In the absence of a system for correcting the spiral distortion, r must be reduced until the spiral distortion falls to an acceptably low level. The chief source of this distortion is usually the final projector lens where the height of the ray r is large. Figure 2 shows schematically the arrangement of the final projection stage of an electron microscope. The projector lens shown in the figure is a low-distortion 'single-polepiece' projector lens (marai and Mulvey 1975) but otherwise the arrangement is conventional. The radial height r (Figure 3) is given by

$$r = \rho f_p / L \qquad \text{....... (3)}$$

where f_p is the projector focal length and L is the "projection distance" between projector lens and viewing screen of photographic plate. In practice, with conventional lenses L may have to be as large as 50 centimetres simply to minimise spiral distortion. At first sight, it might seem easy to correct this distortion by reversing the lens current in the preceding intermediate projector lens. This is usually ineffective with conventional lenses as the ray height r in the preceding lens is usually much less than that in the final projector.

The advent of miniature lenses (Newman and Mulvey 1972) has changed this situation since it is now feasible to place lenses quite close to each other so that the height of the electrons in each lens is comparable in magnitude. Moreover "single-polepiece" projector lenses (Marai and Mulvey 1974) as shown schematically in Figure 2 have made it possible to make significant reductions in the value of the spiral distortion coefficient.

It would therefore seem feasible to consider the possibility of correcting spiral distortion by a judicious arrangement of the last two projector lenses. Such a development could lead to a significant reduction in the height and therefore cost of an electron microscope column, especially that of a high voltage electron microscope. A shorter electron optical column would also be much less sensitive to the effects of external mechanical vibrations and AC magnetic fields.

The correction of spiral distortion

An extensive literature is available on the correction of radial distortion which has now been virtually eliminated from electron microscopes. In particular, radial distortion in the final projector lens can be eliminated by the judicious choice of lens excitation (Liebmann 1952).

Very little has been published about the correction of spiral distortion from either a theoretical or experimental point of view. As Scherzer has often pointed out, without a theoretical model to act as a guide, a purely experimental approach to the correction of aberrations can often be time-consuming and frustrating. It would, therefore, be very useful if a model field distribution of a lens could be used to simulate the situation of two projector lenses each suffering from spiral distortion, but of opposite sign, brought about by lens excitations of opposite sign. It would, of course, be possible to make use of the Glaser bell-shaped field for this purpose, but problems arise since this field distribution extends to infinity, so that as the two field distributions of the opposite sign approach each other, severe cancellation of the field takes place. The magnetic field distributions from real lenses are much narrower so that it would be difficult to correlate experimental and theoretical results. In the rectangular-field model, the axial magnetic field is constant over an axial region of length S and zero everywhere else along the axis.

The paraxial properties of this model have been studied extensively by Durandeau and Fert (1957) and would appear to be very convenient for the investigation of spiral distortion. However, this model is often considered unsuitable for the calculation of aberrations, since the field derivative $\frac{dB}{dz}$ takes on infinite values at the beginning and the end of the field. Fortunately, an inspection of Scherzer's equation 1, shows that in a projector lens, where the integration extends from $z = -\infty$ to $z = +\infty$, no such difficulties should, in fact, arise in the calculation of the spiral distortion coefficient. Applying equation 1 therefore to the square-topped magnetic field distribution in which $B_z = B =$ Constant for $S > Z > 0$ and zero for all other values of Z, one obtains in the absence of electric fields:

$$D_{sp} = \frac{3}{4} \left(\frac{dB^2}{8mV_r}\right)^{3/2} \int_{-\infty}^{+\infty} Y^2 \, dz + \frac{1}{4} \left(\frac{dB^2}{8mV_r}\right)^{\frac{1}{2}} \int_{-\infty}^{+\infty} (Y')^2 \, dz \qquad \text{.........(4)}$$

Where V_r is the relativistically corrected accelerating voltage. In the rectangular field model the paraxial ray Y, for which $Y_o = 1$ and $Y' = 0$ at $z = -\infty$, has the simple form

$$Y = \cos \left(\frac{eB^2}{8mV_r}\right)^{\frac{1}{2}} Z \qquad \text{.........(5)}$$

and

$$Y' = - \left(\frac{eB^2}{8mV_r}\right)^{\frac{1}{2}} \sin \left(\frac{eB^2}{8mV_r}\right) Z \qquad \text{.........(5a)}$$

Inserting Equation (5) in Equation (4) one obtains for the coefficient of spiral distortion:

$$D_{sp} = \left(\frac{eB^2}{8m\,V_r}\right)^{3/2} \frac{S}{2} + \frac{1}{8}\left(\frac{eB^2}{8mV_r}\right) \sin 2 \left(\frac{eB^2}{8mV_r}\right)^{\frac{1}{2}} S \quad \ldots\ldots\ldots\ldots (6)$$

Since BS = μ_oNI, where NI is the lens excitation and $\mu_o = 4\,\pi \times 10^7$ henry-m^{-1}, equation 6 may be written:

$$D_{sp}S^2 = \frac{1}{2}\left(\frac{\mu_o^2 e}{8m}\right)^{3/2}\left(\frac{NI}{V_r^{\frac{1}{2}}}\right)^3 + \frac{1}{8}\,\frac{e\mu_o^2}{8m}\left(\frac{NI}{V_r^{\frac{1}{2}}}\right)^2 \sin 2\left(\frac{e\mu_o^2}{8m}\right)^{\frac{1}{2}}\left(\frac{NI}{V_r^{\frac{1}{2}}}\right) \quad \ldots\ldots\ldots (7)$$

Remembering that the angle or rotation θ of the image for this model field is given by:

$$\theta = \left(\frac{eu_o^2}{8m}\right)^{\frac{1}{2}}\left(\frac{NI}{V_r^{\frac{1}{2}}}\right) = 0.1863\left(\frac{NI}{V_r^{\frac{1}{2}}}\right) \quad \ldots\ldots\ldots (8)$$

Equation (7) can be written in the simpler form:

$$D_{sp}\,S^2 \simeq \frac{\theta^3}{2} + \frac{\theta^2}{8}\sin 2\theta \quad \ldots\ldots\ldots (9)$$

In order to use equation (9) as the basis of a universal curve, let D_{sp_o} denote the value of D_{sp} at an angle of rotation θ_o corresponding to the minimum focal length of the lens.

Then $$\frac{D_{sp}}{D_{sp_o}} = 1.1086\left(\frac{\theta}{\theta_o}\right)^3 + 0.1365\left(\frac{\theta}{\theta_o}\right)^2 \sin 4.06\left(\frac{\theta}{\theta_o}\right) \quad \ldots\ldots\ldots (10)$$

Since $\frac{NI_o}{V_r^{\frac{1}{2}}}$ = 10.9 for this field model (cf.Mulvey and Wallington 1973)

$$\frac{D_{sp}}{D_{sp_o}} = 1.1086\left(\frac{NI}{NI_o}\right)^3 + 0.1365\left(\frac{NI}{NI_o}\right)\sin 4.06\left(\frac{NI}{NI_o}\right) \quad \ldots\ldots\ldots (10a)$$

Equations (9) and (10) indicate that the spiral distortion is closely related to the cube of the image rotation angle θ, and therefore to the cube of the excitation. However, there is an additional oscillatory term of smaller, but not negligible magnitude.

Nevertheless the approximation $\frac{D_{sp}}{D_{sp_o}} = \left(\frac{NI}{NI_o}\right)^3$ which neglects this term, is remarkably accurate for conventional polepiece lenses, as shown in Figure 4. The points in this figure, calculated from Equation (10a), indicate that the error involved in this approximation is about 10% for an excitation $NI/NI_o = 0.77$, falling to 2% at $NI/NI_o = 1.25$. Included in the graph are representative values taken from calculations by Liebmann (1952) for a range of lenses with S/D values between 0.2 and 2. These points also lie close to the corresponding values calculated from Equation (10a). In order to calculate the actual value of D_{sp} or the related constant $C_{sp} = D_{sp}R^2$ (Liebmann 1942) where R is the radius of the lens bore, Table 1 gives the values of $C_{sp_o} = D_{sp_o}R^2$, and $NI_o/V_r^{\frac{1}{2}}$ obtained in recent calculations by the authors. These extend the data previously published by Liebmann (1952). The agreement with the brand of Liebmann's data is good but our calculations are, in general, some 4% lower than those obtained by Liebmann.

TABLE 1

S/D	0.1	0.2	0.6	1	2	4	8
$C_{sp_o} = D_{sp_o}R^2$	1.95	1.87	1.31	0.78	0.25	0.067	.014
$NI_o/V_r^{\frac{1}{2}}$	14.6	14.3	14.0	13.5	12.5	12.0	11.0

Experimental measurements (unpublished) with projector lenses have shown that this oscillatory character of the spiral distortion coefficient shown in Equation (10a) is indeed present in actual lenses, although it is often smoothed out in published calculations (cf. Liebman 1952). The above results therefore give some confidence in the application of the Scherzer formula to the rectangular-field model.

Distortion in the electron microscope

Table 1 above shows that the spiral distortion coefficients of magnetic lenses vary by two orders of magnitude, yet it is known that all these lenses produce a similar amount of distortion for a given image size and projector length L. It is not always realized that the spiral distortion in the final image of the electron microscope is not directly related to the distortion coefficient D_{sp}. Consider the arrangement shown in Figure 3. An incoming ray of height r is magnified by an amount L/f_p giving an image radius ρ on the final screen. Here f_p is the projector focal length and L the "projection distance". The distortion $\Delta\rho / \rho$ produced by the lens is given by $\Delta\rho / \rho = D_{sp} r^2$. Thus if the distortion is not to exceed a given amount $\Delta\rho$, the projection distance L must satisfy the inequality

$$L \geqslant (\sqrt{D_{sp}}\ f_p.) / \left(\frac{\Delta\rho}{\rho}\right)^{\frac{1}{2}} \qquad \text{........ (11)}$$

$$= Q\ \ \rho / \left(\frac{\Delta\rho}{\rho}\right)^{\frac{1}{2}} \qquad \text{........ (12)}$$

where $Q = \sqrt{D_{sp}}.f_p$ is the essential parameter of lens quality that determines the minimum length L. A low Q value therefore indicates a projector lens of good quality. Q is close to unity for twin-polepiece lenses. Taking ρ = 50mm and spiral distortion less than 2% ($\Delta\rho/\rho$ = .02), L must be greater than 354mm. A further condition must also be satisfied in a practical situation. In a real projector lens there will be a limiting aperture of radius R as shown in Figure 3. In a conventional lens this will usually be the lens bore. In order that this aperture should not limit the size of the image

$$L \geqslant f_p \, \rho / R \qquad \text{........ (13)}$$

Thus, if the bore radius is too small, the minimum value of L may have to be made much longer than that set purely by lens distortion.

The projector focal length f_p of the rectangular field is given by (cf. Mulvey and Wallington 1973)

$$f_p = \frac{S}{\theta \sin \theta} \qquad \text{........ (14)}$$

From equation (8) $\sqrt{D_{sp}} = (\frac{1}{2}\,\theta^3 + \frac{1}{8}\,\theta^2 \sin 2\,)^{\frac{1}{2}}/S$

Hence $$Q = \sqrt{D_{sp}}\,.\,f_p = (2\theta + 0.5 \sin 2\theta)^{\frac{1}{2}}/2 \sin \theta \qquad \text{.... (15)}$$

The corresponding equation in terms of the lens excitation parameter NI/NI_o may be readily derived in the way described above. The variation of Q as a function of lens excitation parameter $\frac{NI}{NI_o}$ is shown in Figure 5 for the rectangular field ($S/D = \infty$), calculated from equation (15) and for S/D = 0.2 calculated for S/D = 0.2 by inserting the axial field distribution into Scherzer's equation (1). These two curves confirm that the lens geometry has a negligible effect on the spiral distortion in the image. In the useful region of excitation, around $NI/NI_o = 1$, of maximum magnification and low radial distortion, the value of Q is close to unity for this wide range of lens geometry. These curves also show that one cannot find a lens geometry that will produce a relatively large amount of distortion in an intermediate lens for the purposes of correction of distortion in the final image.

The lowest curve in Figure 5 shows the Q value for the exponential field distribution (cf. Marai and Mulvey 1975) for the favourable direction in which electrons enter the 'tail' of the field, and proceed towards the maximum value. In the region of maximum magnification the Q value is appreciably lower (about 20%) than that of conventional lenses; furthermore, it remains at this low level over an appreciable range of magnification, making the adjustment of a correcting lens less critical. The exponential field distribution is closely realized in single-polepiece projection lenses. The exponential-field model thus suggests that an improved performance is possible in projector lenses by the use of single-polepiece lenses. A further advantage of these lenses is that the absence of a second polepiece bore largely removes the restriction on the radius of the incident beam that occurs with conventional lenses.

The correction of spiral distortion

If the electrons are incident in the opposite (unfavourable) direction, the spiral distortion coefficient of a single-polepiece lens can increase by a factor of nearly two, for the same focal length. This is a valuable property for an intermediate correcting lens, since here one wishes to have as large a distortion coefficient as possible. The reason for this is that the spiral distortion coefficient of this lens is reduced by a factor M^2 when referred to the final image plane, where M is the magnification of the intermediate lens. Thus with the above data the appropriate value of M would be of the order $\sqrt{2}$ for the correction of spiral distortion at maximum magnification. Figure 6 shows the proposed arrangement. The lens excitations are, of course, arranged in opposition so that the spiral distortions will cancel.

In practice such a small magnification is likely to cause difficulties, since the lens fields may tend to reduce each other. For this reason it is preferable to operate the correcting lens in the 'second-zone' focal region i.e. at an increased excitation. Since the spiral distortion of the intermediate lens will increase as the cube of the excitation this will enable a higher intermediate magnification to be employed.

Such a corrected system should allow a substantial reduction in the projection distance L, and therefore of the total instrument height, to be achieved. Reduction of L will, of course, entail a corresponding reduction of total magnification, but this will be compensated by the additional magnification of the correcting lens. Experiments are now in progress to realize these possibilities.

Conclusion

It is clear that electron microscopists are greatly indebted to Otto Scherzer for laying such lasting theoretical foundations for the future development of the electron microscope. This fund of knowledge has not only enabled us to understand the ultimate limits of electron microscopy but has also provided a constant source of practical inspiration for the detailed improvement of the instrument.

References

Durandeau, P. and Fert, C. (1957) Re.Cp.Theor.Instrum. 36, 205-234.

Liebmann, G. (1952) Proc.Phys.Soc. B, 65, 94-108

Marai, F.Z. and Mulvey, T. (1974) Proc.8th Int.Conf.on Elec.Micros. pp. 130-131, Austr.Acad.Sci., Canberra.

Marai, F.Z. and Mulvey, T. (1975) in "Developments in Electronic Microscopy and Analysis" ed. Venables, Academic Press, pp.43-44.

Mulvey, T. and Newman, C.D. (1972) Electron Microscopy 1972 (London, Institute of Physics). pp.116-117.

Mulvey, T. and Wallington, M.J. (1973) Rep.Prog.Phys. 36, 347-421

Scherzer, O. (1937) in "Beiträge zur Elektronenoptik" ed. H. Busch and E. Brüche. J. A. Barth, Leipzig, pp. 34-41.

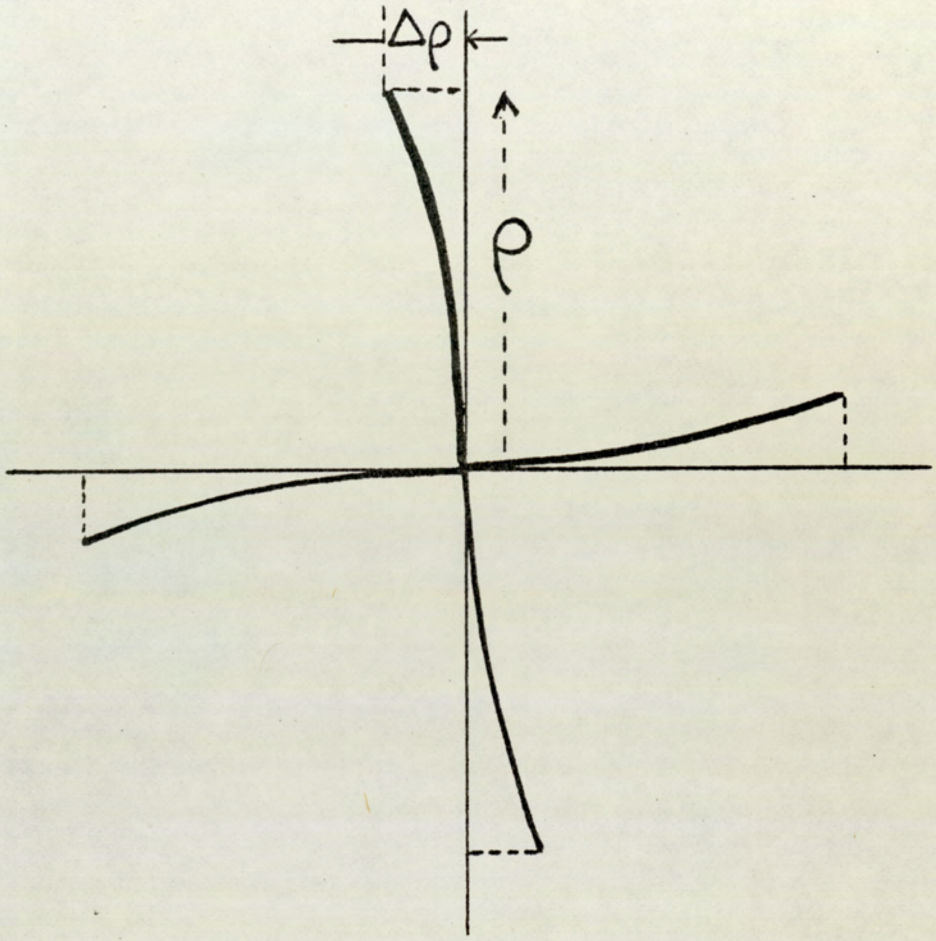

Fig.1 Spiral distortion ($\Delta\rho/\rho$) in the electron microscope image.

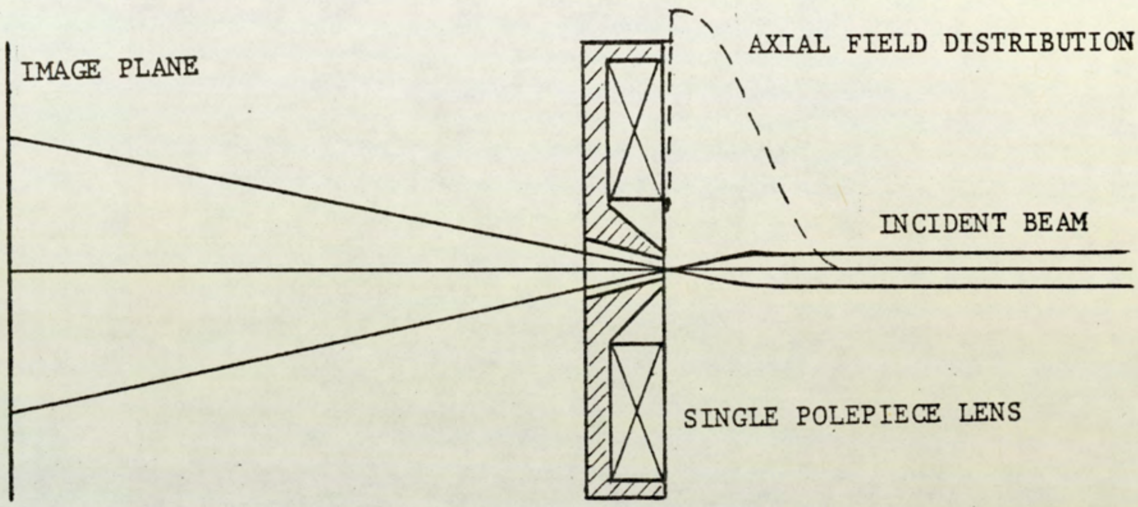

Fig.2 Schematic arrangement of the final projection stage of an electron microscope with single-polepiece projector lens.

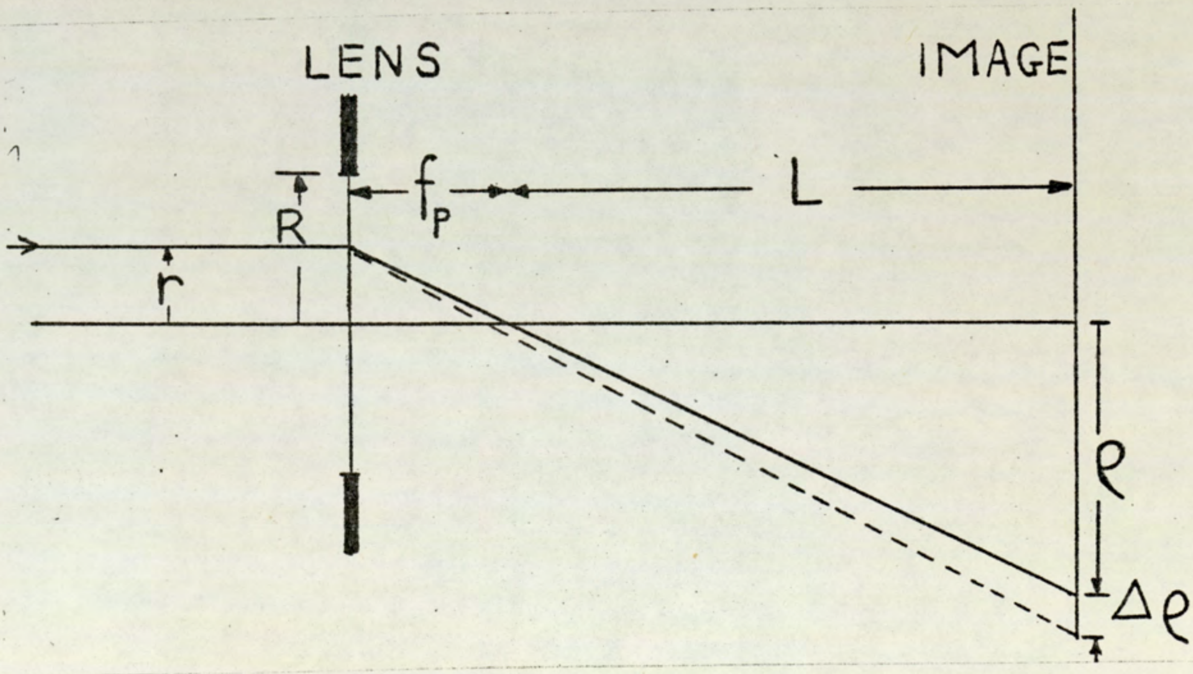

Fig.3 Geometrical relations in the final projector stage of the electron microscope. L-projection distance, r - height of incoming ray, R - radius of lens aperture, ρ - radius of image.

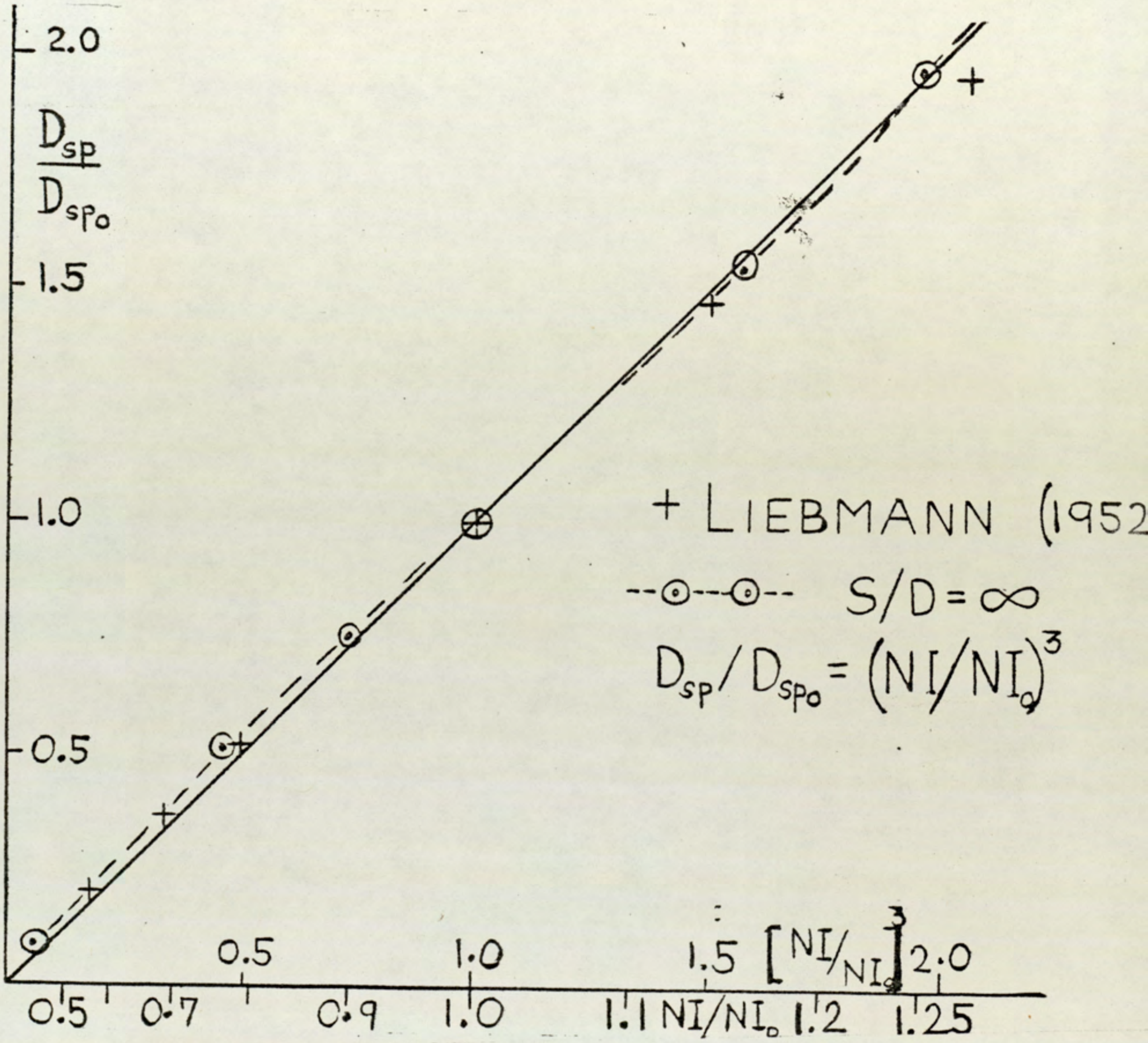

Fig.4 Relative distortion coefficient $\left(\frac{D_{sp}}{D_{sp_o}}\right)$ as a function of the cube of relative lens excitation $\left(\frac{NI}{NI_o}\right)^3$

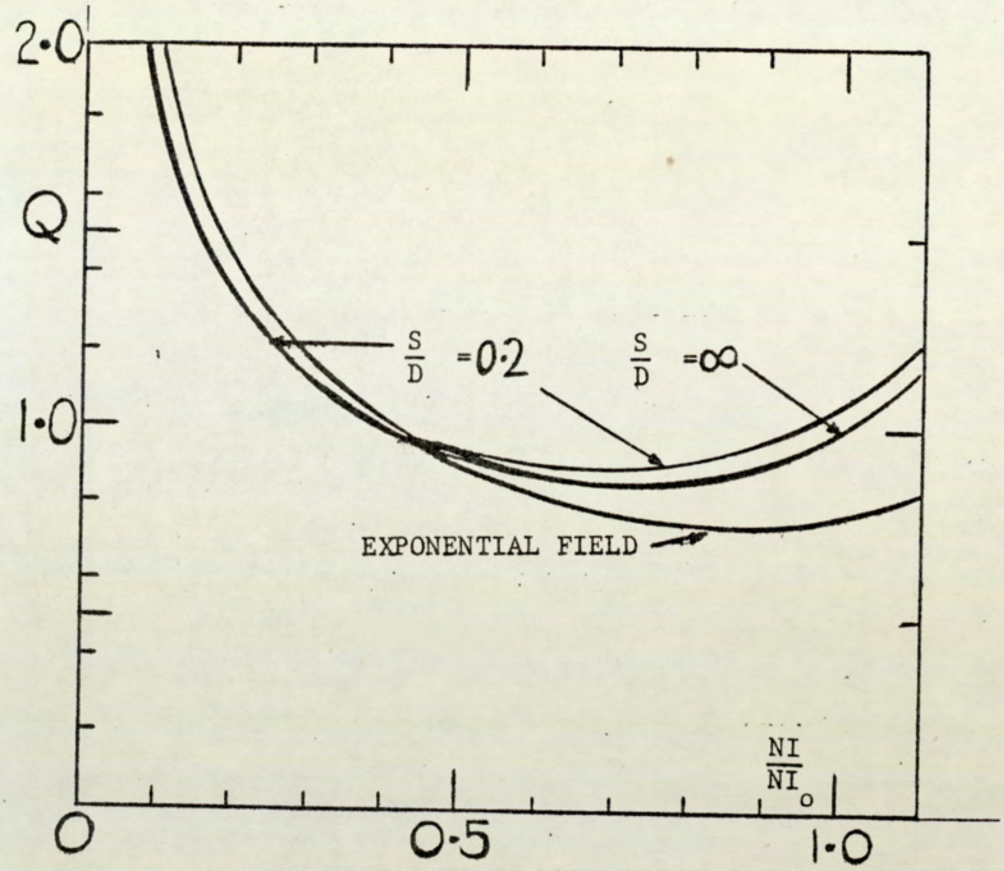

Fig.5 Projector lens distortion-parameter $Q = \sqrt{D_{sp}} \cdot f_p$ as a function of relative excitation, for conventional lenses (top two curves) and for the exponential-field model (bottom curve).

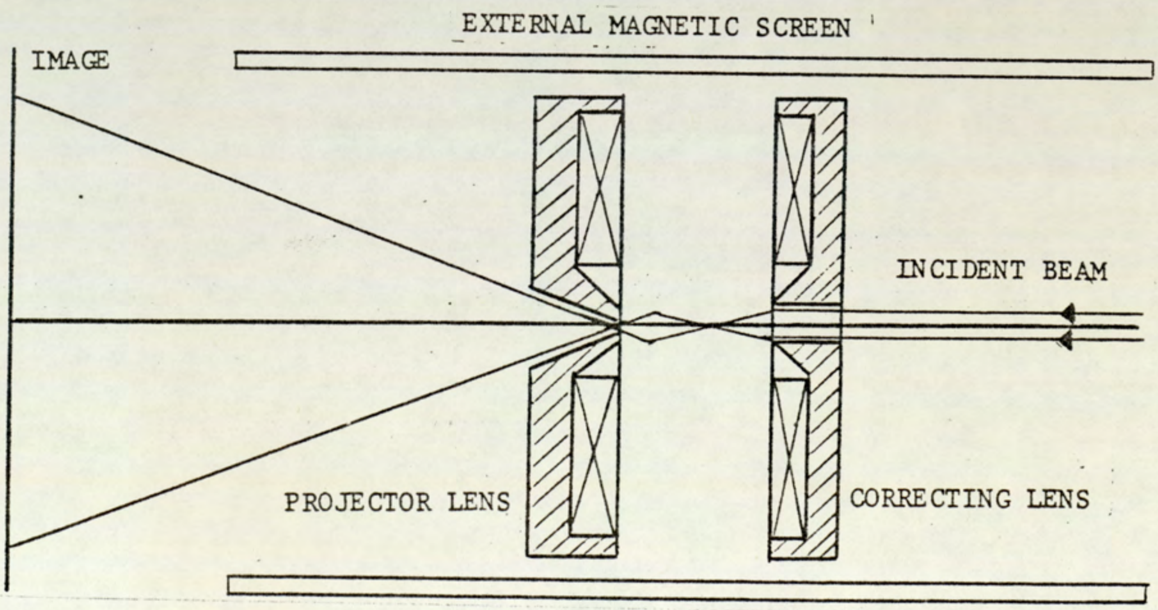

Fig.6 Schematic arrangement for correcting spiral distortion by two rotationally-opposed single-polepiece lenses.

APPENDICES

Appendix 7 : A proof of the relation $C_d = \frac{C_s}{f^3} R^2$ at low lens excitation.

Appendix 7

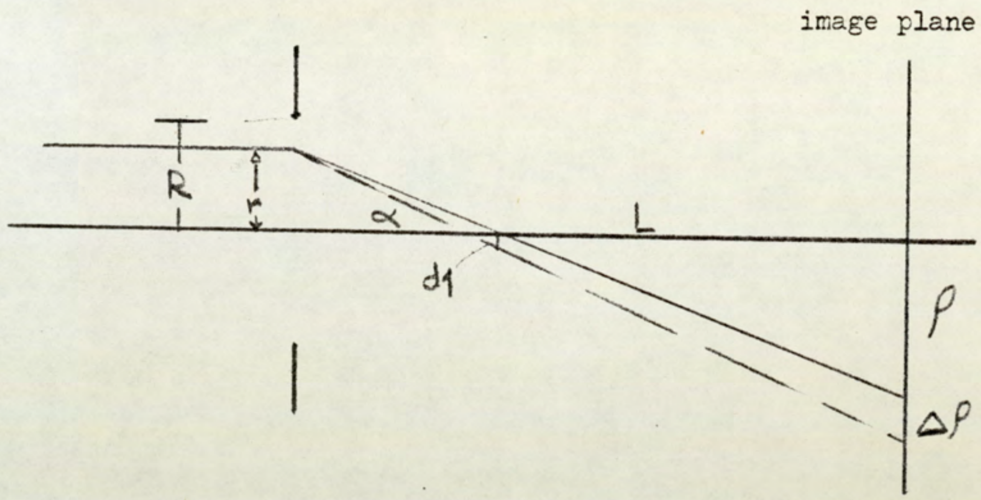

Considering the above figure, we have:

the diameter of the disc of confusion is given by

$d_1 = C_s \alpha^3$, where is the angle subtended by the ray at the axis, and C_s is the spherical aberration coefficient.

If the magnification of the image plane is M, then

$$M = \frac{L}{F}$$

where L is the projection distance, and f is the projector focal length, which is the same as the objective focal length, for weak lens condition. The deviation $\Delta\rho$ from the Gaussian image at the image screen, is given by

$$\Delta\rho = M\, d_1$$

$$= \frac{L}{F}\, C_s \quad {}^{3} \qquad (1)$$

But $\alpha = r/f$, where r is the initial height of the electron beam.

Hence,

$$\Delta\rho = \frac{L}{F}\ \frac{r}{f}^{3}\ C_s, \qquad (2)$$

and $\rho = M_r = \frac{L}{F}\, r \qquad (3)$

The radial distortion of the image is given by

$$\frac{\Delta\rho}{\rho} = C_d\left(\frac{r}{R}\right)^2$$, where C_d is the radial distortion coefficient, and R is the radius of the bore of the lens. Hence

$$\frac{\Delta\rho}{\rho} = C_d\left(\frac{r}{R}\right)^2 = r^2 \frac{C_s}{F^3} \tag{4}$$

or

$$C_d = \frac{C_s}{F^3} R^2 \tag{5}$$